The University Of Sheffield.

The Effects of Particle Reinforcements on Chip Formation and Machining Induced Damage in cutting of modified epoxy Carbon Fibre Reinforced Polymers

Marius Monoranu

A Thesis submitted in partial fulfilment of the requirements for the degree of Doctor of Philosophy

The University of Sheffield

Faculty of Engineering

Department of Mechanical Engineering

February 2022

ACKNOWLEDGMENTS

I would like to thank my parents for their love and support through my academic journey.

I would like to express my appreciation to my supervisors Hassan Ghadbeigi, Patrick Fairclough and Kevin Kerrigan. Hassan is a meticulous person with a high attention to detail, 'a machining book' which made sure that every piece of written content is slashed in red before going out in the world. This way I improved my writing skills and analytical skills making sure I have a solid science backed up thinking. Patrick is a passionate professor with thousands of brilliant ideas which inspired me to delve into the unknown and continuously ask myself questions about my research. Kevin is a world leader in the field of machining of composites which had an invaluable industrial input into my research. Without their time and dedication, I couldn't reach this stage in my career.

Thanks to university staff including Jamie Booth, Dave Webster, Cheryl Shaw, Ian Ross, Richard Kay, Ria Mitchell, Joana Bates for their support in my experimental work. Thanks to Rachel Thorley and Peta Kirk for their GTA help along my PhD. I'd also like to thank to the IDC team and students such as Oscar or Luke who helped me so much during the past 4 years. I've been lucky to have friends like Fernando who always helped me with composite theory questions. Special thanks to Sam who acted as a mentor for composite materials field and with whom I managed to collaborate on several research papers.

Thanks to Edi, Vladut, Gicu for their daily laughs which spiced my daily research life. Thanks to my amazing friends Mihnea, Fanel, Dragos and Nicole who supported me in some crucial moments during my PhD journey.

I would like to express my gratitude to my dearest friend Gabriela who was a source of inspiration at the start of this journey and seen me grow both personally and professionally as the PhD has taken shape.

ABSTRACT

Multifunctional and multiphase materials, such as traditional carbon fibre reinforced polymers (CFRPs), are designed to achieve greater functionality compared to their individual constituent materials. Coupling individual material phases creates new hybrid materials with improved performance by reducing dimensions, weight, expense and energy consumption, while enhancing safety, design, and manufacturing versatility. The unique characteristics of particulate reinforcements such as size, shape, concentration and mechanical properties necessary to create a beneficial change to the polymer matrix (i.e., by increasing the fracture toughness of a brittle polymer), together with the advancement in polymer characterisation and simulation techniques, have generated a great deal of interest in the field of CFRPs with modified epoxy matrices. In manufacturing of epoxy-based composite materials, machining operations are often required to achieve tight geometric tolerances or ensure edge-of-part mechanical performance. Even though cutting process parameters are controlled to minimise machining induced damage, an in-depth assessment of the relation between material removal mechanism, material properties and machining induced damage is required.

The aim of this project is to alter the mechanical properties of the epoxy resin through the introduction of particle reinforcement, to better characterise the subsequent chip formation process and machining induced damage in cutting of epoxy modified carbon fibre reinforced polymers. This is completed through a series of experimental studies which will facilitate the in-situ observations of material removal mechanism in cutting of silica and rubber modified epoxy CFRPs. A manufacturing technique is developed to include silica nanoparticles and rubber microparticles in the epoxy matrix of CFRPs. Tensile and fracture toughness tests were conducted to quantify the effect of particle reinforcements and results are further used in the discussion of the machining results. A novel orthogonal cutting rig coupled with a 2D High Speed Digital Image Correlation (DIC) system was developed to study the material removal mechanism of polymer and CFRP samples at a micro scale level. Current state-of-the-art 3D areal metrics are used to quantify machining induced damage, while microscopy is used to provide qualitative data of the machined surface. The extent of subsurface damage is assessed using micro –

Computed Tomography (CT) scanning. Finally, to address the industrial application of this research, the machining performance of epoxy modified CFRPs under edge trimming conditions is analysed.

It has been found that the addition of rubber microparticles and silica nanoparticles affects the material removal mechanism in both orthogonal cutting and edge trimming conditions as such the cutting forces and machining induced damage tend to decrease with the addition of rubber particles. Design of experiment (DoE) and analysis of variance (ANOVA) methods employed in the edge trimming study showed a statistical correlation between particle concentrations, machining variables, cutting forces and surface metrics. Experimental evidence gathered by white-light and Scanning Electron Microscopy (SEM) showed that rubber toughening mechanism ensured an efficient energy dissipation mechanism limiting crack propagation and extent of subsurface damage. The brittle state of silica and unmodified epoxy proved ineffective in reducing machining induced damage.

This thesis provides fundamental work in the addition of particle reinforcements in the epoxy matrix of a CFRP material, with an in-depth assessment of the optimum cutting parameters and material properties needed to ensure low damage machining processes. Gaining understanding of the physics of chip formation process of particle modified epoxy composites will enable designers and engineers a greater ability to introduce particle reinforcements during Design for Manufacture (DFM) stages of product design leading towards damage-free machining of high-value composite parts.

DECLARATION

I, the author, confirm that the Thesis is my own work. I am aware of the University's Guidance on the Use of Unfair Means (www.sheffield.ac.uk/ssid/unfair-means). This work has not been previously been presented for an award at this, or any other, university.

Publications

1. M. Monoranu, R. L. Mitchell, K. Kerrigan, J. Patrick A. Fairclough, and H. Ghadbeigi, "The effect of particle reinforcements on chip formation and machining induced damage of modified epoxy carbon fibre reinforced polymers (CFRPs)," Compos. Part A Appl. Sci. Manuf., vol. 154, no. December 2021, p. 106793, 2021, doi: 10.1016/j.compositesa.2021.106793.
2. M. Monoranu, H. Ghadbeigi, J. P. A. Fairclough, and K. Kerrigan, "Chip formation mechanism during orthogonal cutting of rubber and silica modified epoxy polymers," Procedia CIRP, vol. 103, pp. 176–181, 2021, doi: 10.1016/j.procir.2021.10.028.
3. M. Monoranu, S. Ashworth, R. M'Saoubi, J. P. A. Fairclough, K. Kerrigan, R. J. Scaife and H. Ghadbeigi, "A comparative study of the effects of milling and abrasive water jet cutting on flexural performance of CFRP", Procedia CIRP, vol. 85, pp. 277–283, 2019, doi: https://doi.org/10.1016/j.procir.2019.09.036.
4. S. Ashworth, J. P. A. Fairclough, M. Monoranu, H. Ghadbeigi, J. Meredith, Y. Takikawa and K. Kerrigan, "Epifluorescent microscopy of edge-trimmed carbon fibre-reinforced polymers: An alternative to computed tomography scanning", Adv. Compos. Lett., vol. 29, pp. 1–8, 2020, doi: 10.1177/2633366X20924676.

Presentations

1. “Chip formation mechanism during orthogonal cutting of rubber microparticles and silica nanoparticles modified epoxy polymers”, in 9th CIRP Global Web Conference, October 2021
2. “A comparative study of the effects of milling and abrasive water jet cutting on flexural performance of CFRP”, 2nd CIRP Conference on Composite Material Parts Manufacturing, October 2019
3. “Analysis of chip formation in orthogonal cutting of UD CFRP using Digital Image Correlation”, Annual IDC Machining Science Conference, May 2019
4. “Characterisation of machining induced damage in composite materials”, AMRC Internal Conference, June 2018
5. “Experimental analysis of machining induced damage of slot-milled CFRPs”, Annual IDC Machining Science Conference, May 2018

Posters

1. “The effect of machining induced damage on flexural performance of slot-milled fibre reinforced polymers (CFRP) specimens”, AMRC Internal Conference, June 2018

TABLE OF CONTENTS

LIST OF FIGURES

Rake angle (degrees)											
	30	I	III	III	III	III	III	IV			
	20	I	III	III	III	III	III	IV			V
	10	I	III	III	III	III	III	IV	V	V	V
	0	II	III	III	III	III	IV	V	V	V	V
	-10	II	IV	III	IV	IV	IV				
	-20					IV		V			V
		0	15	30	45	60	75	90	105	120	135
	Fibre orientation (degrees)										

LIST OF TABLES

NOMENCLATURE

Symbols

α	Rake angle	°
a	Crack length (Fracture toughness tests)	mm
γ	Clearance angle	°
D	Tool diameter	mm
Δh	Enthalpy change	J/g
E	Modulus of elasticity	MPa
ε_f	Strain at failure	%
F	Applied failure load (Fracture toughness tests)	N
F_t	Feed per tooth	mm/ tooth
F_N	Feed per revolution	mm/ rev
F_x	x-direction cutting force	N
F_y	y-direction cutting force	N
F_z	z-direction cutting force	N
λ_c	Waviness filter	mm
K_{IC}	Fracture toughness	MPa $m^{1/2}$
K_Q	Stress intensity factor at failure	MPa $m^{1/2}$
G_{IC}	Fracture energy	J/m^2
h	Specimen thickness (Fracture toughness tests)	mm
l	Sampling length	mm
n	Number of flutes	
N	Spindle speed	RPM
Q	Failure load (Fracture toughness tests)	N
r	Tool radius	µm
$\bar{r}$	Characteristic length	mm
V_C	Cutting speed	m/ min
w	Specimen width (Fracture toughness)	mm

Acronyms

AWJ	Abrasive Water Jet
AMRC	Advanced Manufacturing Research Centre
ANOVA	Analysis of variance
CFRP	Carbon fibre reinforced polymer
CT	Computerized tomography
CVD	Chemical vapour deposition
DAQ	Data acquisition
DGEBA	Diglycidylether of bisphenol A
DIC	Digital Image Correlation
DMA	Dynamic mechanical analysis
DOE	Design of experiment
DSC	Differential scanning calorimetry
EEW	Epoxy equivalent weight
HS	High Speed
HSS	High Speed Steel
MNS	Maximum normal strain (%)
PAN	Polyacrylonitrile
PCD	Polycrystalline diamond
PTU	Programmable timing unit
RT	Room temperature
RTM	Resin transfer moulding
SEM	Scanning electron microscopy
SS	Shear Strain (%)
T_g	Glass transition temperature
UD	Unidirectional
VARTM	Vacuum assisted resin transfer moulding

1. INTRODUCTION

The recent advances in composite materials science and manufacturing technologies have made composites a good alternative to commonly used materials in aerospace, automotive, shipbuilding, railway, sports, or wind energy industry. A relevant example from the aerospace industry is the Airbus A350, CFRP content is more than 50% by weight. CFRPs have a high strength and good stiffness to weight ratio, which drives the weight reduction and increase fuel efficiency of the aircraft [1].

High-performance polymer matrix composites typically use epoxy resins as the matrix for continuous fibres [2] as they have high strength, good chemical resistance, provide excellent adhesion to various substrates and have a low cost compared to their competitors. However, due to their high cross-linked density, epoxy polymers have a poor resistance to crack initiation and growth. The addition of a second phase, which consists of well-dispersed nano/microparticles, can significantly increase the toughness and mechanical properties of the epoxy matrix [3]–[5] with well documented toughening mechanism for a wide range of nanoparticles and epoxies [6]–[12]. The mechanical properties, such as tensile & compressive strength and modulus, flexural stiffness, scratch resistance, toughness of a composite material can be improved by controlling variables of the particulate fillers (e.g. filler type, size, volume, concentration, dispersion) [13]–[15]. Currently, particle-modified composites are used in a wide range of industries including, but not limited to, aerospace [16], automotive [17], medicine [18], microelectronics [19], [20] and wind power [21].

Even though composite components are often made near-net shape, machining operations are often unavoidable. For example, in the Airbus A350 1.2 million holes have to be introduced and CFRP edge trimming operations are required to achieve high tolerances of the components [22]. Due to the anisotropic and inhomogeneous state of CFRPs given by a matrix and a reinforcement with different orientations relative to the cutting edge, traditional metal machining techniques cannot be transferred directly to composite machining. Incorrect application of machining operations lead to creation of machining induced damage, including delamination, intralaminar cracking, matrix shearing and burns, fibre pullouts which affect the structural integrity of the machined part [22].

Similar to conventional composite materials, particle-modified composites require features, such as holes and net edges, to be generated via material removal processes after production to achieve tight geometric tolerances and ensure edge-of-part mechanical performance. However, little information is available on their behaviour under such finishing operations. The ultimate effect of such defects is a potential reduction in mechanical performance leading to catastrophic failure events [23].

The fundamental interaction between cutting tool and workpiece is studied in the literature via orthogonal cutting, where the tool edge engages with the material perpendicular to the direction of the cut. This simplified two-dimension cutting problem avoids the complexity of other machining operations where multiple cutting edges are engaged with the material at the same time and it allows to study the mechanics of chip formation, cutting forces evolution, friction conditions and temperature generated during cutting [22]. This process is affected by a wide range of factors including fibre orientation, tool configurations and cutting parameters, which are all documented in the literature. There are several studies investigating the toughening mechanisms and mechanical properties of a wide range of industrially available nanoparticles and microparticles, in particular silica and rubber, mixed in different epoxy blends and their composites [2], [4]–[8], [10], [11]. However, from the machining point of view the available knowledge is only limited to unmodified epoxy CFRPs. In order to fill this gap in the knowledge, the effect of particulate fillers on material removal mechanism and machining induced damage of epoxy modified CFRPs were investigated. This will provide fundamental work in the incorporation of micro and nano fillers in the epoxy matrix of a CFRP material, with an insight to the optimum cutting parameters to ensure low damage machining processes.

1.1 Aim and objectives of the research

This research project aims to analyse the effects of particle-modified epoxy CFRPs in relation to cutting mechanism including cutting forces, chip formation, surface metrics and subsurface damage. To achieve the aim, the following objectives are set:

- Undertake a literature review on the machining of composite materials covering the fundamental of orthogonal machining of CFRPs and machining operations in different engineering applications. This will highlight the current state of the art in

nanoparticle-modified epoxies, the main factors involved in the chip formation process in conventional machining of CFRPs and machining induced damage.

- Identify the optimum CFRP material architecture/ type and manufacturing technique where the particle reinforcements can be included in the matrix phase and their characteristics (i.e., particulate type, size, concentration) can be controlled.
- Provide a methodological framework to manufacture, characterization and analysis of individual material phases and the mechanical properties of the manufactured CFRP.
- Evaluate the effect of CFRP material variables (i.e., fibre orientation, fibre architecture, layup configuration, matrix mechanical properties, nanoparticle type and volume, composite mechanical properties) on machinability performance in a series of consecutive studies:
    - Effect of nanoparticles in orthogonal machining of toughened epoxy polymers by considering cutting forces, chip formation process, fracture mechanism;
    - Effect of nanoparticle-modified epoxy matrix on chip formation process, cutting forces and subsurface damage in CFRP samples having a UD and woven fibre architecture;
    - A study of effect of particulate-modified epoxy matrix in edge trimming of CFRPs.

1.2 Novelty statement

The novelty of this project consists of understanding the effect of silica nanoparticles and rubber microparticles on machining mechanics as well as machining induced damage of modified epoxy CFRPs. The analysis of material removal mechanism of particulate-modified CFRPs at a micro scale level will improve the fundamental knowledge of chip formation and machining induced damage of CFRPs. This will ultimately result in a better understanding of industrial level CFRP machining operations leading towards damage-free machining of high-value parts. In order to fulfil the novelty statement aligned with aim and objectives of this research project, the following actions were planned:

- In order to investigate the fundamentals of cutting, an experimental set-up orthogonal cutting rig will be designed and manufactured, which will allow in-situ observations of the cutting mechanism and chip formation process at a micro-scale level.
- Assess and provide a statistical correlation of the effect of matrix variables on chip formation process in machining of CFRPs;
- Identify and correlate machining induce damage with chip formation process by considering CFRP material and machining variables;
- The creation of a link between fundamentals of orthogonal cutting and edge trimming in terms of material removal mechanism, machining induced damage, cutting forces and surface integrity. SEM observations of machined surface in orthogonal cutting vs edge trimming trials will be compared to assesses the outcome of particulate reinforcements in both cutting conditions. Cutting force trends for one tool rotation in edge trimming trials will be correlated with cutting force behaviour identified in orthogonal cutting trials. Material removal mechanism detailed in orthogonal cutting trials will be used characterize machining induced damage and surface integrity of CFRP samples machined in edge trimming trials.

1.3 Thesis outline

This thesis contains eight chapters including:

- Chapter 1. Introduction – This chapter states the aim and objectives of the research highlighting the knowledge gap in machining of modified epoxy CFRPs and the actions which are planned to fulfil the stated novelty statement.
- Chapter 2. Literature review – This chapter contains an introduction into composite materials focusing on manufacturing and machining of CFRPs. The importance of the matrix properties is analysed along with methods of improving mechanical properties of the composite by enhancing the properties of the matrix system. The relation between machining and mechanical properties of the composite material is discussed to put the research into context. The history and fundamentals of

machining of CFRPs is presented and current state of the art is acknowledged. Finally, the main research question is formulated.

- Chapter 3. Project Methodology – The methods used to manufacture, characterise and test the CFRP samples used in machining trials are presented in Chapter 3. The carbon fibres, epoxy resin and particulate reinforcement used to manufacture CFRP panels are introduced. The development of an in-situ orthogonal cutting rig coupled with a Digital Image Correlation (DIC) system and description of the machine, cutting tools, and jig design used in an edge trimming machining trial are presented. The post-machining analysis techniques used to characterise machining induced damage are detailed.
- Chapter 4. Characterisation of mechanical properties of polymer and CFRP samples – This chapter presents the results of the characterisation and mechanical tests done in order to ensure that samples provide consistency. The effect of particle reinforcements on mechanical properties of CFRP samples and the individual toughening mechanism were analysed and discussed.
- Chapter 5. Cutting mechanics of particulate-modified epoxy matrices – This chapter presents the results and discussion of the orthogonal cutting trial which analyses the effect of particle reinforcements on machinability of epoxy modified samples. The measured cutting forces are correlated with machined surface features, material removal mechanism and DIC strain evolution maps. Finally, a link is established between the particulate reinforcement failure mechanism and the chip formation process.
- Chapter 6. Cutting mechanics of modified epoxy CFRPs – This chapter provides a study into machining of epoxy modified CFRP samples under orthogonal cutting conditions. The effects of particle reinforcements on the recorded cutting forces, chip formation process and machining induced damage of the epoxy modified CFRP samples are analysed. SEM and micro – CT analysis are used to provide qualitatively and quantitively results on the extent of subsurface damage. Finally, a correlation is established between the reinforcement type, and its concentration and the chip formation process, surface metrics and machining induced damage.

- Chapter 7. Cutting mechanics in an industrial level machining operation – This chapter provides the results of a DoE and ANOVA methods employed in an edge trimming study providing a statistical correlation between particle concentrations of the samples, machining variables, cutting forces and surface metrics.
- Chapter 8. Conclusions & future work – This chapter presents the conclusions from the experiments presented in this thesis. Future work recommendations are done based on the findings of this thesis.

2 LITERATURE REVIEW

This chapter contains an introduction into composite materials focusing on CFRPs, manufacturing methods and machining of composites. The importance of the matrix properties is analysed along with methods of improving mechanical properties of the composite by enhancing the properties of the matrix system. The relation between machining and mechanical properties of the composite material is discussed to put the research into context. Finally, the main research question is formulated along with a comprehensive set of key process variables list for composite manufacture, testing and machining.

2.1 Composite materials

A composite material is made from two or more physically distinct and mechanically separable constituent materials[24]. The combination of the phases results into a material with characteristics superior from the individual components. Historically, composite materials existed on Earth in a natural form – wood and bones. However, over the last forty years, plastics and ceramics based composite materials have been the dominant emerging materials[25]. Composite materials have several advantages when compared to traditional engineering materials including metals and alloys. This includes good mechanical properties (tensile strength, flexural modulus and temperature resistance) and a high strength to weight ratio [26]. As it is shown in Figure 1, composite materials have a high modulus and relatively low density when compared to metals and alloys, which represents a good choice for a wide range of applications and industries such as machine tools, sports goods, automotive industry, wind power energy and biomedical products [26]–[28]. Due to these advantages, the annual production of composite materials is increasing year by year (15%) due to the developments in the manufacturing process and the low cost of production [26]. However, they have several disadvantages compared to traditional materials including costs, highly specialised manufacturing procedures required, brittleness and low fracture toughness.

Composites can be categorized in many ways based on their phase and reinforcement type, individual phase distribution, orientation or form, fabrication process or phase

properties. Figure 2 shows a classification based on the matrix types, which can be metal, ceramic or polymer, and the continuous fibre materials which could be carbon, glass, aramid, or natural fibres. The focus of this thesis is on Carbon Fibre Reinforced Polymers that is discussed in Section 2.2.

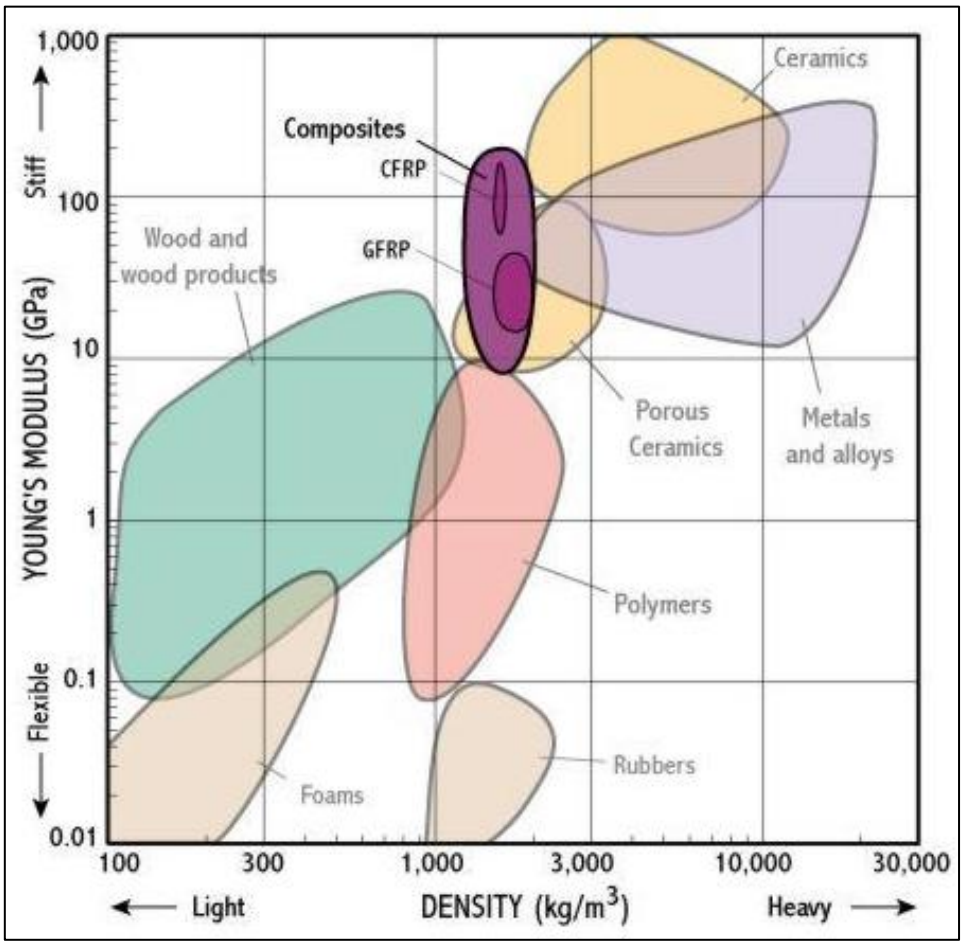

Figure 1 - Young's Modulus vs Density for most engineering materials currently used in the industry **[29]**

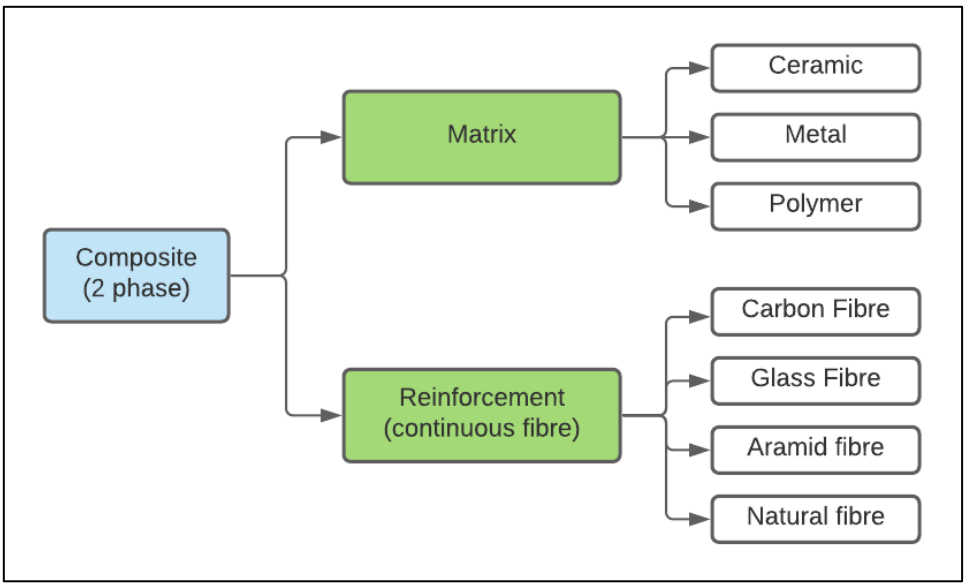

Figure 2 - Composite classification based on the matrix and reinforcement (continuous fibre) **[22], [30], [31]**

2.2 Carbon Fibre Reinforced Polymers (CFRPs)

In a CFRP composite, where the matrix is made out of a polymer, e.g., epoxy, polyester, or nylon, carbon fibres act as reinforcement element bearing the tensile loads, while the matrix transfers the load between the fibres and protects the reinforcement from mechanical damage and outside chemical attack [26]. The contact region between the fibre and matrix is called the interface. Figure 3 shows a typical fibre reinforced composite material at which the combination between the two phases results into a lamina. The fibres are generally organised in sheets of parallel fibres put side by side or weaved in fabric, known as a ply and final laminate or bulk materials are obtained by stacking unidirectional (UD) plies together, often with different angle of fibres and connected with the matrix as it shown in Figure 3 – b. Laminates with UD plies stacked in only one direction are often used to achieve maximum mechanical performance in the direction the CFRP component is loaded.

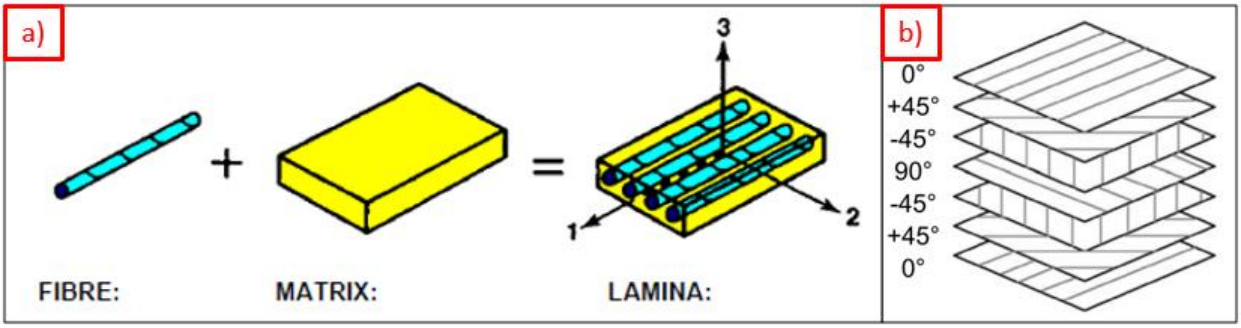

Figure 3 – a) Example of fibre reinforced composite material [5] b) Example of UD Laminate where plies are stacked over each other in different directions

CFRPs dominate the aerospace industry due to the high strength, stiffness and low weight[32].Figure 4 illustrates the percentage of fibre reinforced polymers (FRPs) used in aircrafts produced by leading world manufactures. The aircrafts produced in early 1980's had only 2-7% of FRPs, while currently the percentage increased to 50%. This increase in usage and demand happened due to a series of factors including FRPs mechanical and structural properties, relative low cost of production, high strength to weight ratio, corrosion and electrical properties of FRPs. Overall, polymer matrices are the most used in composite industry due to the wide range of properties that result from different molecular configurations that they can achieve [22].

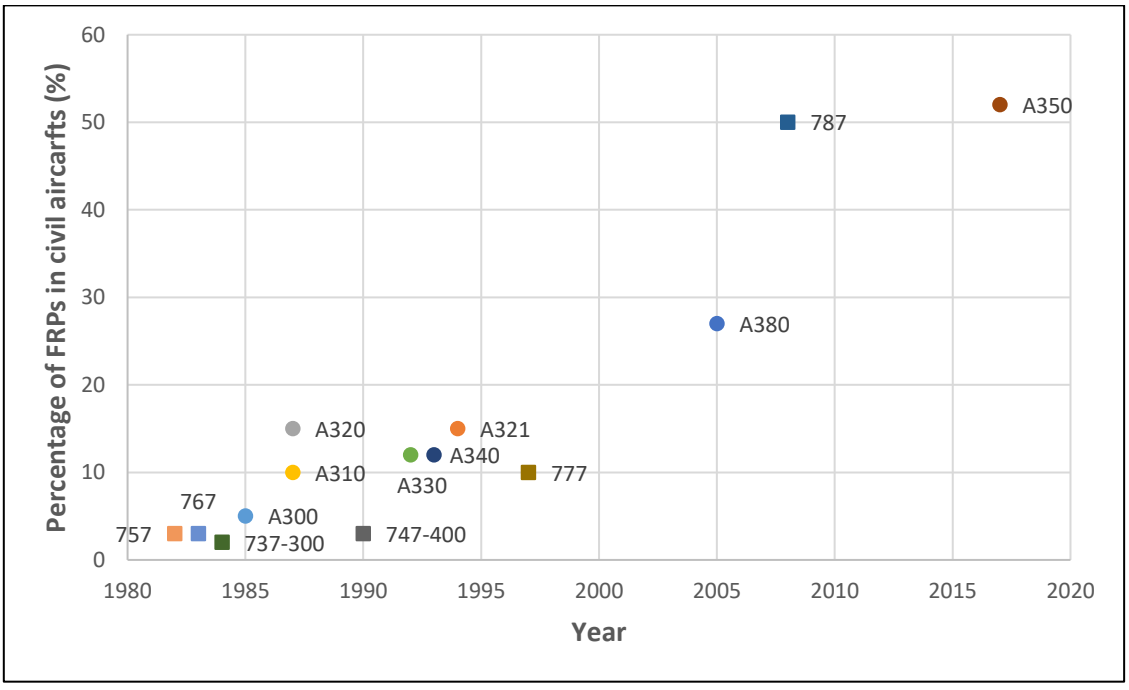

***Figure 4 - Development of FRPs composite mass in structural body of civil aircrafts by Airbus and Boeing* [1]**

2.2.1 Carbon fibres

Carbon fibres are almost universally manufactured from PAN (polyacrylonitrile) [22], with limited manufacture through synthetic methods [33]. Carbon fibres are chosen as a reinforcement based on individual properties such as tensile strength and modulus, thermal and electrical properties, fatigue strength, density, volume and cost. Table 1 lists a classification based on mechanical properties of the fibres. The variation of strength and stiffness is obtained by changing variables in the carbon fibre manufacturing process [22] as illustrated schematically in Figure 5. In the stabilization stage the fibres are chemically altered at 200° - 300°C to improve atomic structure. In carbonization the fibres are inserted into a furnace at 1000° - 2000° C where the non-carbon atoms are lost, therefore the remaining structure has strong bonded carbon atoms. Carbon fibres can be graphitized at an even higher temperature, 2000° – 3000° C to achieve higher carbon content, therefore higher mechanical performance in the fibre direction [34]. HM and UHM fibres require higher temperature and longer dwell times in the furnace, which results in a higher cost. The next steps, surface treatment and sizing are critical to fibre performance as adhesion between fibre and matrix is crucial in carbon fibre reinforced composites. Usually, fibres are coated with a thin layer of material which increase the surface area available for bonding of matrix and fabric. Each fibre manufacturer has its own unique material sizing formulation and it can include plasticizers, anti-static agents, antifoams or rheology modifiers [35]. Fibres are then grouped into towns or yarns consisting of 2 to 12,0000 individual fibres [22].

Table 1 - Classification of carbon fibres based on tensile properties **[22], [36]**

Properties	Fibre type					
	General purpose grade	HS (High Strength type)	SHS (Super High Strength & High strain type)	IM (Intermediate Modulus)	HM (High Modulus)	UHM (Ultra High Modulus)

Tensile Strength (MPa)	500-1200	2400 - 4500	5000 - 6000	3000 - 5500	2000 - 2500	2000 - 2500
Tensile modulus (GPa)	50 - 100	200 - 250	200 - 250	265 - 320	320 - 440	> 440
Strain to failure (%)	0.5 - 2	1 - 2	> 2	1 - 2	0.5 - 1	< 0.5

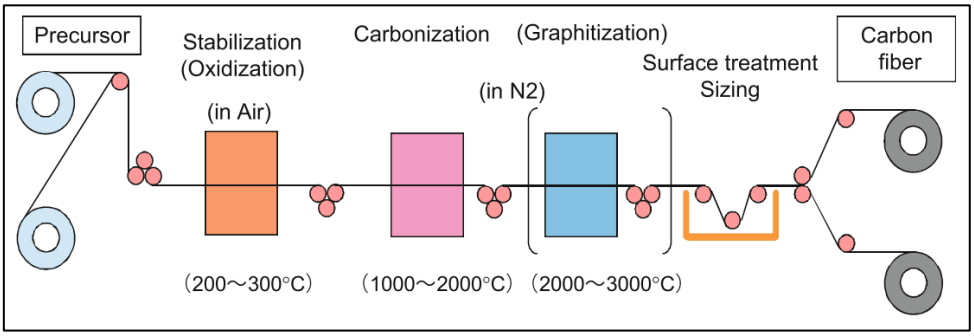

Figure 5 – Heat-treatment process for PAN carbon fibre production (adapted from* [34]*)

In a CFRP laminate with continuous fibre reinforcement, each ply of carbon fibre tows can have a different arrangement; it may include unidirectional tows, woven or non-woven fabrics (bi-dimensional or bi-directional) and multidimensional fabrics with fibres oriented along several directions. A fabric is defined as an assembly of continuous fibres which produces a sheet of one or more layers of fibres [37]. Figure 6 shows various fibre architecture options available on the market. A suitable fibre architecture is chosen at the design stage based on the load that CFRP component is subjected to, i.e., if the component has to resist to torsion loads, a 2D fabric is recommended, while in the case of one directional load, the user should choose UD plies. In UD fabrics, the fibres are held together using an adhesive strip or fine weft or in the case of 0/ 90° fabrics, 0° and 90° fibres can be stitched on the same ply. Woven fabrics are the most used due to a wide range of pattern which can be create using warp (0°, up and down orientation) and weft (90°, left and right orientation) fibre tows. In a plain wave, the tows are following an over/ under pattern giving the fabric stability as fibres are maintaining the orientation and weave angle. Plain

weaves are mostly used in flat sheets and geometries which are simple and do not have complex contours. Twill weave is the most recognized carbon fibre fabric. Either in a 2x2 or 4x4 pattern, it can be used in complex geometries and at the same time the stability of the fabric is maintained [37]. Satin weaves are fundamentally twill weaves modified to produce fewer intersections of warp and weft, while basked weave is the same as plain weave except that two or more warp fibres alternately interlace with two or more weft fibres [37]. Fabrics in leno weave are normally used in conjunction with other weave styles due to their gaps between fibres, which cannot produce a viable composite material.

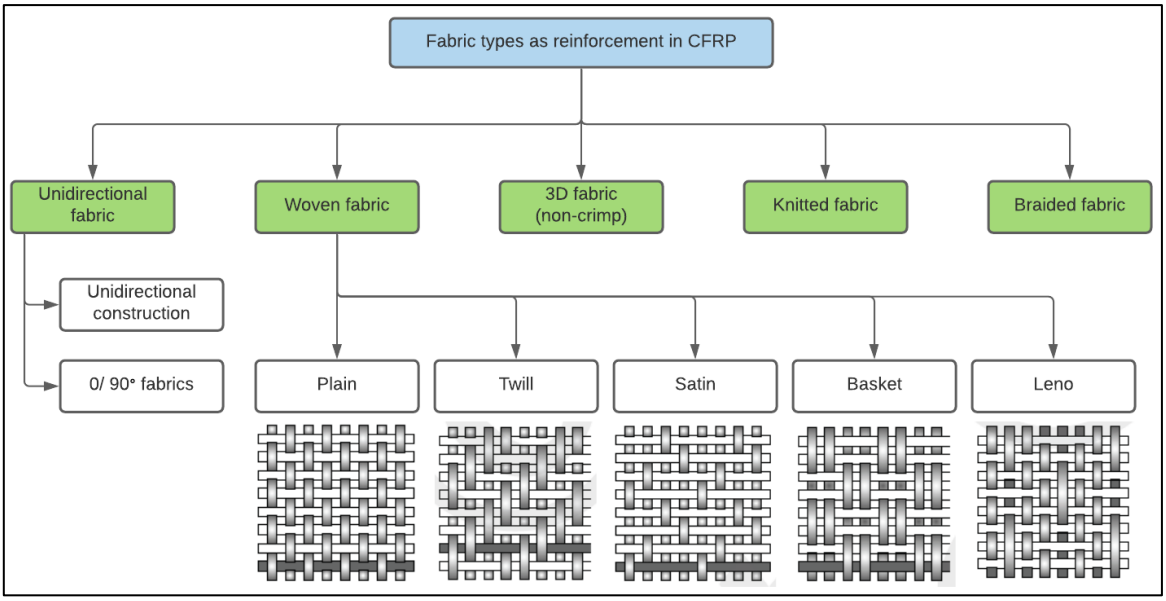

Figure 6 – Fabric types as reinforcement in CFRP (adapted from* [37] *and* [38]*)

2.2.2 Matrix system

The principal functions of a matrix are to keep the fibres in place in the structure, help to transfer the load between fibres and to protect the filaments from external environment and handling [39]. Polymer matrices are the most used one in composite industry due to the wide range of properties that result from the different molecular configuration that they can achieve [22]. Figure 7 shows a classification of existent polymer matrices, while their mechanical properties are shown in Table 2.

Thermosets consists of long hydrocarbon molecules with primary bonds holding the atoms in the molecule together [22]. Thermosets undergo chemical reactions with a hardener that crosslink the atomic polymer chains and thus connect the entire matrix together in a

three-dimensional network. This process is called curing. Thermosets tend to have high dimensional stability, high-temperature resistance, and good resistance to solvents, because of their three-dimensional cross-linked structure [40]. Unlike the curing process of thermosetting resins, the processing of thermoplastics is reversible, and, by simply reheating to the process temperature, the resin can be formed into another shape if desired [26]. Thermoplastics can be melted, while thermosets when heated enough start disintegrating and they may ignite. The curing process for thermosets usually takes a couple of hours at an increased temperature, while for thermoplastics the curing can finish in couple of seconds.

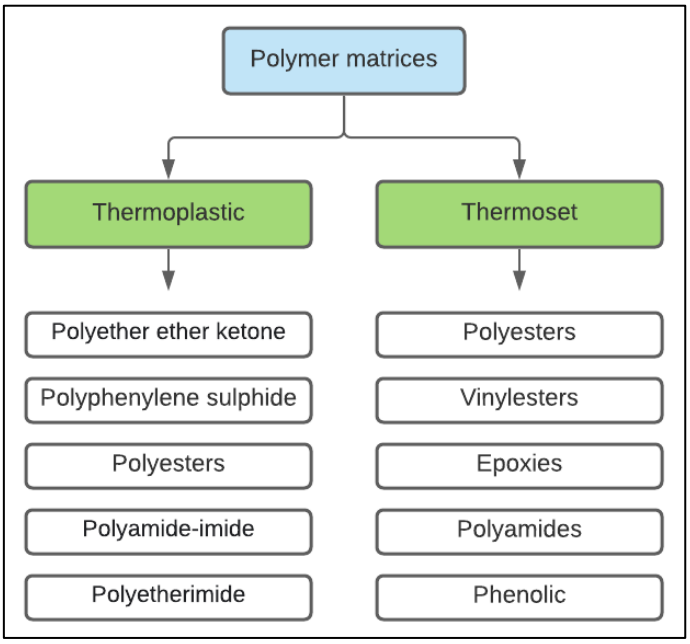

Figure 7 – Types of polymer matrices **[40]**

Table 2 - Mechanical properties of polymer matrix materials at room temperature [22]

	Density (mg/m^3)	Young's modulus (GPa)	Tensile strength (MPa)	Strain to failure (%)
Thermoplastic				
Polyether ether ketone	1.26 – 1.32	3.2	93	50
Polyphenylene sulphide	1.36	3.3	84	4.0

Polyetherimide	1.27	3.0	105	60
Polyamide-imide	1.4	3.7 – 4.8	93 – 147	12.17
Thermosets				
Polyesters	1.10 – 1.23	3.1 – 4.6	50 – 75	1.0 – 6.5
Vinylesters	1.12 – 1.13	3.1 – 3.3	70 - 81	3.0 – 8.0
Epoxies	1.10 – 1.20	2.6 – 3.8	50 – 75	1.5 – 8.0
Phenolics	1.00 – 1.25	3.0 – 4.0	60 – 80	1.8

Epoxy thermoset resins are important industrial polymers and first used in aerospace industry in secondary aircraft structures, but currently are used in primary structures, such as wings and fuselages [41]. These provide an attractive combination of handling characteristics, processing, flexibility, composite mechanical properties, ease of manufacture, acceptable cost[39]. As shown in Figure 8, there is a large number of epoxy combinations, which include different curing agents, fillers, diluents, accelerators and fillers for an epoxy resin. The user will mainly choose the right epoxy matrix system based on desired composite properties and manufacturing method. The glass transition temperature, T_g, is generally defined as the temperature at which a material alters state – going from rigid to a more flexible, rubber compound and an epoxy cured with an aliphatic amine tend to have a low T_g, and it cannot be used in a high temperature environment, while an aromatic amine require elevated curing temperatures which produce a high T_g which is suitable for composites used in high temperature environment [40]. Accelerators are mostly used to speed up the curing reaction. In some cases, some hardeners in low percent per weight are used as accelerators to speed up the curing reaction. On the other hand, to control the viscosity of the polymer, diluents are added to the mixture that have an important role where the manufacturing method is based on impregnation of fibres with resin. Fillers, also known as particle reinforcements are usually combined with the epoxy matrix to improve the properties of composite system. Particulate fillers are further detailed in section 2.2.3.

The work in this thesis focuses on epoxy resins used frequently in aerospace composites coupled with a cycloaliphatic polyamine hardener. This system of epoxy – hardener was chosen to comply with CFRP manufacture requirements, which involves impregnation of carbon fibres with different fibre architectures.

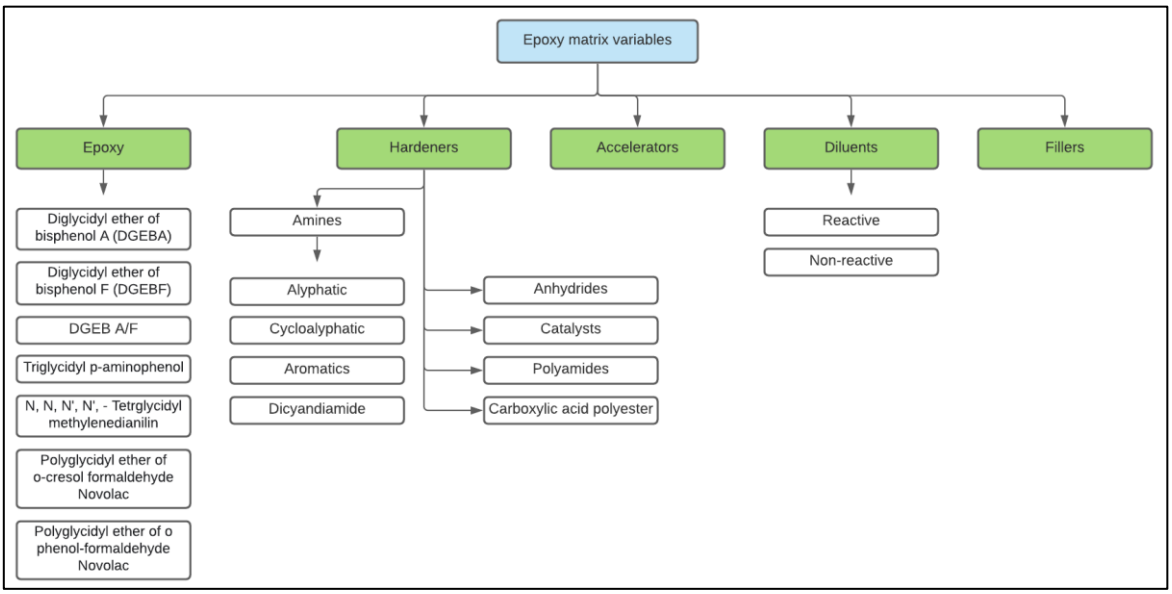

Figure 8 – Epoxy matrix variables **[14], [42]**

2.2.3 Particulate fillers

There is a wide range of fillers, which can be used to modify the properties and characteristics of epoxies. Figure 9 shows the main filler variables and typical epoxy properties which can be modified. As would be expected, incorporation of filler, invariably produces a substantial increase in mechanical and physical properties, the magnitude of which being dependent on the filler type and its characteristics [14]. Other benefits may include greater thermal conductivity given by mineral fillers, reduction of shrinkage during curing of thermoset polymers which reduces the warpage or cracking of the moulded parts, increased electrical conductivity for electronic and electrical applications [14], [43]. However, adding filler has several disadvantages including increased weight and viscosity which is likely to influence the processing behaviour of the epoxy system. Another major disadvantage is that incorporation of fillers create machining difficulties as the condition of material is changing [14]. This aspect is further elaborated in section 2.4.5.

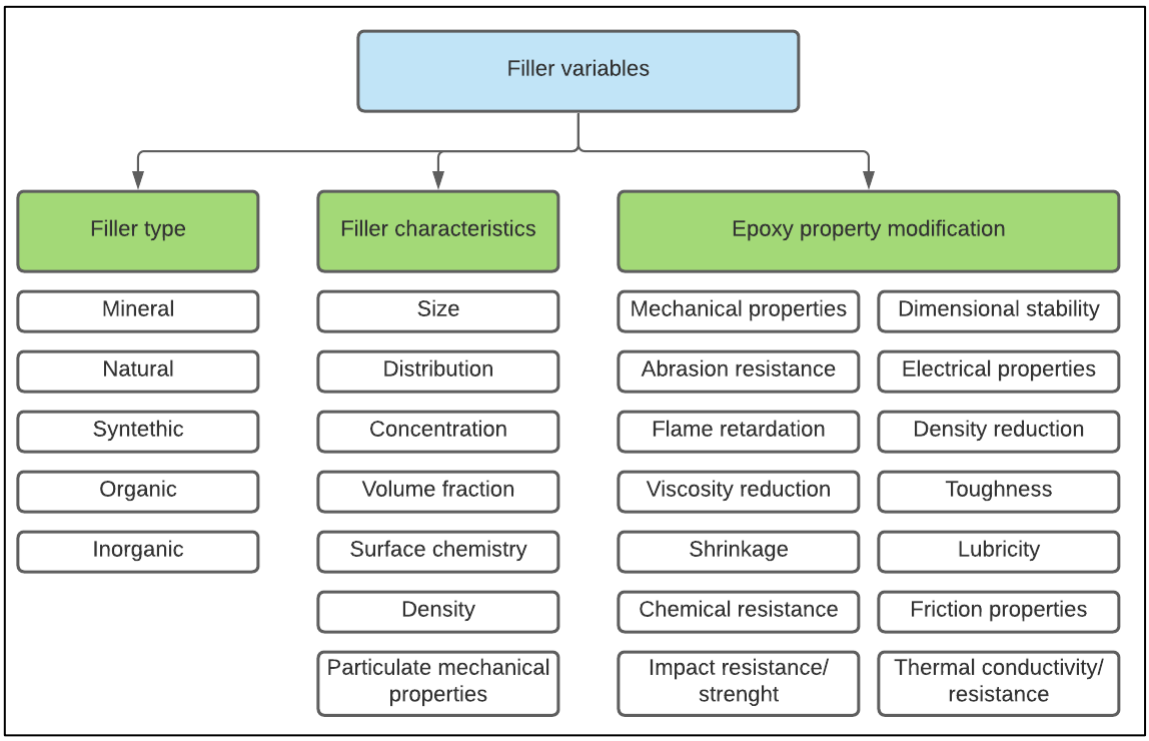

Figure 9 – Filler variables **[43]**

Thermoset epoxy polymers are rigid and brittle due to their high degree of crosslinking [4]. This brittleness and lack of crack growth resistance limit their structural application as engineering materials. Therefore, toughening of epoxies has become a necessity to ensure the feasibility of these materials for practical applications [3]. Toughening refers to the improvement of fracture resistance of a material. The addition of a second phase, either rigid or soft, can be a solution to improve the resistance of the polymer matrix against crack initiation and subsequently increasing the fracture toughness of brittle epoxies. Fracture toughness is measured in either the energy-based terms of G, the energy-release rate (the sum of the energy release as new surfaces are formed, and by plasticity processes) at which fracture occurs, or as a stress intensity factor K. A possible change in the values of either of these parameters is related to the application of particulate fillers.

Rubber particles are the most commonly used, and generally effective, modifiers for toughening epoxy polymers [4]. Even though there is an increase in toughness, rubber particles can lower the strength and modulus of the epoxy. On the other hand, the rubber particles can increase the viscosity of the polymer during manufacture, which is a disadvantage in composite manufacturing process [44]. In the past 20 years, commercial

grade surface-modified silica nanoparticles were introduced in the market and proved to improve properties such as tensile strength & modulus, flexural stiffness, scratch resistance and toughness [11]. Due to their small size, usually 20nm in diameter, silica particles increase the resin viscosity only slightly and can penetrate between fibres easily during composite manufacturing process [11].

2.2.4 Rubber and silica toughening mechanism

Figure 10 shows the toughening mechanism due to the presence of both rubber and silica fillers in a polymer matrix. The mechanisms that could occur due to the presence of a secondary phase in the matrix include shear band formation near particles, fracture of the particles, debonding and tearing of particles, crack deflection, crazing, developing of a plastic zone at craze tip, crack pinning or shear yielding of the particles. These failure modes may occur individually or simultaneously in a toughened polymer depending on the loading and particle type. Each mechanism contributes to the energy absorption and have an impact on the crack growth resistance.

Material removal mechanism in machining of composite materials is a series of intermittent fractures occurring in front of the cutting tool [22], therefore toughening mechanism of particulate reinforcements of modified epoxy CFPRs could modify chip formation process. This could result in a reduction in machining induced damage, which needs further investigation.

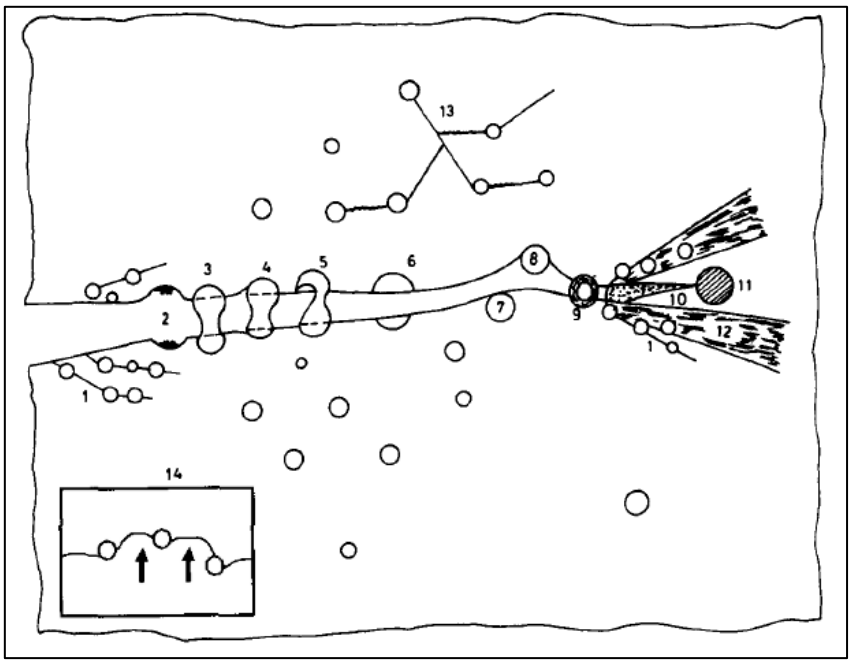

Figure 10 – Crack toughening mechanism in rubber/hard particle modified polymers: (1) Shear band formation near rubber particles; (2) Fracture of rubber particles after cavitation; (3) Stretching; (4) Debonding and (5) Tearing of rubber particles; (6) Transparticle fracture; (7) Debonding of hard particles; (8) Crack deflection by hard particles; (9) Voided/ cavitated rubber particles; (10) Crazing; (11) Plastic zone at craze tip; (12) Diffuse shear yielding; (13) Shear band/ craze interaction; (14) Crack pinning (adapted from* [45], [46]*)

The toughening mechanism of rubber particles in epoxy thermoset polymers is well analysed in the literature [2], [3], [44], [47]–[49]. Yee and Pearson [48] and Kinloch et al. [49] reported that crack growth resistance in the rubber-modified epoxy is due to the large energy-dissipating deformation occurring in the vicinity of the crack-tip [45]. This toughening mechanism is backed-up by micrographic evidence and several modelling studies which supports the theory [4], [47], [50], [51]. The deformation process of a polymer toughened by addition of rubber microparticles consists of (a) plastic shear-banding in the epoxy polymer (Figure 10 – (1)) and (b) particle cavitation and subsequent plastic void growth of the epoxy polymer (Figure 10 – (9)) [4], [48], [49]. Plastic void growth of the epoxy matrix occurs after particle cavitated and represent the main energy dissipation method [7]. Figure 11 shows an example of fractured surface containing voids in the observed surface generated due to rubber cavitation mechanism. The evolution of crack growth and fracture process ahead of the crack tip is shown in Figure 12 where the cavitation of rubber particles results in voids initiation that leads to the shear bands formation ahead of the crack tip. The stress concentration zones around the particles

initiate shear sites for plastic shear deformation to occur. This zone blunts the crack that results in plastic deformation in the material below and above the surface of the crack. The creation of this plastic zone through shear yielding is considered the major source of energy dissipation [45], [51]. The crack propagates further through the material when the link between the voids can no longer support the applied stress. There is a general agreement that the cavitation itself has negligible contribution to fracture energy, however, rubber cavitation is a prerequisite to plastic deformation of the matrix [3].

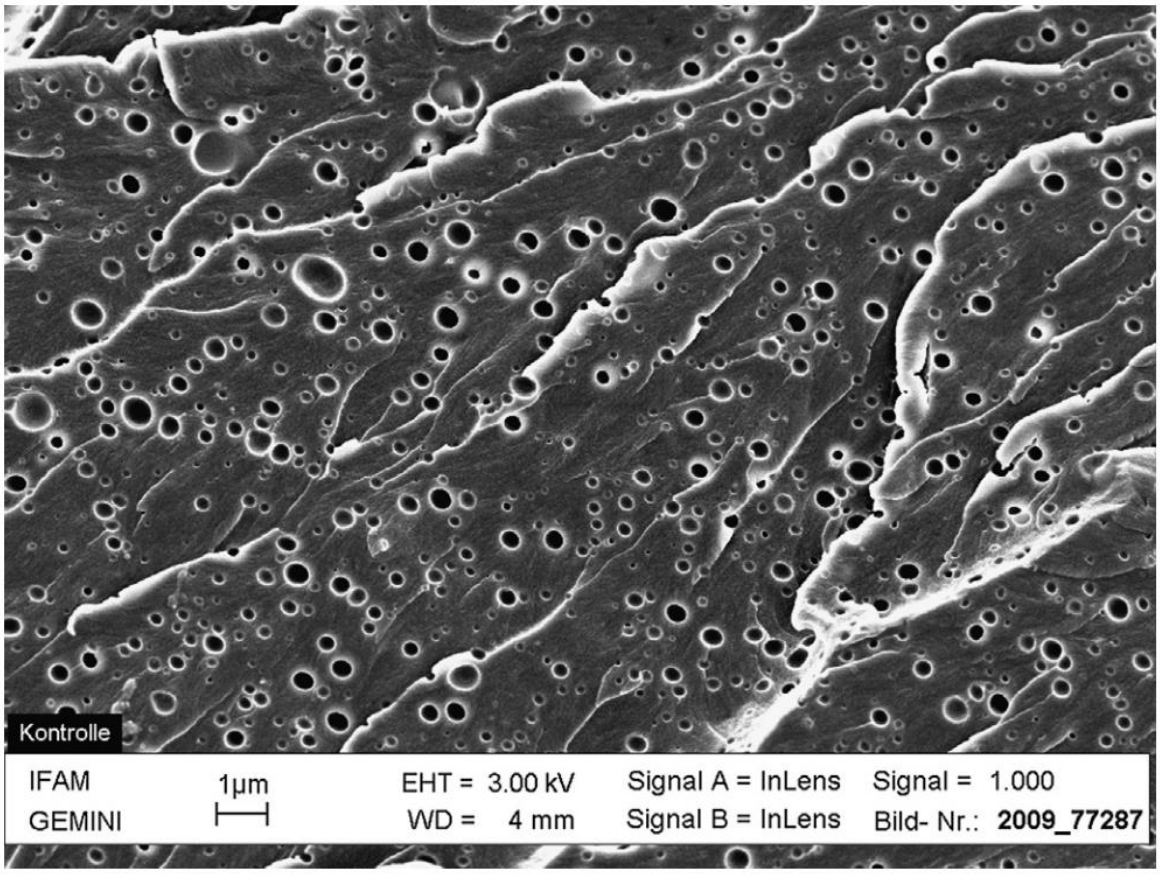

Figure 11 – SEM image of the fracture surface of an epoxy polymer with 5.5% rubber microparticles

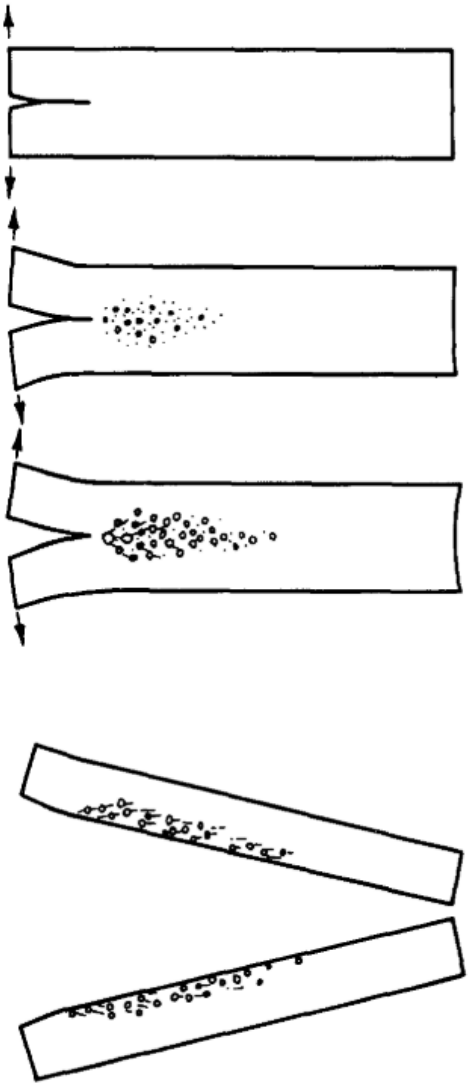

Figure 12 – A schematic representation of the deformation processes ahead of the crack tip in a rubber-modified epoxy polymer (adapted from* [48]*)

With respect to harder particles such as silica nanoparticles, it is reported that the notable difference is that silica particles debond at the silica/ epoxy interface, while rubber particles undergo internal cavitation [4]–[6], [8], [11]. The toughening mechanism of silica nanoparticles consists of (a) localized plastic shear-band yielding initiated by the stress concentration acting around the periphery of the silica nanoparticles and (b) the debonding of silica particles from the epoxy polymer and subsequent plastic void growth. High-magnification fractography of silica modified epoxy are shown in Figure 13, where not all silica particles debond and initiate void growth in the epoxy matrix [6]. This led to the conclusion that if only a fraction of particles are involved in the void initiation, then

the predicted fracture toughness will be lower than if all particles will debond. Thus, the improvement of the epoxy resin may not be fully translated into the composite system [11]. This is further discussed in the following section.

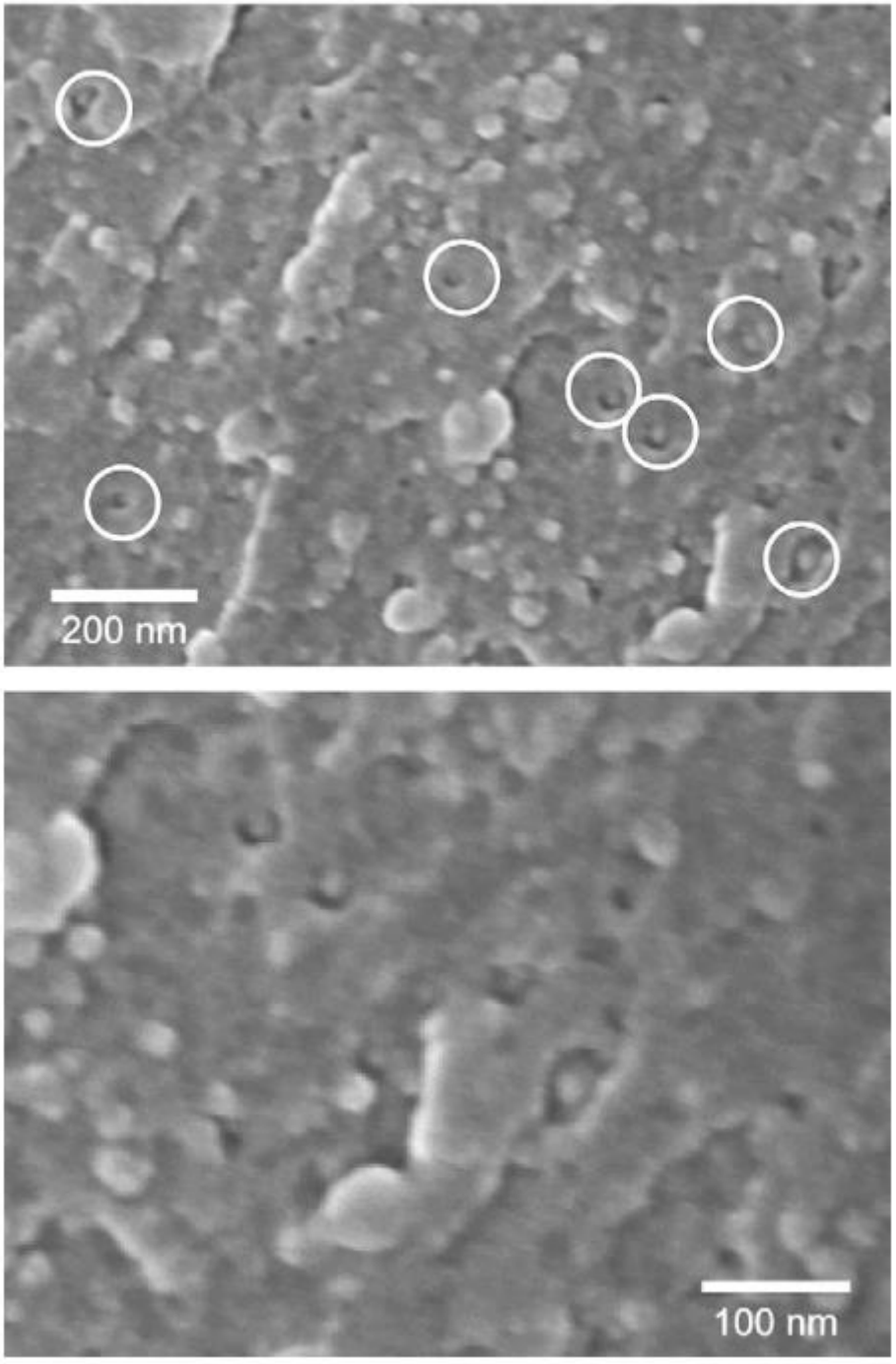

Figure 13 – SEM of the fracture surface of epoxy polymer containing 9.6 vol % silica nanoparticles (voids with nanoparticles are circled in white)

2.2.5 The effect of particle modified epoxy on fracture performance of composites

It is reported that properties of modified epoxies do not always transfer well into composites [11][52]. However, mode I and mode II fracture energy of modified epoxy composites have been found to increase compared to conventional epoxy systems [53]. Kim et al. [54] compiled data from a variety of researchers to show the transition from toughened epoxies and carbon fibre composites. The values presented in Figure 14 are for mode I steady-state crack growth than for crack initiation. It is noted that as the resin toughness, G_{ic}^{m}, increases over 0.5 kJ/m^2, the incremental increase in the composite fracture toughness, G_{IC}^{C}, is much smaller than the resin G_{ic}^{m}, and there may be little gain to the composite toughness for G_{ic}^{m} value above 2 kJ/m^2.

Sprenger [55] compiled available data in the literature for toughened epoxy resins and showed, Figure 15, that G_{IC} of laminates increases by improvement of G_{IC} of the bulk resin when a modified epoxy resin was used. The nature of the epoxy resin, hardener and fibre reinforcement was not considered, which might affect the toughening mechanism of the particulate fillers, hence the measured fracture toughness values. The fitted line does not go through origin, meaning that a minimal improvement of G_{IC} of the composite exists. It is noted that a 100% improvement of resin G_{IC}, results in a 18% increase for the composite laminate [55]. Several studies [2], [4], [8], [56]–[58] reported an increase of resin G_{IC} 90-1100 % when silica or rubber fillers were used in different concentrations in an epoxy resin, which further led to a 3-250% improvement of the G_{IC} of the composite.

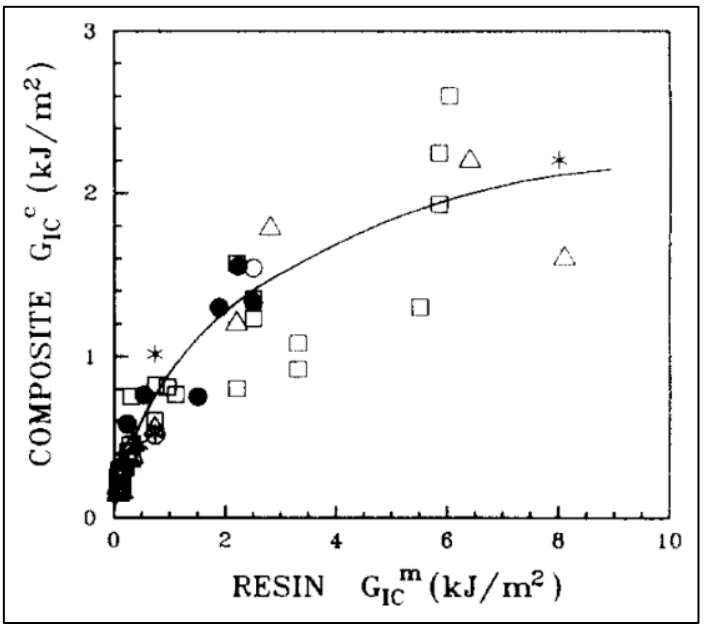

Figure 14- The relationship between resin fracture toughness G_{IC}^{m} and composite G_{IC}^{C} from various studies [54] [59] [60]

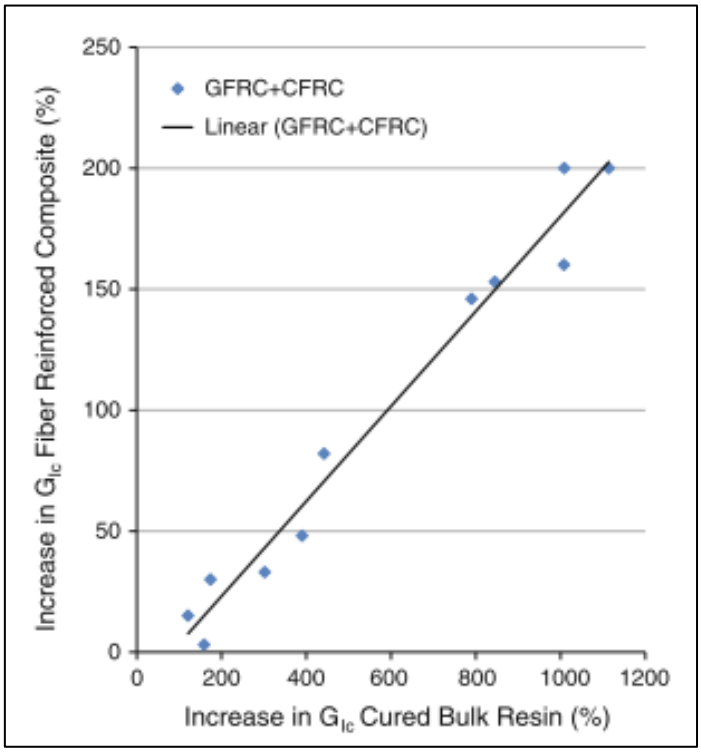

***Figure 15 – Relative improvements of G_{IC} of bulk resins versus laminates; data from various studies* [55]**

2.3 Manufacturing methods of Carbon Fibre Reinforced Polymers

Figure 16 shows the main CFRP manufacturing methods available in industry. The final goal of a manufacturing method is to produce a good quality fibre reinforced panel with a void-free continuous phase ensuring the resin is evenly distributed and fully cured. Potter [61] defines an ideal composite manufacturing process as having high productivity, minimum material cost, maximum geometrical flexibility, and minimum finishing requirement. The use of pre-impregnated resin (prepreg) plies is a widely available manufacturing method. These consists of plies of material which have been impregnated with resin and then stored in a frozen environment to delay the curing process. The plies are then stacked into a laminate and cured at either room temperature (RT) or oven or in an autoclave under both heat and pressure. The consistency of the resin which is impregnated into the plies and the ease of use of this manufacturing process can be an advantage. On the other hand, the main disadvantage is that the information on the constituent phases is limited.

Another basic composite manufacturing method is the wet lay-up method in which dry fabrics are laid out and are then wetted either by brushing or spraying. The laminate quality are dependent on the skills of the laminators and parts usually have a high percentage of voids with non-uniform fibre-resin distribution [62].

Infusion processes, such as Resin Transfer Moulding (RTM) or Vacuum Assisted Resin Transfer Moulding (VARTM) overcome the disadvantages of wet lay-up method and high fibre volume laminates with a low void content can be obtained [63]. Moreover, the laminate thickness can be controlled along with the properties of the polymer matrix and fibres. For the purpose of this work where the matrix and filler concentration need to be controlled, RTM and VARTM were selected to produce CFRP samples.

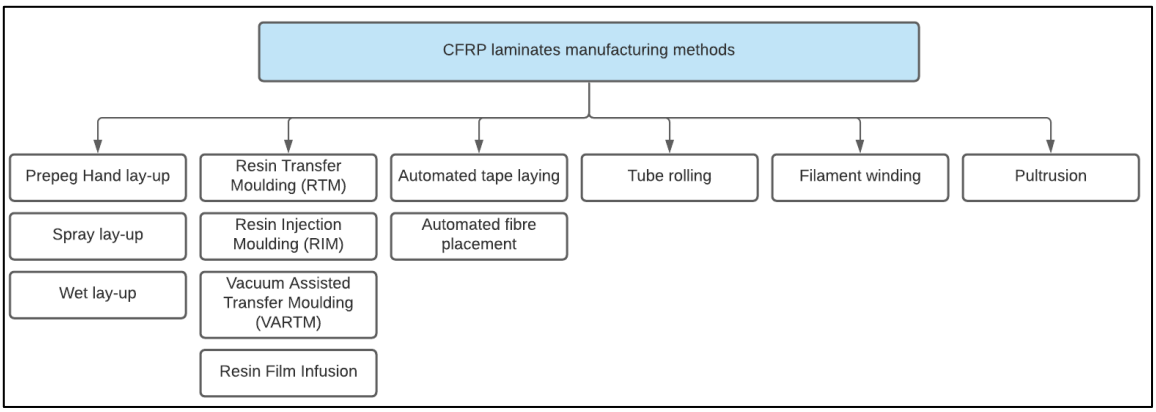

Figure 16 – CFRP laminates manufacturing methods [43], [61], [62], [64]

2.3.1 Resin Transfer Moulding (RTM)

RTM is an emerging process for cost effective manufacturing of CFRPs [65]. The process involves the injection of resin into the reinforcement which is enclosed into a sealed mould. The resin flows through the fibres arranged in the sealed mould and polymerizes. The resulted composite panel is cured to complete the crosslinking between the resin and the matrix. A schematic of the process is showed in Figure 17. The advantage of the process is that it can be used with different types of fabrics and resins and the strength and stiffness of the component can be controlled by resin injection parameters. However, high pressure is required to inject the resin through the dry fabric. In this case, usually steel mould tools are used to prevent any kind of deformation of the injected fabric and support mould.

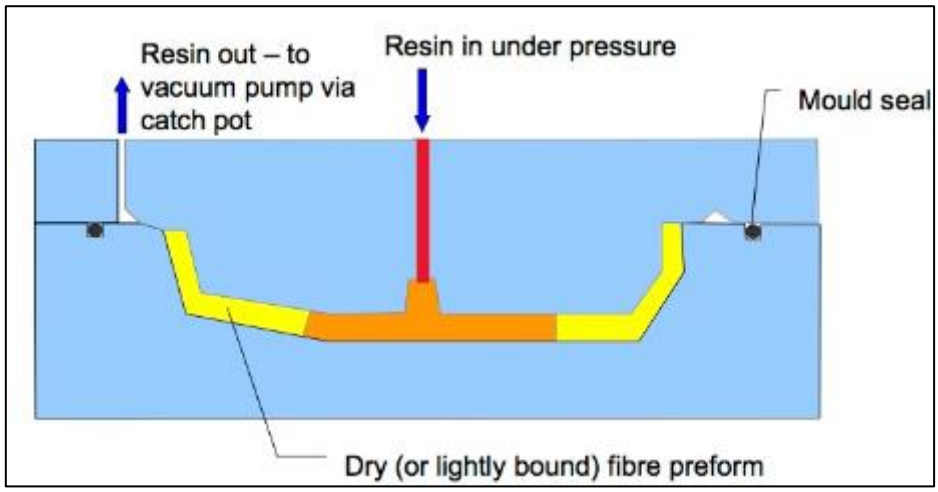

Figure 17 - Resin Transfer Moulding (RTM) schematic [61]

2.3.2 Vacuum Assisted Resin Transfer Moulding (VARTM)

VARTM differs from RTM in the pressure conditions under which the resin is injected into the dry fibre. In VARTM, the pressure is applied by the atmosphere against an evacuated system [62]. A typical VARTM set-up is shown in Figure 18. The process draws resin into dry reinforcement on a vacuum bag tool. A spiral tubing and distribution medium is used on top of the fabric to ensure the full distribution and penetration of the resin. A hot plate is used to decrease the viscosity of the resin and achieve a smooth flow of the resin as the viscosity drops by increased temperature. Although the high-quality surface finish is obtained on only one side of the composites manufactured by VARTM, it is significantly cost effective compared with the RTM method where custom made moulds are used. VARTM is used to manufactured large parts, while RTM is limited to small-medium size parts [62].

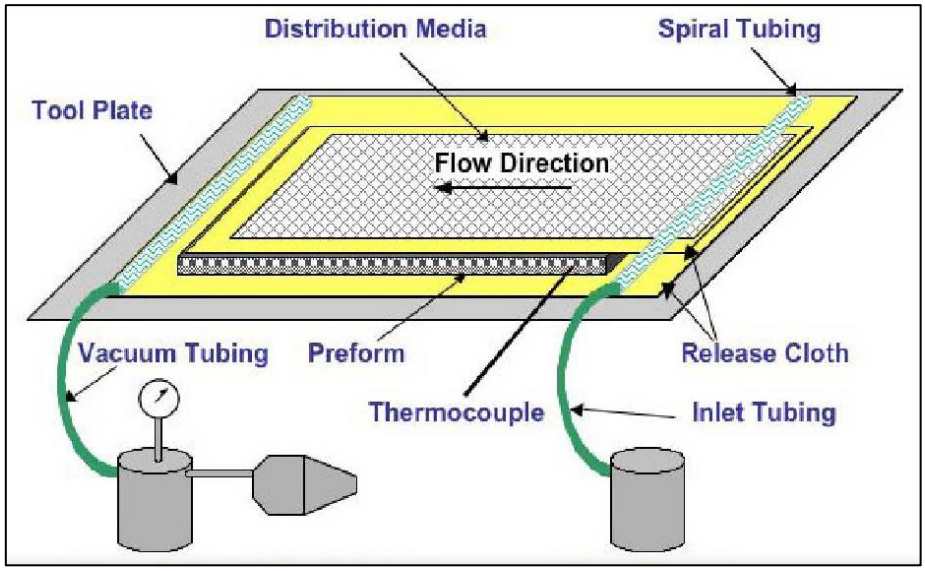

Figure 18- Illustration of a typical VARTM set-up [66]

2.4 Machining and chip formation process in composites

Machining is an important manufacturing process and the growth of the manufacturing-based economies of the world can be traced largely to the development of various machining operations [67]. Machining is mainly used in metal products, but it is also used for wood, plastics, ceramics and composites[67]. The predominant cutting action in machining metals involves shear deformation of the work material to form a chip and generate a new surface. However, machining of composites differs significantly in many

aspects from machining of conventional metals and their alloys [68]. Due to the anisotropic and inhomogeneous state of CFRPs given by a matrix and a reinforcement with different orientations relative to the cutting edge, traditional metal machining techniques cannot be transferred directly to composite machining. Incorrect application of machining operations lead to creation of machining induced damage, including delamination, intralaminar cracking, matrix shearing and burns, fibre pullouts which affect the structural integrity of the machined part [22]. Due to these complexities associated with machining of composites, there is a need to understand the effect of individual constituents in the material on the machining and subsequent machining induced damage. Thus, for any newly developed material, a thorough understanding of the chip formation process and material removal mechanism is required.

2.4.1 Machinability of composite materials

Machinability is not a single measurable characteristic, but it is generally defined as the ease with which the material is machined [69]. The assessment of machinability of a material involves a series of factors including cutting tool performance, machining parameters, cutting forces and temperature, surface integrity assessment and chip formation analysis [70]. Figure 19 shows the main factors affecting machinability of CFRP in conventional machining operations with defined edge geometry. These machining processes are complex having multiple cutting edges engaged with the material at the same time. Typical conventional composite machining processes include milling, drilling, turning, while ABWJ is a popular non-conventional machining choice. However, slot milling or edge trimming are most frequently used in machining of composites to the existing knowledge from metal or wood machining industry [71].

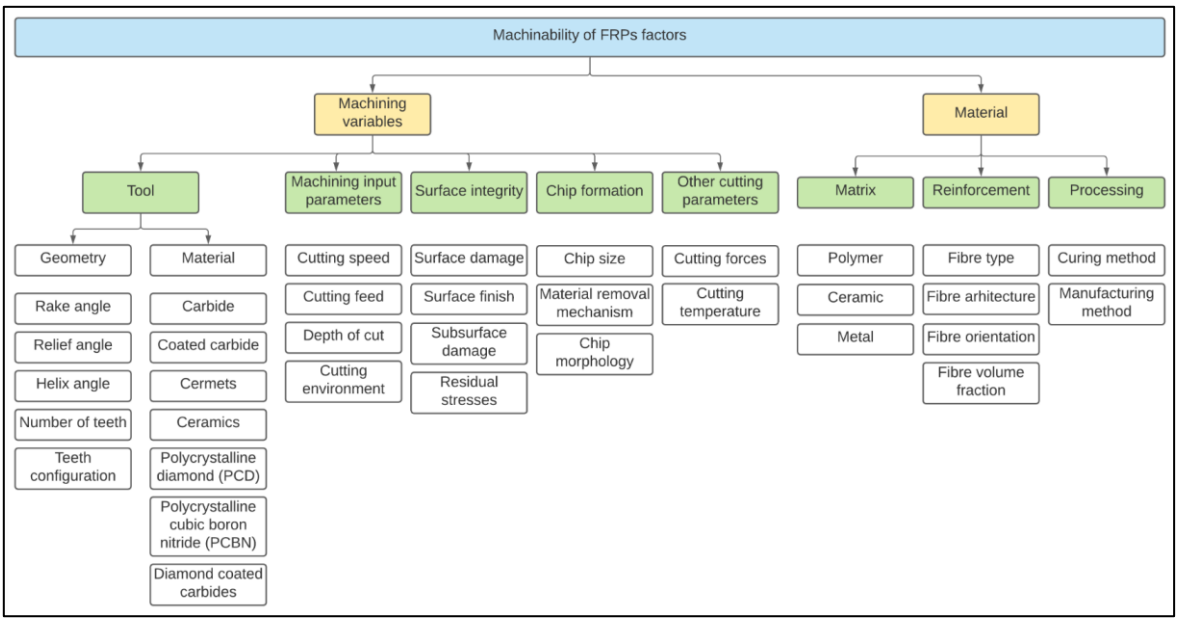

Figure 19 – Factors affecting machinability of FRP composites (adapted from [38], [42], [70]***)***

2.4.2 Orthogonal cutting

Orthogonal machining is represented by a two-dimensional cutting problem where the tool edge is perpendicular to the direction of the cut. A schematic of the process is shown in Figure 20. A shear plane AB is formed in front of the cutting tool when the tool is pushed into the material. This shear zone ahead of the cutting tool is mainly responsible for generation of the chip. In case of ductile materials, such as aluminium or mild steel, the material undergoes plastic shear deformation which pushes the chip upward on the rake face of the tool. For brittle materials, such as most thermoset polymers, chips are formed by brittle fracture due to initiation and propagation in the shear zone ahead of the cutting tool [22].

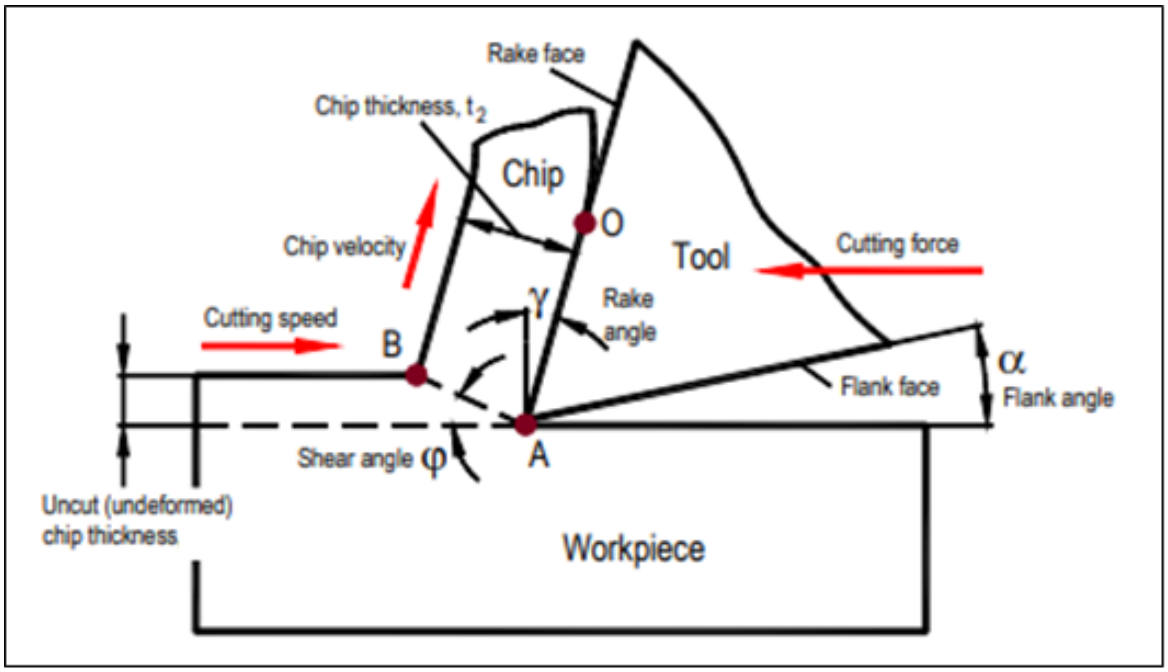

Figure 20 – Schematic representation of orthogonal cutting (adapted from [72]***)***

2.4.2.1 Material removal mechanism during orthogonal cutting of FRPs

Koplev et al. [73] were the first to study the chip formation process in orthogonal cutting tests of UD laminates and concluded that the tool does not actually cut into the specimen, but a pressure is applied into the fibres which results in fibre breakage. This further leads to the chip formation which is dependent on the fibre orientation. The effects of tool geometry and operating conditions have been investigated by Wang et al. [74] who reported that the chip formation process varies with fibre orientation and to some extent with tool parameters. Figure 21 shows a schematic of material removal mechanism, which is dependent on cutting speed, tool parameters and change of matrix and fibre properties. In a Type I chip formation (Figure 21 – a, 0° fibre orientation), a crack is formed in front of the tool which propagates along the fibre-matrix interface. The peeled layer advances on top of the rake face causing a bending in the fibres followed by their fracture forming small chips and the process repeat itself again. Type II (Figure 21 – b, 0° fibre orientation), also called fibre buckling, occurs due to the compressive loading along the direction of the fibres where a tool with negative rake angle is used. The advancement of the tool causes sliding or in plane shearing and fracture of the fibre-matrix interface [22]. Type III chip formation (Figure 21 – c and d, positive and negative raking angle, 45° fibre orientation) is governed by in-plane shear proprieties of the UD composite material. The chip type is

continuous; the fracture is formed by the smooth flow of the chip up the tool face. In Type IV (Figure 21 – e, 90° fibre orientation) the chip formed is discontinuous; the fracture is almost perpendicular to the fibre length. Relief angle had a more significant importance on the 90° fibre orientation than in 0°, due to the large springback of fibres on the flank face of the cutting tool. This phenomenon happens due to the elastic bending of fibres when a part of the material in the cutting path is pushed down during the cutting but sprang back partially after the tool passed away that is commonly used in machining of FRPs. Type V (Figure 21– f, 135° fibre orientation) is governed by compressive stress which causes the matrix and fibres to crack, and a discontinuous chip is created.

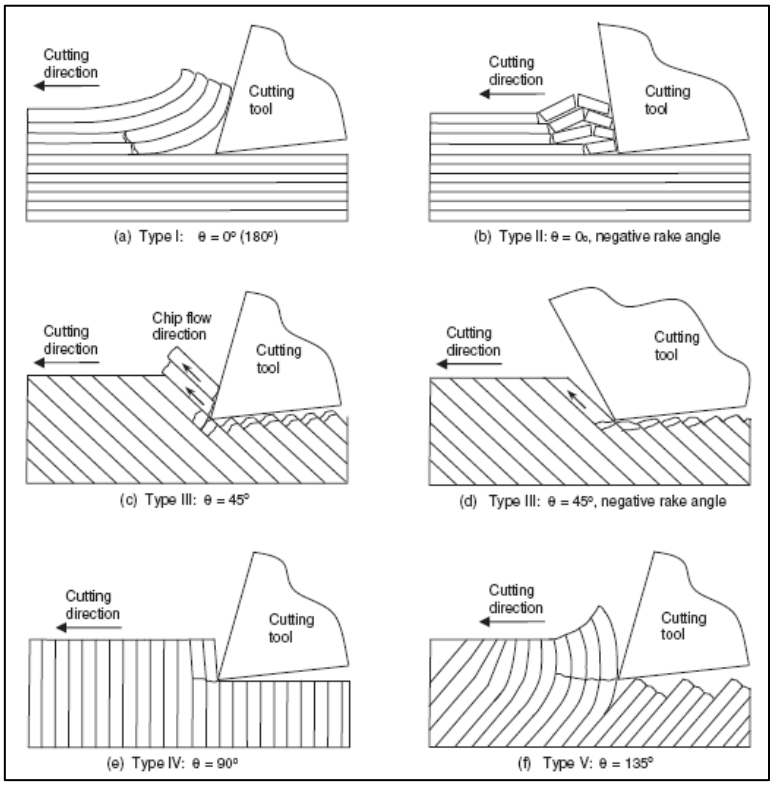

Figure 21 – Cutting mechanism in orthogonal machining of UD FRPs (adapted from [22], [75]***)***

The chip formation process during orthogonal cutting process of FRPs is influenced by the following in descending order: fibre orientation, tool geometry and cutting parameters [76]. In the analysis of the machinability of UD CFRP laminates during orthogonal cutting tests [77], it was found that the subsurface damage is related to the depth of cut, fibre orientation and rake angle. An et al. [78] reported that by increasing the cutting speed in orthogonal cutting of CFRPS, the forces are reduced as such a suitable high cutting speed

with appropriate large cutting depth is helpful for stable machining of CFRP. Additionally, the increasing of cutting speed was also found to reduce the fibre deformation and the affected area before fibre fracture [79].

The presented studies along with their machining parameters are briefly listed in Table 3 that shows chip formation process in machining of CFRP is influenced by fibre orientation, tool geometry and cutting parameters. However, the individual effect of matrix and fibre properties on the material removal mechanism was not taken into consideration. Moreover, each study had a CFRP material with a different system of fibres and matrix which gave different magnitudes of cutting forces and machining induced damage. The tool type, geometry and conditions are chosen based on the orthogonal cutting literature summarised in Table 3.

Table 3 – Orthogonal cutting of CFRP studies containing tool geometry and cutting conditions

Author	Year	Tool type	Tool geometry	Cutting conditions
Koplev et al. [73]	1983	High-Speed steel, Cemented Carbide	Rake ° = 0, 5, Relief ° = 5, 10, 15	Cutting depth (mm): 0.05 – 0.2 Cutting feed (mm/min): 14 - 48
Kaneeda and Takahashi [80]	1989	-	Rake ° = -10, 0, 10, 20, 30 Relief ° = 10	Cutting depth (mm): 0.03 – 0.25 Cutting feed (mm/min): 5 – 21.5
Wang et al. [75]	1995	PCD	Rake ° = 7, 17 Relief ° = 0, 5, 10	Cutting depth (mm): 0.127, 0.254, 0.381 Cutting feed (m/min): 4, 9, 14
Arola et al. [76]	1996	PCD	Rake ° = 7, 17 Relief ° = 0, 7 Edge radius (µm): 10, 15,20, 25	Cutting depth (mm): 0.127, 0.254, 0.381 Cutting feed (m/min): 4, 9, 14

Wang and Zhang [77]	2003	Tungsten carbide	Rake ° = -20, 0, 20, 40 Relief ° = 7	Cutting depth (mm): 0.001 – 0.25 Cutting feed (m/min): 1
Q An et al. [78]	2015	CVD – diamond coated carbide	Rake ° = 25 Relief ° = 15 Edge radius (µm): 15	Cutting depth (mm): 0.005 – 0.025 Cutting feed (m/min): 100 - 300
Agarwal et al. [81]	2015	PCD tool	Rake ° = 10 Relief ° = 15 Edge radius (µm): 20	Cutting depth (mm): 0.1 – 0.2 Cutting feed (m/min): 0.3 – 0.5
Li et al. [82]	2017	Tungsten carbide	Rake ° = 15 Relief ° = 20 Edge radius (µm): 5	Cutting depth (mm): 0.1 – 0.2 Cutting feed (m/min): 0.5
Su et al. [83]	2017	Cemented carbide	Rake ° = 25 Relief ° = 5 Edge radius (µm): 5	Cutting depth (mm): 0.01 – 0.05 Cutting feed (m/min): 0.5
Su Y [84]	2019	PCD	Rake ° = 0 Relief ° = 5	Cutting depth (um): 20 – 100 Cutting feed (m/min): 0.5 -180

2.4.2.2 Influence of tool geometry in orthogonal cutting of UD CFRP

Arola and Ramulu [75] determined different fracture modes for their CFRP studied material based on the applied tool configuration. The results are shown in

Rake angle (degrees)											
	30	I	III	III	III	III	III	IV			
	20	I	III	III	III	III	III	IV			V
	10	I	III	III	III	III	III	IV	V	V	V
	0	II	III	III	III	III	IV	V	V	V	V
	-10	II	IV	III	IV	IV	IV				
	-20					IV		V			V
		0	15	30	45	60	75	90	105	120	135
	Fibre orientation (degrees)										

Figure 22 where: Mode I – delamination, Mode II – fibre buckling, Mode III- fibre cutting continuous chip, Mode IV- fibre cutting discontinuous chip, Mode V – macro fracture discontinuous chip. Cutting parallel to the fibres with a high positive rake angle produces chips by delamination and brittle fracture (peel fracture), while cutting with zero and negative rake tools produces chips by buckling of fibres perpendicular to fibre orientation by compression. An et al. [85] investigated the effects of tool parameter on cutting force development during orthogonal cutting of UD CFRPs. It was reported that rake angle influenced the cutting forces for all fibre orientations by affecting the material removal modes. Large angle was found to improve the chip separation, hence reducing the cutting forces. Similar results were reported by Ahmad [22], where an increase in the rake angle, the cutting and thrust forces decrease with an improvement of the machined edge. On the other hand, the relief angle had a more significant effect on cutting forces in 0° fibre orientation than 90° due to large springback on the flank face of cutting tool [85]. It is reported that [77] the relief angle slightly affects the chip formation process. However, a large clearance angle improves machined surface quality as it avoids the sliding of the tool with material during cutting.

Rake angle (degrees)											
	30	I	III	III	III	III	III	IV			
	20	I	III	III	III	III	III	IV			V
	10	I	III	III	III	III	III	IV	V	V	V
	0	II	III	III	III	III	IV	V	V	V	V
	-10	II	IV	III	IV	IV	IV				
	-20					IV		V			V
		0	15	30	45	60	75	90	105	120	135
	Fibre orientation (degrees)										

Figure 22 – Fracture mode in function of rake angle and fibre orientation in orthogonal cutting of UD FRPs [22]

2.4.2.3 Influence of tool material in machining of CFRP

Machining of CFRP is difficult due to the abrasive nature of the carbon fibres of the component and the load which is generated by the fracture during the machining. Depending on the application and composite material proprieties, the tool materials can be divided in several categories as shown in Figure 23, where hardness is a measure of abrasive wear resistance and toughness is a measure of fracture resistance of the tool material. The resistance of the cutting edge to abrasion wear is important as the loss of acuity can cause significant damage in the composite material [86]. An ideal tool material for machining of CFRPs will have a high hardness and toughness at the same time.

High speed steels (HSS) have started to be manufactured around 1950's and they have a high toughness and a low hardness. As the fibres have an abrasive surface, these tools with low hardness are normally unsuitable for CFRP machining. On the other hand, ceramic tools have a low toughness, and they suffer from failure by chipping when used in heavy cuts or under interrupted loads. The advantages of ceramic tooling in machining FRPs could not be realized because of their tendency to fail by chipping and the inability to produce them in sharp edges [22]. Therefore, the majority of CFRP machining is done with carbides or Polycrystalline Diamond (PCD) tools. Furthermore, tool life is higher if the tool is used in the right condition. Diamond can also be used as a coating for carbides but is difficult to build a sharp edge on the tool due to low adhesion properties of diamond. Several studies were completed in the literature [68], [87], [88] recommended the use of carbide or PCD tools. PCD tools are preferred for their better resistance to wear, while carbide tools are chosen for their lower cost [86] .

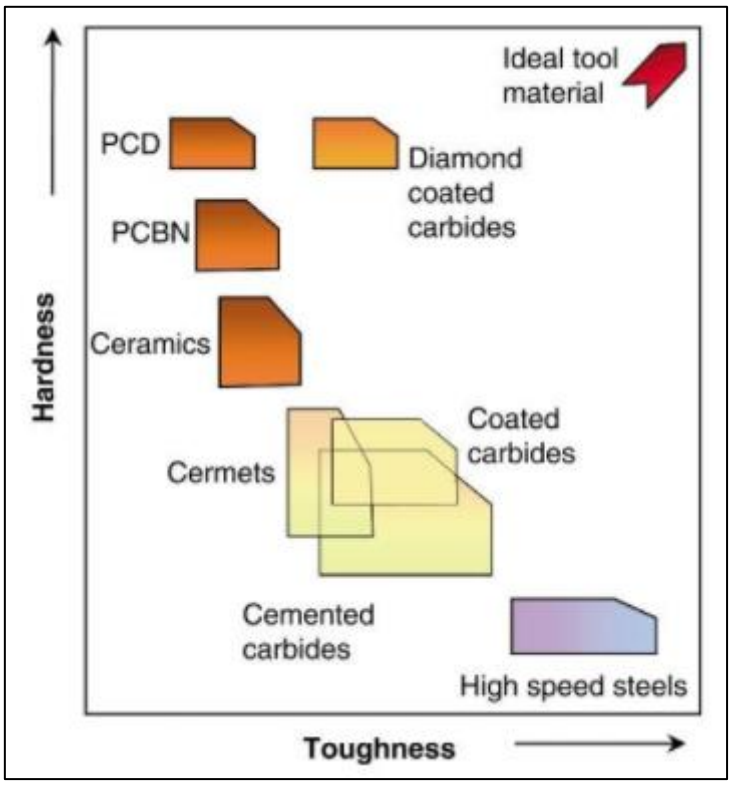

Figure 23 - Tool material graph **[22]**

2.4.3 Milling

Milling is defined as a conventional machining operation that uses geometrically defined cutting edges which are engaged with the workpiece in order to mechanically remove the material. The types of milling operations that are most common in machining of FRPs are peripheral milling or edge trimming and end milling [22]. In edge trimming the axial engagement encompasses the entire thickness of the workpiece, while in end milling the axial engagement may be less than the thickness of the machined part. These operations are further classified into up milling (or conventional milling) and down (or climb milling) as shown in Figure 24. Up/ conventional milling is the process where the cutter rotation opposes the feed direction of the material and results in high material removal rate. On the other hand, down/ climb milling occurs where cutter and feed direction is the same and results in better surface finishing. The cutting forces are high for down milling and result in pushing the workpiece against the work holding surface.

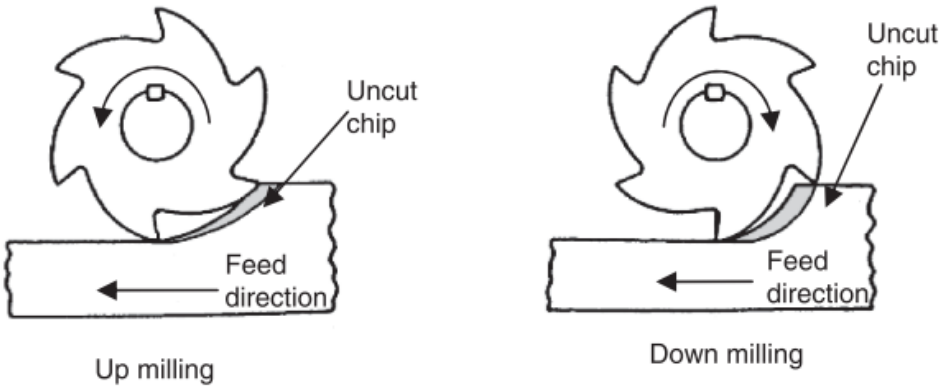

Figure 24 – Example of up and down milling operation (adapted from* [22]*)

2.4.3.1 Cutting mechanics of CFRPs milling

The geometry and cutting mechanics of up and down milling have been thoroughly investigated in the literature [89], [90] . However, the chip formation process and material removal of CFRPs is different compared metals. The main difference is that when cutting with a rotating tool in a milling operation, the fibre orientation angle, θ, is not constant, but is constantly changing with the cutting edge position relative to cutting axis as shown in Figure 25. This will result in cutting force fluctuations, interrupted chip size, which continuously vary with tool edge rotation. To overcome these difficulties, orthogonal cutting is used to gather information about mechanics of chip formation, chip type and size, cutting forces, friction conditions and cutting temperatures [22]. Orthogonal cutting is discussed in depth in section 2.4.2.

In relation to multidirectional ply laminates, the overall cutting mechanism is identical to the UD laminate, with a slight difference in the 90° and 135° fibre orientation as the result of the influence from adjacent plies as previously discussed by Arola and Ramulu [74]. Excessive out-of-plane damage in multidirectional occurs at 90° or greater in UD laminates, while the damage in multidirectional laminates, at these angles, is limited due the support of adjacent plies. The damage aspect is further detailed in section 2.4.4.

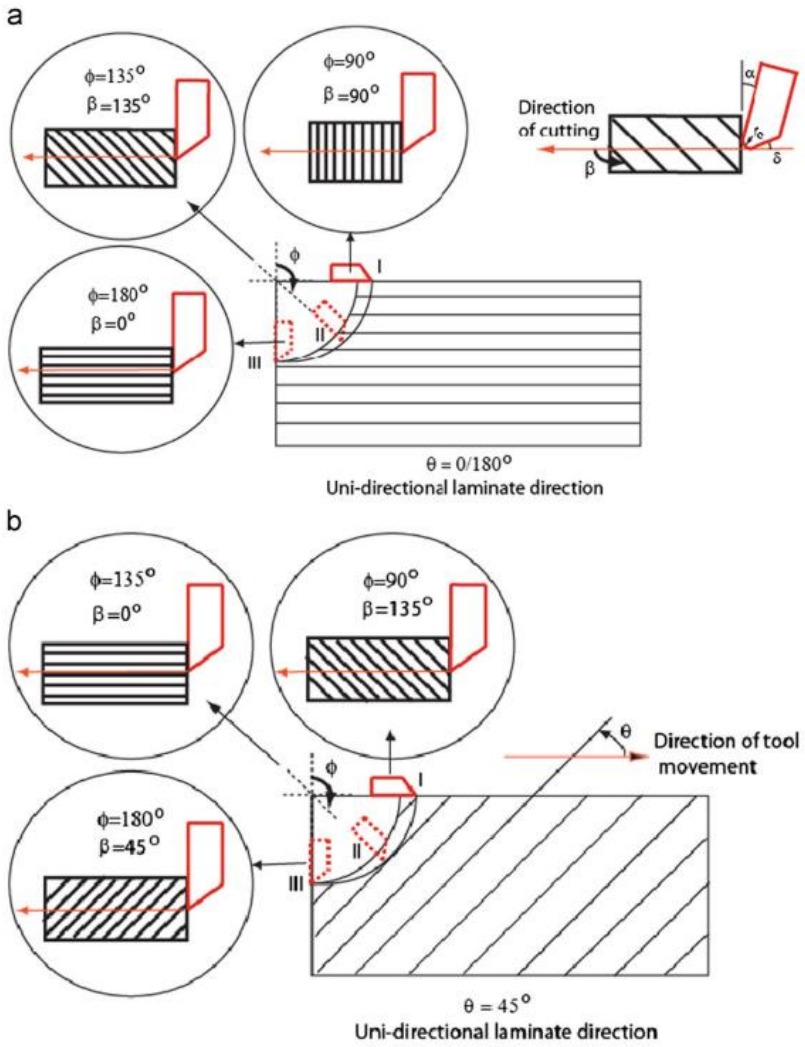

Figure 25 – Fibre cutting angle (β) as a function of tool edge rotation angle (Φ) and fibre direction of the laminate (ϑ) a) 0°/ 180° b) 45° orientation (adapted from [91]***)***

2.4.3.2 Milling tools geometry

Milling tool geometries can range from straigth one flute, upcut/ downcut helical tool to more complex shapes involving multiple cutting edges such as burr or flutte tools (Figure 26). Each individual geometrical feature has its own advantage and disadvtange. For example, the straight flute has a versatile geometry provindg a clean cut and a good surface finish, however, it has poor ability of chip disposal and tends to clog very shortly after use [22]. Helical tools are used to reduce fatigue on the tool as force are transmitted in the axial direction of the tool. The greater the helix angle of the tool (the angle between the helix and axial line) the more force can be transmitted axially. More complex cutting tools such as double-spiral compression tool, burr or flutted are reported to reduce cutting

forces and machining induced damage and are a preffered choise for CFRP edge trimming operations [23], [92], [93].

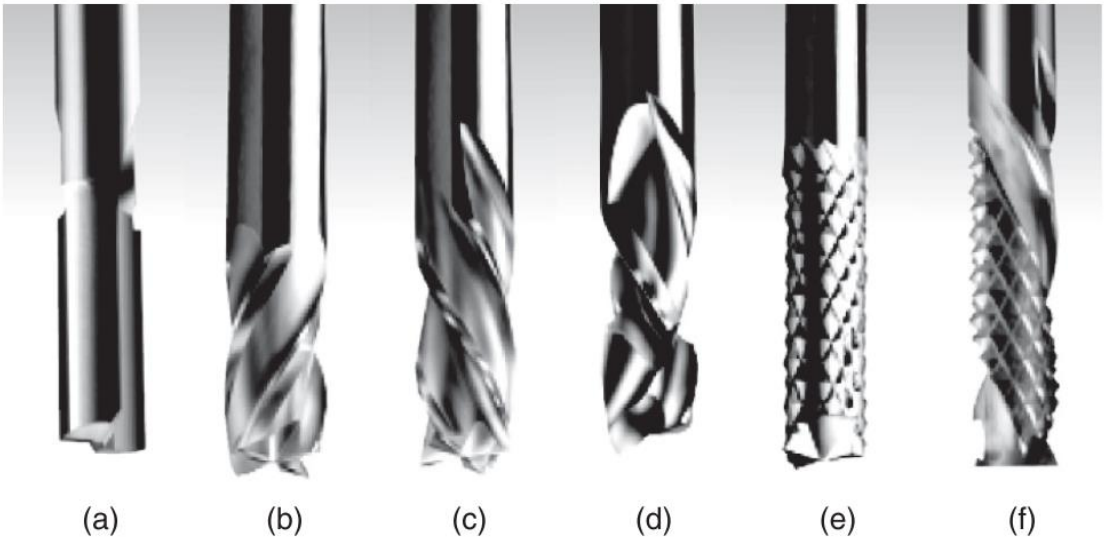

Figure 26 - Geometry tools for milling composite materials (a) Straight flute (b) upcut helical tool (c) downcut helical tool (d) double spiral compression tool (e) burr tool (f) flutted bur (adapted from* [22]*)

2.4.4 Machining induced damage

Machining induced damage is an artefact of machining processes and deformation conditions of the material. The severity of it in composite machining could be linked to an inappropriate selection of cutting parameters in relation to fibre orientation, fibre to volume ratio and material properties. In CFRP materials, machining induced damage can be categorized in mechanical, thermal and chemical damage [87]. Representative mechanical damage for CFRP include fibre pull out (Figure 27 – a), fibre breakage (Figure 27 – b) and delamination (Figure 27 – d). Matrix smearing (Figure 27 – c) is a type of thermal damage where the heat generated during the machining process exceeds the matrix degradation temperature. Chemical damage typically occurs when water ingress into the resin and damage the interface region between carbon fibre and matrix.

The delamination defect is characterized by the separation of plies in the thickness of the composite and by the formation of interlaminar cracks in the material [87]. Delamination was also split in three distinct phases as shown in Figure 28 [22]. Type I occurs when surface plies are delaminated from the rest of the laminate inwards from the trimmed edge. This is typical for 45 - 90° fibre orientation. Type II occurs when uncut fibres protrude

from the trimmed edge. Type III takes place when long fragments of fibres cracks parallel to the machined edge. This is typical for 0° and 90° laminates.

The above observations were successfully completed in machining of UD laminates in terms of machining induced damage type, machining operation and fibre orientation. However, there is a significant gap in the knowledge regarding the effect of matrix properties on machining induced damage.

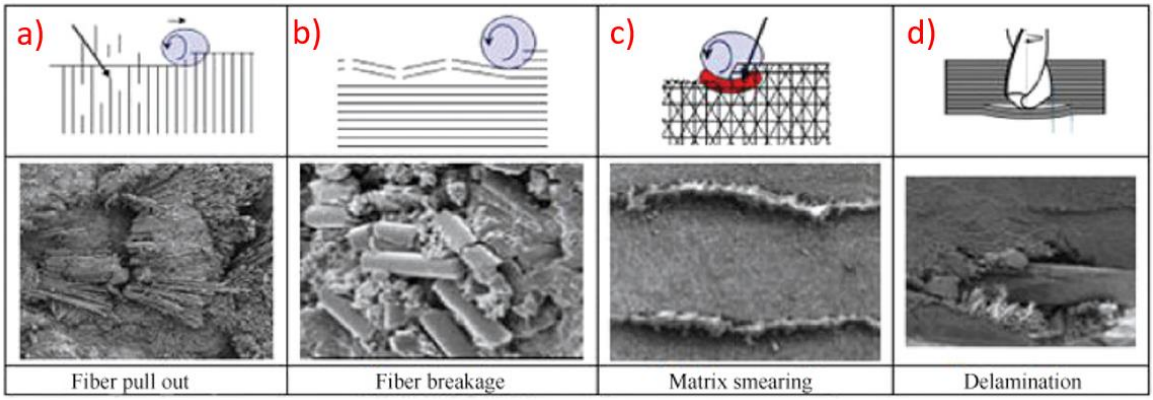

Figure 27 - Representation of machining induced damage in composite materials **[32]**

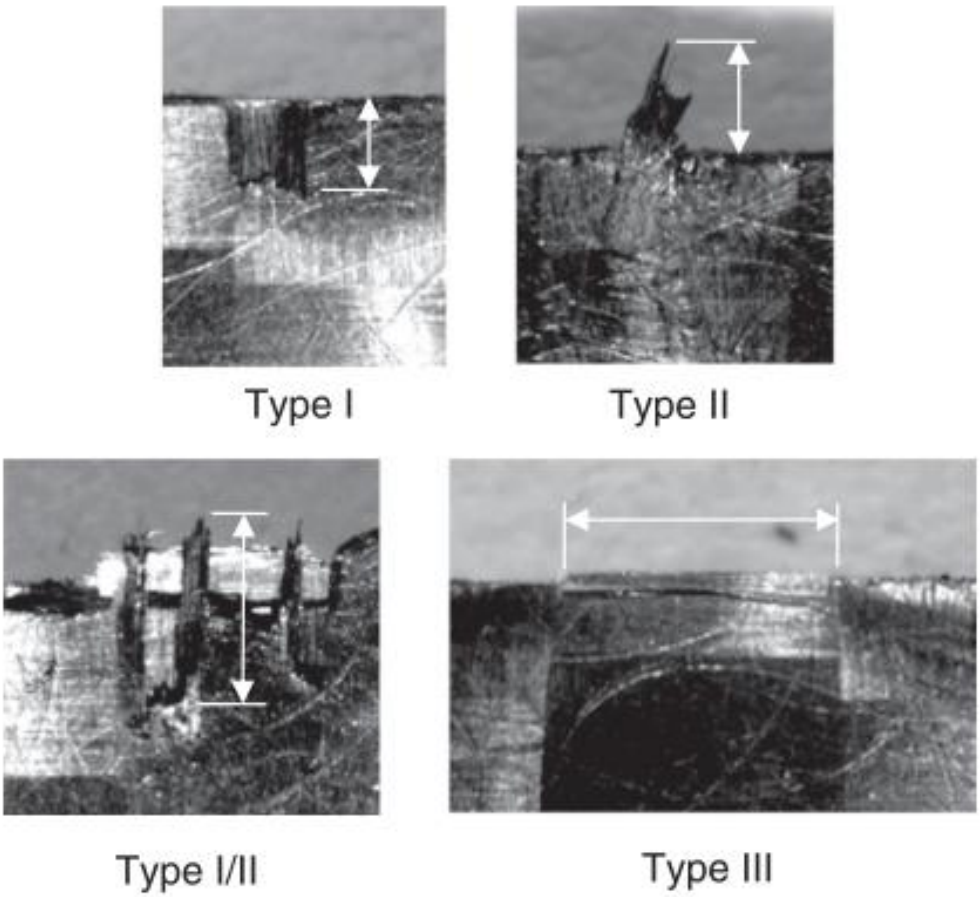

Figure 28 – Delamination types in machining of CFRPs **[22]**

2.4.5 The effect of CFRP material constituent phases properties on machining performance

The thermoset matrix of CFRP materials has a lower strength and stiffness compared to the fibres, but its low thermal conductivity affects the heat build-up zone in the cutting process. Heating up the matrix over the glass transition temperature (T_g) will result in the thermal softening of the matrix makes it unable to support the adjacent fibres, which let the creation of subsurface pits, cracks and fibre pullout [93], [94]. The mechanical properties of carbon fibres are stable up to 1000°C [95], therefore they are not affected thermally by the interaction of cutting tool and material. To avoid machining induced thermal damage such as matrix smearing or burning, the machining process should take place below the glass transition temperature of the matrix.

There are limited studies covering in-depth analysis of the effect of CFRP constituent phases properties in relation to machining performance. Wang and Zhang [77] used a

MTM56 prepreg system cured under different conditions in order to alter the mechanical properties of the resin. Tensile strength and modulus of the samples was changed by altering the curing condition of the resin. Results proved that cure degree did not influence the machined surface quality but contributed slightly to the change of the cutting forces. Wang. et al [96] studied the cutting mechanism of epoxies with different crosslink densities to modify epoxies properties. The T_g, tensile modulus and strength and toughness were altered by the use of two different amine-based hardeners. The crosslink density was found to affect the chip formation behaviour as it controls the post-yield deformability and material mechanical properties. Based on the depth of cut and material crosslink density, three types of chips were reported: (i) elastic brittle chips; (ii) elasto-plastic discontinuous chips; and (iii) rigid-plastic continuous chips. Perez et al. [97] studied the influence of workpiece constituents of different carbon fibre architecture and resin formulations with different T_g on cutting forces developed in conventional drilling of CFRP composites. It was reported that the matrix has a significant impact on the recorded maximum thrust force, whereas the type of carbon fibre fabric and cutting speed were found negligible. The authors explained the contribution of resin by the dominance of their thermomechanical properties of the resin, which is higher for resins with higher degrees of cross-linking (improved elastic modulus and T_g) [97].

Thakur and Singh [13] published a review on the influence of particulate fillers on polymeric composites during conventional machining process including drilling, milling and turning of composites with modified epoxy matrix using various fillers such as graphene, nanoclay, multi-walled carbon nanotubes (MWCNT), carbon nanotubes (CNT) and nano Silicon Carbide (SiC) particles. It is reported that these types of fillers can be used to optimise machinability in terms of cutting forces, surface roughness and delamination depending on filler type, mechanical properties and physical characteristics. A comprehensive list of the studies investigating the effect of fillers on the machinability during a milling process is shown in Table 4. Sharma et. al [98] conducted an experimental milling study on MWCNT modified GFRP (Glass Fibre Reinforced Polymers). Experimental results showed that the inclusion of MWCNT in GFRP lead to a better surface finish compared to GFRP laminates. Arora el. al [99] studied the effect of graphene platelet (GPL) on the machinability of modified epoxy in a micro-milling experiment. Cutting forces were

observed to increase with GPL concentration, which was attributed to the improvement in mechanical properties (tensile strength, fracture toughness, and Young's modulus). GPL content of the modified epoxy was found to a have a non-significant effect on the surface roughness measurements. Fu et al. [100] investigated the effect of graphene nano platelet (GNP) on the machinability of GNP modified epoxy in a micro-milling process. It is reported that GNP modified epoxy experienced different crack trends compared with the plain epoxy, which is attributed to the change in fracture toughness properties due to addition of GNP. The effect of graphene fillers on milling of epoxy based GFRPs/CFRPs was studied in [101]–[103]. Experimental results show a decrease in surface roughness in graphene dominated materials, while ANOVA results showed the graphene % had a significant effect.

Shyha et al. [104] produced two different matrix nanocomposites, one made of graphene/ epoxy and the other made of nanoclay/ polyester, for curving out micro-slotting to investigate cutting forces and surface roughness. The study reported that higher cutting forces are required for materials reinforced with nanofillers. The nanoclay/ polyester composite had an average surface roughness of 0.21 µm, while the graphene/ epoxy composite had a surface roughness of 0.27 µm. While in the above mentioned studied the machinability behaviour was changed by the addition of particulate fillers, the complications which emerged in the material removal process were not discussed. The detailed explanation of chip formation with the application of fillers on polymer composite materials needs to be investigated at a micro-scale level. Moreover, the above-mentioned studies mainly focused the machinability of particulate modified epoxy matrices during milling processes, while machining studies involving CFPRs with different fibre architecture and particulate modified matrices are limited.

Table 4 – Research studies covering milling of particulate modified epoxy-based composites (adapted from [13])

Author	Fibre	Filler type	Matrix	Machinability indicator
Sharma et. al [98]	Glass	MWCNT	Epoxy	Surface roughness
Arora el. al [99]	-	Graphene	Epoxy	Cutting forces, chip morphology, tool wear

Fu et al. [100]	-	Graphene	Epoxy	Cutting forces, chip morphology, tool wear
EI-Ghaoui et al. [101]	Glass	Graphene	Epoxy	Cutting force & temperature, surface roughness
Thakur et al. [105]	-	Graphene	Epoxy	Surface roughness
Thakur et al. [102]	Glass	Graphene	Epoxy	Surface roughness
Thakur et al. [103]	Carbon	Graphene	Epoxy	Surface roughness
Shyha et al. [104]	-	Graphene and nanoclay	Epoxy and polyester	Surface roughness and cutting force

In the above-mentioned studies, the thermomechanical changes of the matrix where the crosslink density, T_g and the addition of fillers in polymeric composites influenced the machining behaviour. However, the complications in material removal process occurring during milling and turning, the detailed explanation of chip formation with the application of fillers on polymer composite materials needs to be investigated at a micro-scale level.

2.4.6 Surface integrity characterisation

Leach [106] defines surface as a feature which interacts with the environment in which the component is housed or in which the device operates. Machining processes influence surface integrity, which in turn may significantly affect the way the component functions in service. It was previously shown that 90% of engineering components fail through a surface initiated defect [107], [108]. Therefore, the measurement of machined surfaces quality is important for quality control and identification of potential machining induced damage defects. In this respect, there are several methods to quantify machining induced damage at both surface and subsurface level.

2.4.6.1 Surface finish assessment

Machining processes generate a wide variety of surface textures, generally referred to as surface finish [109]. Figure 29 shows the main components of surface texture which is made from surface roughness, waviness, errors of form and flaws. Lay is used to designate the direction of the predominant surface texture. Roughness refers to the finely spaced surface irregularities and it is measured by the height of the irregularities with respect to

an average line [109]. Waviness is surface irregularity of greater spacing than in roughness. Waviness it may be the result of warping, vibration, or the work being deflected during machining. Cut off length refers to the sampling length used for the calculation of the roughness height. As per ISO 4288 [110], for composite machined surfaces, a cut off length of 0.8 mm is used.

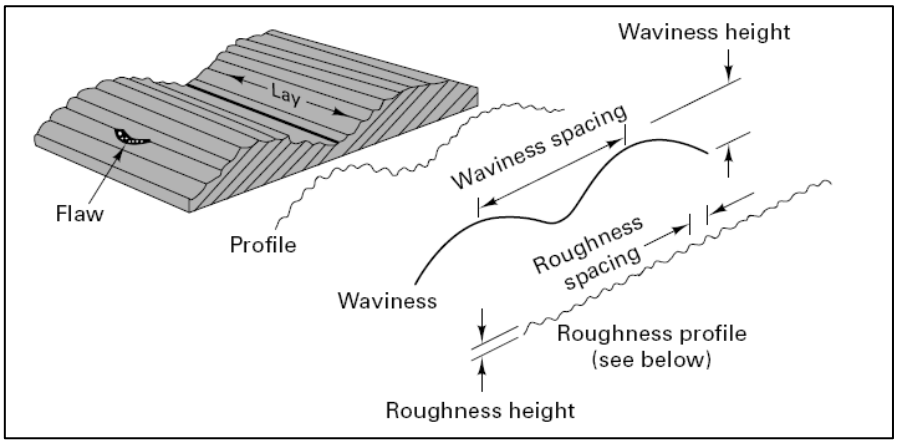

Figure 29 – Surface profile adapted from [109]

Surface roughness is evaluated by different roughness parameters such as arithmetic average height (R_a) and maximum peak to valley distance of the profile (R_t). Other parameters are also used to represent a more in-depth image of the surface, including Skewness (R_{sk}) and Kurtosis (R_{ku}). These are dimensionless unit parameters: Skewness is a measure of symmetry of the profile about the mean line, while Kurtosis measures the sharpness of a profile. Hocheng [111] stated that in composite industry the most used parameter is Ra. Teicher et al. [112] reported that Ra, as an assessment parameter for a machined fibre composite is not perfectly suitable because surface defects due to machining such as delamination and fibre pullout are displayed insufficiently. The usage of 2D (profile) roughness parameters will give an incomplete representation of the real surface topography, therefore it is suggested the usage of areal (3D) parameters for a better characterisation of the surface topography [106]. This is attributed to a better repeatability and a more substantial surface being measured. It is reported that S_a (arithmetical mean height of the surface), the extension of R_a could provide a better representation of the surface roughness [113], [114]. Profile methods provides useful

information about the manufacturing process change, but more functional information about the surface can be gained from an analysis of the areal surface topography [115].

Stylus instruments are commonly used to measure surface roughness. The stylus contacts the surface of work piece, and its vertical and horizontal movement is converted into an electrical signal. Commercial stylus usually has a diamond tip with a radius of curvature between 2 to 10 μm. The limitations of the stylus instrument can be given by its tip shape which is unable to penetrate into the valleys of the surface resulting into distorted areal surface. The main disadvantages associated with stylus instruments are given by surface deformation, finite stylus dimensions, lateral deflection, quantisation, sampling and dynamic effects [115].

Several studies used optical instruments on the assessment of CFRP machined surfaces. Duboust et al. [114] compared an optical system with a stylus profilometer in assessing the surface characteristics of a milled CFRP material. The results proved that the optical tool is a useful research tool for measuring surface roughness of machined composites. The main disadvantage of the system is given by the size of the parts, which should be relatively small due to the distance between the optical lens and work piece. A similar study used a focus variation instrument in characterising surface roughness of a machined multi-directional composite which proved useful in extracting the areal surface parameters of the CFRP material [116]. Davila et al. [117] used a high-speed phase-shifting interferometry to detect the sub-surface delamination defects in carbon fibre specimens. Dhieb et al. [118] analysed the surface damage of unidirectional CFRP under reciprocating sliding in ambient air. The wear in the sliding tests were investigated using coherence scanning interferometry (CSI), commonly known as white light interferometry. Dunkers et al. [119] did a comparison study between optical coherence tomography and confocal microscopy results from an impact test on e-glass composite. The confocal microscopy provided high contrast images which made visible the failure mechanism of the material. The limitations of optical coherence tomography were that the fibre architecture is not imaged clearly along the entire thickness of the specimen.

2.4.6.2 Surface and subsurface morphology assessment

In order to have a good understanding of the effects of machining on the surface of materials, an adequate imagining resolution is needed to be able to visualize the matrix defects, fibres and particulate fillers. This is barely possible using conventional light microscopy due to the limited resolution and depth of focus, therefore, Scanning Electron Microscopy (SEM) are widely be used [120].

Delamination morphology and surface artefacts of material removal mechanism in AWJ machining of CFRP samples were investigated using SEM [121]. Moreover, fracture mechanism in slot-milled UD-CFRP laminates was investigated using SEM [122]. In addition, CFRP manufacturing defects and machining induced damage artefacts were identified using SEM [123]. Typical microstructures showing different type of damages are shown in Figure 30. Moreover, toughening mechanism of particulate fillers was identified using high magnification (>20k) SEM [8], [10], [49], which proves SEM as a reliable technique to analyse the behaviour of epoxy modified matrix and to characterise machining induced damage.

Figure 30 - Microstructure of CFRP samples a) Manufacturing defects due to incorrect degree of curing b) Cracks and damages due to machining c) Matrix smearing [77]

Other non-destructive techniques such as X-ray computerized tomography (CT) and ultrasonic C-scan technique were implemented to assess machining induced damage at a subsurface level. Tsao and Hocheng [124] used those techniques to measure the extent of delamination in drilling of composites. Garcea et al. [125] described in a comprehensive review the capability of CT to provide important information across applications ranging from manufacturing process, tensile and compression tests, fatigue and impact damage. In recent years the spatial resolution of CT scans improved significantly, which allowed the detection of fibre-matrix debonding, matrix cracks, resin rich areas or voids. C-Scan technique is mostly used to detect defects and damage in composite structures caused

during manufacture and in-service conditions. A disadvantage of a CT scan system is the temporal resolution, where a single scan may take a few hours if high resolution is required (i.e. less than 1 µm) [125]. As fibre has a diameter of 7 µm, high resolution CT scans will be needed to capture individual machining defects in fibre reinforced composite materials.

In order to get a full picture of machining induced damage, a combination of surface topography, surface and subsurface morphology techniques will be used to characterize the machined surfaces. This will provide both quantitative and qualitative results, which will be linked to failure mechanism, material properties and machining parameters.

2.5 Full-field optical techniques to study the material removal mechanism at a micro scale level

In order to have an in-depth understanding of the cutting mechanics of composite samples, an adequate in-situ full-field optical deformation technique needs to be implemented in order to have both qualitatively and quantitively data of the chip formation process. A full-field measurement technique will offer information about the deformation zones forming in the chip formation zone ahead of the cutting tool as the material is removed. The resulted data will be linked with cutting force values and it will provide a full picture of the material deformation behaviour. Table 5 shows a comprehensive list of available optical methods listing their advantages/ disadvantages. Digital Image Correlation (DIC) was chosen as the main technique to monitor chip formation process due to a series of advantages including high data acquisition availability, high-resolution images, capability of measuring high strain levels, ease of use and current applications in composite materials analysis. DIC technique is further discussed in the following chapter.

Table 5 – Full-field strain measurement techniques [126]–[129]

Method	Advantages	Disadvantages
Thermoelastic Stress Analysis	• Non-contacting measurements • Full-field analysis • Can be applied to most materials • Similar to strain gauges • Range of applications • Fast stress visualisation	• Cyclic loading needed (might be advantage eg fatigue) • High capital cost ($90K to $160K) • Edge data may be poor • Liquid Nitrogen required (for some models)
Digital Image Correlation	• Relatively simple to use under both laboratory and field conditions • In-plane displacements and strain levels over 2000% have been successfully measured with measurement resolution as low as 10 microstrain possible. • Successfully used to make measurements on a range of specimen sizes from microns to several metres • Data processing speed up to 135,000 data points/sec • Accuracy unaffected by large in-plane rotations or translations	• Calibration is really important and is hard to do for micro scale without a certified calibration plate • Can be less accurate than traditional testing • The cost can be high
Photoelasticity	• Full field technique • Provides stress directions • Static and dynamic loadings • Low cost • Can be used in the interior of a specimen	• Not in situ • Needs a transparent birefringent body • Time consuming when shifted to 3D
Reflection Photoelasticity	• In-situ, real components • Full-field • Simple equipment to use	• Difficult detailed analysis • Limited temp range • Surface preparation • Limited to flat surfaces
Moire interfenometry	• Best for high strain, high temp, long term stability • High resolution, high sensitivity	• Can be only used for in-plane

2.5.1 Digital Image Correlation

DIC is a full-field, non-contact and non-destructive experimental analysis technique used to measure the in-plane displacements and strains on the surface of a specimen. The working principle involves tracking the movement of a speckle pattern applied on the surface of the material. The system uses video cameras to record images which are stored and analysed to produce full field shapes, deformation and strain maps [130]. A schematic of DIC process is shown in Figure 31. The recorded images are subdivided into an array of interrogation cells, or subsets, that provide the full-filed data map over the specimen surface. A correlation function is used to track speckle changes between images. The function can be relative to the first reference image, or to the incremental variations during the deformation [131]. The calculated displacement fields are then used to generate the full-field strain maps.

DIC systems are classed based on the recording rate (frames per second) as low speed, HS (high-speed) and UHS (ultra-high speed). HS and UHS DIC have started to be used both in industry and academia as it provides a series of advantages when compared to other non-destructive test methods. A disadvantage can be represented by the high processing time due to the large amount of data acquired using a HS DIC system.

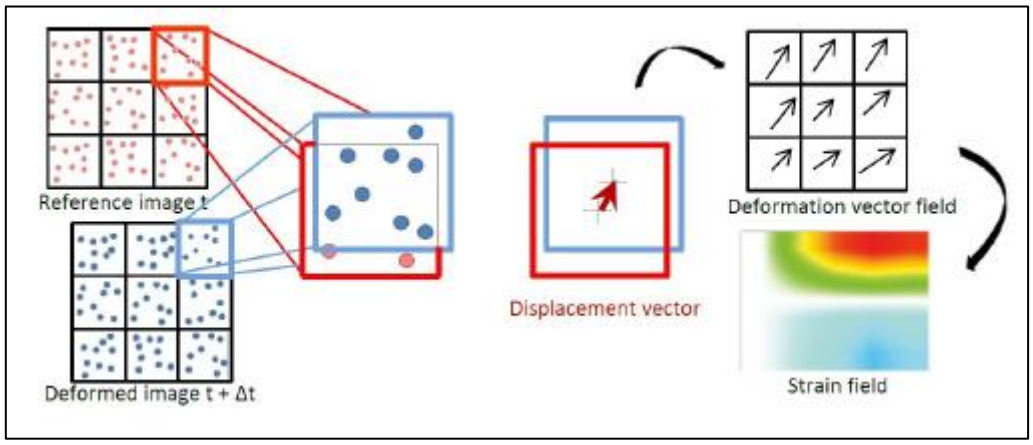

Figure 31 - DIC schematic process [132] ***(viewers are advised to use a colour version of the Figure)***

2.5.2 DIC Full-field deformation analysis in machining

The literature contains several studies [121], [130], [133]–[136] characterizing the deformation of composites using DIC, however the knowledge on the deformation evolution during machining of CFRPs is limited to schematic analyses and generic assumptions. Tekieseli et al. [136] successfully used DIC in providing strain maps in tensile tests of composite specimens. The crack propagation of the specimens was also investigated providing location, distance, and width of the cracks. Pollock et al. [134] analysed the elastic properties of woven glass/ epoxy composites under tensile loading. The method proved useful in extracting both in-plane normal strains and shear strain fields. Koohbor et al. [133] investigated the fracture response of a woven carbon fibre reinforced composite using a DIC method. Initial observations revealed that crack initiation occurred before the failure load was achieved. Scalici et al. [135] used DIC to estimate the effect of fibre orientation on failure behaviour of composite thick beams in a 3 – point bend flexural test. The failure mechanism and the interaction between composite layers was explained using DIC method. Aparna et al. [130] reported that a high speed DIC system is well suited for characterisation of flexural material proprieties due to the fast data acquisition.

However, there are limited studies available where the deformation of material during the chip formation process is quantitatively measured. Agarwal et al. [81] proposed a study of cutting mechanism and strain deformation process in orthogonal cutting of CFRPs. The change in the strain fields was identified for a certain fibre orientation, however due to the low image acquisition rate and the quality of speckle pattern did not result in any solid conclusions. Baizeau et al. [137] employed an orthogonal cutting setup for monitoring chip formation process of aluminium samples using DIC. The authors successfully generated displacement fields of the material removal process, which were further used to validate a cutting model. In another study [138], DIC was used to measure deformation, strain fields and strain rate during orthogonal cutting of aluminium. Following the mentioned literature, DIC can be successfully employed as an in-situ optical technique to study the material removal mechanism, however a high imaging acquisition rate and a quality speckle pattern is needed to generate strain field at a micro scale level.

2.5.3 Quality of speckle pattern and error assessment in DIC

The specimen preparation involves the creation of speckle pattern which can be done by spray paint, etching, printed, lithography, spin coating, scratching and abrading [139]. According to several studies [140]–[142] a good pattern will allow the correlation to be made with high confidence and produce low noise in the measurements. The literature contains a series of parameters used to investigate the quality of the speckles. These parameters are best used as comparative assessment tool to inform application methods and inform error analysis of DIC measurements [143]. Parameters such as sum of square of subset intensity (SSSIG) [144] and subset entropy [145] are local parameters which were developed based on the sum of squared differences used in the correlation algorithm. It is noted that SSSIG method was considered the most effective and widely adopted local parameter for quantitative assessment of speckle patterns [139]. However, SSSIG is only limited to analyse the local speckle pattern within an individual subset. A global parameter, Mean intensity gradient (MIG) was developed by Pan et al. [146] using SSSIG theory. A good speckle pattern should have a large MIG as it proved that it produces less bias error and standard deviation error [139]. Liu et al. [147] proposed Shannon entropy to assess the pattern quality through measures of the information content of the speckle and it was concluded that a good quality speckle should have a large Shannon entropy. To the contrary, Crammond et al. [143] reported that global pattern quality parameters, including Shannon entropy, are not sufficient to assess the quality and properties of a speckle pattern. A summary of the existing local and global parameters is shown in Table 6.

There are two types of errors associated with DIC measurements, i.e. variance errors and bias errors. The source of the variance errors are the camera noise, and matching errors during the correlation process. Bias errors include lens distortion, incorrect camera calibration, out of plane movements of the test specimens in 2D DIC. In most of the cases, bias is not known, and variance error can be calculated from static images recorded prior to test [131]. The variance error can be quantified based on the images taken before the test in the same condition as the actual test. There is a trade off between variance and bias error. Large subset sizes, low step sizes can reduce noise measurements, but it can introduce bias errors in the measurement.

Table 6 - Quality assessment parameters of DIC speckle pattern [143]

Pattern Assessment Criteria	Global or local	Remarks	Reference
Sum of square of subset intensity gradients (SSSIG)	Local	Capable of detecting the proper subset size	Pan et al. [144]
Subset entropy	Local	An indication of the fluctuation or 'randomness'	Sun et al. [145]
Mean intensity gradient	Global	Intensity gradients used in the sum of squared differences procedure	Pan et al. [146]
Shannon entropy	Global	Large number preferred	Liu et al. [147]
Speckle radius distribution	Global	Easy to implement	Lecompte et al. [148]
Speckle size	Global	Optimal speckle should be between 2 to 5 pixels	Zhou et al. [149]
Average speckle size	Global	Easy to implement	Hung et al. [150]

In this thesis, a High Speed DIC system is used to monitor the strain deformation during cutting of composite materials. A new technique was developed to obtain a speckle pattern suitable for micro-scale DIC analysis. A combination of local and global parameters is implemented in order to quantify the quality of created speckle pattern. Variance error will be calculated to ensure the validity of the results.

2.6 Summary

The mechanical properties and various production methods of composite materials are already covered in the literature for unmodified CFRPs where no fillers are used in their production. Moreover, the effect of fillers on mechanical properties such as toughness,

tensile and compressive strength is thoroughly investigated for modified epoxy composites.

However, having known that the presence of fillers would significantly affect mechanical, thermal, and structural integrity of modified epoxy composite systems and the need for finishing operations in the produced composite structures that is mostly done through mechanical cutting, the mechanics of interaction between cutting tools and modified epoxy CFRPs requires further understanding. Machining induced damage can be quantitatively characterised in relation to the reinforcement properties and machining parameters in order to develop a Design for Manufacture (DFM) strategy for epoxy modified CFRPs. Therefore, this research will focus on the effect of particulate-modified epoxy matrix in machining of CFRPs, where the effect of particulate fillers will be quantified in relation to mechanical properties of modified epoxy CFRPs – failure mechanism – chip formation – machining induced damage in conventional machining of CFRPs with the ultimate goal of damage free machining.

3 PROJECT METHODOLOGY

This chapter introduces the selected materials and manufacturing methods within the course of this research to produce the required CFRP samples. Material characterisation and mechanical testing methodologies are explained in detail together with the machining induced damage characterisation techniques. The developed in-situ orthogonal cutting rig, and the rig designed and implemented for high-speed edge trimming are also explained in this chapter. Additionally, the cutting tools and jig design used in an edge trimming machining trial are presented. Mechanical testing and characterisation of the manufactured samples was implemented to determine the effect of particulate fillers on manufactured samples.

3.1 Material selection

This section describes the matrix and fibres used to manufacture CFRP samples. The selection of the base epoxy system, the particulate reinforcement, fibre type and architecture are discussed.

3.1.1 Epoxy resins

The base epoxy resin and hardener system was chosen based on a set criterion which will allow the mixing with available particulate fillers from the market and to be used in composite manufacturing methods which are based on an infusion process. Therefore, the ideal epoxy system will have a low viscosity, ideal for RTM or VARTM, will not use extra unknown compounds such as diluents, toughеners or accelerators which might interact with the particulate fillers. Additionally, the selected system should have an extended pot life to ease the handling during manufacturing of CFRP samples. Diglycidyl-ether-of-bisphenol-A (DGEBA) was chosen in this context and its applications in the automotive and aerospace industries [151] and the availability in the market. Figure 32 shows different DGEBA and hardener systems based on their viscosity at various temperatures that improves the handling and flow of the resin during an infusion process. DGEBA MY790, LY 1564 and LY 1564 have a low viscosity ($P < 0.1$) at 60° C and are designed for composite injection manufacturing processes such as VARTM and RTM. Based on the availability on the market and further discussion with epoxy manufacturer representative (Huntsman, UK), DGEBA LY1564 and Aradur 2954 (cycloaliphatic polyamine) were chosen as the epoxy

system. This combines low viscosity with long pot life (> 100 mins) at elevated temperatures being suitable for RTM and VARTM.

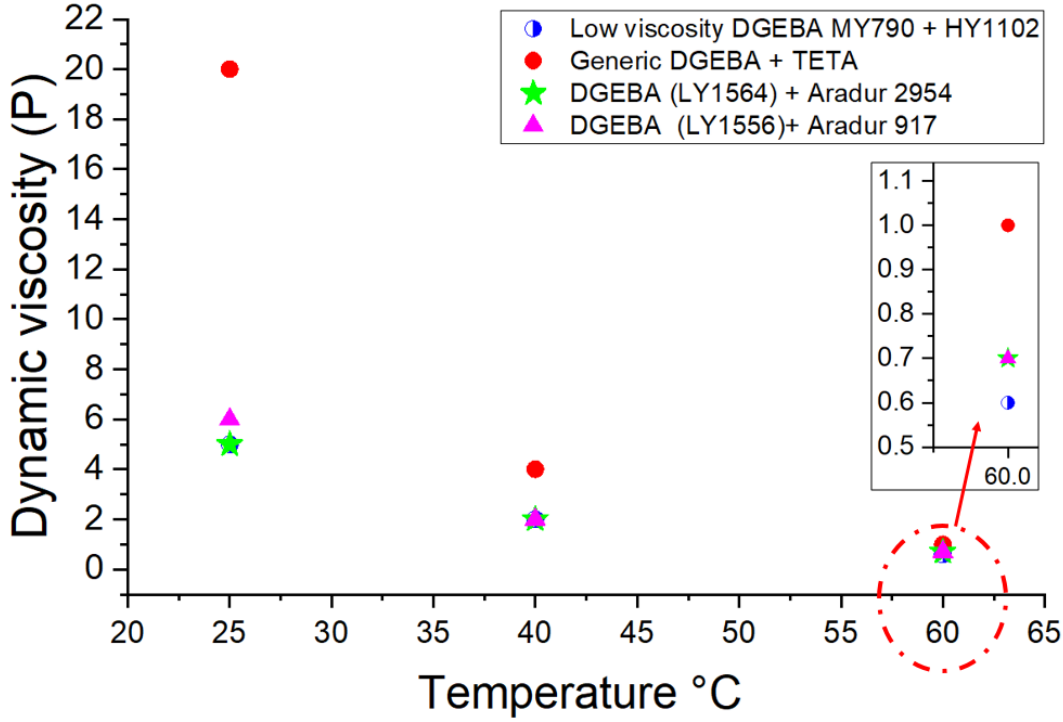

Figure 32 – Dynamic viscosity of epoxy resin systems based on their operating temperature (based on Huntsman data sheet*[152]*)

3.1.2 Particulate reinforced epoxy resin

The particle reinforcement consists of silica nanoparticles (SiO_2) and liquid carboxyl-terminated butadiene-acrylonitrile (CBTN) rubber. These particular fillers were chosen as their toughening mechanism and their effects on mechanical properties of modified epoxy composites are well documented in the literature as discussed in section 2.2.3. The silica nanoparticles (SiO_2) were supplied at a concentration of 40 wt% in a DGEBA epoxy resin (EEW of 295 g/eq, Nanopox F400, Evonik, Germany). The CTBN rubber was obtained as a CTBN-epoxy adduct with a rubber concentration of 40 wt% in a DGEBA epoxy resin (EEW of 330 g/eq, Albipox 1000, Evonik, Germany). The base epoxy resin consists of a low viscosity DGEBA with an epoxide equivalent weight (EEW) of 167 g/eq, 'LY1564' supplied by Huntsman, UK. Technical data for the chosen epoxy resins and hardener is shown in Table 7 and Table 8, respectively.

Table 7 - Technical data of the selected epoxy resins (based on manufacturer data sheets)

	Albipox 1000 (rubber nanoparticles)	**Nanopox F400 (SiO_2 nanoparticles)**	**LY 1564 low viscosity epoxy resin**
Nanoparticles content (%)	40	40	0
Base resin	Bisphenol A epoxy resin	Bisphenol A epoxy resin	Bisphenol A epoxy resin
Viscosity at 25 °C (P)	2000	60	12
Epoxy equivalent weight (g/eq)	330	295	167

Table 8 - Technical data of the hardener (Aradur 2954) (based on manufacturer data sheet)

	Aradur 2954
Description	Cycloaliphatic polyamine
H+ equivalent (g/eq)	60
Viscosity at 25 °C (P)	1
Typical mixing ratio with LY 1564 (g/100g)	35

3.1.3 Carbon fibres

Carbon fibre fabrics were chosen to be able to investigate and compare the effect of particulate-modified epoxy matrices on chip formation mechanics of CFRPs. There is a wealth of knowledge about machining of UD-CFRP materials compared with materials based on woven fabrics as discussed in section 2.2.1. Woven fabrics are mostly used in industrial applications due to their superior multi-directional load bearing capabilities. Therefore, a combination of both UD and woven fabrics were selected to investigate the fundamental physics of chip formation and to conduct machining trials at industrial conditions. The fibre type and properties are shown in Table 9. The UD non crimp fibre

(NCF) is made of T700 carbon fibres, while the twill weave fabric is made of T300 carbon fibres (Sigmatex, UK). Those fabrics were selected based on the availability on the market, compatibility with the epoxy resin, being the standard modulus industrial fibre used in various automotive and aerospace applications.

Table 9 - Carbon fibre properties [153], [154]

FIBRE PROPERTIES	**T700**	**T300**
Fibre architecture	UD – Non Crimp Fabric	Twill weave 2x2
Tensile Strength (MPa)	4900	3530
Tensile Modulus (GPa)	230	230
Density (g/cm^3)	1.8	1.76
Filament Diameter (um)	7	7
Tow	12K	3k
Fabric density Gsm	294 +/- 5%	200 +/- 5%

3.2 Composite panels manufacture

The selected epoxies and carbon fibres were used to manufacture the required CFRP panels of which quality was assessed after the production using the specified techniques detailed in section 3.3. The manufacturing procedures used for the UD and woven samples and the critical factors affecting the quality of the parts are described in this section.

3.2.1 Epoxy – filler – hardener mixture calculation

The base epoxy resin, LY1564 was mixed with given amounts of Albipox 1000 and Nanopox F400 as per

Table 10. This results in a mixture with 10 and 20% wt. concentration of silica and rubber particles. These concentrations were selected based on previous literature discussed in section 2.2.4, where a significant change in fracture toughness and tensile modulus was reported for modified epoxy blends and their composites, whilst the failure mechanism of the particulate fillers at these concentrations was thoroughly analysed. The correct amounts by weight to combine are determined by calculating the weight of curing agent

that contains one chemical equivalent of amine hydrogens (Amine H eq wt in Eq. 2) and matching that with the equivalent of epoxide that contains one chemical equivalent of epoxide groups (Epoxy Equivalent of mixture – EEW in Eq. 1 and 2) [43]. The produced EEW value of the blend was calculated using Eq. 1, while the phr (parts per hundred resin) needed in each case were calculated using Eq. 2. The resulted calculations are shown in Table 10.

$$EEW_{mix} = \frac{Total\ weight\ of\ mixture}{\frac{WT1}{EEW1} + \frac{WT2}{EEW2}} \quad (1)$$

$$phr = \frac{Amine\ H\ eq\ wt\ x\ 100}{EEW_{mix}} \quad (2)$$

Table 10 - Mixing calculations for the epoxy and nanoparticles blends

Nanoparticles by weight% in resultant blend	Name (resultant matrix name based on % and type of particles)	LY1564 (g)	Albipox 1000 (Rubber 40% wt.) (g)	Nanopox F400 (SiO_2 at 40% wt.) (g)	EEW of resin mixture	Phr hardener (per hundred parts of epoxy) (g)
Unmodified epoxy	DGEBA	100	0	0	167.00	35.93
Rubber 20%	R20	50	50	0	221.77	27.05
Silica 20%	Si20	50	0	50	213.27	28.13
10% silica, 0% rubber	Si10	75	0	25	187.32	32.03
10% rubber, 0% silica	R10	75	25	0	190.53	31.49
10% silica, 10% rubber	Si10R10	50	25	25	217.44	27.59

3.2.2 Mixing procedures

Due to the high viscosity of Albipox 1000 and Nanopox F400 at room temperature, the resins were heated up to 80 °C for 2 hours and then mixed with the base DGEBA resin, LY1564, as recommended by the resin manufacturer. The epoxy blends were mixed using a mechanical stirrer running at 600 RPM for 1 hour to obtain a homogenous mixture. These mixing parameters were selected based on available literature [5]. At the end of the mixing process, the resultant epoxy blends were degassed in a vacuum oven for 30 minutes to remove any trapped bubbles. Prior to composite infusion process, the prepared degassed resins were heated to 60 °C and mixed with the hardener according to

Table 10, followed by an additional degassing step for further 10 minutes in a vacuum oven at 60 °C.

3.2.3 Manufacturing of UD carbon fibre panels using Vacuum Assisted Resin Transfer Moulding

VARTM technique is illustrated in Figure 33 was used to manufacture UD CFRP samples to characterise mechanical properties of the produced composite panels and study the chip formation mechanics in machining trials (Chapter 5). A preliminary study was conducted to determine the limits of the designed process with respect to the maximum number of UD NCF carbon fibre layers and it was found out that the full impregnation can be achieved for up to four layers due to the viscosity of resin and fibre architecture. The arrangement of VARTM layers is illustrated in Figure 34 and can be described as follows:

- Carbon fibre layup sits between two layers of peel ply (AeroGrade Nylon 66, EasyComposites, UK) which should cover the entire surface of the carbon fibres (300 x 250 mm). In this case, the peel ply was cut slightly larger. Peel ply was removed after curing of the panels;
- The infusion mesh (FM105 EasyFlow Knitted polypropylene, EasyComposites, UK) is larger than the carbon fibre layup. Two layers of mesh where used to have a better infusion across the whole thickness of the layup;
- Vacuum bag film which covers the whole layup of different layers;
- Silicone resin outlet ports (EasyComposites, UK) which are temperature resistant.

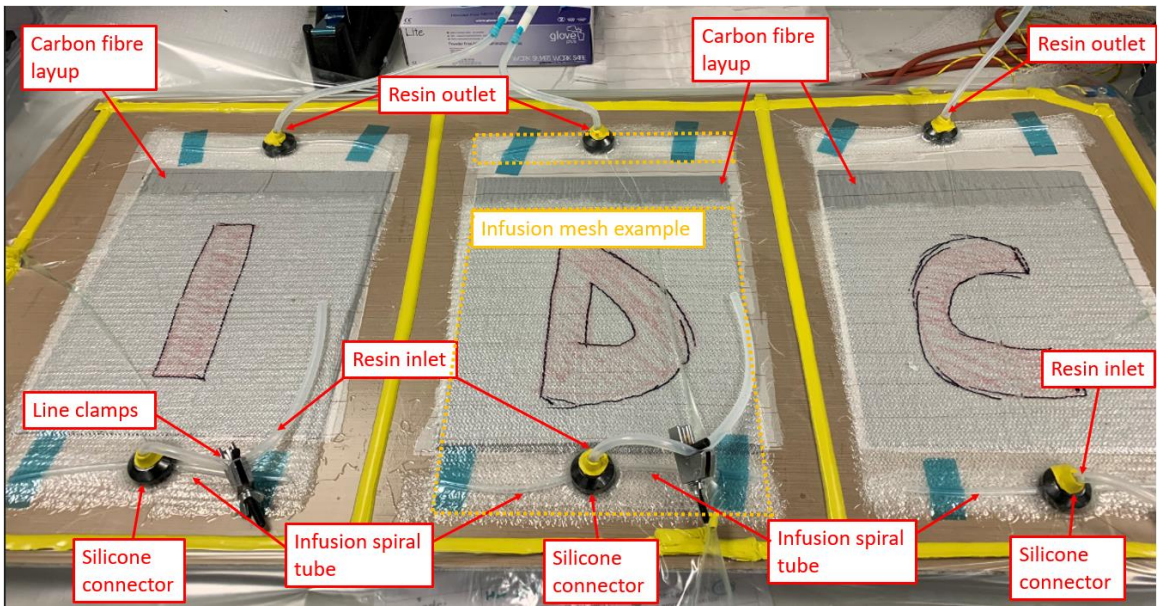

Figure 33 - Vacuum Assisted Resin Transfer Moulding setup

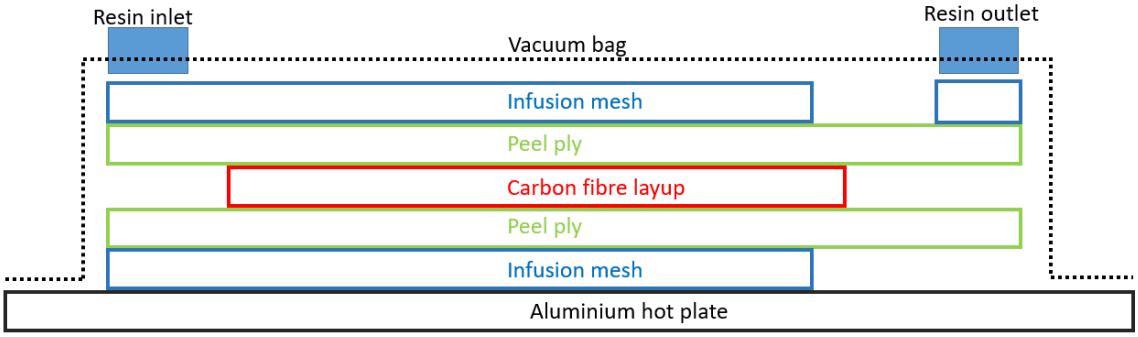

Figure 34 - Schematic of VARTM layers

Prior to resin injection, debulking process was done to allow a better compaction of the fibres by compression the vacuum bag and then releasing it. This was done by applying 2 cycles with a full vacuum for 10 minutes and then a release of air trapped inside the bag. The injection of the epoxy and hardener mixed as discussed in Section 3.2.2 was done at a pressure of 0.95bar and a temperature of 60 °C in order to keep a low viscosity to help the resin flow through the carbon fibres. All the pipelines, infusion spiral, vacuum bag and sealant were selected to be capable of withstanding temperatures higher than 80 °C and the resin flow was adjusted using the resin line clamps showed in Figure 33. Once the layup is fully impregnated and resin flow reaches the outlet port, the inlet port is clamped off. The outlet port is left open for 10 minutes more to let any bubbles trapped in the layup to bleed out and then is clamped off. No dry spots or regions were noticed after the injection.

The composite panel is then cured for one hour at 80 °C on the aluminium hot plate. The laminate was then post-cured in the oven for 2 hours at 140 °C with a 2 ºC ramping cycle. This curing cycle was selected based on manufacturer data sheet [155]. The resulted cured laminates had a thickness of 1.2 ± 0.05 mm measured using a digital Vernier calliper.

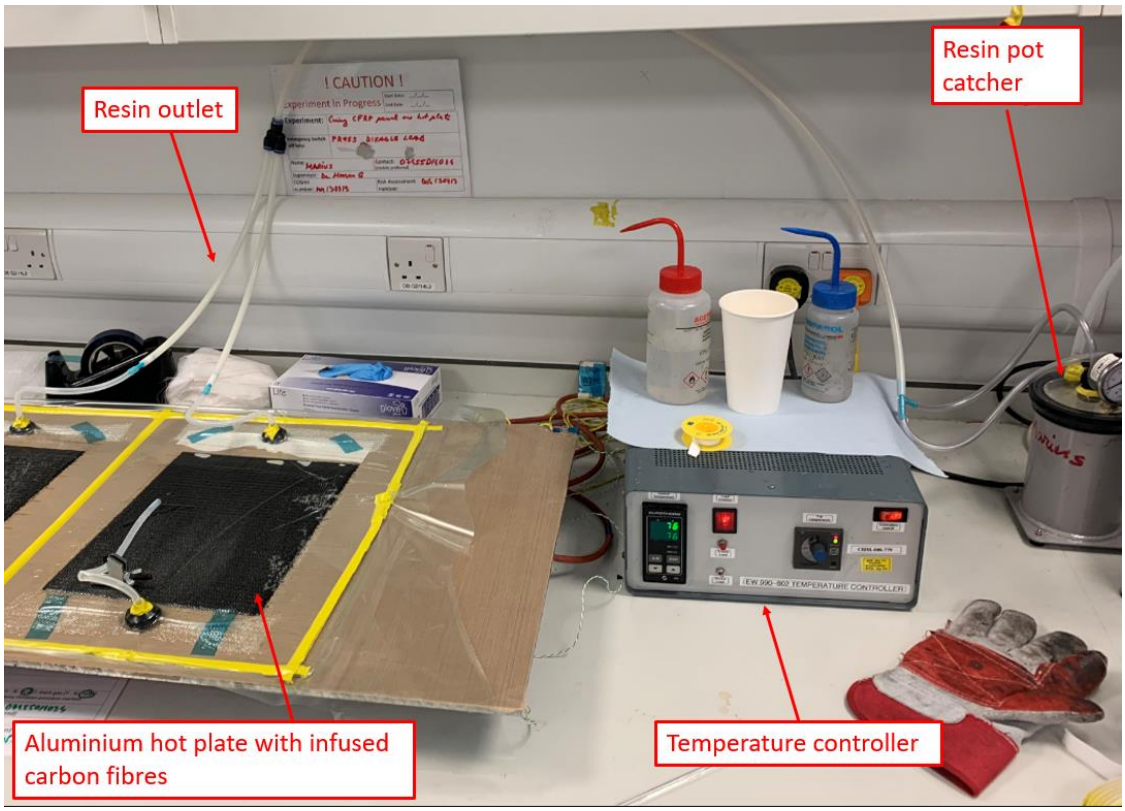

Figure 35 - Fully impregnated panel and temperature controller

3.2.4 Manufacturing of CFRP panels and epoxy sheets by Resin Transfer Moulding

A Hypaject Mk1 RTM machine together with a steel mould and resin catch pot were used to manufacture 300 x 300 mm of epoxy resin sheets, as well as UD and woven CFRP panels for machining trials (Chapter 5 and 6). The steel mould has two injection flow gaps on the sides and a vacuum port in the middle as shown in Figure 36. A layer of release agent (Easy Lease, Easy Composites, UK) was applied on the surface of the mould and to pipefittings prior to injection. The mould was placed into a 20-ton press, so that the resulted panel will have a uniform thickness. A total of 460g of mixture of resin and hardener were injected into the steel mould that was heated in a vacuum oven at a temperature of 60 °C to reduce the viscosity of the resin mixture and facilitate a better impregnation and resin flow. The

CFRP panels were made of 14 woven plies or 10 UD NCF layers to prevent fibre washout or marcelling – a process where fibres slide on top of each other as resin is injected into the mould due to a lack of compression force [156]. The woven plies were stacked symmetrically about the mid-plane in a balanced manner to give [((0,90)/(+45,−45))3/(0,90)]s, while UD plies were placed over each other with fibres in the same direction across thickness. The uncured woven ply thickness is 0.28mm which gives a nominal laminate thickness of 3.92 mm. The RTM injection process was done in steps starting at a pressure of 2 bars to a maximum of 7 bars using a Hypaject pump (Magnum Venus Products, UK) as shown in

Table 11. CFRP panels were cured as per curing cycle defined in Table 12.

For manufacturing epoxy sheets, a constant injection of 1 bar was used and the process was completed in less than 1 minute. Panels were cured at a maximum temperature of 140 ºC as defined in Table 12. The resulted cured laminates had a thickness of 3 ± 0.03 mm measured using a digital Vernier calliper.

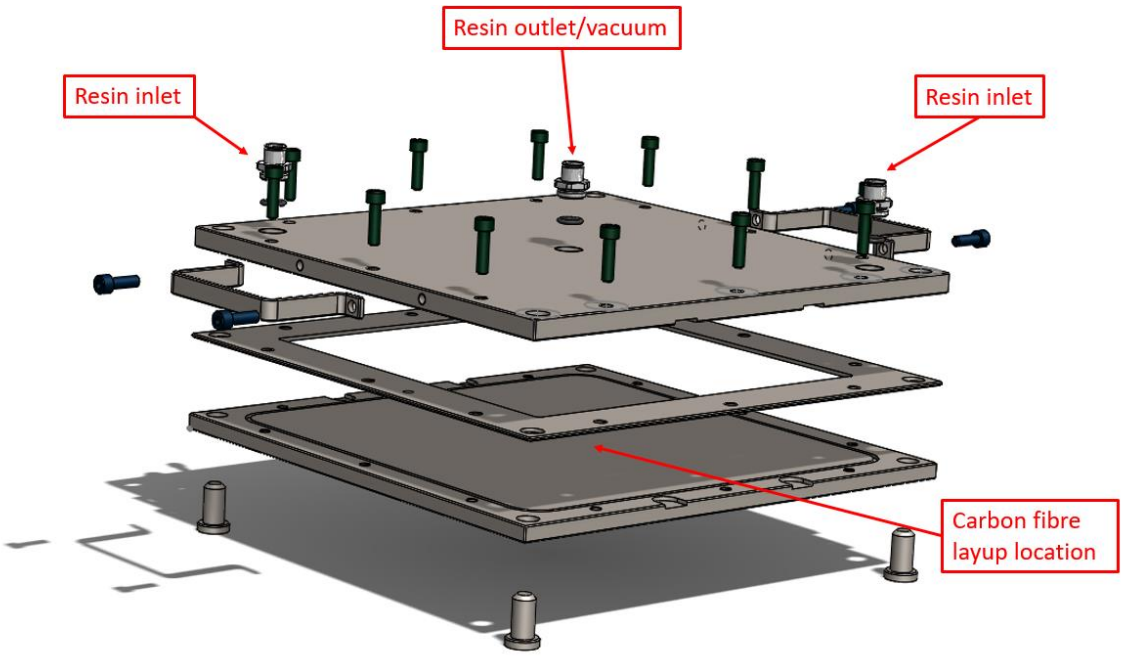

Figure 36 - Schematic of Resin Transfer Mould assembly

Table 11 - RTM resin infusion steps

Infusion steps	Duration (minutes)	Pressure (Bars)
1	5	Vacuum
2	10	2
3	20	3
4	20	5
5	20	7

Table 12 - RTM panel curing cycle

Curing cycle
80 ºC dwell for 60 minutes
Remove panel from CFRP mould
Ramp at 2 ºC/min to 140 ºC
140 ºC for 120 minutes
Ramp at 2 ºC to room temperature

3.2.5 Manufacturing of tensile test end tabs

Pre-impregnated carbon fibre (prepreg) MTM46-36%-12KHTS40-250-300 (Solvay, UK) were used to manufacture specimens used as end-tabs for composite tensile test samples. This solution was adapted based on material availability in the university composite laboratory. Seven layers of material were used in a (0,90) sequence to ensure on the thickness required as per ASTM D3039 [157]. The prepreg stack was placed on a glass plate and it was covered on top and bottom with a nylon peel ply (AeroGrade Nylon 66, EasyComposites, UK). This generated a rough surface which facilitates a better adhesion with the composite tensile samples. A layer of breather (Air Weave N-10, Tygavac, UK) was used to provide a path for removal of air and other gases during curing. The layup was then

sealed in a vacuum bag and placed in the autoclave (Premier Autoclave Solutions, UK) and the curing cycle shown in Table 13 was applied.

Table 13 - Autoclave curing cycle

Cycle segment	Temperature target (ºC)	Temperature ramp rate (ºC/min)	Pressure (bar)	Pressure ramp rate (bar/min)	Dwell time (minutess)
1	120	2	6.2	0.2	60
2	180	2	6.2	-	60
3	20	3	0	0.5	-

3.3 CFRP material characterisation

Fibre-volume fraction analysis was performed to ensure that the resulted composite panels have a low void volume and high fibre fraction regardless of the resin and particle reinforcement used. Digital scanning calorimetry (DSC) and thermomechanical analysis (TMA) were used to determine the material glass transition temperature (T_g) and degree of cure. T_g is important for thermoset epoxy composites, as above this temperature, the material enters a rubber-like state and fibres are not fully supported by the epoxy matrix. This will ultimately affect the cutting behaviour of CFRPs, therefore is important to have a constant T_g for all manufactured panels, so that the machining behaviour between samples with different concentration of reinforcement particles can be compared.

3.3.1 Fibre-volume fraction

To ensure the consistency of manufactured panels, the fibre and resin content was measured. Two random sections from each panel were cut to determine the fibre-volume fraction prior to machining to ensure and assess the consistency of the panel quality. The samples were mounted using Epocolor resin (Buehler, UK) and polished using a Buehler Automet 250. The polishing parameters used are adapted from [42] and are shown in Table 14. Five images were taken from each polished sample using a Nikon optical microscope. These were analysed using Pax-it! 2 software (USA) which calculated the ratio of matrix,

voids and fibres through contrast analysis of the pictures. A set of final values was calculated based on the averaged results of the measurements of each image.

Table 14 – CFRP polishing steps

Step	Abrasive	Lubricant	Force (N)	Time	Platen speed (RPM)	Head speed (RPM)	Relative Rotation
1	P600	Water	22	Until plane	175	60	Contra
2	P1200	Water	22	00:50	175	60	Contra
3	15 µm diamond	15 µm Polycrystalline Diamond Suspension	22	00:50	175	60	Contra
4	6 µm diamond	6 µm Polycrystalline Diamond Suspension	22	04:00	100	60	Contra
5	0.05 µm diamond	0.05 µm Suspension	18	01:30	75	60	Contra
6	0.05 µm diamond	0.05 µm Suspension	18	01:30	75	60	Comp

3.3.2 Differential Scanning Calorimetry (DSC)

Differential scanning calorimetry (DSC) was used to characterise thermal properties of materials. It looks of how material's heat capacity is changed by temperature. As the material is heated, the heat flow of the material is measured. The mass of material was measured and placed within a pan, which is heated against an empty pan so that the amount of heat flow running in and out of the material placed on the pan can be calculated. As well as measuring the T_g of material, the degree of cure can be measured by observing the transition in the heat flow diagram which appear as an exothermic reaction,

when the energy is expelled by the material, i.e. crystallisation or endothermic reaction, when the energy is absorbed by the material, i.e. melting [158]. If the polymer is fully cured, no exothermic reaction will be shown on the resulted graph. The degree of cure is calculated using Eq. 3, where Δh is known as the enthalpy value. DSC is used to provide a T_g estimate, while other techniques such as DMA (Dynamic Mechanical Analsysis) or TMA (Thermomechanical Analysis) are used to calculate a reference T_g value. DSC, TMA and DMA measure different processes and therefore, the T_g vary and scientists have agreed to accept a single temperature as the indicator per certain standards [159].

$$\% \, cured = \left[1 - \frac{\Delta h \, cured}{\Delta h \, uncured}\right] x100 \tag{3}$$

A PerkinElmer DSC6 was used to calculate the degree of cure. Samples were taken off from polymer sheets cured using the same curing cycle as the CFRPs panels. 10 ± 2mg of material per pan were used and the following thermal cycle was applied:

- Hold for 1 minute at 25 °C
- Heat from 25 to 250 °C at 10 °C/min
- Hold at 250 °C for 10 min
- Cool from 250 to 25 °C at 10 °C/min
- Hold 1 minute at 25 °C
- Repeat cycle

The repeated cycle was used to ensure that the polymer sample is fully cured. If the sample was not fully cured, the Δh of the second run could be added to the first, however this was not the case for the polymer materials used in this thesis. The maximum temperature of 250 °C was chosen based on polymer data sheets in which the maximum T_g was 180 – 185 °C and as previously noted that temperatures above 250 °C makes the DGEBA and cycloaliphatic polyamine hardener unsuitable for scanning and potentially damaging the DSC machine.

3.3.3 Thermomechanical Analysis

The basis of thermomechanical analysis is the change in dimension of a sample as a function of temperature. For polymer samples, the change in the free volume is recorded. This is associated with the absorption or release of heat, the loss of stiffness or by the change in relaxation time [160]. A Perkin Elmer Pyris Diamond thermomechanical analyser

(TMA) was used to record T_g of the epoxy blends. Rectangular samples with a dimension of 12.5 x 3.5 x 3 ± 0.1 mm were cut from the manufactured epoxy sheets. At the start of the test, the temperature was equilibrated at 25 °C. Specimens were then heated to 200 °C at 10 °C/min, while a constant force of 200 mN was applied through a probe on the polymer samples as shown in Figure 37. As the temperature increases, the sample expands and the change in dimension is recorded via the glass probe. The change in dimension relative to temperature known as coefficient of thermal expansion (CTE), can be observed at the T_g point as T_g in a polymer corresponds to the point in the expansion curve where the free volume begins to allow greater chain mobility usually seen as an inflection or bend in the thermal expansion curve. T_g was found as midpoint of the transition range using the first derivative of the dimension change versus measured temperature by following the analysis method outlined in ISO 11359-3: 2019 [161]. Further details and interpretation of the data are given in the results section, 4.1.3.

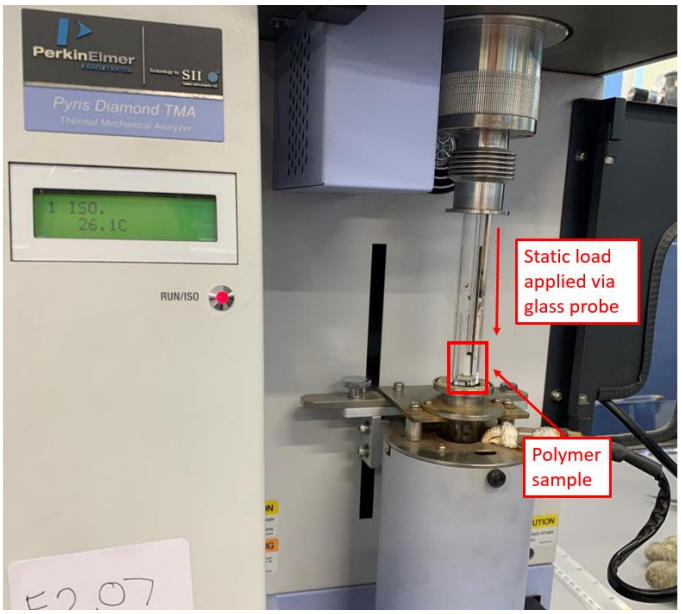

Figure 37 – Perkin Elmer Thermomechanical analyser

3.4 Mechanical testing

Tensile and fracture toughness tests were conducted to determine the effect of silica and rubber particle reinforcement on the mechanical performance of polymer modified epoxy and modified CFRP material. It was already reported and discussed in section 2.2.5 that nanosilica and rubber microparticles are improving the mechanical properties of polymers

such as strength and fracture toughness & energy. Toughening mechanism effect was discussed in studies where polymer tensile and fracture toughness tests were used [2], [4]–[8], [47]. The translation of modified epoxy matrix to the CFRP composite was tested through transverse tensile tests and mode I fracture toughness tests. For this thesis, a combination of tensile and fracture toughness tests of modified polymer and the subsequent composite was used to clearly identify the effect of particle reinforcement on the mechanical performance of CFRPs.

3.4.1 Tensile tests of polymer samples

Uniaxial tensile tests were conducted in accordance with ASTM D-638 [162]. Tensile 'dog-bone' Type IV samples were AWJ machined according to ASTM D-638 standard [162] (Figure 38) from epoxy sheets manufactured using the RTM technique described in Section 3.2.3. The tests were carried out using a Tinius Olesen H5K-s general test frame at a displacement rate of 5 mm/min as per standard recommendation. The tensile Young's Modulus, E, yield stress, σ_y, and strain at failure, ε_f were recorded and average of 5 repeats were used to report the measured values.

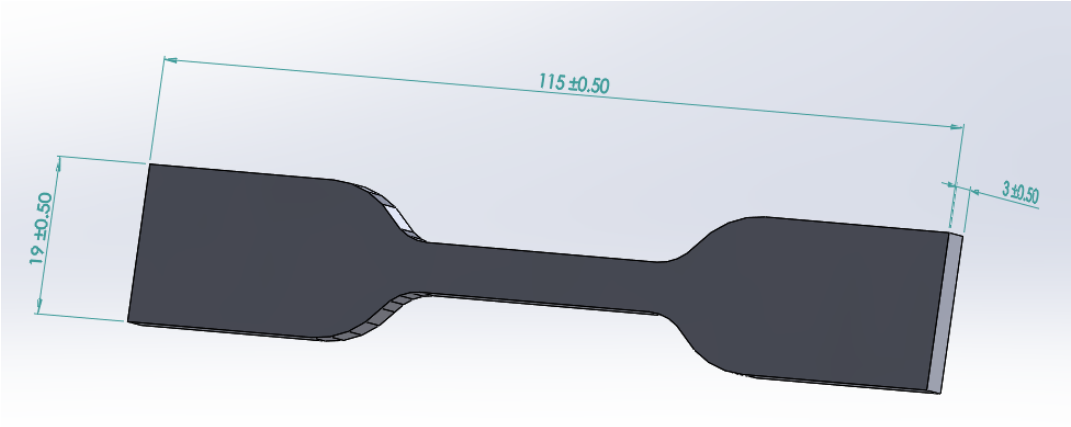

***Figure 38 – Type IV sample as per ASTM D-638 s*tandard (units are in mm)** [162]

3.4.2 Fracture toughness test of polymer samples

Compact tension (CT) samples were used to determine the fracture toughness of the produced samples in accordance with ASTM-5045 [163] to study the effect of particle reinforcements on the modified epoxy blends. Meso-scale CT samples were manufactured according to ISO-13586 [164]. Samples, shown in Figure 39, were cut from epoxy sheets manufactured by RTM as described in Section 3.2.3 using the AWJ machine and the

gripping system was designed and manufactured according to [165]. The thickness of the samples was defined by the limits of the RTM mould, and it was 4 ± 0.15 mm. A sufficiently thick specimen, i.e., where the thickness is larger than the fracture process zone radius, can be assumed to be in a state of plane strain and it is reported that the plastic zone radius for brittle polymers such as the epoxies used in this thesis is smaller than 1 mm [165], therefore the selected dimensions should fulfil the plane strain conditions required by the ASTM-5045 standard. The validity of the applied assumptions is reported in section 4.2.2.1 and shows that plane strain conditions are successfully accomplished.

The initial crack was generated by tapping a fresh single-edged razor blade into the notch using a toolmakers clamp and the crack length was measured using a DinoLite USB microscope. As per standard, 5 tests were carried out at a speed of 1 mm/min using a Tinius Olsen H25K tensile machine to determine fracture energy, G_{IC}, and fracture toughness, K_{IC}.

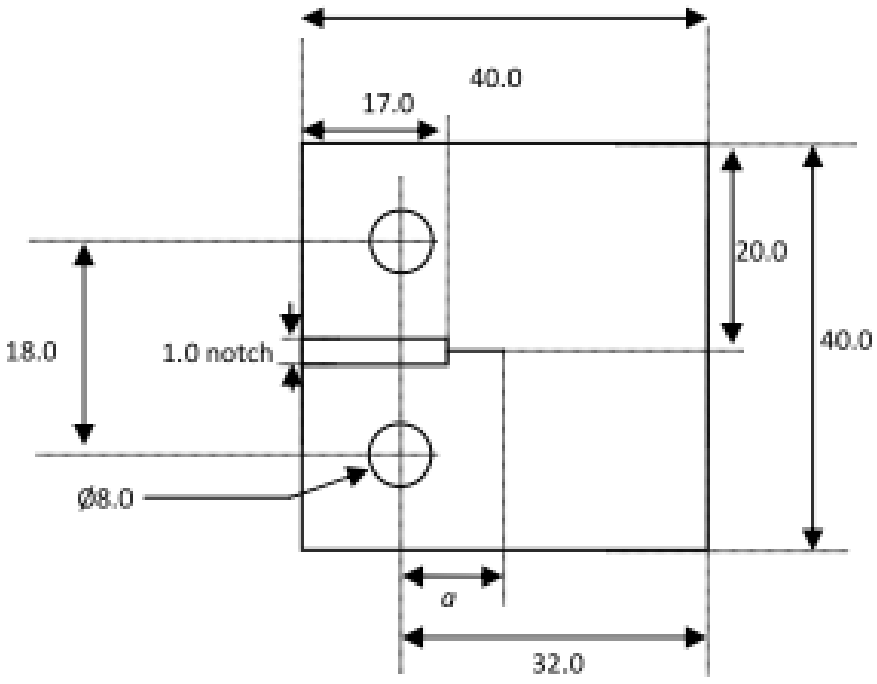

Figure 39 – Fracture toughness test specimen dimensions according to [166] ***(units are in mm)***

3.4.3 Tensile tests of CFRP samples

Tensile tests were carried out in such a way that the loading direction was aligned (UD - 0°) and normal (UD - 90°, transverse) to the fibres of the CFRP samples according to ASTM D3039 [157]. The UD samples were used to investigate the effect of epoxy resin on the tensile properties and fracture mechanism of the produced parts, which is known to be dominated by the fibre orientation. Specimen width, thickness and length along with end tabs dimensions are shown in Table 15. Five tests for each batch of samples were carried out at room temperature with a crosshead displacement rate of 2 mm/min. The deformation of the samples within the gauge section was recorded with a mechanical extensometer, Figure 40, from which the % elongation and strain at failure, ε_f were calculated along with the tensile Young's Modulus, E, and yield stress, σ_y.

Table 15 – CFRP tensile sample size

	UD 0°	**UD 90°**	**End Tabs UD 0°**	**End Tabs UD 90°**
Thickness (mm)	1.2	1.2	1.5	1.5
Width (mm)	15	25	15	25
Length (mm)	250	175	55	25

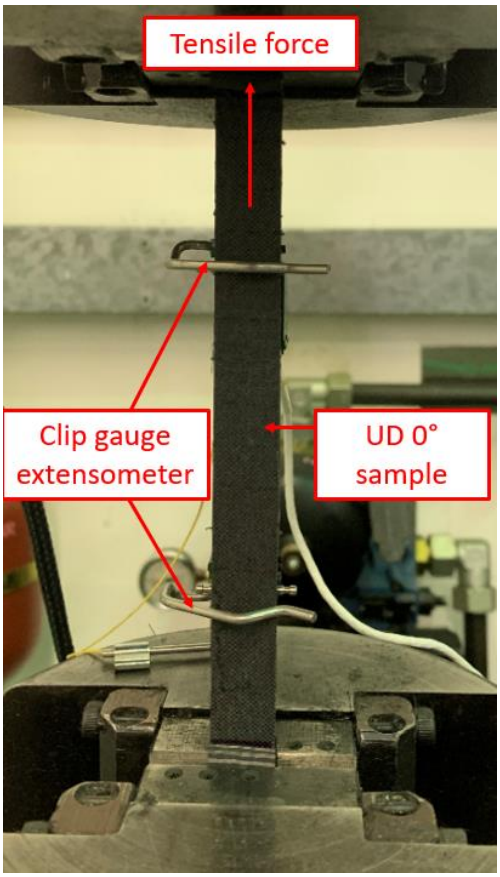

Figure 40 – Tensile test of CFRP sample in 0° UD direction

3.5 Investigation of chip formation process

This section presents the methodology developed to study the chip formation process of polymer and CFRP samples at a micro scale level including the design and manufacture of an orthogonal cutting rig coupled with a 2D High Speed Digital Image Correlation (DIC) system. The working principles of the DIC system and the methodology used are discussed.

3.5.1 Preparation of samples

The same AWJ machine that was used to cut other samples was used with set settings to achieve the maximum surface quality as shown in Table 16. The cut samples were manually removed after the machined panel was taken out from the machine tool bed and measured with a Digital Vernier Calliper within a tolerance of + 0.05 mm after AWJ machining.

AWJ machining was chosen due to several advantages compared to other common CFRP machining operations used in industry including milling or trimming. The ease of use of

AWJ, flexibility and no need for complex tooling, no need for complex extraction unit, as well as quantified machining induced damage [23], made AWJ a good solution for cutting CFRPs. This damage was removed by polishing the surface of the specimen across the thickness, so that the results of the orthogonal cutting trials will not be affected. An example of machined polymer samples is shown in Figure 41.

Table 16 - Abrasive Water jet cutting parameters

Pressure (MPa)	Nozzle orifice (mm)	Stand of distance (mm)	Feed rate (mm/min)	Abrasive mesh size	Abrasive type
204	0.2	1.3	310	80	Garnet

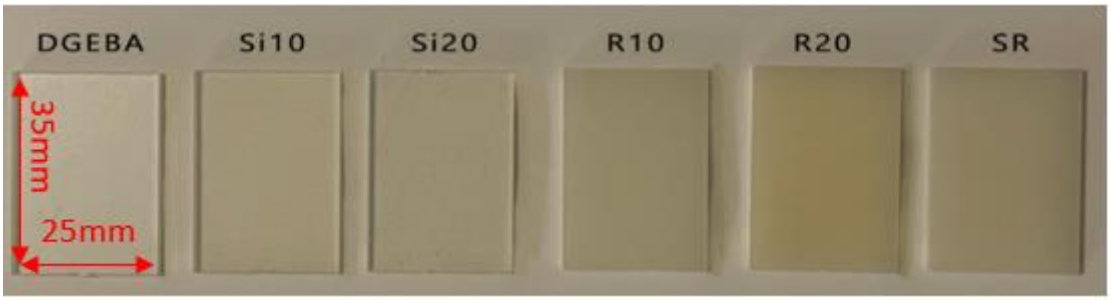

Figure 41 – Epoxy samples manufactured for orthogonal cutting tests

3.5.2 Cutting rig assembly and force measurement

The in-situ orthogonal cutting rig consists of a rectangular block workpiece sliding throughout a vertical channel of a fixed assembly under plane strain conditions as shown in Figure 42. The main body of the rig is made out of steel with a T-shaped cross section, a horizontal channel for the cutting insert and vertical channel for sliding the sample (Figure 42 – b)). The workpiece (25 x 25 x 3mm) is pushed at a speed of 1 m/min (corresponds to 1m/min feed in cutting operations) throughout the vertical channel with a plunger attached to the cross head of the tensile machine (Tinius Olsen 25ST). The depth of cut can be set (in this case range of 30 to 200 µm) with a digital micrometre with a resolution of 1 micron, attached to the left-hand side of the cutting rig assembly (Figure 42 – a)). To restrict out of plane deformation and ensure plane strain deformation status, a sapphire glass is placed against the cutting insert where the cutting tool engages with the workpiece

(Figure 42 – c)). This provides the required viewing window for the high-speed image acquisition and facilitates the alignment of the cutting insert and workpiece. The cover plate is painted in black matt and secured by 4 screws as shown in Figure 42 – a), while the rig is fixed on a Kistler Dynamometer to measure cutting forces. Further details about the cutting rig working principles and dimensions are available in the literature [167].

Kistler dynamometers operate using pre-loaded force piezo electric sensors for x, y and z force components which sit within 4 sensors located in the dynamometer plate [168]. A Kistler 9257B dynamometer, calibrated annually, was used to measure the cutting force due to the high acquisition rate compared to the load cell of the tensile machine. The dynamometer was connected to a 4 channel charge amplifier (Kistler type 5070A12100) which was connected to a NI DAQ acquisition card. A LabView programme was used to collect the raw data and a Matlab script was used for post-processing. The dynamometer was fixed on the tensile machine bed using a steel bed and four screw bolts. Channel sensitivity and ranges were set as per Table 17. A sampling rate of 10 kHz was set and synced with the imaging frequency to have a better understanding of the material removal mechanism

Prior beginning the machining experiment, force measurement accuracy was checked using dead weights and digital load cells. A set weight was used to check the forces in z-direction (Figure 43). Force in x and y-direction were checked by applying a compression force measured with a point load cell and compared with the recorded value of the dynamometer. However, due to the restricted movement of the sample inside the provided slot, the measured F_x force is deemed to be not accurate enough to interpret the required forces.

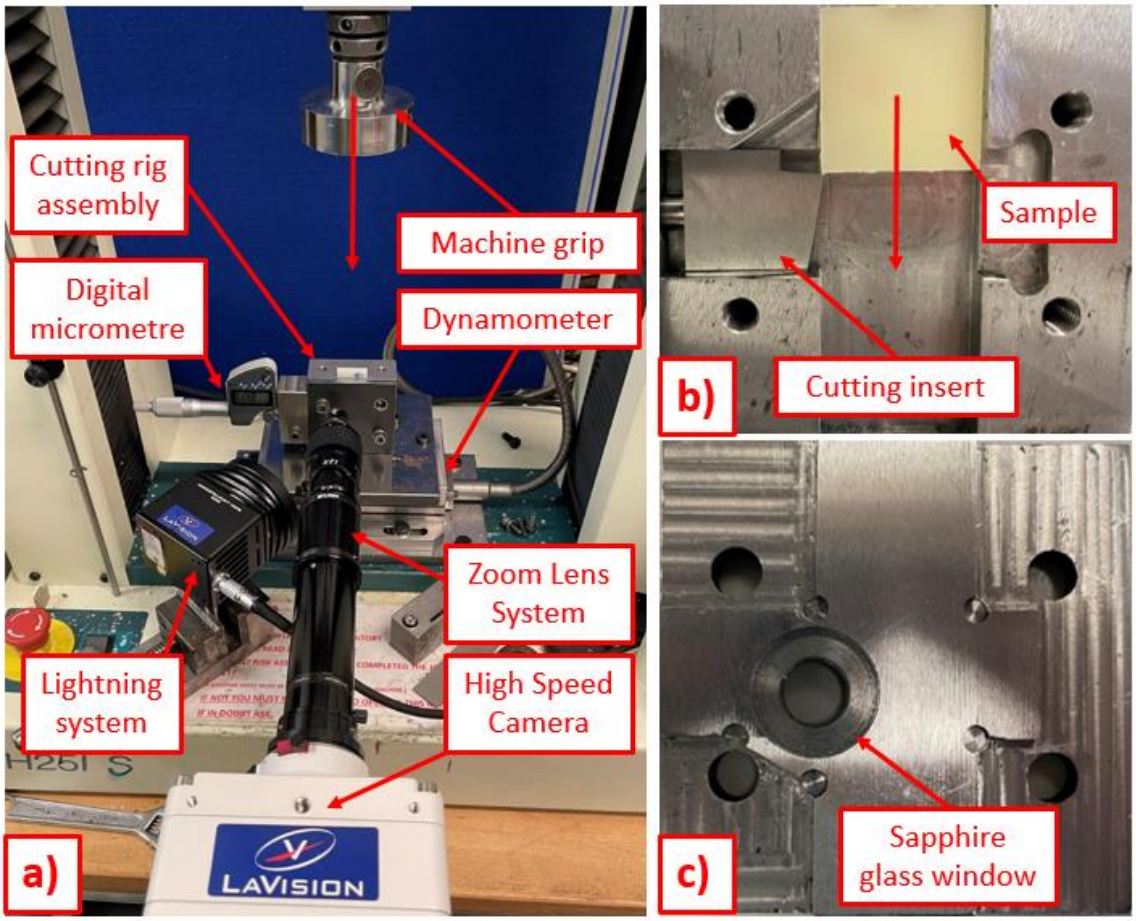

Figure 42 – Orthogonal cutting rig setup a) General setup including DIC cameras and machine grip b) Steel wedge block, cutting insert and sample c) Top plate containing the sapphire glass window

Table 17 – Dynamometer channel sensitivity and ranges

Direction	Channels	Sensitivity (pC/N)	Measuring range (kN)
F_x	1	0.389	0 – 1
F_y	2	0.347	0 – 1
F_z	3	0.452	0 – 1

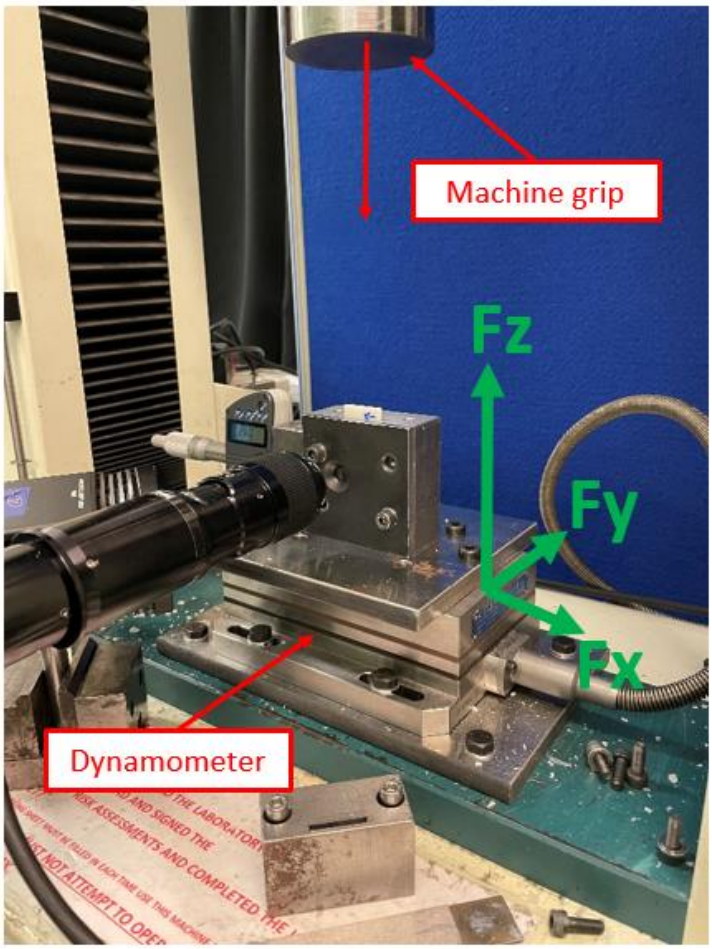

Figure 43 – Dynamometer force axis system

3.5.3 Cutting inserts

High-speed steel cutting inserts with a rake angle α=10°, clearance angle γ=10° and edge radius r=10 µm were used (Figure 44 – a)). The cutting tools were manufactured using precision grindings and geometrical features of all the tools were measured using an optical focus variation system, Alicona Infinite Focus SL and 2.7% variation was recorded which deemed to be negligible. An example of cutting edge radius measurements is shown in Figure 44 – b). The cutting tools were replaced regularly to ensure the cutting performance was not affected by the tool wear. The plastic deformation of the inserts was visible after each cut on the images recorded using the DIC system. Once this was spotted, the insert was changed with a fresh one. A single set of cutting tool geometry was used in this research project, as the aim is not to determine the effect of various cutting tool geometries, but to better understand the mechanics of cutting in this newly developed epoxy-modified samples.

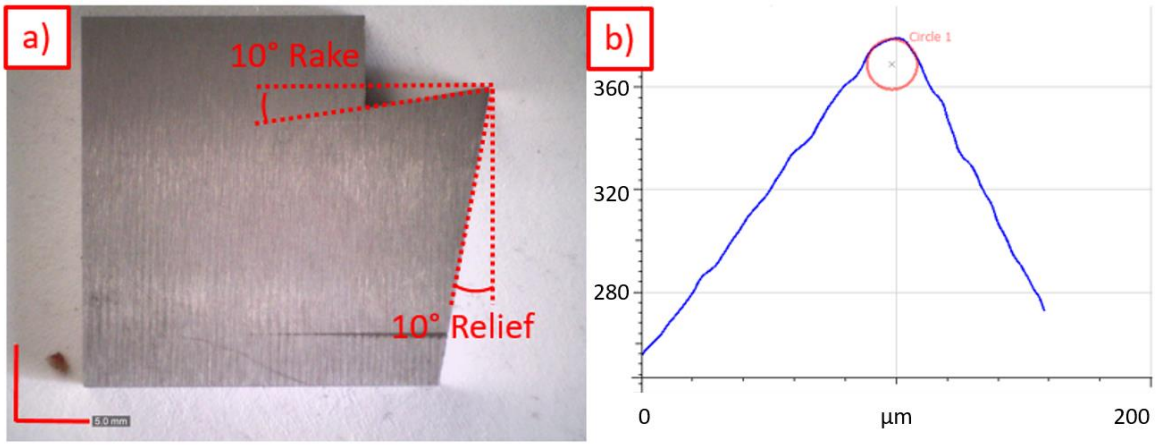

Figure 44 – High-speed cutting insert example a) Side view of cutting insert b) Measurement example of cutting edge radius

3.5.4 High-Speed 2D Digital Image Correlation (DIC) set up

A 2D High Speed (HS) DIC (LaVision, GmbH) system was used to investigate the material removal mechanism. HS DIC system is composed from a HS Phantom V410L camera, Navitar 12x zoom lenses, NI DAQ acquisition card, HS light system, HS PTU (Programmable timing unit) and a dedicated laptop with LaVision Davis software used for image acquisition with the parameters shown in Table 18. The chosen subset size and step size was found to produce acceptable noise levels as discussed in Section 3.6.4. The correlation mode was set relative to the first image, which represent the undeformed specimen before the tool workpiece interaction.

Table 18 - High Speed 2D Digital Image Correlation parameters

Parameter	**Value**
Technique	2D High Speed DIC
Software	Davis 10.1
Subset size	29 x 29 pixels
Step size	9 pixels
Camera	Phantom V410L
Lens	Navitar 12x Zoom Lens system
Image resolution	796 x 1277 pixels
Field of view	1.025 x 1.644 mm
Frame rate	1 to 10 kHz

Spatial resolution	0.11 mm

3.5.5 Application of speckle pattern for DIC

The DIC speckle patterns were applied using a fine coat of white paint together with the speckle pattern created by spraying copier toner powder using a dust atomizer (Goodson, USA). An example of the created speckle pattern is shown in Figure 45. ImageJ software was used to determine the subset and step size. It was found that the average speckle size was 58 ± 4 px^2 by observing an image of 350 x 350 pixels. If it is assumed that each individual speckle is circular, the individual diameter of the speckle is 8.59 pixels. According to Sutton, Orteu and Schreier [126], a subset should contain at least three speckles, this result in a subset size of 25.77 pixels. Even though 25.77 is the exact size, a larger subset size should be chosen as not all the speckles are circular. ImageJ analysis also showed a speckle density of 47.76 ± 6.5 % (black), where 10 set of speckle images were analysed.

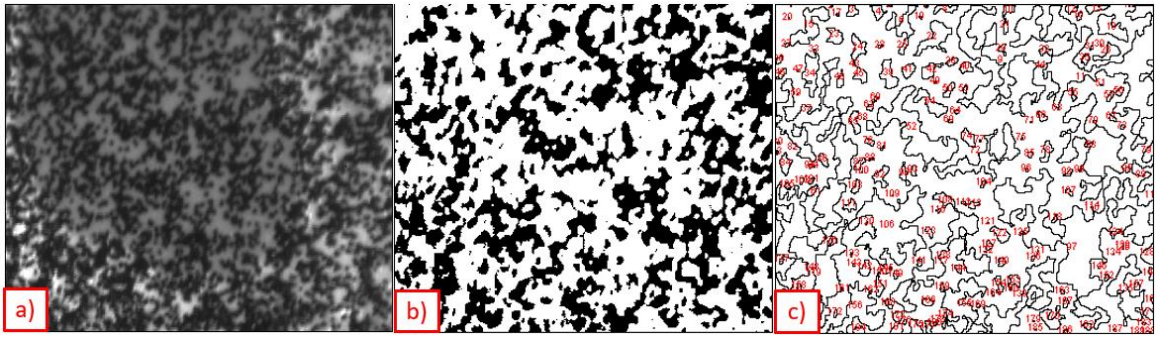

Figure 45 – ImageJ processing images for calculating the average speckle size showing a) Speckle pattern b) Binary image of speckle pattern c) The result of image processing

The variance error was calculated using static images recorded prior to test [169]. By analysing 100 static images prior to the interaction of cutting tool and workpiece, the rigid body motion error and the optimum step value were found. Figure 46 shows the results of the analysis where a subset size of 27 and 29 pixels, with three different step sizes were used. The lowest variation in the data, 0.42 %, was found for a step size of 29 pixels and step size of 9 pixels. The average rigid body motion error can be used as standard deviation for any presented strain results.

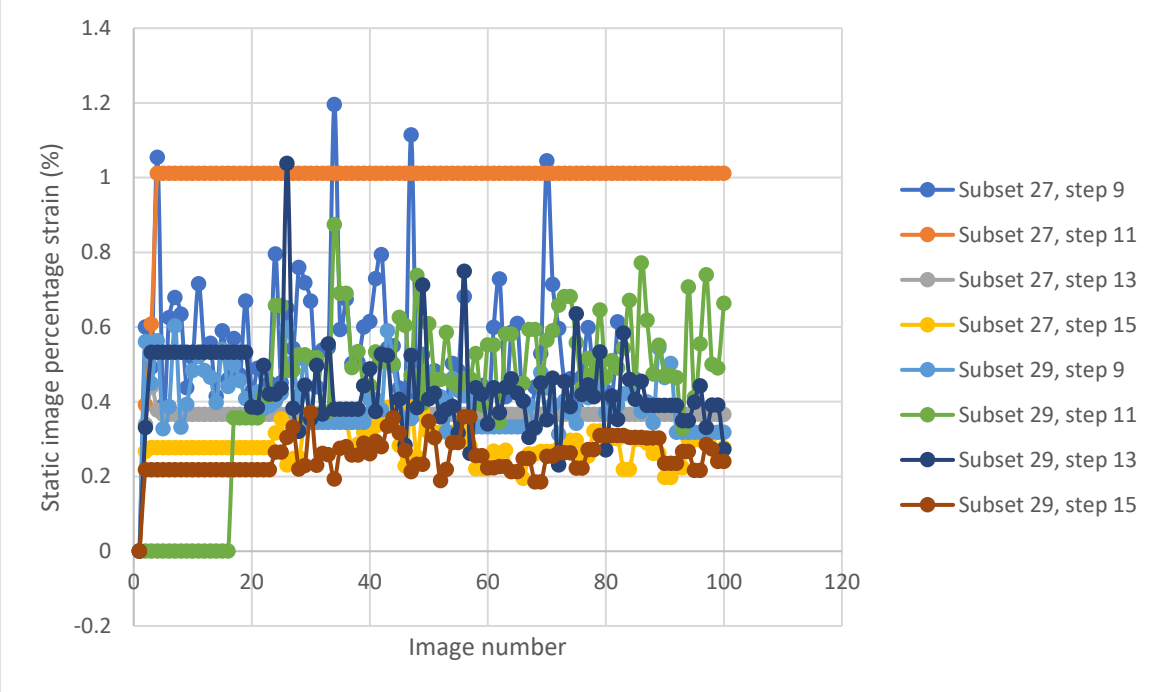

Figure 46 - Rigid body motion error calculated in function of subset and step pixel sizes

Standard calibration procedure [170] was followed using a 1 µm graticule (MP1 LaVision calibration plate) to ensure the images are calibrated and the possible image rotation correction is applied on all the images prior to the start of the experiments.

3.6 Edge trimming of CFRP samples

This section details the edge trimming trial which was done in an industrial level machining environment. Machining trials took place in a CNC machine equipped with a specially designed milling fixture and carbon fibre dust extractor, where the cutting forces were measured using a Dynamometer.

3.6.1 Milling fixture set-up

A XYZ 1060HS VMC 3-axis milling machine was used to trim the produced CFRP samples. These were attached to a specially designed milling fixture as shown in Figure 47. The fixture allows the cut of 3 samples of 25 x 25 x 3 mm in one linear movement of the CNC tool bed. The cutting forces were measured using a Kistler 9275 Dynamometer mounted on the tool bed. The dynamometer was connected to a 4-channel charge amplifier (Kistler type 5070A12100) which was connected to a NI DAQ acquisition card. A LabView programme was used to collect the raw data and a Matlab script was used for post-

processing. Channel sensitivity and ranges were set as per Table 17. A sampling rate of 50kHz was set to have enough data points of material removal during the cutting process. Prior beginning the edge trimming study, the dynamometer was further checked for correct force measurements. A set weight was used to check the forces in z-direction. Force in x and y-direction were checked by applying a compression force measured with a point load cell and compared with the recorded value of the dynamometer.

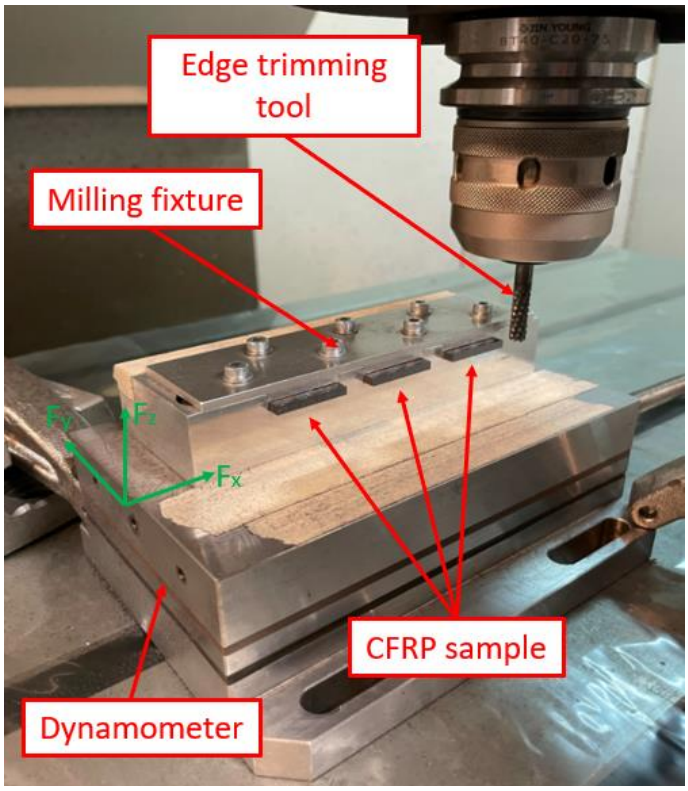

Figure 47 - CFRP edge trimming fixture

3.6.2 Specific cutting power calculation

Typically cutting and tangential cutting forces can be calculated by applying a mechanistic force modelling approach using Eq. 4 and 5 [22], [91]:

$$F_r(\varphi) = K_{rc} a h(\varphi) + K_{re} a \quad (4)$$

$$F_t(\varphi) = K_{tc} a h(\varphi) + K_{te} a \quad (5)$$

Where $K_{rc}, K_{tc}, K_{re}, K_{te}$ are cutting shear force coefficients and edge force coefficients for radial and tangential direction, φ is tool rotation angle, h is instantaneous chip thickness and a is depth of cut.

For the woven carbon fibre composites combined with the double helix angle used in research results in more complex as the specific cutting energy coefficients which needs to be calculated for each ply orientations and mechanistic models needs to applied to summate these forces [22]. Additionally, the use of radial tangential forces does not include the z force components (along the length of the tool) which are also a significant factor when using tools with helix angles which direct forces into the tool axis [171]. An alternative is to calculate the specific total power which will be used to compare the machining behaviour between the different materials and cutting feeds used in this experiment. As the cutting forces are cycling depending on feed and speed of the cutter, the sum of integral of the cutting forces for one tool rotation is calculated (Nm) as shown in Figure 48. This is divided by the total volume of material removed (mm^3) to provide U_T (N/mm^2), specific total power, as shown in Eq. 6. U_T is defined by the specific algebraic sum of forces (Nm) divided by the total volume of material removed (mm^3):

$$U_T = \frac{\int F_x dx + \int F_y dx + \int F_z dx}{V} \qquad (6)$$

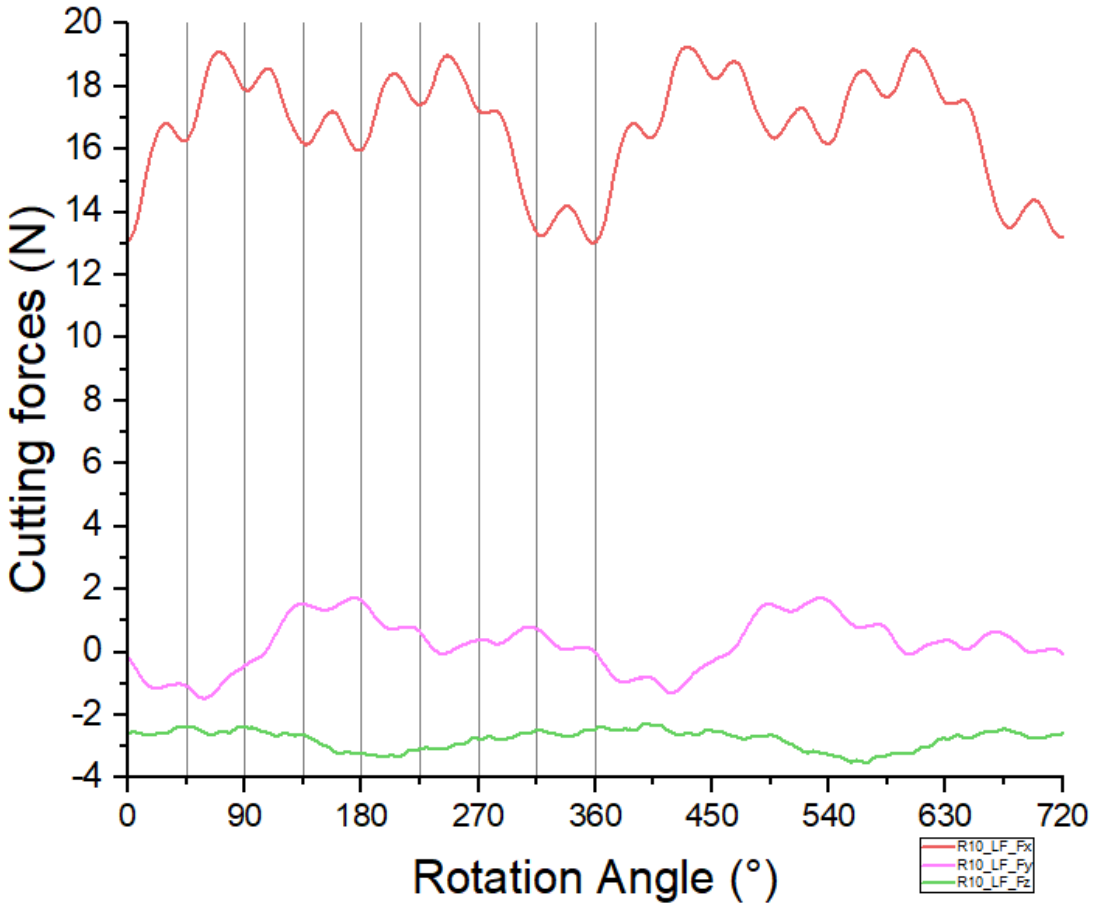

Figure 48 – Example of cutting force behaviour for 2 full tool rotations for R10 sample

3.6.3 Cutting tool parameters

As detailed in the literature review, section 2.4.3.2, various milling tools geometries and diameters are available for milling CFRP. For this particular edge trimming operation, a diamond coated fine nicked router designed for CFRP trimming is used. The patented nick and flute form shown in Figure 49 is designed to eliminate uncut fibres and delamination. The tool geometric properties are listed in Table 19. This particular tool was recommended and supplied by the tool manufacturer, OSG Corporation.

Figure 49 - DIA BNC edge trimming cutter [172]

Table 19 - Edge trimming tool geometry features

Tool	Overall length (mm)	No. Flutes	Helix Direction	Helix angle (°)	Relief angle (°)	Rake angle (°)	Suggested RPM	Recommended feed rate (mm/rev)
DIA - BNC	68	8	Double	15	18	8	5.300 – 9.500	0.1 – 0.12

Cutting parameters are given in Table 20. The cutting speed recommended by the tool manufacturer range from 5300 to 9500 RPM, while the feed rate range from 0.1 to 012 mm/rev or 1140 mm/min and 1900 mm/min. A fixed cutting speed of 179 m/min (9500 RPM) was selected for this edge trimming trial. Two feed rates were selected, 0.12 mm/rev and 0.20 mm/rev, the last one being outside the recommended parameters. This high feed was selected in order to elicit detrimental change in the machined surface of the material and to further check if the presence of fillers have a significant effect on the cutting forces and machining induced damage compared to bulk composites. An initial clean cut with a depth of cut of 0.3 mm was done to ensure each sample is aligned and any form of machining induced damage from AWJ machining is removed. At this low depth of cut the machining induced damage created shall not affect the results generated at the larger depth of cut. Even the samples were polished to remove any form of damage as previously done in the orthogonal cutting tests, a clean cut is necessary to align the three specimens on the rig making sure the depth of cut is constant. The depth of cut was set to 1 mm based on existing edge trimming of composite literature [88], [94], [173], [174].

Table 20 – Edge trimming parameters

Tool Ø	Flutes	Vc (m/min)	RPM	FPT	Vf Feed Rate (mm/min)	Feed Rate (mm/rev)
6	8	179	9500	0.025	1900	0.200
6	8	179	9500	0.015	1140	0.120

The parameters listed in Table 20 were calculated using the following formulas:

$$V_f = N\ x\ F_N \qquad (4)$$

$$V_C = \frac{\pi DN}{1000} \qquad (5)$$

$$F_t = \frac{V_f}{Nn} \qquad (6)$$

Where V_f is the feed rate describing the linear velocity of the workpiece (mm/min), *N*is the spindle speed (mm), F_N is the feed per revolution (mm/rev), V_C is the cutting speed in m/min, D is the diameter of the cutting tool (mm), F_t is the feed per tooth (mm/tooth) and n is the number of flutes on the tool.

3.6.4 Design of experiments setup

A full factorial DoE matrix is implemented for the edge trimming experiment to link the physics of chip formation process discussed on the orthogonal cutting tests to the results from the edge trimming experiment. The DoE information is given in Table 21. 9 repeats for each case were chosen to provide enough data to create a statistical response comparison based on the factors and levels used. Based on this DoE, ANOVA is conducted to create a statistical link between particle type, concentration, and feed and cutting force behaviour and machining induced damage being quantified by surface metrics parameters.

Table 21 – DoE Factor information

Factor	**Levels**	**Values**
% Rubber	5	0, 5, 10, 15, 20
% Silica	5	0, 5, 10, 15, 20
Feed	2	Low Feed (LF = 1140 mm/min), High Feed (HF = 1900 mm/min)
Number of repeats for each case: 9		

3.7 Post machining analysis

3.7.1 Areal Surface Measurements

Areal surface scanning was conducted using an Alicona Infinite Focus SL optical focus variation system using 20x magnification. The working principle of a focus variation microscope consists of taking images at different focal lengths and stitching them together

to create a surface topography used for areal surface measurements as previously discussed in Literature Review, section 2.4.6.1.

Samples were put in a 3D printed sample holder in order to scan the machined surface (Figure 50). This holder allowed the use of an automated script which decreased user error in location of the samples. Exposure was set to 7.25 ms and contrast set to 0.7, in order to create the necessary contrast to be able to distinguish different surface features without altering the surface topography measurements. A vertical resolution of 200 nm and a lateral resolution of 1 µm were set to meet the requirement criteria described in BS EN ISO 4288 [110] and Alicona recommendations [175]. An area of 5 x 3 mm (thickness of the sample) was scanned and the image was cropped to remove edge defects which can create extrapolation and extensions of the profile (Figure 51). After surface levelling, λ_c filter was applied before spatial and autocorrelation textural parameters were collected from Alicona IF-Measurement Suite software in accordance with ISO 2517 [176]. λ_c is a cut off ratio which separates roughness from the form and waviness of the measured item. Alicona guidance [175] recommend a cut of value 5 times greater than the R_a value in order to completely remove the effects of waviness. R_a is defined as the average of a set of individual measurements of a surface peaks and valleys. For an Ra value of 0.1 and 0.2 um and based on BS EN ISO 4288-1996 [110], a cut-off value λ_c of 0.8 mm was applied. This also met the requirement of λ_c to be 5 times greater than Ra. Five-line measurements were taken in the transverse direction of the fibres covering the full thickness of the specimen as shown in Figure 51. The full list of measured parameters is shown in Appendix A.

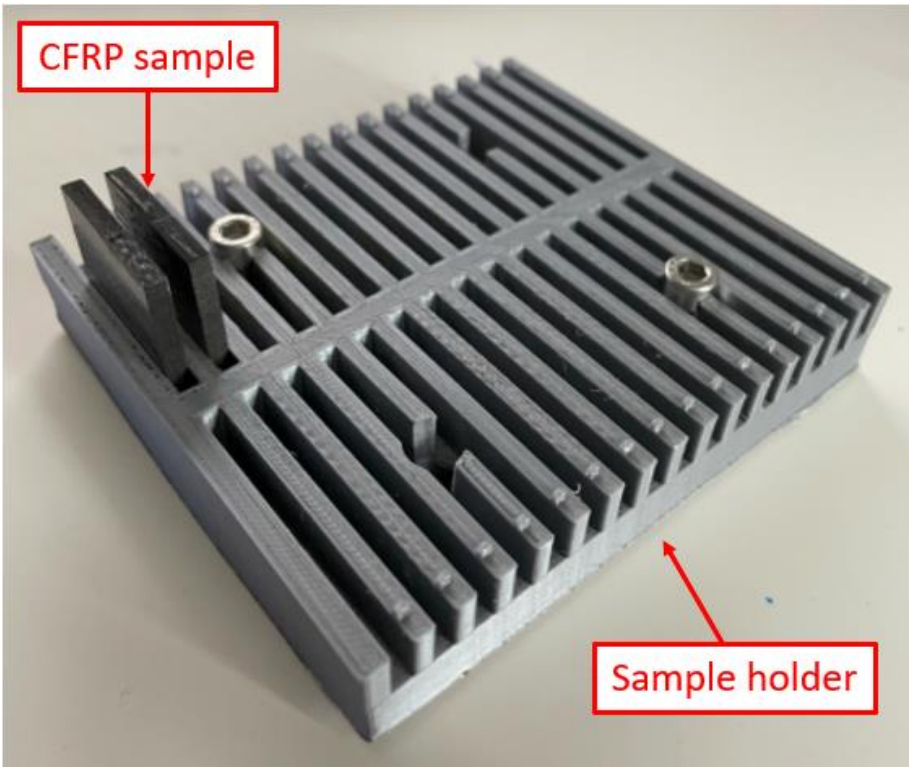

Figure 50 – CFRP sample holder for Alicona measurements

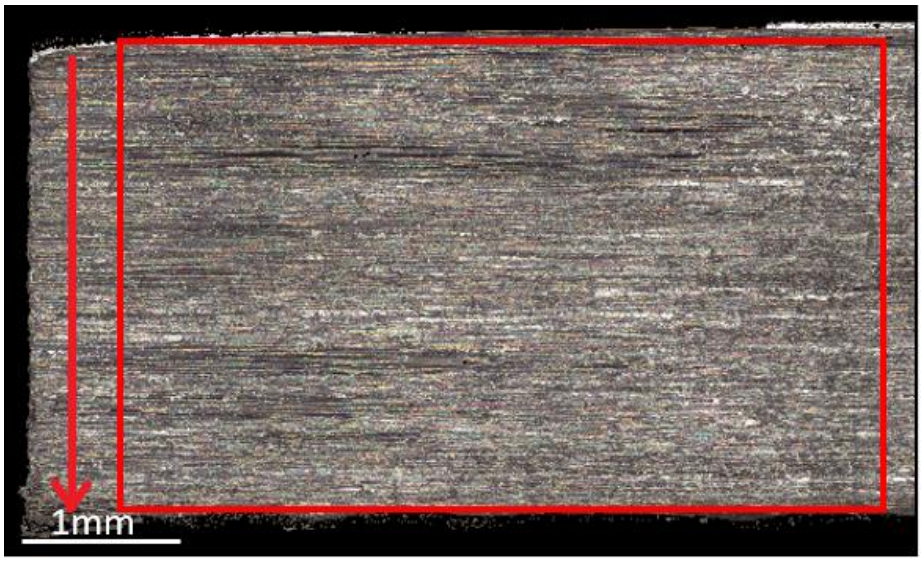

Figure 51 – Alicona surface measurement image showing cropping area to remove minor edge defects

3.7.2 Scanning Electron Microscopy

In order to assess the morphology of the machined surface, SEM was used to collect images at high magnifications. SEM uses an electron gun to fire a focused beam of electrons onto a material under vacuum. A detector then receives the reflected electrons, and the signals are used to produce an image of the surface. Conductive surfaces are

needed to prevent the electron beam from charging the scanned surface which can cause thermal damage of the sample.

In this thesis, samples were mounted on aluminium stubs using Electrodag 1415 silver conducting adhesive. This was also used on the side of samples to the mounting surface of the stub to allow an earth path around the sample to avoid any sort of thermal damage to occur. Samples mounted on the stubs were then coated with 5 nm of gold using a Quorum Q150R S plus (London, UK) sputter coater. An FEI Inspect F (Hillsboro,Oregon, USA) and a TM3030Plus tabletop SEM (Hitachi Europe, London, UK) were used at a 5kV accelerator voltage and a level 2 post size to obtain the required resolution for the imaging features of interest on the surface of the machined samples.

3.7.3 Micro-CT scanning

Micro-CT scanning is a method which uses X-rays to penetrate carbon fibre sample and a detector is used to capture the rays which passed through the sample (Figure 52). The sample is rotated 360° while the detector collects images which are then stitched together to provide a 3D image. The machining induced subsurface damage was characterised using a Zeiss Xradia Versa 620 X-ray Microscope (Pleasanton, Ca, USA) housed within Sheffield Tomography Centre (STC) at the University of Sheffield, UK. This method was utilised specifically for non-destructive 3D imaging. The sample was glued to a cocktail stick and screwed onto one of the Versa sample mounts to ensure it did not move during the scan. X-rays were generated from a tungsten transmission target and collected on a CCD (charge coupled device) 16bit 2000 x 2000 pixel detector camera. Five samples (DGEBA, R20, Si20) were scanned under varying conditions; X-ray tube voltages ranged between 50 and 60 kV, tube currents between 90 and 108 µA, source power between 4.5 and 6.5 W, and exposure times between 2 and 3 seconds per projection. The number of samples were limited based on the associated costs and equipment availability. 1601 projections were collected for each scan over a scan time of 2 hours. On the whole, inserting a filter to filter out low energy X-rays was not necessary; however a filter (LE2) was inserted for some scans. Variable scan conditions were needed because of variations in sample thickness, meaning X-ray penetration was more difficult for the thicker samples and needed a higher power. For all scans an objective lens was used giving an optical magnification of 4x, while binning

was set to 2 producing an isotropic voxel (3D pixel) size of 2.5 µm at a field of view of 2.5 x 2.5 mm for each scan. A filtered back projection method was used to reconstruct the data, and reconstructed .txm files were converted to 8bit greyscale 2D .tiff stacks using Zeiss Scout and Scan Reconstructor software. Details about parameters used for each batch of samples are given in Appendix B – CT Scan parameters. The Scout and Zoom methodology were used to create targeted high-resolution regions of interest (ROIs) from lower resolution scans (at ~10 µm voxel size), which were also collected. 3D volume information was segmented and visualized in Dragonfly, a specialised tomographic software (Object Research Systems, Montreal, Canada).

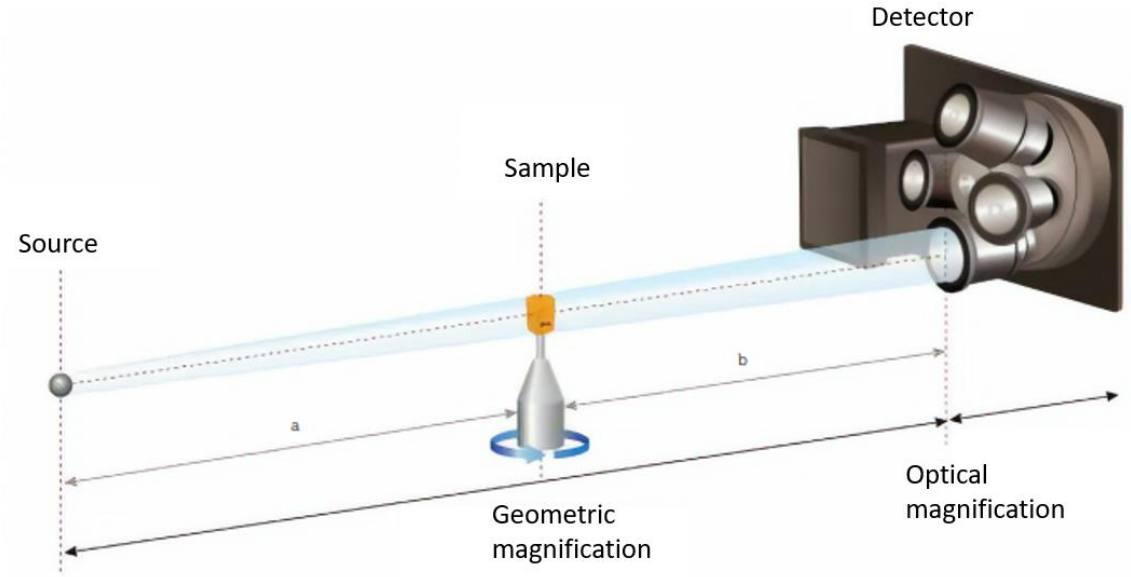

Figure 52 – Working principle of a Versa CT scanner [177]

3.8 Health and safety aspects

In the presented machining trials methodology, it was ensured that extraction of carbon fibre dusts was present. The chips generated during machining of CFPRs remain in the air after machining and are a potential hazard to the machine operator as analysed in [178]. The possible infection areas based on the size of the generated chips are shown in Figure 53. To further minimise risk during machining, the cutting of CFRPs and polymers has always been done in an enclosed space. A waiting period of 2 minutes following each cut was taken, in order to let the dust to settle on the bed of machine prior to cleaning with the vacuum system. A Karcher 001 NT 35/1 Tact Te H was used to filter the particles

generated in the machining trials. Respiratory disposable masks, Boole eye protection and nitrile gloves were used to ensure the adequate protection against dust when mounting/ unmounting samples.

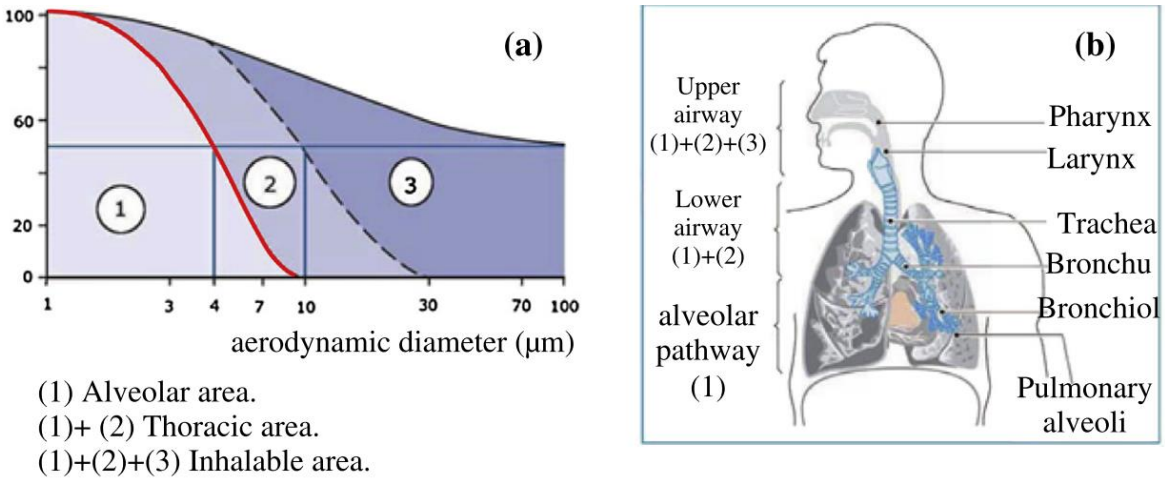

Figure 53 – Inhalation and penetration of particles in human lungs (a) Classification of particles in 3 categories b) Areas of action of each category (Figure reproduced from [178]***)***

3.9 Methodology summary

Table 22 summarises the applied experimental investigations to manufacture, analyse, characterise and assess machinability of the modified CFRP samples and determine the role of implemented particulate-fillers on the chip formation mechanics and machining induced damage. The results of the designed and conducted experiments are presented and discussed accordingly in Chapters 5 – 7.

Table 22 – Experimental methods demonstrated in Chapters 5 – 7

	Chapter 5	Chapter 6	Chapter 7
	Chip formation process in modified epoxies	Cutting mechanics of epoxy modified CFRP samples	Edge trimming of epoxy modified CFRP samples
Material	Epoxy modified samples	Woven CFRP samples	Woven CFRP samples
Manufacturing technique	Enclosed mould	RTM	RTM
Machining platform	Orthogonal cutting rig coupled with HS-DIC system and Dynamometer for cutting force measurements		CNC machine
Cutting parameters	Depth of cut: 30, 50 and 100 µm Cutting feed: 1m/min	Depth of cut: 200 µm Cutting feed: 1m/min	Depth of cut: 1 mm Cutting speed: 9500 RPM Cutting Feed: 1140,1900 mm/min
Tool materials	Tool rake and relief: 10°, Cutting edge radius: 10 µm		OSG Composite router tool
Sample characterisation	DSC, TMA, Tensile and fracture toughness tests, SEM, white-light microscopy	DSC, TMA, Void content analysis	DSC, TMA, Void content analysis
Post machining assessment	Strain analysis, SEM, cutting force analysis	DIC Strain analysis, SEM, CT – scans, surface metrics, cutting force analysis	SEM, surface metrics, cutting force analysis

4 CHARACTERISATION OF MECHANICAL PROPERTIES OF MODIFIED EPOXY CFRP SAMPLES

Characterisation of the manufactured samples was done to ensure that samples provide consistency. This way the behaviour of the samples which undergo machining operations will be linked to particulate reinforcements effect and not to any manufacturing induced damage, i.e., increased void content, incomplete curing cycle, and discrepancy in the glass transition temperature. Mechanical testing results are used to quantify the effect of particulate fillers and further used in the discussion of the machining results.

4.1 Material characterisation

This section presents the material characterisation results covering the fibre-matrix-void content analysis, degree of cure and T_g of the manufactured samples.

4.1.1 CFRP fibre-matrix-void content analysis

A representative UD configuration of the produced panels is shown in Figure 54 with fibres in 0° and 90° orientation. Figure 55 shows the average voids, matrix and fibre content (%) for all manufactured panels taken from 5 specimens for VARTM and RTM manufactured panels using the method described in section 3.2. The void content is low with an average of 1.51 ± 0.2 % and 0.56 ± 0.15 % for all 30 analysed samples for VARTM and RTM, respectively. The lower void percentage of RTM vs VARTM is expected and previously reported in the literature [171]. It is noticed that void content (%) in VARTM samples increases with rubber content as shown in Figure 55 – a). The increase of void content is related to the increase of viscosity of the modified epoxy resin with the increase concentration of rubber, which lowers the impregnation quality during the VARTM process. Si10 and Si10R10 samples had a void content (%) in the standard deviation of DGEBA, while Si20 showed an increase which is attributed to increased viscosity of the resin mixture as discussed in Section 2.3. An increasing trend in void content (%) with increasing particle concentration, however the maximum void content for RTM samples is

0.8 ± 0.18 % for R20 sample. Overall, panels have an acceptable quality, with a maximum void content of 2.24 ± 0.24% for R20 sample.

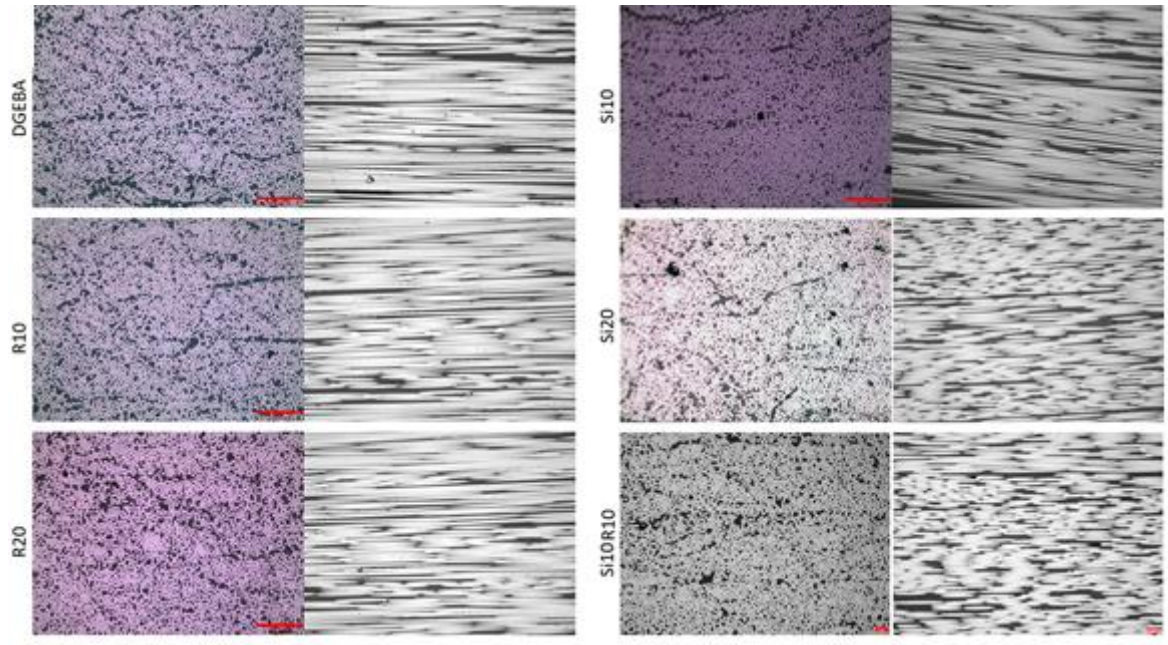

Figure 54 – Example of optical microscopy micrograph for UD CFRP VARTM manufactured samples where left samples have UD 90° orientation, while right samples are UD 0°

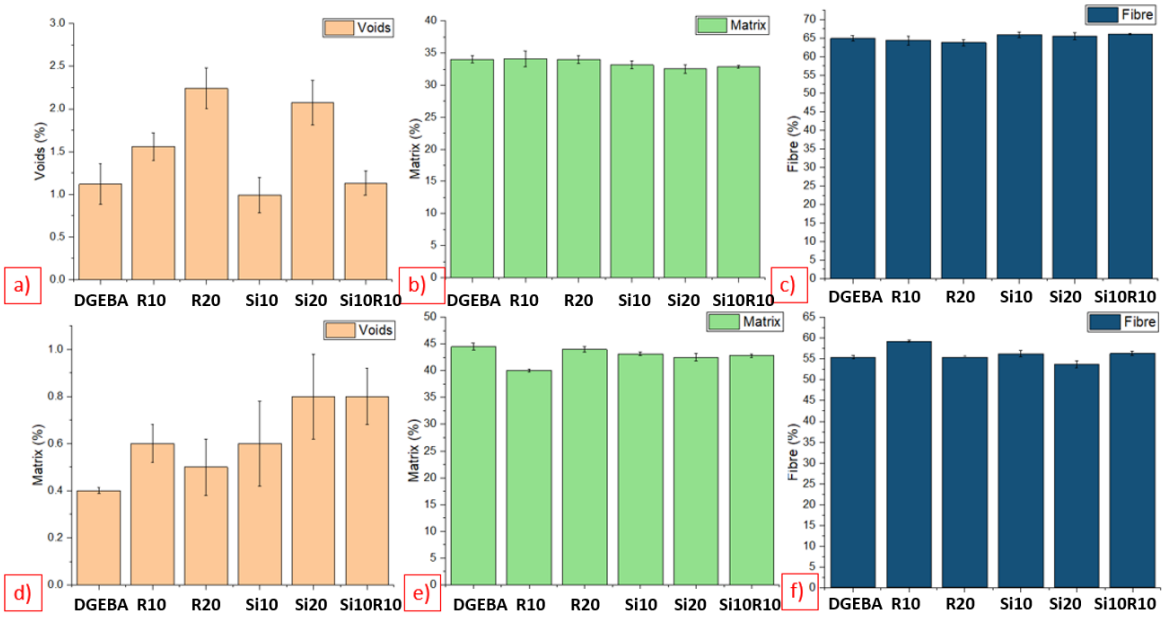

Figure 55 - Average VARTM and RTM content results from 5 samples +/- standard deviation for a, b, c) VARTM d, e, f) RTM

4.1.2 Degree of cure measured assessment

Degree of cure (%) was calculated using DSC following the method outlined in section 3.3.2 using Perkin Elmer analysis software and results are shown in Table 23. Almost consistently, all the panels were cured within > 99 % range, which highlights the fact that rubber microparticles and silica nanoparticles are not affecting the crosslinking process. As the samples are almost fully cured, the heat generated during machining will not affect further the degree of cure, therefore surface metrics and damage generated during machining will be independent of degree of cure.

Table 23 – Measured degree of cure for CFRP samples

Sample name	Degree of cure (%)
DGEBA	99.3
R10	99.1
R20	99.2
Si10	99.4
Si20	99.2
Si10R10	99.3

4.1.3 Glass transition temperature (T_g)

Following the method outlined in section 3.3.3, the raw data from Perkin Elmer analysis software was processed using Origin software. The first derivative of the expansion curve is plotted in Figure 56 and T_g was taken as the midpoint of the transition region. A Voigt peak was fitted to identify the lower peak of each curve. T_g results for all samples are shown in Figure 57, where standard deviation is the standard error from Voigt peak fitting. The average measured T_g of the samples is 151.7 °C with a panel-to-panel variation of ± 2.3 °C (~1.5%) which is deemed to be negligible. The low standard deviation indicates that the panel manufacturing process is repeatable and the rubber microparticles and silica nanoparticles are not significantly affecting the T_g of the manufactured panels.

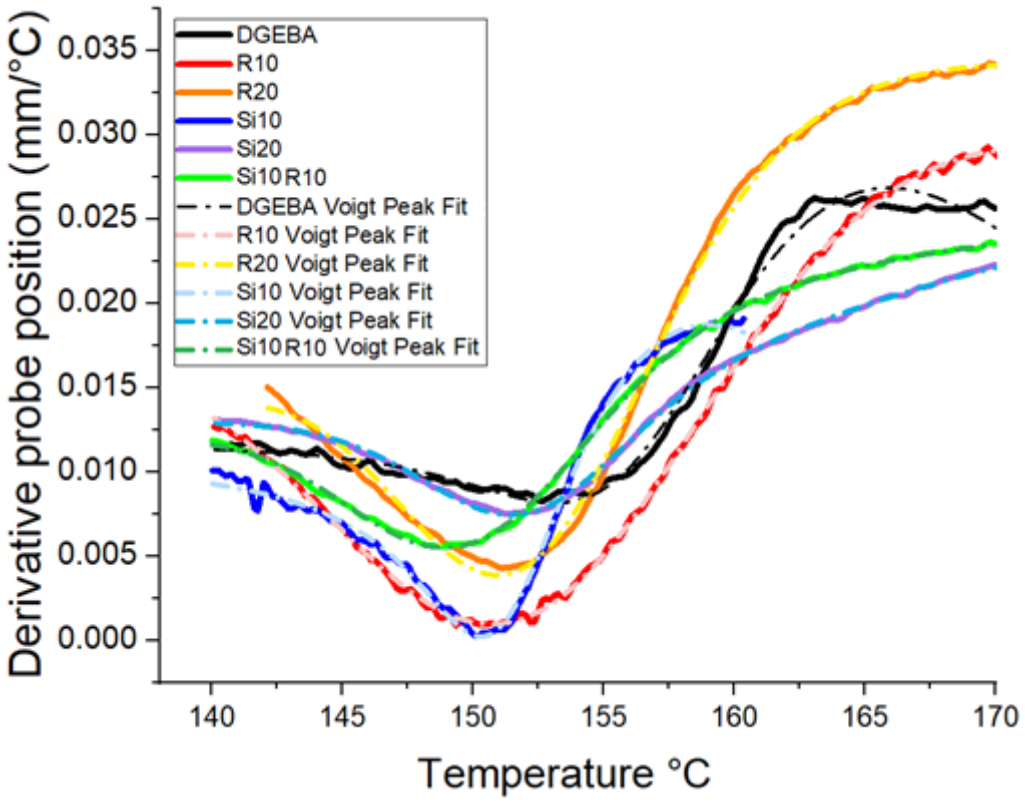

Figure 56 – TMA analysis graph showing derivative of the probe position vs measured temperature

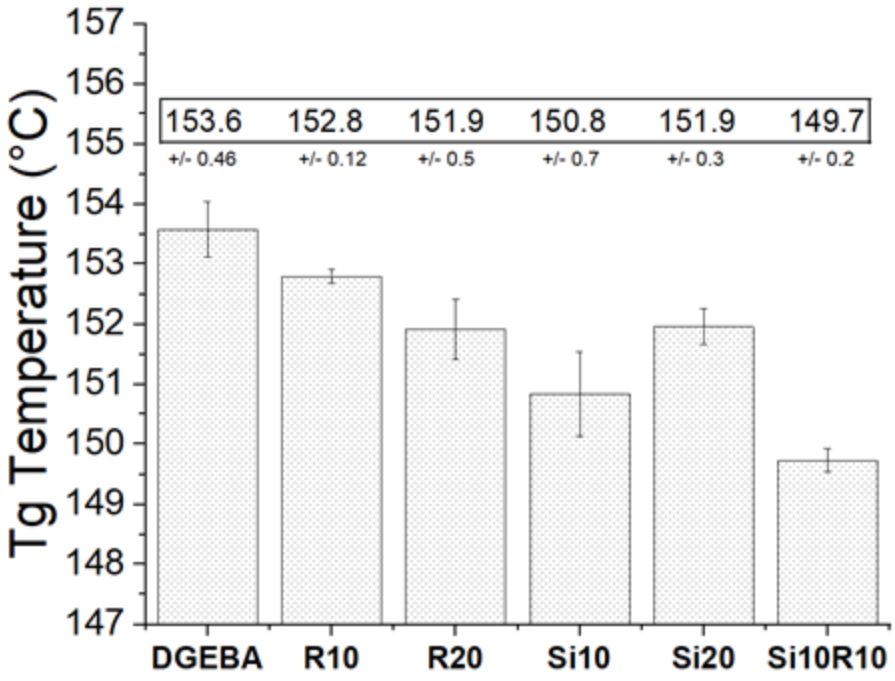

Figure 57 – T_g of epoxy samples measured by TMA

4.2 Mechanical test results

The results of tensile and fracture toughness tests are presented in this section together with the discussion on the effects of the applied particulate reinforcements on the measured properties of the tested samples.

4.2.1 Polymer tensile test results

The elastic modulus of the epoxy polymers modified with the silica nanoparticles and rubber microparticles are shown in Figure 58. An elastic modulus of 1.92 ± 0.27 GPa was measured for the unmodified epoxy polymer that was found to increase with nanosilica content. As the silica content increases from 10% to 20% wt., there is an increase of 8% and 22% in the measured elastic properties of the material compared with the DGEBA epoxy as a reference. On the other hand, the presence of rubber microparticles decreases the elastic modulus from reference epoxy, DGEBA 1.92 GPa to 1.62 GPa for R10 polymer, and 1.29 GPa for R20. This behaviour is linked to the rubber toughening mechanism, namely the cavitation of rubber microparticles and plastic deformation of the epoxy matrix ahead of the crack tip. This allows a greater extent of energy to be dissipated in the plastic deformation of the epoxy matrix, hence increasing the fracture toughness and decreasing the elastic modulus. The addition of 10% wt. of silica to the Si10R10 'hybrid' epoxy blend restored the modulus to 1.73 GPa.

The strain at failure increased for rubber-modified epoxies and decreased for epoxies containing silica nanoparticles. This could be linked to the rubber toughening mechanism where the debonding of rubber microparticles reduces the stress at the crack tip and allows the epoxy to deform plastically via a void-growth mechanism [8]. The toughening mechanism is further discussed in the literature review, section 2.2.4. Figure 59 shows the stress vs strain graph of epoxy samples where the effect of toughening mechanism of rubber microparticles is noticed on R10, R20 and Si10R10 curves. The large strain to failure of those samples is attributed to the rubber microparticles which cavitate and experience a large strain to failure followed by the plastic deformation of epoxy matrix. The modulus increase of Si20 samples is also visible in the stress vs strain graph, which highlights the fact that both toughening mechanisms for silica and rubber reinforcement were present in the failure process during the tensile tests.

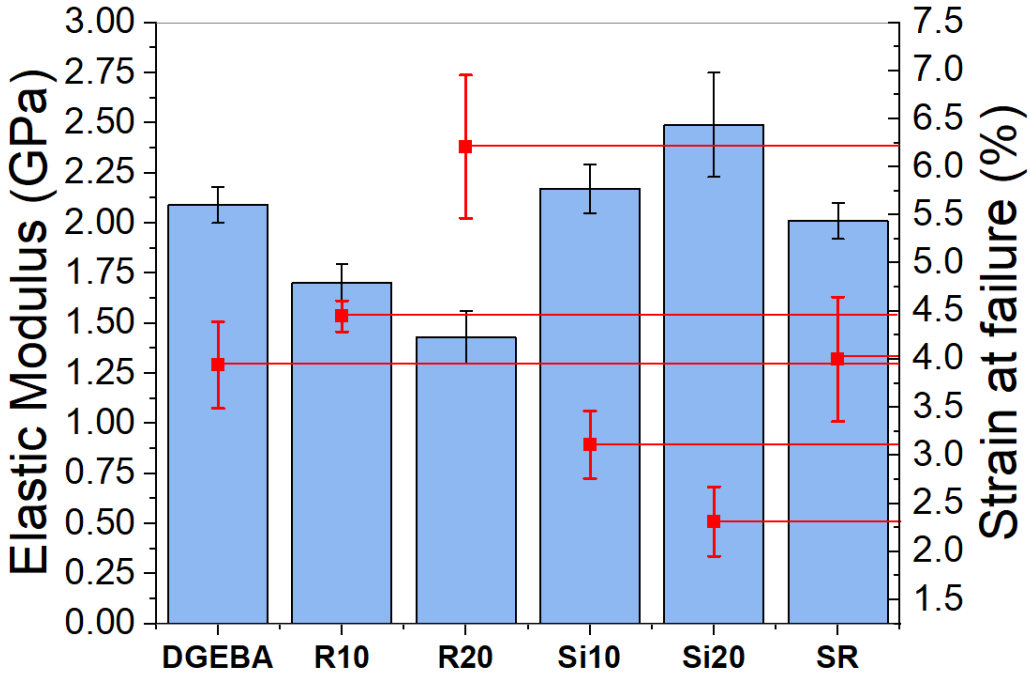

Figure 58 – Modulus (GPa) showed as bar chart with standard deviation for 5 samples and Strain at failure (%)with y-axis on the right with standard deviation for 5 samples of the epoxy tensile test samples

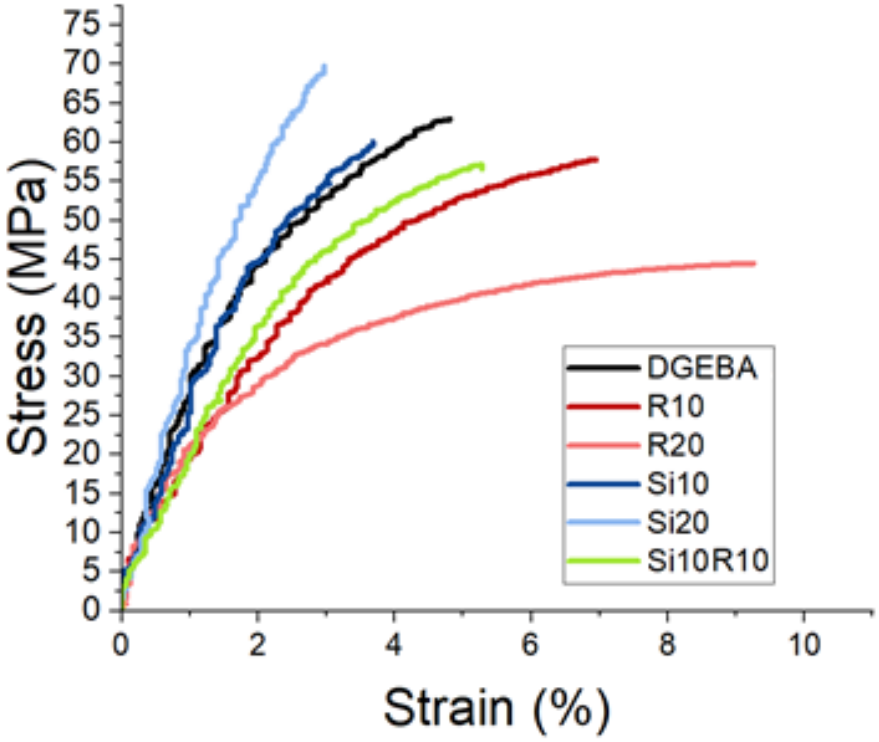

Figure 59 – Stress (MPa) vs strain (%) for epoxy tensile test samples

Figure 60 shows SEM micrographs of the fracture surfaces for Si20 and R20 sample. The fractured surfaces of silica and DGEBA epoxy are both brittle in appearance (Figure 60 – a). The observed feather markings illustrate that crack forking took place. This phenomenon occurs when energy is absorbed fast in a brittle material and it was previously reported in the literature in fracture toughness results of silica modified polymers [6]. The fractured surface of rubber modified epoxy (Figure 60 – b) shows ridges due to crack tilting and river lines formed during fracture. Moreover, the voids formed in the cavitation process are well-dispersed throughout the material, which highlights that rubber toughening mechanism was present in the epoxy failure mechanism. This is similar to results reported in the literature [2], [8], [44], [47], [49], [179].

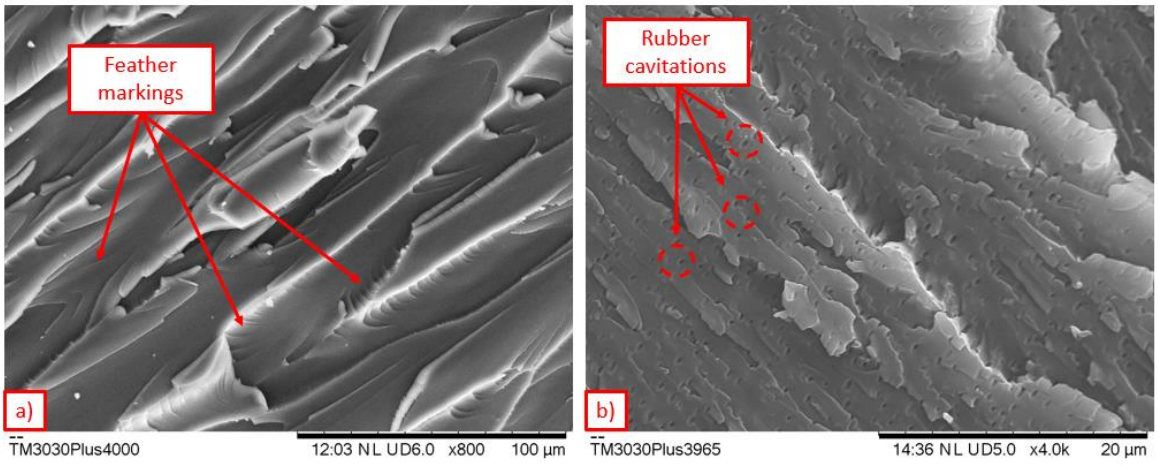

Figure 60 – SEM micrographs of fractured surfaces of epoxy samples a) Si20 b) R20

4.2.2 Fracture toughness test results

4.2.2.1 Validation of the fracture toughness calculations

Following the ISO 13586 standard [164] , K values (stress intensity factors) were calculated at applied failure load, where $F = Q$, where failure load Q represents the highest load value before unstable fracture occurred. For the stress intensity factor at failure, K_Q to be admissible as a plain strain fracture toughness K_{IC}, several criteria must be met, as follows:

K_Q is calculated by Eq. 7:

$$K_Q = f\left(\frac{a}{w}\right)\frac{F}{h\sqrt{w}} \quad (7)$$

The term $f\left(\frac{a}{w}\right)$ is a geometrical function of crack length (a), w (specimen width) and h (specimen thickness) which is listed in ISO 13586 standard [164]. The function was calculated for each sample and results are briefly shown in Table 24, while Appendix C contains the full calculation procedure.

Table 24 – K_Q calculation based on geometrical function f (a/w)

Sample name	**Crack length a (mm)**	**Failure load F (N)**	**K_Q (MPa $m^{1/2}$)**
D2	10.79	100.20	0.89
D3	10.97	90.62	0.81
D1	10.99	95.32	0.85
R10 7	10.53	145.20	1.26
R10 8	10.33	135.30	1.15
R10 9	10.58	120.10	1.05
R20 1	10.72	160.20	1.35
R20 2	10.82	159.17	1.40
R20 6	10.78	158.12	1.26
Si10 6	11.80	92.32	0.88
Si10 10	10.89	93.12	0.83
Si10 11	10.50	97.60	0.85
Si20 6	10.85	103.00	0.92
Si20 7	11.72	95.10	0.91
Si20 8	11.25	98.20	0.93
Si10R10 1	10.20	145.37	1.23
Si10R10 2	9.80	145.98	1.19
Si10R10 3	10.15	142.65	1.18

The size of the process zone (the area in which plasticity or similar energy absorption mechanisms such as shear yielding occurs) is required to be suitably small compared to

the length and specimen thickness [165]. The characteristic process zone radius r̄ can be estimated by Eq. 8, where σ_y is the Yield stress.

$$\bar{r} = \frac{{K_Q}^2}{{\sigma_y}^2} \qquad (8)$$

In order to satisfy plane strain conditions according to BS ISO 13586 [164], 2.5 x r̄ should be significantly smaller than thickness, crack length and width of the tested samples. As this condition is satisfied for each individual sample (detailed in Appendix C), K_Q can be regarded as K_{IC}.

4.2.2.2 Fracture toughness results

An average fracture energy, G_{IC} of 314 J/m^2 was measured for the unmodified epoxy polymer as shown in Figure 61. Standard deviation for both G_{IC} and K_{IC} are calculated based on 5 samples which passed the validation steps discussed in section 4.2.2.1. The fracture energy increases with the addition of particulate fillers with a maximum G_{IC} of 478 J/m^2 and 1429 J/m^2 measured for polymers reinforced with the Si20 and R20 particulate fillers, respectively. The fracture energy of the 'hybrid' epoxy, Si10R10, increased to 841 J/m^2. This value is higher than R10 and S10, which emphasizes that both rubber and silica toughening mechanisms were present as previously being reported [8] using high-resolution SEM imaging. The higher fracture energy of rubber modified epoxy was expected and is related to the individual toughening mechanism of rubber microparticles, cavitation of rubber microparticles and plastic deformation of epoxy matrix in front of the crack tip. Similar increasing trend was found for the fracture toughness, K_{IC}. Similar to polymer tensile tests results micrographs (Figure 60), both toughening mechanisms for silica and rubber reinforcement were present during the fracture tests as shown by trends identified in the fracture toughness results. There are already several reports [2], [4], [7], [8], [11], [47] showing the micrographs of fracture mechanism of silica and rubber particles in fracture toughness tests which indicated that individual toughening mechanism took place, therefore no SEM imaging was done on the fractured surfaces at this stage.

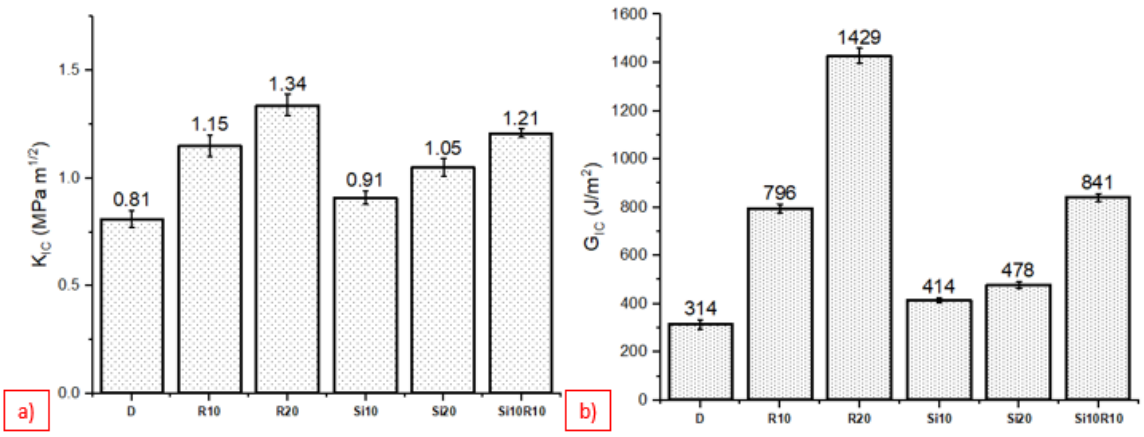

Figure 61 – Average fracture toughness results a) K_{IC} b) G_{IC} where error bars are standard deviation for 5 samples

4.2.3 UD CFRP tensile test results

Figure 62 shows the tensile results for samples in 0° orientation. An average modulus of 120 ± 3.21 GPa was recorded for all samples and strain at failure of 1.52 ± 0.15 %, which suggests that sample rupture is dominated by the fibre failure mechanism and particle reinforcements do not have a significant effect on the 0° fibre orientation samples.

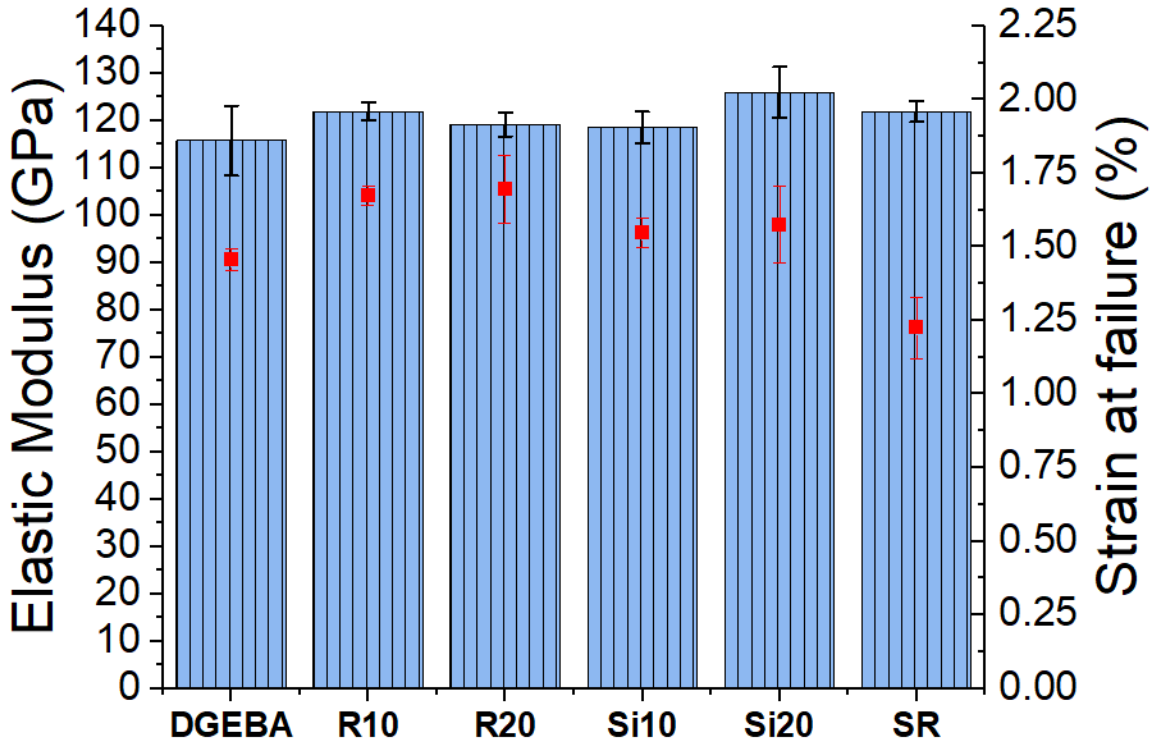

Figure 62 - Tensile test results for UD CFRP composite in 0° orientation where left Y-column is the Elastic Modulus (GPa) (column bars) and right Y-column is the strain at failure (%) (points)

The transverse tensile (UD 90°) test results of UD CFRP laminates are presented in Figure 63; linear elastic stress–strain curves until fracture were observed for all CFRP laminates. The transverse tensile modulus is decreasing with rubber content (R10 – 6.5 GPa and R20 – 5.7 GPa) and increasing for silica modified samples (Si10 – 6.7 GPa and Si20 – 7.5 GPa). On the other hand, the strain to failure is increasing for rubber modified samples (R10 – 0.47 %, R20 – 0.6 %) and decreasing for silica modified samples (Si10 – 0.42 %, Si20 – 0.25 %). The failure of transverse samples (UD 90°) are dominated by the matrix behaviour, hence by the toughening mechanism of particulate fillers which is found to be active in fractured surface of both epoxy and UD CFRP transverse (UD 90°). The effect of toughening mechanism on the mechanical properties was thoroughly discussed in section 2.2.4. Moreover, similar trend in modulus and strain at failure (%) was found for the bulk epoxy polymers (Figure 58).

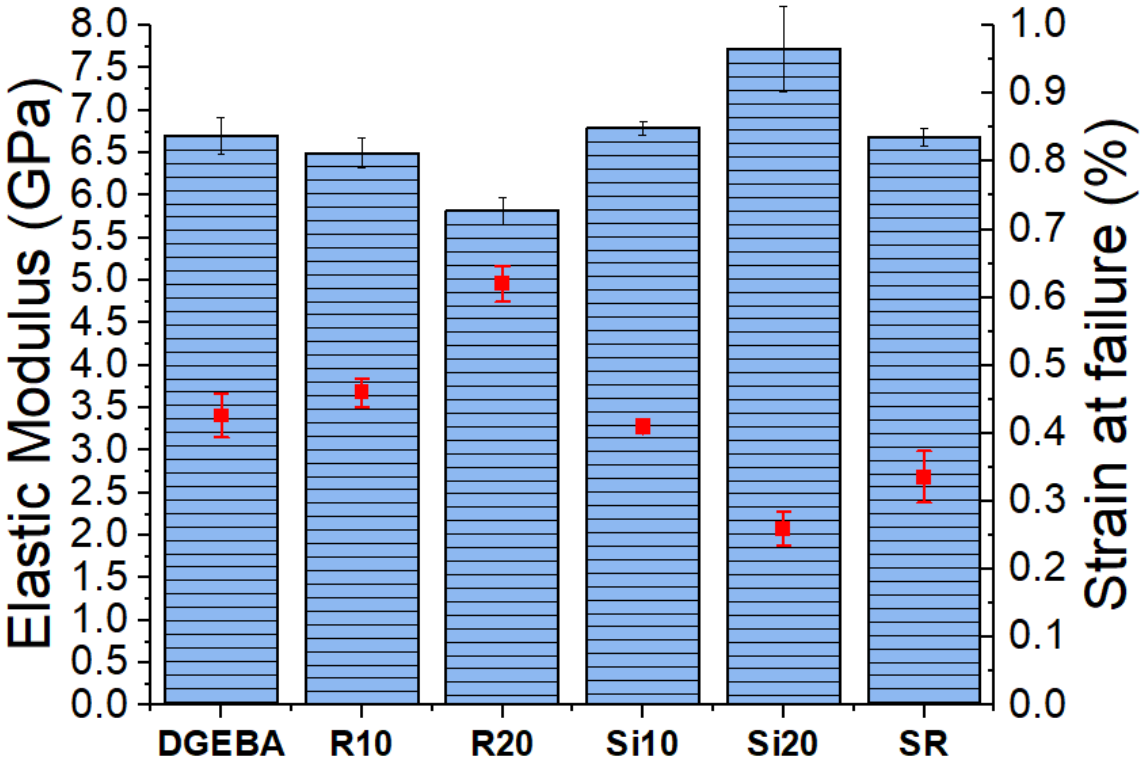

Figure 63 – Tensile test results for UD CFRP composite in transverse (90°) orientation where left Y-column is the Elastic Modulus (GPa) (column bars) and right Y-column is the strain at failure (%) (points)

SEM micrographs of the fractured surface for transverse tensile samples show artefacts of matrix rupture for silica modified samples, which correlates with the increased transverse

tensile properties of the laminates (Figure 64 – a). On the other hand, cavitations in the matrix between the fibres is observed for rubber modified samples (Figure 64 – b). However, all samples showed fibres with a clean surface, which suggest that failure also occurred at interfacial level between matrix and fibre independent of particle reinforcement type and concentration.

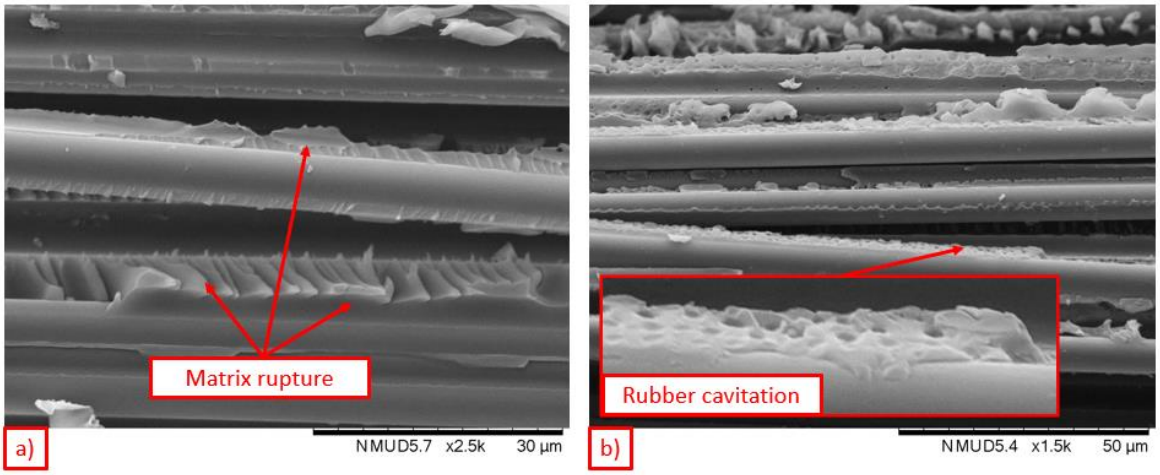

Figure 64 – SEM micrographs of the composite tensile transverse (UD 90°) orientation fractured surfaces a) Si20 b) R20

4.3 Summary

Characterisation results show that the developed manufacturing processes were consistent and repeatable. This ultimately demonstrates that experimental variation due to the manufacturing of samples (degree of cure, glass transition temperature, void content) have been largely mitigated. It is therefore unlikely that any results related to material removal mechanism are due, in significant part, to such material variations, but more likely to particle reinforcement type and concentration. Moreover, it was found that epoxy mechanical properties are translated into the composite material properties.

5 CUTTING MECHANISM IN ORTHOGONAL CUTTING OF PARTICULATE MODIFIED EPOXIES

In this chapter, the results of orthogonal cutting trial which analyses the effect of particulate reinforcements on machinability of modified epoxy samples which are used as the main matrix in CFRP samples are presented. Epoxy samples were manufactured using the technique described in section 3.2.4 and characterisation results of the produced parts showed that experimental variation due to condition of supplied material (degree of cure, glass transition temperature, void content) have been largely mitigated as discussed in Chapter 4. The in-situ orthogonal cutting rig described in section 3.5 was used to study the effects of particulate fillers on the recorded cutting forces, chip formation process and machining induced damage of the epoxy modified polymer samples. Machined surface features identified using SEM micrographs and optical images were used to quantify machining induced damage and further correlated to chip formation process and measured cutting forces. The cutting parameters used in this machining trial are summarised in Table 22 and the DIC parameters used for image acquisition and analysis are listed in Table 18.

5.1 Cutting force evolution

Figure 65 shows the average cutting force for the epoxy polymers machined at a cutting depth of 30 µm where error bars represent the standard deviation for the population of each reinforcement type and concentration. Due to limitations of the experimental setup discussed in section 3.5.2, only cutting force (F_x) is used to investigate the chip formation process. This depth of cut was chosen as it provides reliable comparison data, while for the large depth of cuts (50 and 100 µm) the material is removed by a brittle process of 'knocking lumps out' [180] which produced highly unstable cutting forces. Experimental evidence and further discussion on this aspect is described in section 5.3. A gradual increase in cutting force is noticed for rubber modified epoxies with respect to the DGEBA polymer. DGEBA, Si10 and Si20 samples had an unstable cutting force with predominant 'stick-slip' [96] force traces as shown in Figure 66 and Figure 67. Furthermore, Si10 and

Si20 showed larger force fluctuations compared with the other samples. By contrast, R10 and R20 exhibited less variations in the measured cutting forces.

Statistical analysis of the results (T-tests) shows that there is a significant difference in cutting force between rubber and DGEBA epoxy (p value < .05), while such a trend was not observed for silica and DGEBA epoxy (p value > .05 were not listed on Figure 65).

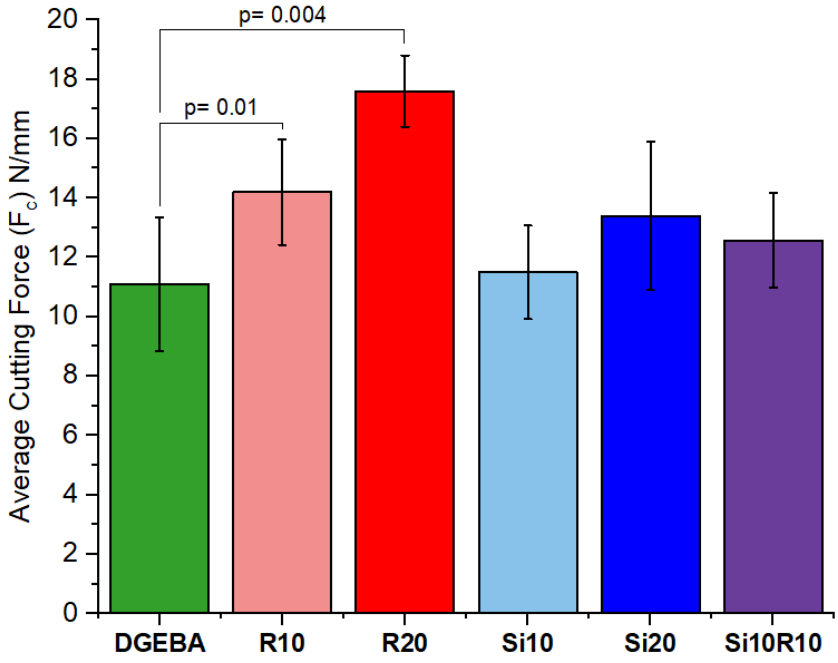

Figure 65 - Average Specific Cutting Force (F_c) for the epoxy blends at a cutting depth of 30 µm

As shown in Figure 66 and Figure 67, higher cutting forces in the steady state zone were measured for the rubber-modified epoxy compared to silica and 'hybrid' polymer. Here steady state zone refers to the full engagement of the cutting tool with the workpiece (i.e. Figure 66 – a displacement higher than 0.25 mm correlated with Figure 67 – D 2, Si20 2, R20 2). This can be correlated to the fact that more energy is required to produce the fracture phenomena in rubber epoxy, as reported by fracture toughness results shown in Figure 61. The toughening mechanism of the rubber particles initiate as the material fractures at the crack tip, which involves the cavitation of rubber particles, which generates the plastic deformation of the polymer epoxy. Hence, more energy is needed to plastically deform the material, therefore higher cutting forces measured for the rubber-modified epoxy. This is shown by the fracture toughness results, section 4.2, where the fracture

energy is higher for rubber samples. However, these findings contradict the results of Wang et al. [181] where the authors used DGEBA epoxy modified with 10 % wt. silica nanoparticles and rubber (CTBN) microparticles in orthogonal cutting tests with depth of cuts varying from 30 to 120 µm, a cutting speed of 180 mm/min where higher cutting forces are reported for silica than rubber epoxy and no relationship was found between epoxy blends cutting force behaviour and their fracture properties. Moreover, the authors attributed the higher cutting force to the higher tensile properties of silica modified material, which could potentially lead to difficulties in the chip formation process due to incorporation of rigid silica nanoparticles. This aspect is further discussed in section 5.2.

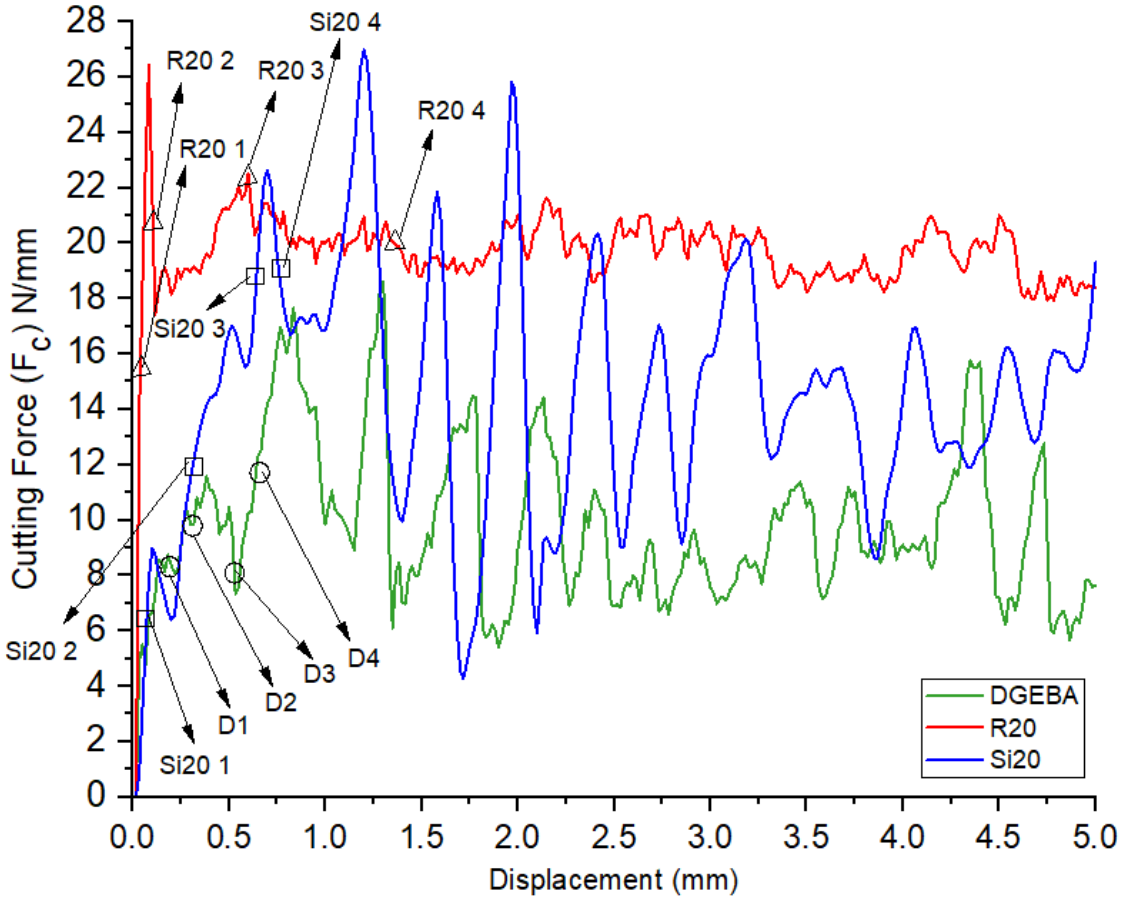

Figure 66 - Cutting force (F_c) graph for DGEBA, R20 and Si20 epoxy at a cutting depth of 30 µm with circles showing the frame locations for D, rectangles for Si20 and triangles for R20 corresponding to images of Figure 68

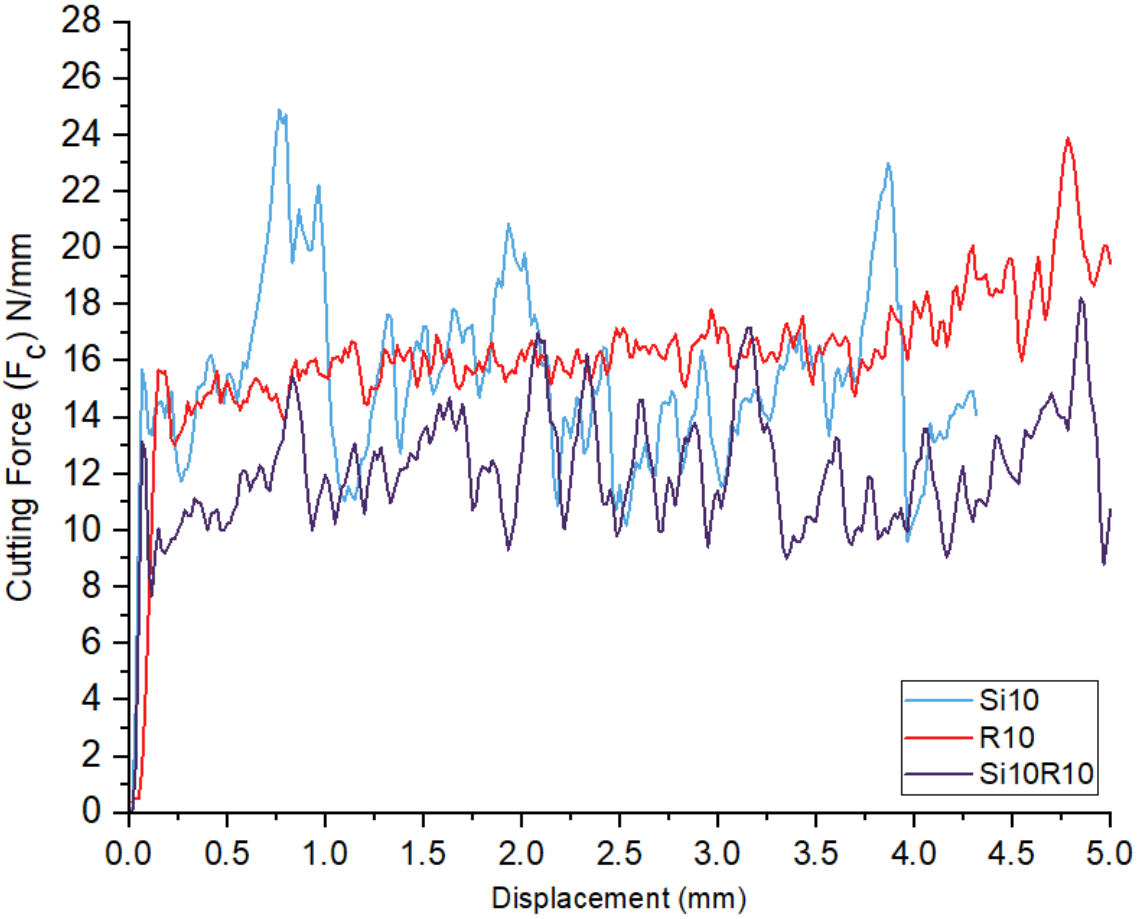

Figure 67 – Cutting force (F_c) graph for Si10, R10 and Si10R20 epoxy at a cutting depth of 30 µm

5.2 Chip formation analysis and deformation evolution

Figure 68 shows the chip formation evolution from the initial contact of the cutting tool with the sample corresponding to the data points shown in Figure 66 for all the tested materials at a 30 µm depth of cut, where 4 frame locations are marked on Figure 66 and corresponds as follows: circles for DGEBA, rectangles for Si20 and triangles for R20 samples. At the early stages of the chip formation process, the material piles-up on the rake face of the tool (Figure 68– D1, Si20 1, R20 1). The amount of piled-up material is equal to the volume of material displaced by the tool since no crack is yet formed at the tip of the tool. An initial peak in the cutting force is found at this stage for the R20 sample, while DGEBA and Si20 samples experienced a much lower initial force, as shown in Figure 66. This is supported by the larger strain magnitude measured for the R20 sample (Figure 69 – c)), which shows that the material experiences a large plastic deformation at the vicinity of the tool tip within the chip formation zone. As the tool advances into the

material, microcracks are generated ahead of the cutting tool (Figure 68 – D2, Si20 2). The strain fields generated for DGEBA and silica samples (Figure 69 – a) and b)) shows a large localised strain magnitude at certain direction with respect to the cutting force which could indicate the failure initiation, hence the crack propagation within the material. This is further explained by Figure 68 where the cracks are observed at the initiation point and grow in a similar manner. As the cutting tool engages with the workpiece and the forces increase, the tool wedge effect results in further crack initiation and growth (Figure 68 – D2, D3). As the friction force between the rake face and material starts gaining importance, the resultant force starts pointing towards the undeformed region of the material [182]. As the material has shown a brittle fracture behaviour with very low fracture toughness, the initiated crack will grow rapidly with very small strain to failure in DGEBA and silica modified epoxy. The generated cracks within the deformation zone ahead of the tool tip are then deflected towards the free surface of the workpiece (Figure 68 – D3, D4, Si20 4) as this is the minimum resistance path given that there is less force and material to resist the crack growth. The cyclic crack initiation and generation results in discontinuous chip formation (Figure 68 – D3, Si20 2, Si20 3) and the process will not reach a steady state as it is reported in most of metal machining [183]. This effect can be seen in the cutting force oscillations in Figure 66 and Figure 67 (DGEBA and silica samples). The forces start from zero where there is no contact between the cutting tool and material and increase gradually as a result of a stress build-up before the onset of crack initiation is reached (Figure 68 – Si20 2 and Si20 3 correlated with the cutting force graph shown in Figure 66). A discontinuous chip is formed when brittle fracture occurs in front of the cutting tool (Figure 68 – Si20 4) and the force further drops, and the cyclic crack initiation process will start again. Si10 sample experienced a brittle chipping behaviour, similar to Si20 and DGEBA sample. Rubber modified samples formed a curly chip (Figure 68 – R20 4) due to toughening mechanism which stops the crack propagation ahead of the tool tip, limiting the machining induced damage. This is correlated with the steady state zone of the cutting force graph (Figure 66 – R20 sample). The plastic zone is also highlighted by the localised strain distribution around the cutting tool as shown in Figure 69 – c). Similar behaviour was observed for R10 and Si10R10 ‘hybrid’ sample for which the rubber toughening mechanism governs the failure mechanism as previously discussed in section 2.2.4 and 4.2.

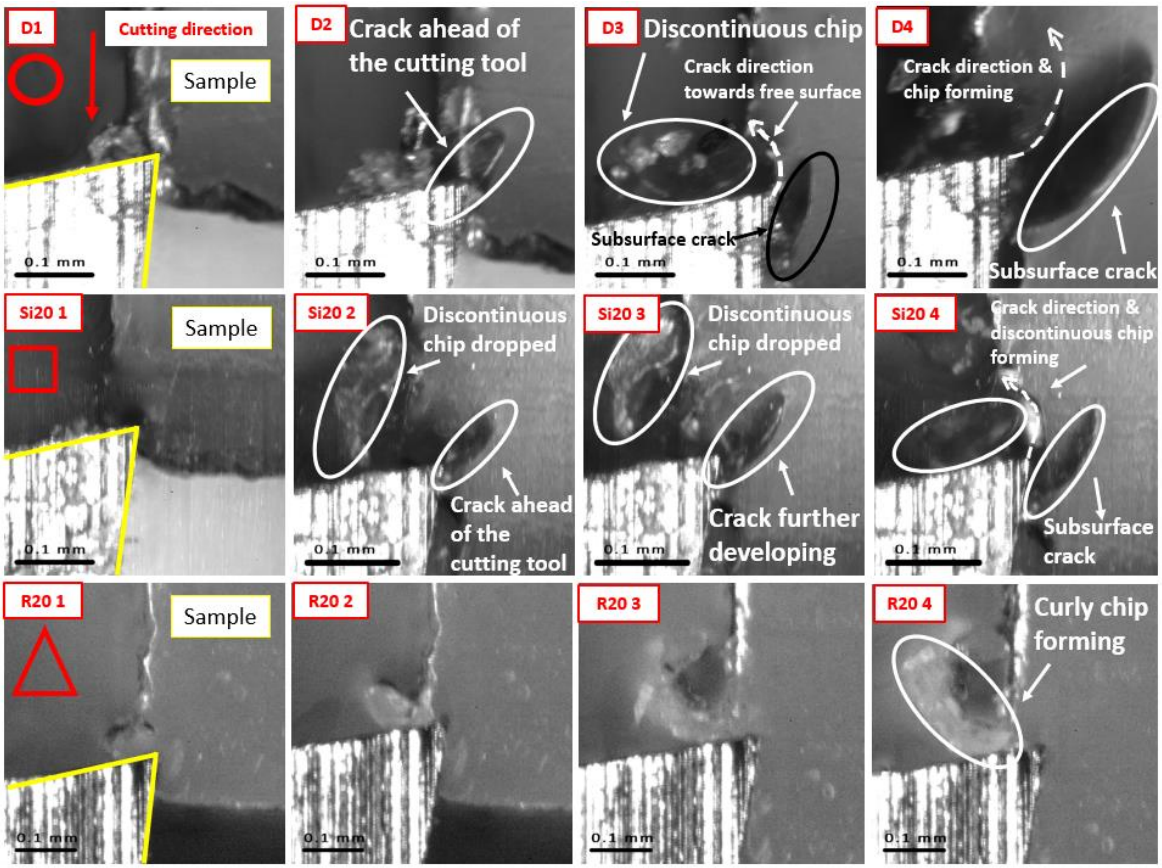

Figure 68 - Cutting frames for Cutting Force Graph shown in Figure 66 with circles showing the frame locations for D, rectangles for Si20 and triangles for R20

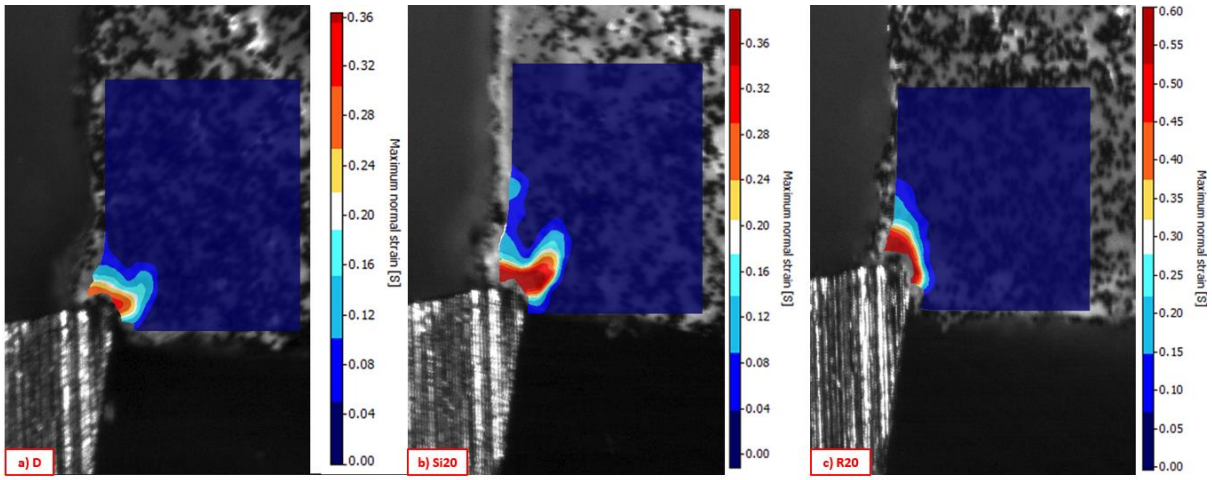

*Figure 69 - Maximum normal strain [S] at the initial tool entry of the cutting tool inside the material for a) DGEBA b) Si20 c) R20 *note that the colour bars are not at similar scale **reader is invited to use a colour version to be able to interpret the figure*

5.3 Analysis of the machined surface morphology

At larger depth of cuts, 50 and 100 µm, the chip-workpiece separation behaved in a brittle fashion for DGEBA and silica modified epoxies. This phenomenon was explained previously by Atkins [184] using cube-square scaling principles and successfully applied in orthogonal cutting of polymers by [96]. The cube-square scaling principle states that the energy stored in a cracked body depends on its volume, but the energy required to separate the body depends on the area of the cracked surface. Therefore, it is expected that at larger depths of cut, the fracture will be brittle with larger cracks. Experimental evidence showed that cracks length is increasing with depth of cut. The cracks are observed after machining took place (see red rectangles in Figure 70) and also took place during machining as shown in Figure 68 – D4, Si20 4. The material is removed by a brittle process of 'knocking lumps out' [180]. This phenomenon resulted in highly unstable cutting forces, which cannot be used for comparison with the other epoxy blends. Similar behaviour was found in the literature in orthogonal cutting of other epoxy polymers [96], [180]. On the other hand, rubber modified epoxy samples produced a continuous chip at larger depth of cuts. This is correlated with the previously explained void growth mechanism and the large strain to failure of the rubber material. Additionally, the cracks are also constrained due to the plastic deformation of the material within the chip formation zone. The microcracks occurring in front of the cutting tool were deflected towards the free surface, which facilitated the formation of a continuous chip. R10 and Si10R10 samples, which have rubber microparticles in a lower concentration, showed features similar to the R20 machined surface.

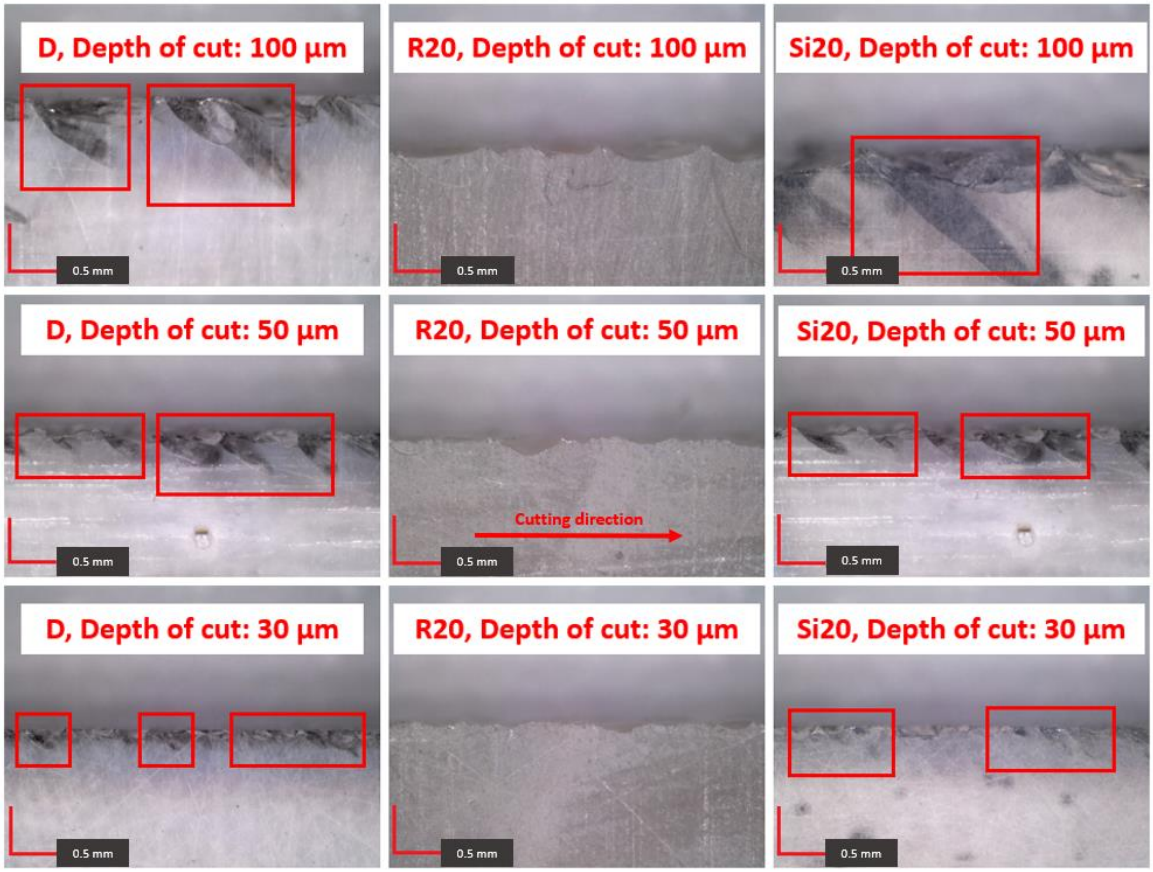

Figure 70 – Optical images of the side of DGEBA, R20 and Si20 samples machined at a depth of cut of 30, 50 and 100 µm where red rectangles show the subsurface cracks

The start of the subsurface cracks is identified on the SEM micrographs of the machined surface (Figure 71 – a, b)). A zone with a smooth and glassy surface is pointed, which is typical for a brittle epoxy polymer [6]. Steps and changes in the level of the crack are observed in the smooth crack growth region. These features are feather markings, which shows that crack forking took place. This phenomenon occurs when energy is absorbed fast in a brittle material and it was previously reported in the literature in fracture toughness results of silica modified polymers [6]. Similar micrographs were identified for Si10 samples.

SEM micrographs of the R20 machined surfaces (Figure 71– c)) showed the evidence of the cavitation process enabling the subsequent toughening mechanism – the higher diameter of the created voids compared to the microparticles indicated that plastic void growth of the polymer has taken place. As previously discussed in section 4.2.2, this toughening mechanism is typical for rubber-modified epoxies and indicate a greater extent of energy

required to fracture. This is correlated with the higher cutting force measured for rubber-modified epoxies. The plastic deformation of the polymer ahead of the cutting tool within the chip formation zone constrained the initiation of subsurface cracks limiting the machining induced damage. This resulted in an increase plastic zone ahead of the crack tip within the polymer and the energy is dissipated creating the toughening effect.

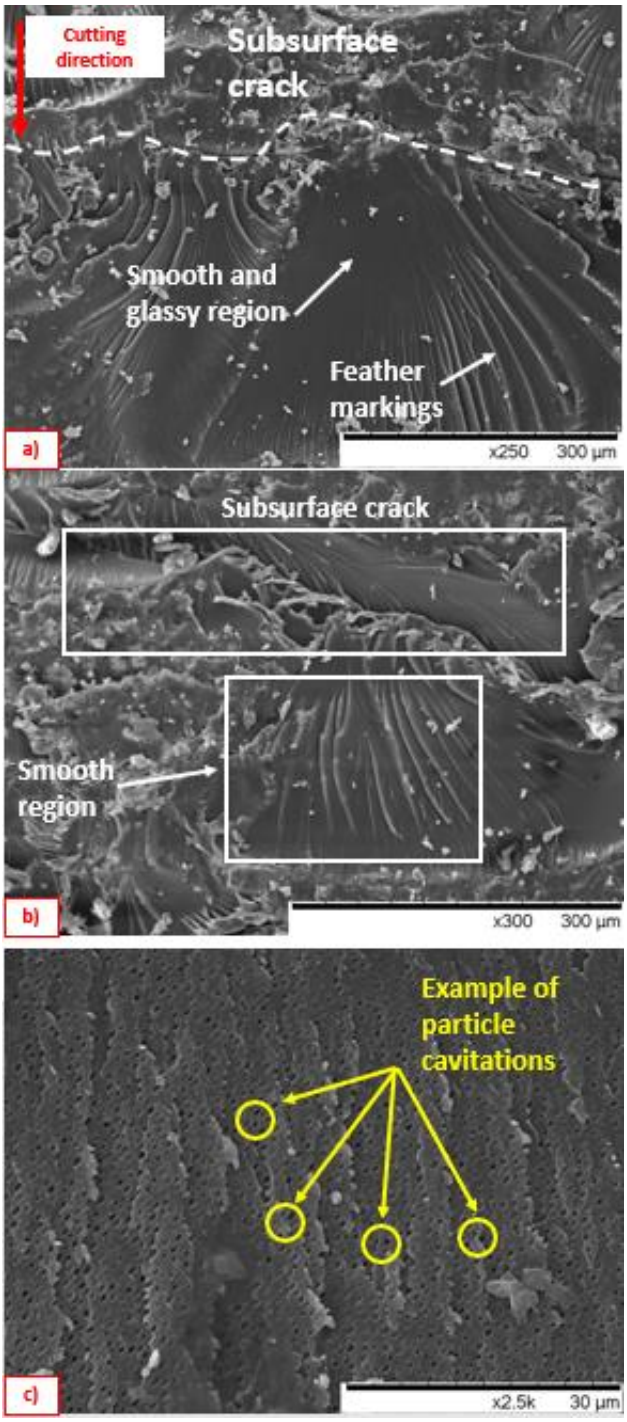

Figure 71 – SEM micrographs of the machined surfaces for a) Si20 b) DGEBA c) R20 sample

5.4 Summary

In the orthogonal cutting of epoxy modified samples it was discovered that rubber modified epoxies experienced the highest cutting force (p – values < 0.05 when compared with DGEBA samples), while due to high variation of forces experienced by DGEBA and silica samples the difference was not significant. Experimental evidence showed that chip formation process is governed by a series of intermittent fractures occurring in front of the cutting tool. Chip formation in bulk and silica-modified polymer produced discontinuous chips with large cracks at the machined surface level and subsurface within the chip formation zone. This was linked with the low fracture toughness of DGEBA and silica modified epoxies compared to rubber modified epoxies. On the other hand, rubber modified material produced a continuous curly chip due to large plastic deformation of material as the toughening mechanism of rubber microparticles was present. At the same time, the microcracks were constrained within the chip formation zone. The 'hybrid' Si10R10 epoxy experienced similar chip formation process as rubber samples, while the mechanical properties were close to the bulk epoxy.

SEM micrographs of machined surfaces of DGEBA, Si10 and Si20 samples showed a smooth and glassy surface, which is typical for a brittle polymer. Feather markings were observed, which occur when energy is absorbed fast in a brittle material. On the other hand, R20 samples showed the evidence of the cavitation process, which is the rubber fracture toughening mechanism where a great extent of energy is absorbed in the fracture process.

In this chapter it was concluded that chip formation process of particle modified epoxy samples is governed by the effect of particle reinforcement failure mechanism on the epoxy matrix. The material removal mechanism of silica and rubber modified epoxy samples was studied and discussed at a micro scale level and experimental evidence was used to characterise machining induced damage. However, such epoxies are mostly often used as a matrix in high performance composites which undergo a series of machining operations to achieve required features and tight geometric tolerances. Therefore, the chip formation process and subsequent machining induced damage of particle modified epoxy CFRPs needs to be investigated. The particle modified epoxy matrices used in this chapter will be used as base matrices in manufacturing of CFRP samples, which will be cut

in orthogonal cutting conditions to further analyse the material removal mechanism of epoxy modified CFRPs in Chapter 6.

6 CUTTING MECHANICS OF MODIFIED EPOXY CFRPs

In this chapter, the results of an orthogonal machining trial on epoxy modified CFRPs are presented and discussed in order to investigate the effect of particle reinforcement on chip formation process and subsequent machining induced damage. The observed behaviour is investigated and linked to the underlying mechanism of failure by adding the rubber and silica particulate reinforcements. A correlation is done between particulate reinforcement failure mechanism, chip formation process, surface metrics and machining induced damage.

6.1 Orthogonal cutting of CFRP samples – preliminary study

CFRP samples were manufactured using RTM and VARTM technique having different fibre architecture and thickness as described in section 3.2. Due to experimental limitations of each manufacturing method, three difference fibre architecture and thicknesses were used as per Table 25. The three sample types were tested in the orthogonal cutting rig to check the cutting force behaviour and the possible out-of-plane displacement which might occur and obstruct the camera view of the chip formation process. Figure 72 shows the onset of the cutting process when the tool is fully engaged with the materials (tool penetration is larger than 1 mm). Woven samples (Figure 72 – a)) showed limited out of plane displacement and the chip formation process is visible. The UD sample manufactured by VARTM showed excessive out of plane displacement (Figure 72 – b)) regardless of the fibre orientation used and material removal mechanism is not visible. Due to the low thickness and out-of-plane displacement, the plane strain condition of the orthogonal cutting rig is not fulfilled for low thickness UD samples. To overcome this issue, UD samples with a thickness identical to woven samples were tested along with a sapphire glass pressed into the sample, designed to restrict the out of plane displacement of the fibres. Even though this solution proved feasible and successfully restricted the fibre movement, the cutting insert fails prematurely under the compression force of the UD material at higher fibre orientations (> 45°). Here tool failure refers to the plastic

deformation of the cutting tool at the tool tip, which results in a change in the rake and relief angle and increased cutting edge radius. A possible solution to overcome this issue was the manufacturing of tool inserts from a higher hardness material as discussed in section 2.4.2.3, however such observations at such a high magnification were made for the first time and adjustments will be made for future experiments.

Even though the study of chip formation process is done in the literature using UD samples, the cutting in the multidirectional ply laminate is similar to the UD laminate (in this thesis woven samples manufactured by RTM – section 3.2.4), with a slight difference in the 90° and 135° fibre orientation as the result of the influence from adjacent plies as previously discussed by Arola and Ramulu [74]. Excessive out-of-plane damage in multidirectional occurs at 90° or greater in UD laminates, while the damage in multidirectional laminates, at these angles, is limited due the support of adjacent plies. This facilitates the analysis of the material removal mechanism for each ply and fibre orientation based on analogous UD plies. As out of plane displacement of the fibres does not obstruct the view of the removal process on the surface plies, the plane strain conditions were fulfilled, the tool did not fail during the cutting process, woven CFRP samples were used in this orthogonal cutting trial. The cutting conditions used in this chapter including depth of cut and cutting speed are detailed in Table 22.

Table 25 – Orthogonal CFRP sample assessment

Sample type	**Manufacturing method**	**No of plies**	**Thickness (mm)**
Woven (multidirectional laminate)	RTM	14	3
UD	VARTM	4	1.2
Thick UD_RTM	RTM	10	3

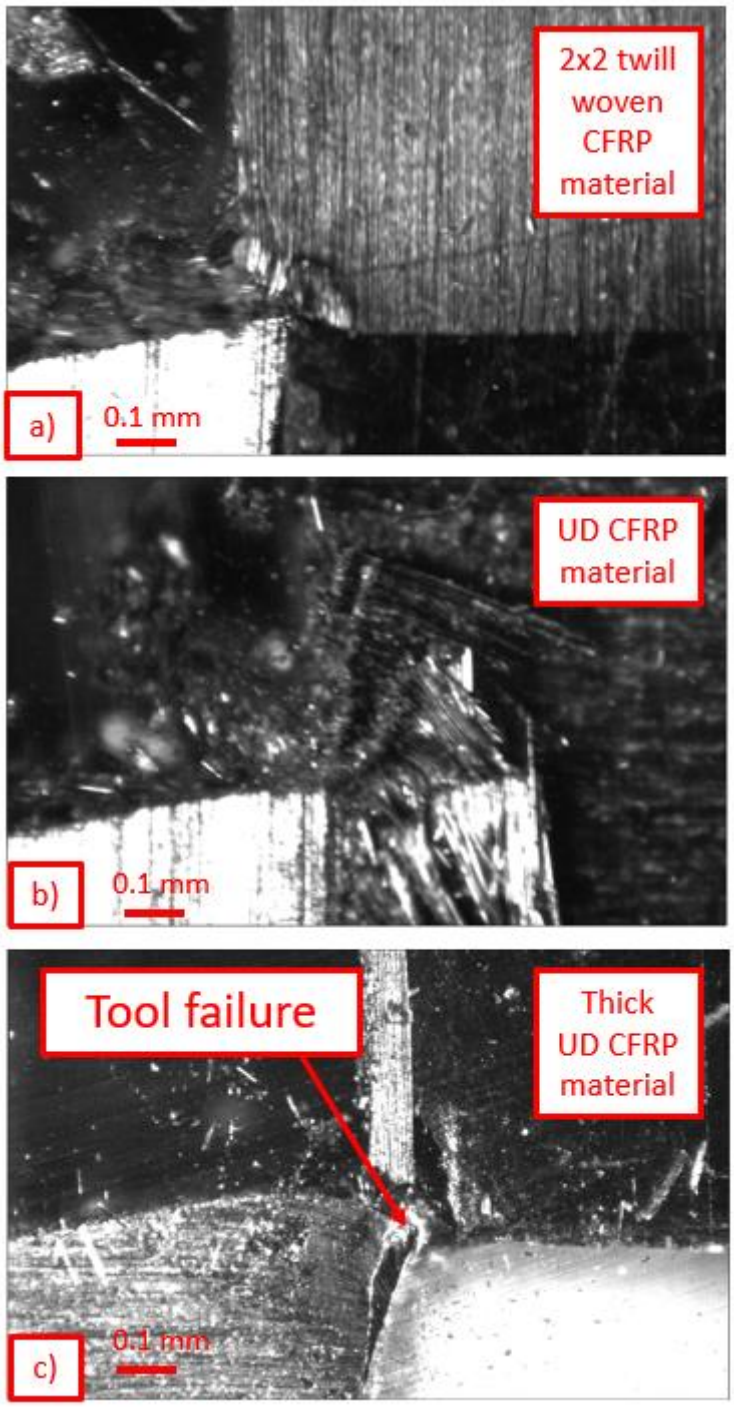

Figure 72 - CFRP samples in orthogonal cutting rig a) Woven (only the top 0 – 90° ply is visible in this figure) b) UD c) Thick UD_RTM sample showing tool failure

6.2 Effect of matrix type on cutting force evolution

Figure 73 – a) shows the average values of measured cutting forces for each material together with standard deviation error bars. Unpaired T-statistical tests were run to compare the difference between the cutting force magnitudes, and it was found that

adding the particulate reinforcements will result in statistically significant differences in cutting forces between unmodified (DGEBA) and modified samples (R10, R20, Si20, Si10R10). A 20.2% decrease was found for R10, followed by a further 42.4% for R20 samples compared to DGEBA. The Si20 samples showed a decrease of 14.2% in cutting force magnitude, while 'hybrid' sample (Si10R10) showed a decrease of 24.1%. It is noticed that Si10R10 had similar cutting force magnitude to R10 specimens, which suggests that in a 'hybrid' composite the rubber microparticles are governing the material removal process. This is linked to the rubber toughening mechanism and this aspect together with experimental evidence is discussed in 6.6.

The amount of spring back was measured after each cut using a digital micrometre (resolution < 1 µm) and further checked using the recorded cutting images as shown in Figure 73 – b). The brittle-matrix epoxy represented by unmodified (DGEBA) and silica epoxy (Si10, Si20) experienced the lowest elastic recovery and highest cutting force. On the other hand, the presence of rubber microparticles (R20) increased the elastic recovery and the lowest cutting forces were recorded. The increased elastic recovery due to rubber particles is related to toughening mechanism and large strain to failure of rubber modified composites [8], [48], [49]. Additionally, the decrease in the cutting forces is correlated with a smaller volume of material removed, despite the large elastic deflection. Wang and Zhang [77] reported that in orthogonal cutting of UD-CFRPs the magnitude of spring back is related to the cutting edge radius of the tool, when all the other conditions are the same. Considering that all the cutting parameters in this study, including the tool geometry and cutting conditions are identical between the investigated samples, the observed trend in the measured spring back could only be due to the local mechanical properties of the modified epoxy matrix indicating that the presence of reinforcements has a significant effect on spring back. A difference of 16 µm was found between the largest springback distance (R20 sample) and lowest value (Si20 sample) as shown in Figure 73 – b).

The evolution of cutting forces (Figure 74) indicates that there is less variation in the cutting force when cutting rubber modified samples, while a large oscillation was observed in the graphs related to the reference material (DGEBA) and the silica-modified samples (Figure 74 – a)). The cutting force signal for R10 and Si10R10 samples (Figure 74 – b))

showed a similar pattern. This was previously discussed in orthogonal cutting of rubber and silica modified epoxy polymers in section 5.1, where the chip formation process was mainly influenced by the presence of rubber microparticles, rather than silica nanoparticles in the 'hybrid' sample. It has been previously reported [8] that in a 'hybrid' modified CFRP, the rubber toughening mechanism is the dominant failure mechanism. This aspect and the effect of chip formation process in relation to particulate reinforcements and cutting force behaviour is further discussed in the section 6.4.

The cutting force is increasing with rubber content for polymer samples (Figure 65), while in the case of epoxy modified CFRPs is decreasing (Figure 73). This difference in cutting force trend is attributed to amount of material removed and large strain to failure of rubber particles which governs the failure mechanism of rubber modified epoxy composites. Even the rubber toughening mechanism is present in both polymer and composite sample, the chip formation and material removal mechanism are different for each sample type. In a composite sample, the overall failure mechanism is governed by the fibre failure and its subsequent orientation with respect to the cutting tool. However, rubber toughening mechanism alters the fibre failure mechanism, as it will be discussed in section 6.4.

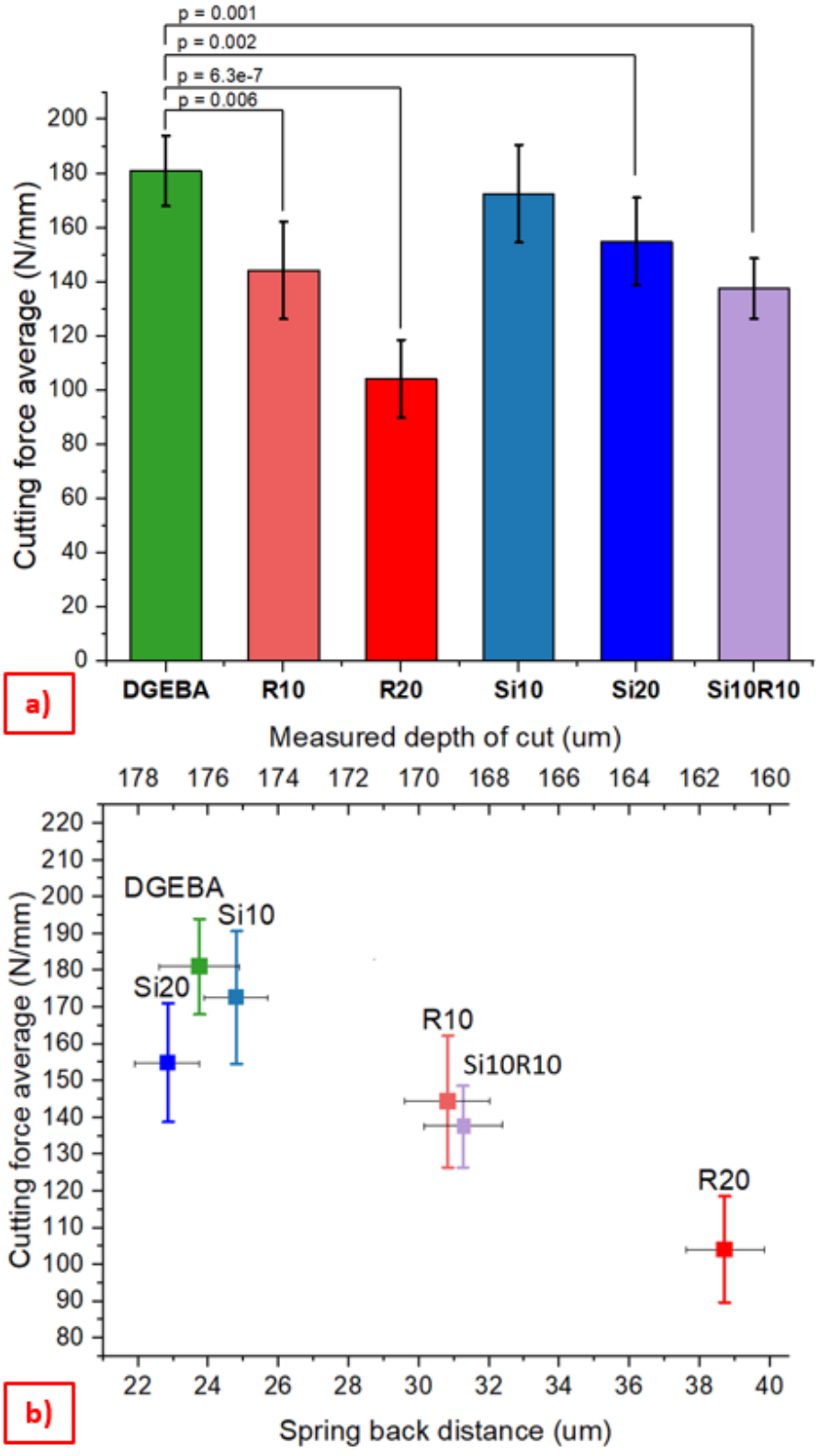

Figure 73 - Cutting force analysis graphs with error bars representing standard deviation of the test samples a) Cutting force average (only p-values which are statistically significant values are shown) b) Cutting force average vs spring back distance & actual depth of cut

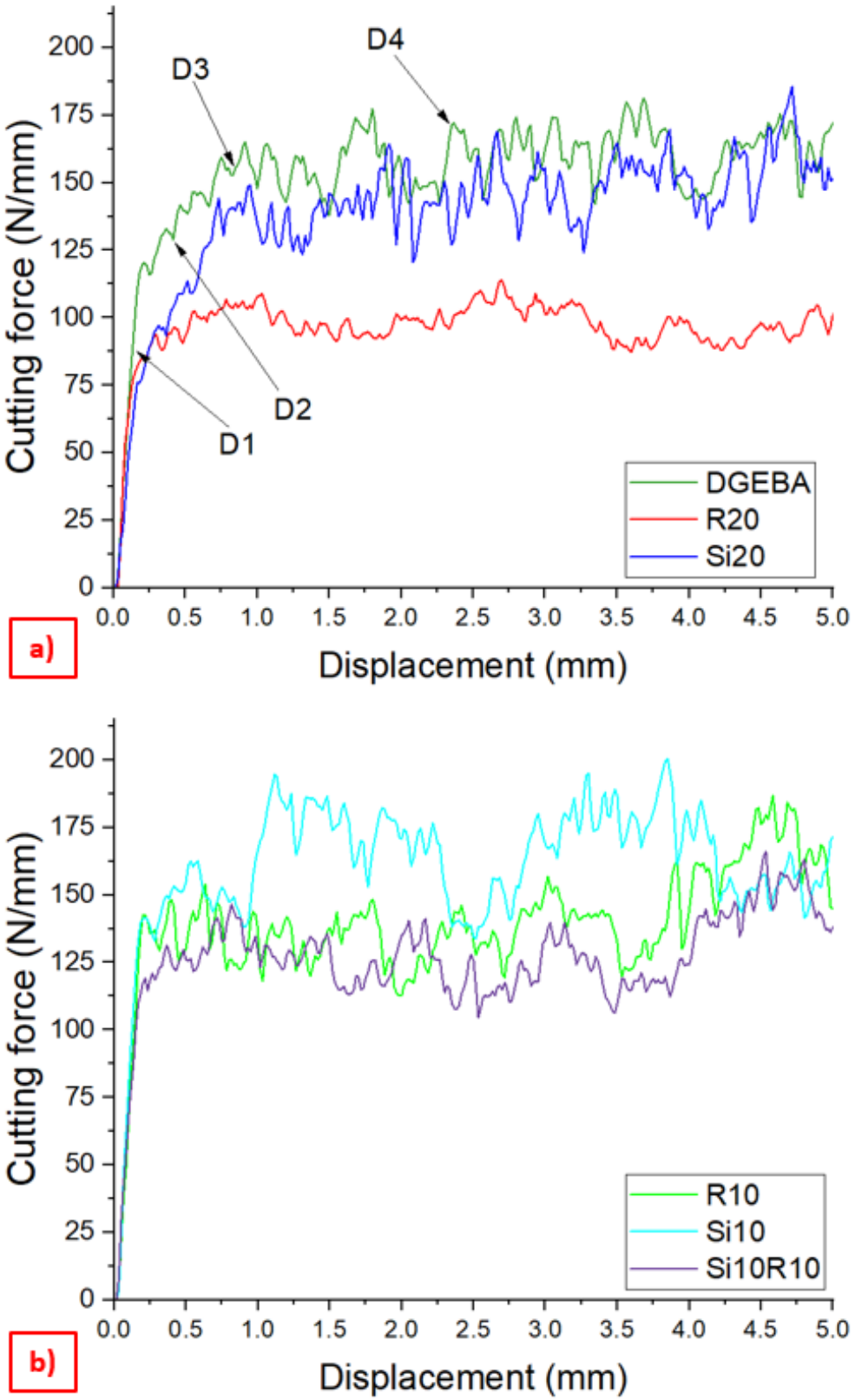

Figure 74 - Cutting force vs displacement for a) DGEBA, R20 and Si20 where D1, D2, D3, D4 indicate the time steps corresponding the cutting images in Figure 75 and b) Cutting force vs displacement for R10, Si10 and Si10R10

6.3 Effect of matrix modification on strain evolution and deformation mechanics

Figure 75 shows the evolution of chip formation as observed by the High Speed DIC system where the individual frames are correlated to the time steps shown in the force-displacement diagram of Figure 74 – a). As the tool advances into the work piece, the fibres at 0° are compressed (shown by curved dash line of Figure 75 – b)) and by further displacement of the cutting edge a chip forms on the rake face of the cutting tool (Figure 75– b)). Relaxation and material recovery occurs at the flank side of the tool (shown by straight dash-dot line in Figure 75 – b)). The material pile on the rake face of the tool and a continuous chip is formed, while 0° fibres are bending and fracture in front of the cutting tool (Figure 75 – c)). This is primarily due to the low cutting speed and high bending limit of the 0° fibres used for this experiment. Considering the 2x2 twill woven fibre architecture of the samples (carbon fibre placed in a 0/90° – 45/135° configuration with 0/90° on the top/ bottom plies), the tool will encounter 0° and 90° fibres on the top plane as the sample is cut. As the tool enters a region with 90° fibre orientation, large cracks (>500 µm) are generated in the matrix between fibres on the top ply (Figure 75 – d)) due to excessive bending of fibres along their axis. These long cracks are only present on the top ply, as fibres can readily deform-out of plane and cracks are formed from a combination of bending and debonding from the matrix. CT-scan images did not show these features on the layers below the surface. This aspect is further discussed in section 6.4. No noticeable difference was found between side view images of the particle-modified samples and DGEBA specimen, the chip formation process shows the same behaviour.

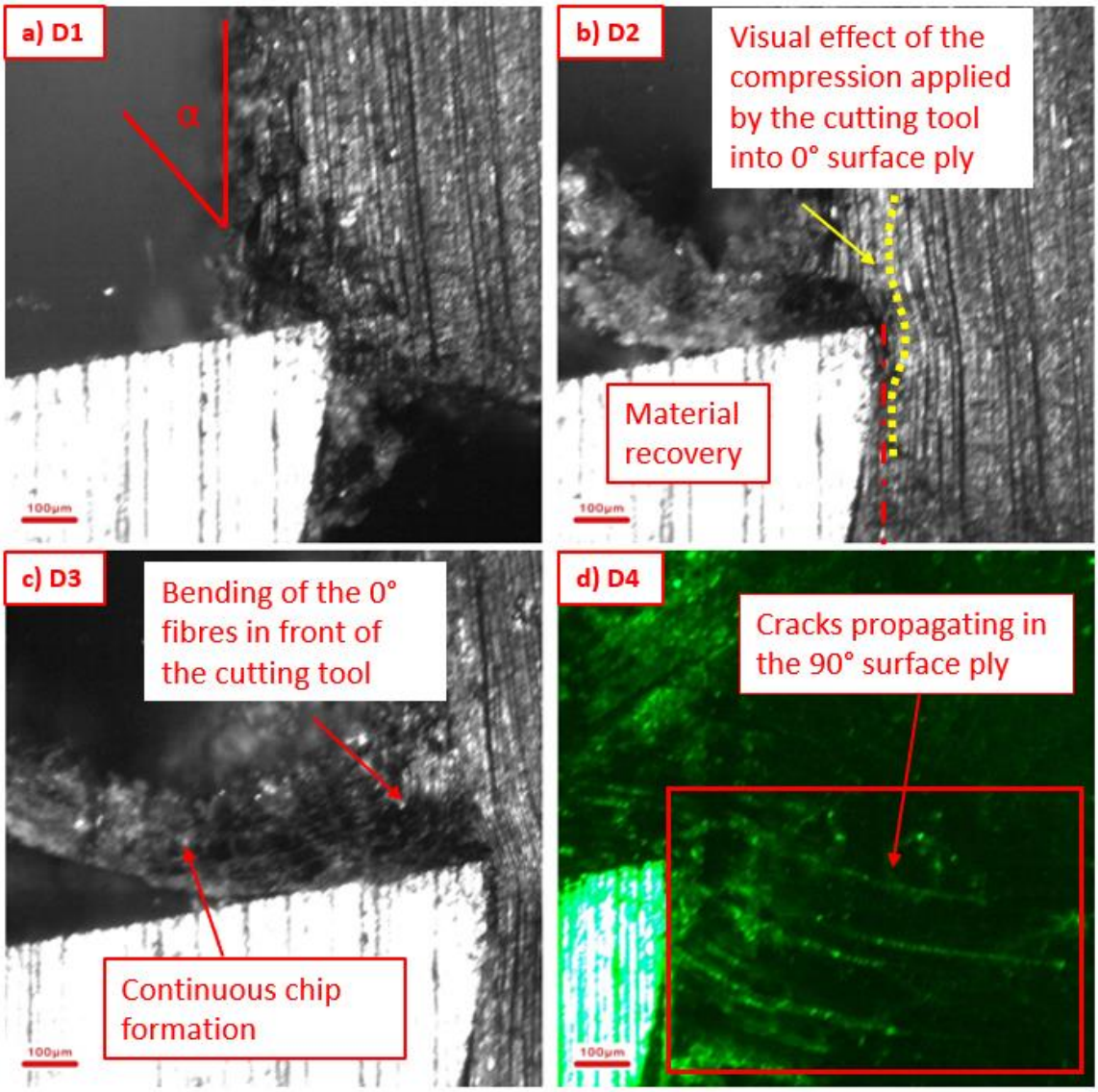

Figure 75 - Chip formation process images a-d) corresponding to the selected time steps of D1-D4 Figure 2 – a), d) D4 has a false colour black-green contrast to highlight the surface ply crack propagation for 90° fibre orientation where α is the fibre orientation angle

Strain maps shown in Figure 77 and Figure 78 are linked to the cutting force signal of Figure 76. Maximum normal strain (MNS) and shear strain (SS) have been calculated for each test condition according to the parameters given in Table 18 and represent the onset of steady state cutting zone (Figure 77 and Figure 78 – a), c), e)) and full engagement of the cutting tool with the material which starts to build up on the rake face of the cutting tool (Figure 77 and Figure 78 – b), d), f)). MNS maps of DGEBA (Figure 77 – a)) showed a larger deformation zone compared to rubber modified samples (Figure 77 – c)) in which strain contours are situated close to the cutting tool. On the other hand, Si20 sample had the

lowest MNS value of 0.11, followed by R20 sample with 0.27 and DGEBA with 0.45. Si20 sample (Figure 77 – e)) showed a more localised strain map, which could potentially illustrate a crack initiation point. As the material is deformed due to further penetration of the cutting tool, the local strain values increase for all samples, while strain contours are still localised around the cutting tool for R20 and Si20 samples ((Figure 77 – d, f)). DGEBA sample (Figure 77 – b)) shows the highest MNS value of 1.1, however the strain contours are dispersed around the cutting tool in two zones: (i) one that is extended ahead of the cutting tool (ii) on that penetrates approximately 45° into the subsurface.

The high value of MNS of DGEBA sample and the strain contours dispersion is attributed to the deformation and fracture of the material. In the case of rubber modified sample, toughening mechanism took place [8], [48], which increased the plastic zone ahead of the cutting tool, hence limiting the fracture and deformation of material. The shear strain maps (Figure 78) show a compression area (negative value of SS) formed across the relief face of the tool, while a tensile area (positive value of SS) is formed on the rake face. Similar to MNS contours, R20 sample (Figure 78 – c), d)) showed the SS contours distributed close to the cutting tool edge. The increased stiffness of the silica particle should make a contribution to the load carrying capacity of the composite, however, the stress concentration effect due to the presence of silica nanoparticles weakens the material [4]. This aspect coupled with experimental evidence is discussed in section 6.6.

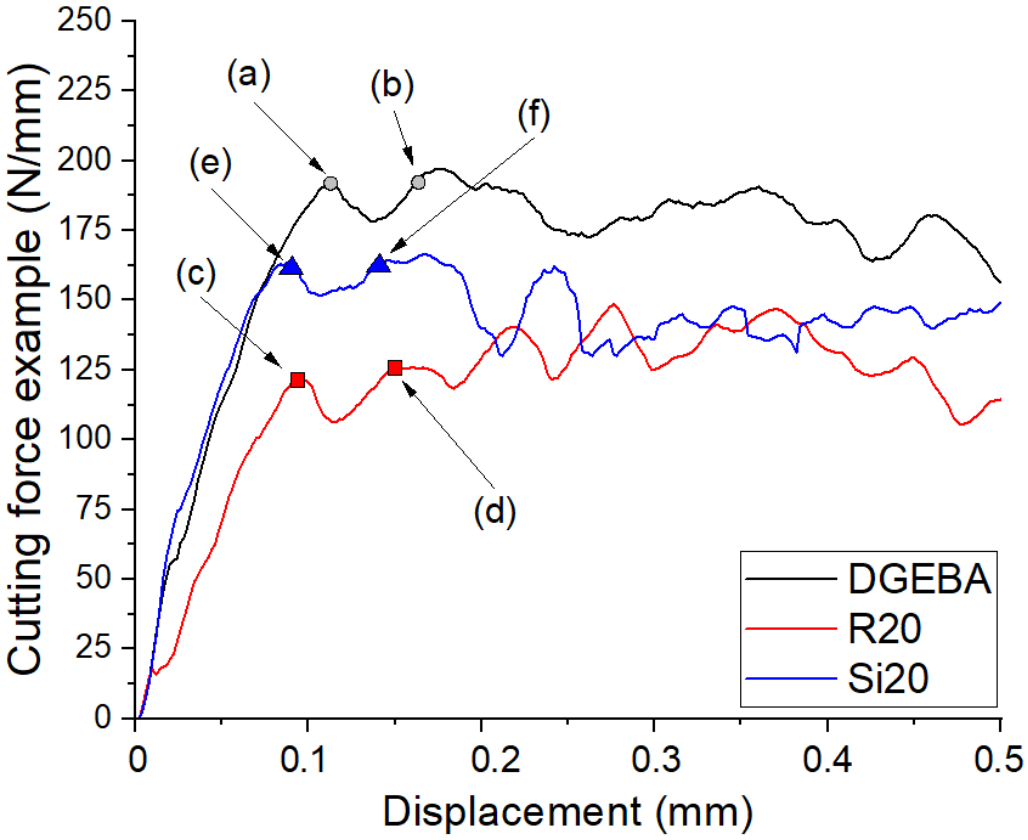

Figure 76 - Cutting force vs displacement for D, Si20 and R20 samples where (a) – (f) have corresponding time stamps to equivalent strain maps of Figure 77 and Figure 78

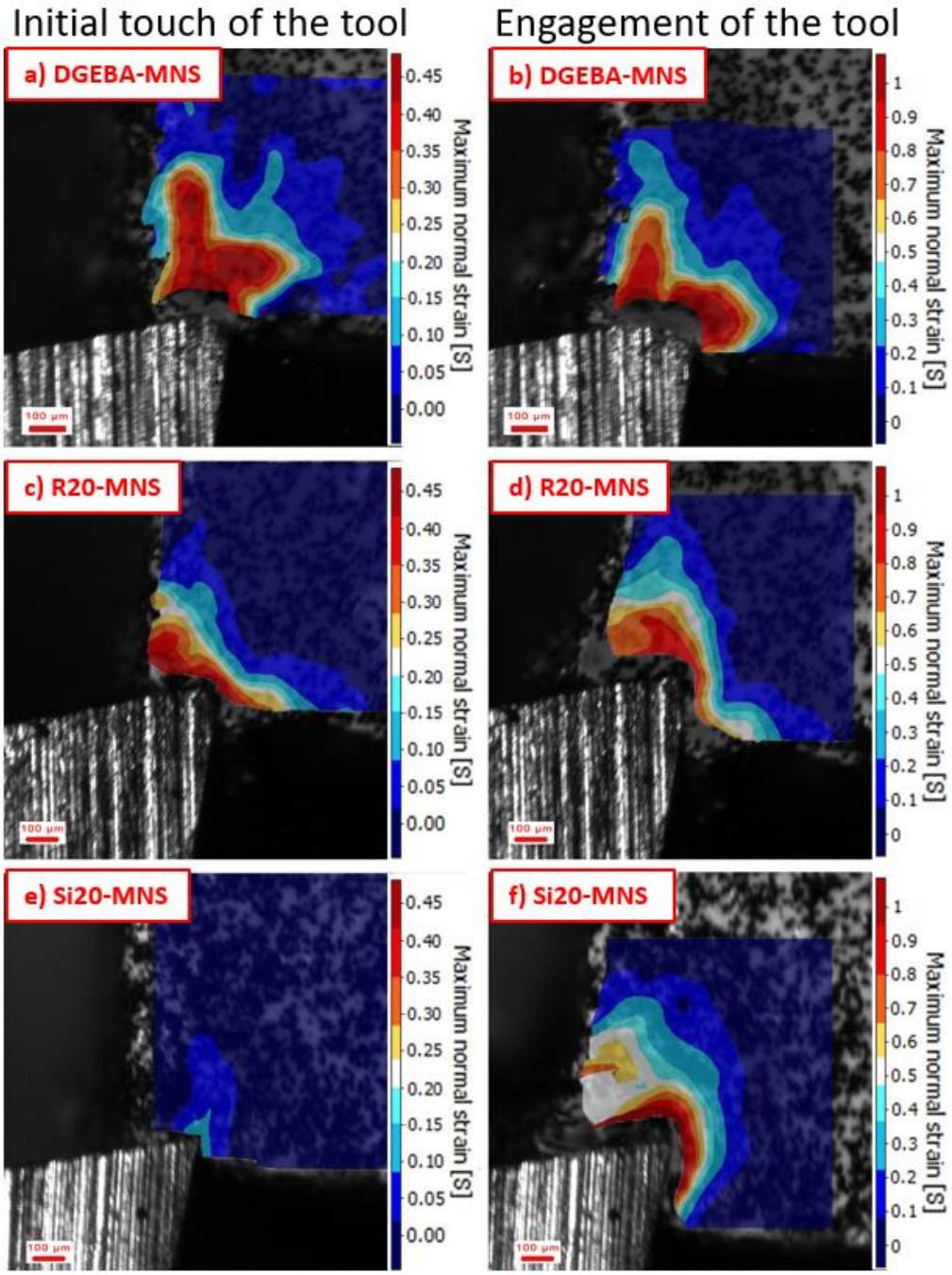

Figure 77 - Maximum normal strain [S] (MNS) maps for a - b) DGEBA c - d) R20 e - f) Si20 corresponding to the time force points marked a - f on Figure 76

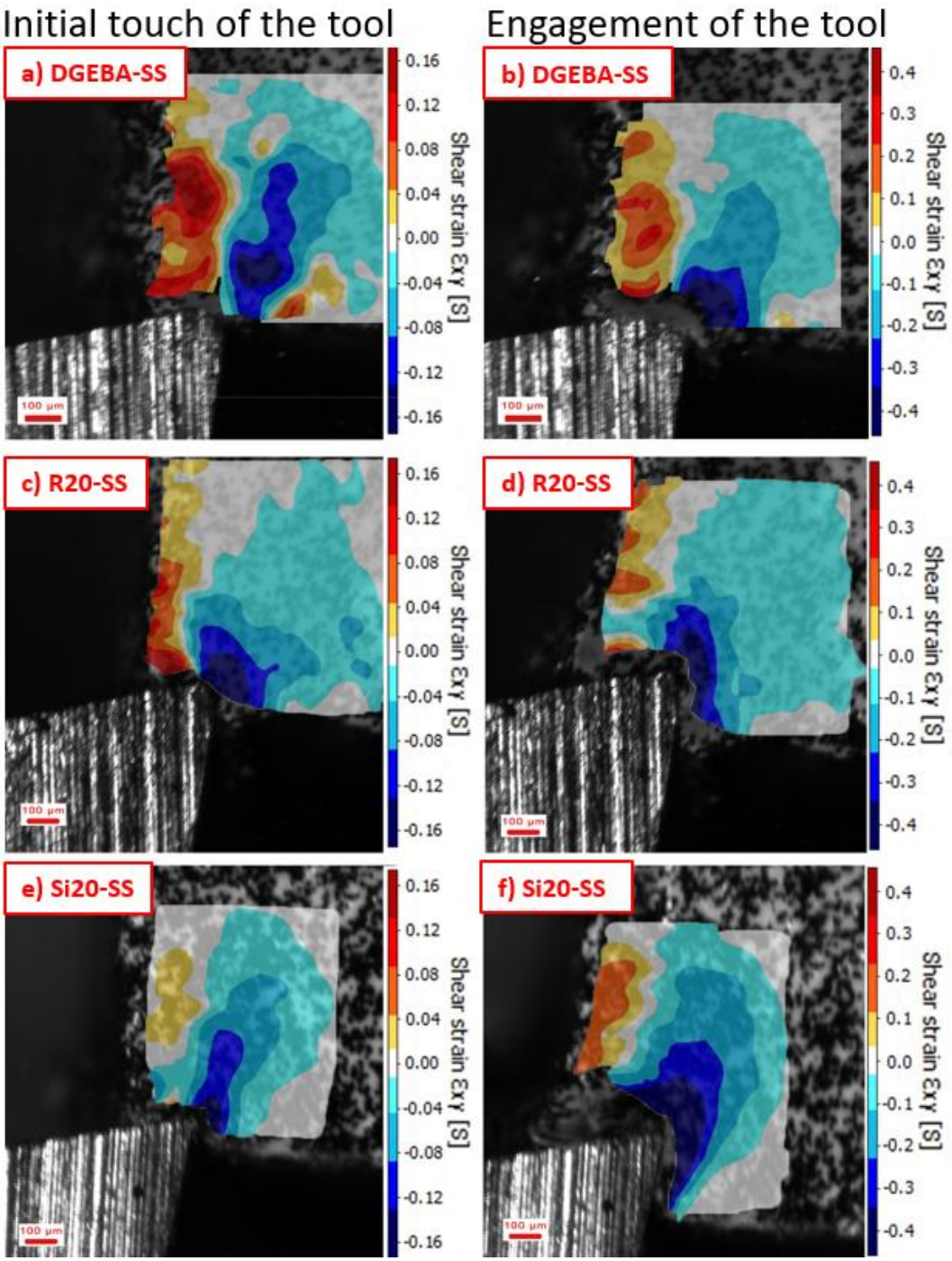

Figure 78 - Maximum shear strain [S] (SS) maps for a - b) DGEBA c - d) R20 e - f) Si20 corresponding to the time force points marked a - f on Figure 76, with negative values corresponding to compression force due to the flank face compression

6.4 The effect of chip formation process on subsurface damage

The cutting process was interrupted in the middle of the cut and the sample was analysed with 3D micro-CT to quantify both the subsurface damage under the machined surface and damage initiation ahead of the cutting tool during the chip formation process as shown in Figure 79. 2D slices were extracted for processing from the middle of the specimen ensuring that the chosen part of material was cut in plane-strain conditions. The subsurface damage was quantified in terms of maximum damage depth and area of damaged zone. As we cannot discriminate between damage induced by the cutting edge or damage from compression due to the flank fae, then damage refers to any type of defect which is induced by the orthogonal machining process. Depending on the fibre orientation, this can include matrix cracks, fibre breakages, fibre bending, matrix/ fibre pullouts and uncut fibres. A MATLAB® script [185] was used to calculate the area of the damaged zone based on processed binary images. The volume of indentations (craters) observed on the 135° plies was calculated using the Dragonfly CT segmentation software (Figure 79– b)). These have previously reported during machining of CFRPs [171], [186] and it was found that they adversely affected the mechanical properties of the samples [23], [187], [188].

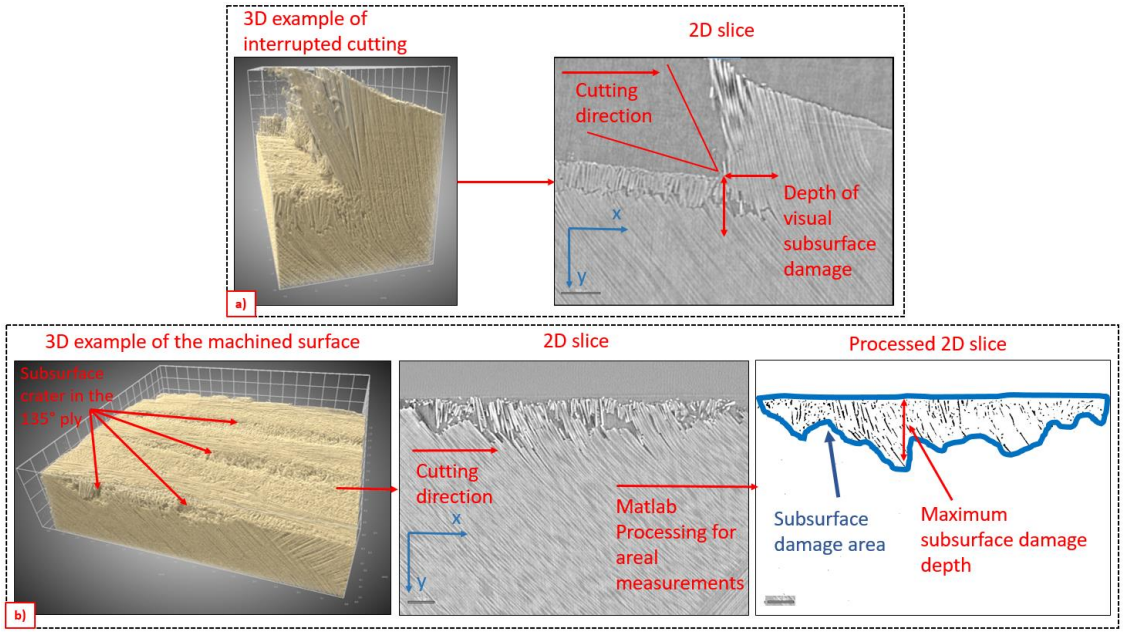

Figure 79 – a) Subsurface damage measurement example of DGEBA sample for chip formation process in an interrupted cutting b) Subsurface damage assessment

All the machined surfaces showed significant matrix smearing across all fibre orientations. Due to project budget limitations, DGEBA, R20 and Si20 were chosen as representative examples for the subsurface damage assessment. Figure 80 shows the calculated subsurface damage for the machined materials, however as no quantifiable surface intrusion or subsurface damage was identified for 0° fibres, therefore Figure 80 does not include 0° orientation in damage comparisons.

For a single material, changing the fibre orientation from 45° to 135°, shows an increase in the damage area. However, within an individual fibre orientation, defined by a ply layer, the addition of rubber or silica reinforcements results in reduced subsurface damage. The calculated maximum subsurface damage depth (Figure 80 – a)) shows a decrease for all fibre orientations when silica or rubber was added to the epoxy matrix. Moreover, the R20 sample had the lowest level of damage, which can be attributed to rubber toughening mechanism which is active during material removal. Moreover, damage in front of the cutting tool, areal damage and crater volume has the lowest values for the R20 samples. An increase in damage in front of the cutting tool was found for Si20 sample in the 90° fibre orientation, however the measured values are not significant. However, there is no well known industry limit for crater volume acceptance level, therefore it requires further investigation from the machining induced damage metric point of view.

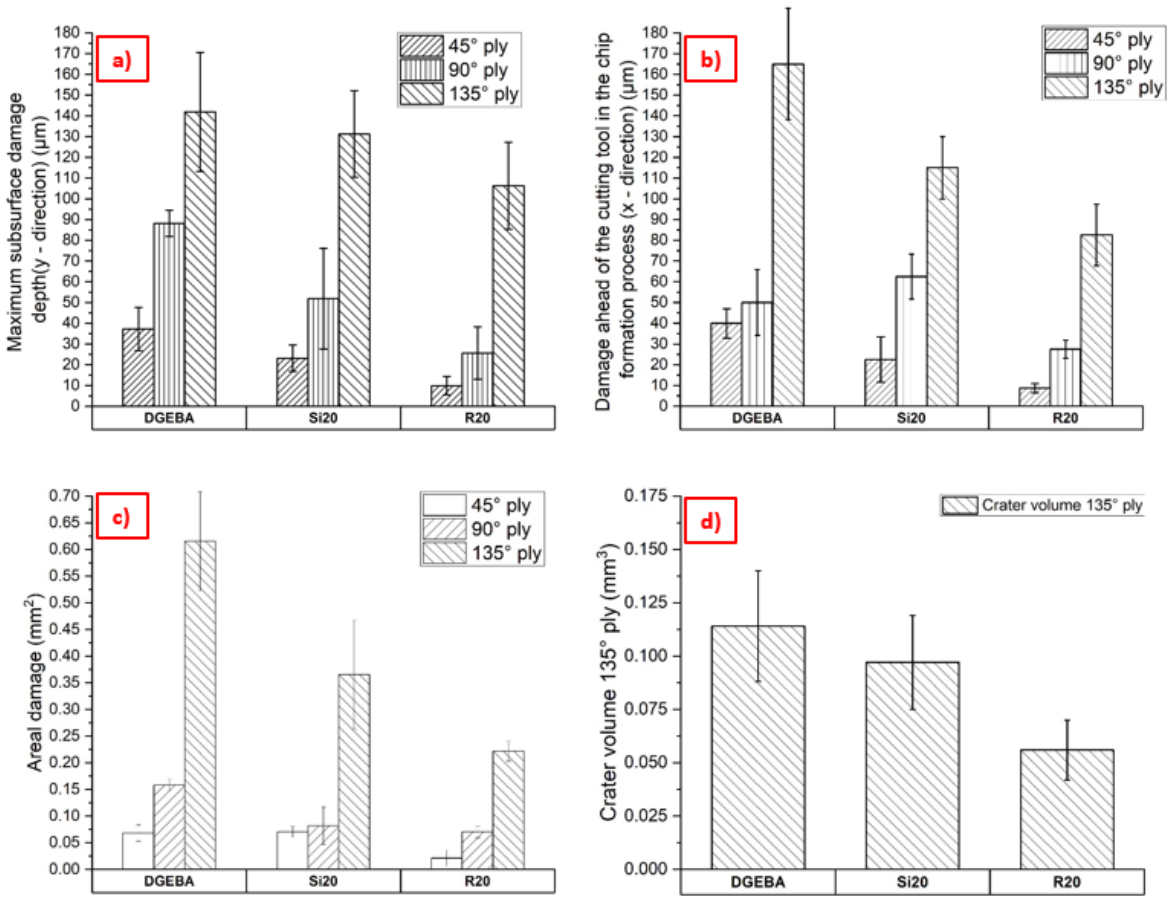

Figure 80 – Subsurface damage assessment with error bars showing the standard deviation of the assessed images a) Maximum subsurface damage b) Damage in front of the cutting tool c) Areal damage d) Crater volume (0° fibre orientation did not show damage by these measurements)

The measured subsurface damage is further explained when considering fibre orientation and the fracture mechanism, based on the 2D interrupted cutting images (Figure 81) and the representative subsurface damage examples (Figure 82). Appendix D contains an example of 3D images which were used in the generation of 2D slices. The material removal mechanism for each ply was studied based on analogous UD 2D slices.

According to [22] the cutting mechanism can be grouped as Type I, III, IV and V chip formation process depending on the fibre orientation. Type I chip formation describes 0° fibre cut via crack propagation ahead of the tool where the fibres are peeled from the surface then bend and fracture (Figure 81 – a), b), c)). Fibres on the machined surface fracture perpendicular to their long axis due to the compression from the cutting tool applied against the front surface. For 0° fibre orientation, the reinforcement particles did not show any noticeable effect on the chip formation process or subsurface damage. This

is attributed to the fibre – matrix interface failure of the samples where the particulate reinforcements embedded into the epoxy matrix do not have a significant contribution.

Type III is typical for 45° fibre orientation where chip formation consists of fracture from compression-induced shear across the fibre axis followed by interlaminar shear fracture along the fibre-matrix interface as the tool advances into the material. The shearing mechanism at the fibre-matrix interface is clearly visible in Figure 81– d), e), f). During the compression stage of the material removal mechanism, fibres are fractured, and cracks are generated below the cutting plane as shown in Figure 82 – d), e), f). The extent of damage is limited for the R20 sample compared with the other samples which is also shown quantitatively by graphs of Figure 80 – a), b), c). This is associated with the presence of rubber particles, which makes the fracture less brittle due to toughening mechanism of rubber particles and efficient energy dissipation of the energy within the material. This is also observed in Figure 76, where i) the cutting force in rubber has the smallest value and ii) there are more constant chips formed (based on the wavelength shape and dips in the force curve).

As the fibre orientation increases to 90°, interlaminar shear increases, leading to the fracture of the fibre and fibre and the matrix. The compressive stress within the contact region between cutting tool and fibre will reach the failure value of fibres at a small deformation or movement of the fibre. This is typical for Type IV chip formation process. Fibres fracture at the tool tip position for R20 sample (Figure 81 – i)) or a crack is developed on the cutting plane in front of the cutting tool (Figure 81 – g), h)). The crack propagation in front of the cutting tool is facilitated by the brittle state and low fracture toughness of silica and unmodified epoxy compared to the rubber modified sample. The critical strain to failure is reached earlier for unmodified and silica samples as observed in tensile and fracture toughness results and discussed in section 4.2, while rubber sample experienced a larger strain to failure.

Similar to 45° fibre orientation, the presence of rubber particles reduces the fibre crushing effect. Unmodified epoxy composite showed a continuous line of subsurface fracture fibres (Figure 82– g)) which are suspected to fail due to excessive bending as the cutting tool advances into the material. Crushing-dominated fibre fracture is replaced by bending-

dominated fibre fracture when a large cutting edge radius of the cutting tool is adopted [189]. However, in this study, the cutting tool edge radius is the same for all machined samples. Moreover, subsurface bending fracture in the 90° laminate plane is difficult to achieve due to the strong constraining effect of the neighbouring fibres [189]. Therefore, it is assumed that the matrix-fibre interface starts to debond as the surface contact pressure is building up with the motion of the tool, which will lead to bending and fracture of the fibres at subsurface level. The interface failure aspect is further discussed in section 6.6 where high-magnification SEM micrographs are used as experimental evidence.

In Type V for 135° fibre orientation, bending is caused by flank face compression – as the tool advances of the cutting tool into the material. This causes the matrix to crack and fibres to fracture (Figure 81 and Figure 82 – k), l), m)). This further results in material becoming detached and allowing material to pullout, which leads to the formation of craters below the cut surface. The calculated crater volumes are shown in Figure 80 – d). A 50.8 % decrease is found between R20 and DGEBA samples, while the subsurface damage area and maximum damage depth for 135° plies decreased by 63 %, and 25 %, respectively. These results are linked with the high fracture toughness of the rubber modified epoxy, limiting the crack growth along the matrix in 135° fibre orientation, thus decreasing the amount of pullout material and subsurface damage.

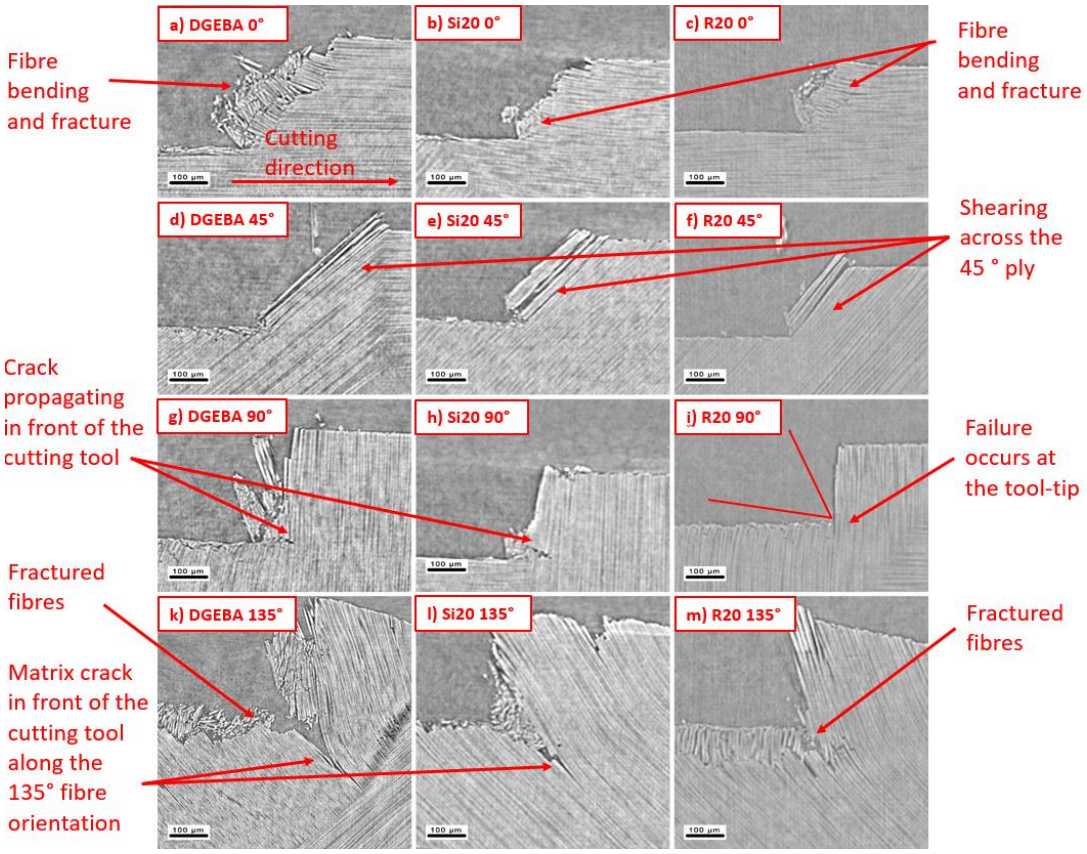

Figure 81 – 2D slice examples of interrupted cutting for DGEBA (a, d, g, k), Si20 (b, e, h, l) and R20 (c, f, i, m) samples showing machining induced damage

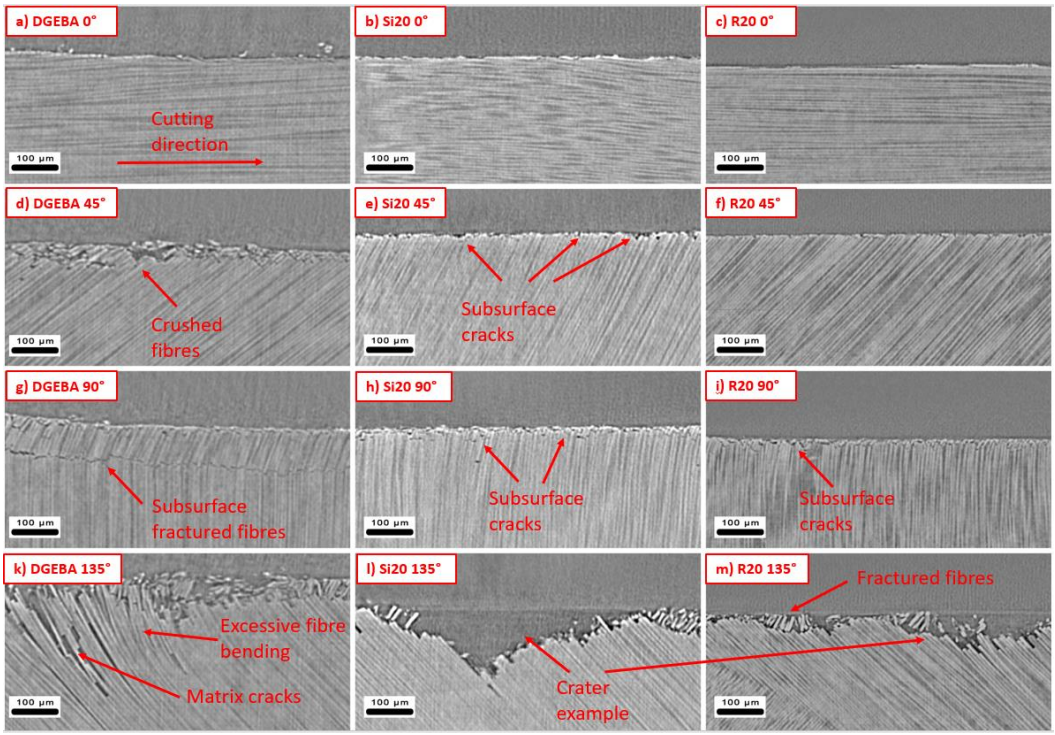

Figure 82 – 2D slice examples of subsurface damage for DGEBA (a, d, g, k), Si20 (b, e, h, l) and R20 (c, f, i, m) samples

6.5 Machined surface characterisation

Figure 83 shows the variation of selected metrics to investigate machined surfaces in the samples. Due to waviness and twill-weave architecture of the carbon fibre plies of the CFRP material, individual ply surface topography analysis was not possible; hence, measurements across the full-machined surface were used. As shown in Figure 82 and previously in the literature [171], [185], [186], fibre orientation has a strong influence on the generated surface topography after machining. DGEBA samples represent the reference material in Figure 83. As the rubber content increases (Figure 83 – a)), the S_a (average height of scanned area) parameter decreases. R_a parameter (average roughness of profile) shows a similar trend, however it is reported that S_a provides greater reliability of roughness measurement for multidirectional laminates [190]. Adding silica nanoparticles from 10% to 20% wt. causes S_a to increase. These have been balanced in the 'hybrid' Si10R10 sample which contains 10% silica and 10% rubber. A similar trend was found for the S_v (maximum valley depth of scanned area) measurements Figure 83 – b). Interestingly, Si10R10 sample showed the lowest S_v value (Si10R10: S_v - 42), followed by rubber (R20: S_v - 61), silica (Si10: S_v - 63, Si20: S_v - 92) and DGEBA sample (DGEBA: S_v - 102). CT-scan images (Figure 10 – k), l), m)) showed that the maximum depth of damage occurs in the 135° fibre orientation plies and surface metrics are measured on the entire surface of the specimens, therefore the measured S_v values are attributed to the 135° plies. However, it is noted that maximum depth of subsurface damage (Figure 8 – a)) is 35 – 40 % higher than S_v measurements (Figure 83 – b)). This is accounted for by the fractured fibres and matrix which were not completely pulled out and remained on the bottom of subsequently generated craters, hence influencing the topography measurements (example in Figure 82 – k), m)). This highlights the fact that surface metrics assessment of the machined surfaces is insufficient to characterise machining induced damage.

The variation of surface Kurtosis (S_{ku}) and surface Skeweness (S_{sk}) parameters (Figure 83 – c), d)) show that DGEBA and silica modified composites (Si20) had the highest value of Kurtosis indicating a surface with sharp peaks and valleys. A negative Skeweness was found for all samples, which is a characteristic of a surface with deep cracks and voids. This type of features is typical for 135° plies, as CT results (Figure 82) showed no similar features for

the other fibre orientations. Similar to subsurface damage results discussed in Section 3.4, R20 experienced the lowest S_{sk} value (Figure 83 – d)) which is correlated with limited material pullout that is linked with the rubber toughening mechanism, followed by silica and unmodified epoxy composite. As the fact that the most damage is created in the 135° plies was previously reported in the literature [116], [191], S_{sk} is considered an effective parameter which is able to link the subsurface damage to surface metrics results for 135° fibre orientation.

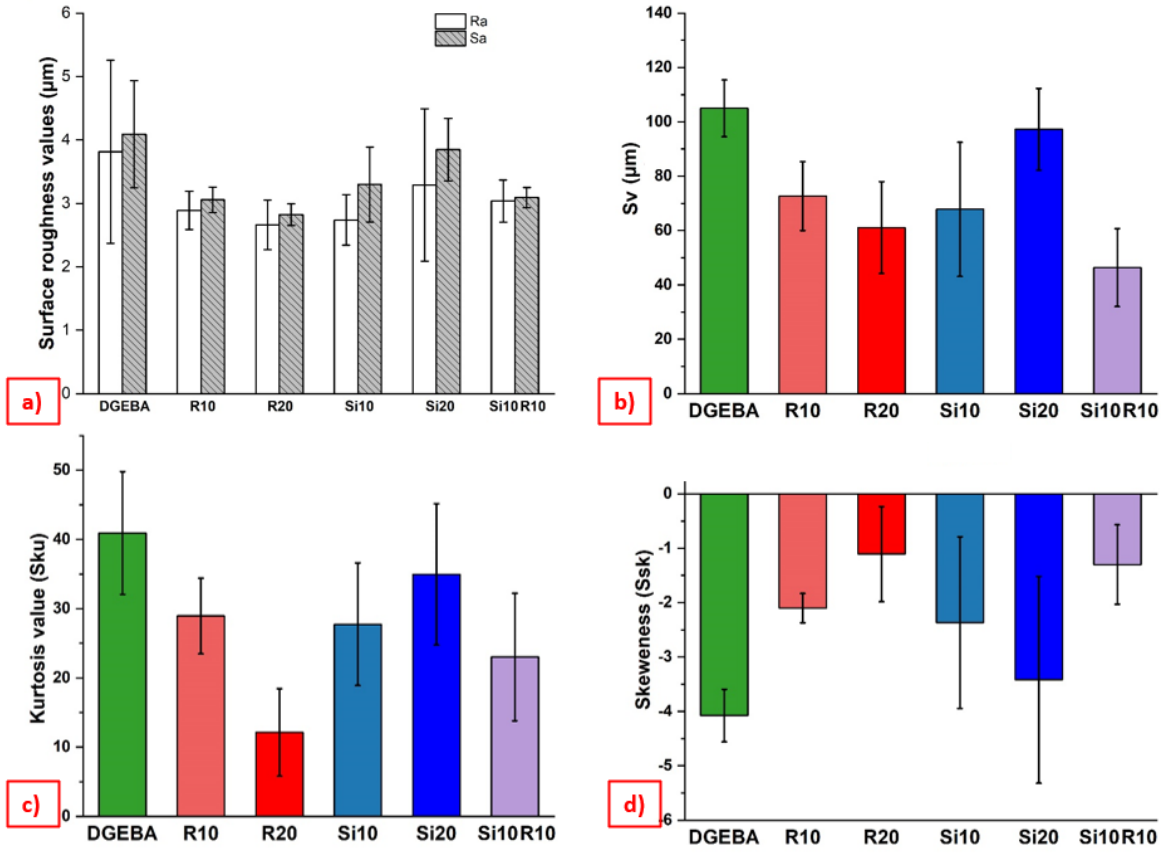

Figure 83 – Surface metrics measurement a) Surface roughness (R_a, S_a) b) Maximum valley depth (S_V) c) Kurtosis (S_{ku}) d) Skeweness (Ssk)

6.6 Surface morphology assessment

Even though the machined surfaces showed significant smearing across all fibre orientations which hide the artefacts of toughening mechanism and chip formation process, there were still several sites of craters and material pullout showing specific signature of each modification on the fracture process on the machined surfaces. Material

pullout regions and fibre-matrix debonding were observed for DGEBA and silica sample (Figure 84 – a), b)). The fractured fibres show a clean surface which leads to the conclusion that the composite material failed at the interface region between the fibre and matrix. On the other hand, the fractured material of R20 sample (Figure 84 – c)) showed fibres with matrix attached, which indicates that polymer debonding did not occur fully. The debonding is directly related to the fibre and matrix adhesion and the particle reinforcement of the epoxy does not have a significant role in the individual fibre toughening mechanism (e.g., fibre debonding, fibre pullout). However, the presence of rubber microparticles and their subsequent toughening mechanism, facilitated the fracture energy dissipation, which ultimately limited the fibre debonding and pullout.

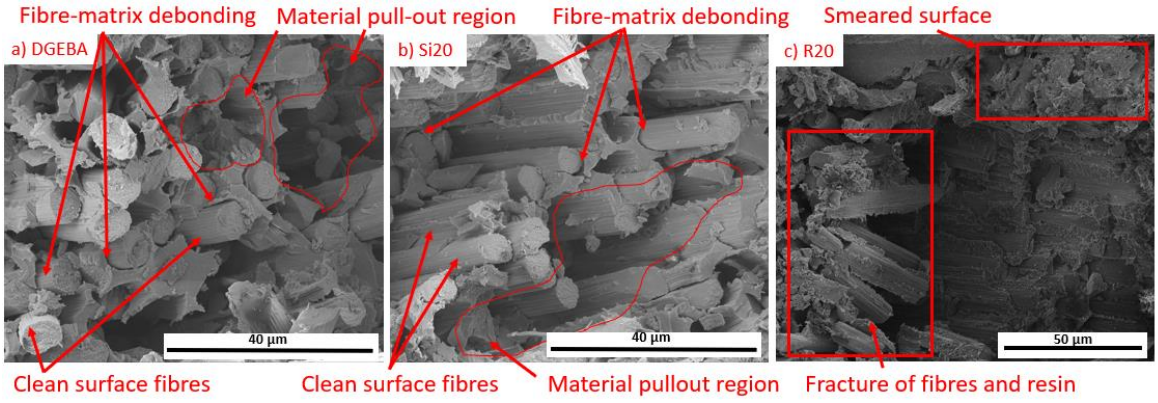

Figure 84 – Typical micrographs of machined surface of a) DGEBA b) Si20 and c) R20 samples, where 'Clean surface fibres' means the fibres have debonded from the matrix by adhesive failure

The principal toughening mechanism of rubber micro-particle and silica nanoparticle were previously discussed in the Literature Review, section 2.2.4, and identified in the machined surface micrographs. Figure 85 shows the high-resolution SEM micrographs of the machined surface of rubber modified samples cut at 135° where the present voids are evidence of the cavitation process. The original mean diameter of the rubber micro-particles was 0.54 µm [8], while the cavitated areas were measured to be 1.02 ± 0.16 µm. This indicates that the cavitation of the rubber particles is followed by a large plastic deformation in the matrix that dissipates the energy at the machining zone resulting in a reduced crack initiation and propagation below the surface. Plastic deformation of the epoxy matrix is visible on the edge of the voids generated on the polymer matrix surface due to the cavitation process (Figure 85 – b)). It is also noticed that fibres are attached to

the machined surface and are still encased in epoxy matrix, which further highlights the fact that fibre-matrix interface failure does not occur in rubber-modified samples. The rubber toughening mechanism allows the fracture energy to be dissipated, this limits the extent of subsurface damage from the compression induced by the flank face. These are correlated with the low oscillations of cutting force signal shown in Figure 74 – a).

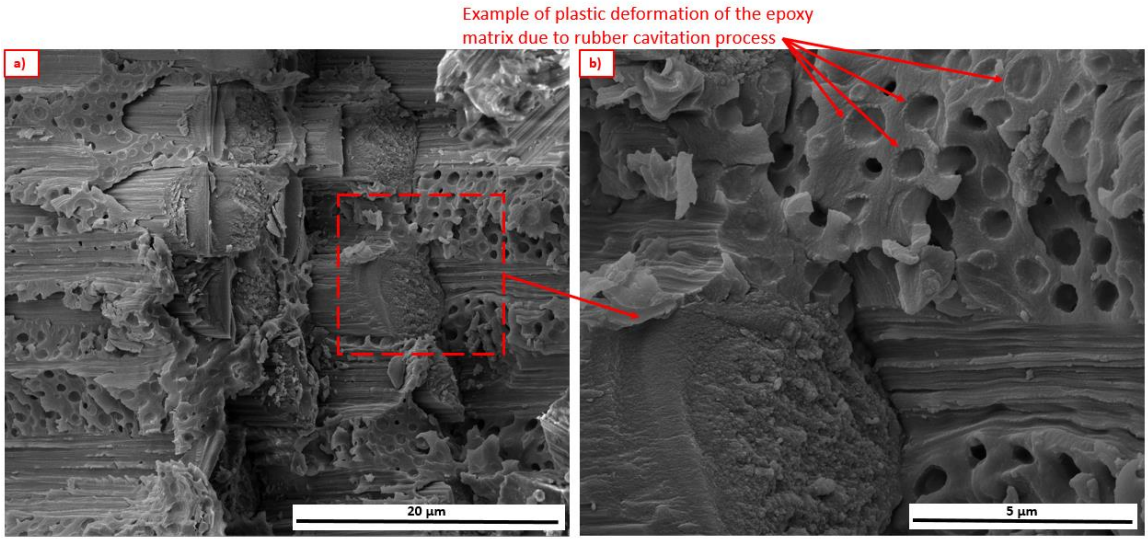

Figure 85 – High-resolution FEG-SEM micrographs of R20 machined surface a) Fibre and rubber cavitation process artefacts b) High-magnification example of plastic deformation of matrix due to rubber cavitation process, where rectangle shows a fibre bonded to the surrounding matrix

High-magnification SEM micrographs of Si20 machined surface (Figure 86 – a)) clearly illustrate the fibre pullout and fibre-matrix debonding. The fractured surface of the matrix is relatively smooth, which is typical for a thermoset polymer. Similar features were found on high-magnification images of unmodified epoxy composite in section 5.3. Feather markings are observed (Figure 86 – a)), which are caused by crack forking due to the high energy associated with the relatively fast crack growth that was previously identified and is typical for a brittle epoxy material [6]. The presence of voids and silica nanoparticles on the high-resolution image (Figure 86 – b)) indicates that plastic void growth of the material was initiated by the debonding of silica nanoparticles. Even though the samples were gold coated prior to SEM analysis, the artefacts of silica debonding in silica modified samples were not observed on unmodified epoxy composite. This shows that the identified artefacts are solely related to the presence and failure mechanism of silica nanoparticles and are not an artefact of the applied gold coating. However, it can be seen that not all

particles initiated the void growth mechanism. Is has been previously reported that only a fraction of the nanoparticles debond [4]–[6] and the considerable difficulty of quantifying the number of debonded particles. Hsieh et al. [5] discussed the reasons for the incomplete debonding of silica, namely (i) a purely statistical aspect of the fracture process (ii) that once a silica nanoparticle, or group of such particles, have debonded and the epoxy polymer undergoes plastic void growth, then the stress which drives such a mechanism is relieved in the adjacent region. The general conclusion is that if only a fraction of particles initiates plastic void growth, the toughening mechanism will be affected, thus decreasing the expected fracture toughness of the silica modified epoxy composite. Thus, the identified silica-toughening mechanism proved ineffective in the machining of CFRPs in terms of reducing machining induced damage and reducing cutting forces in comparison to rubber micro-particles.

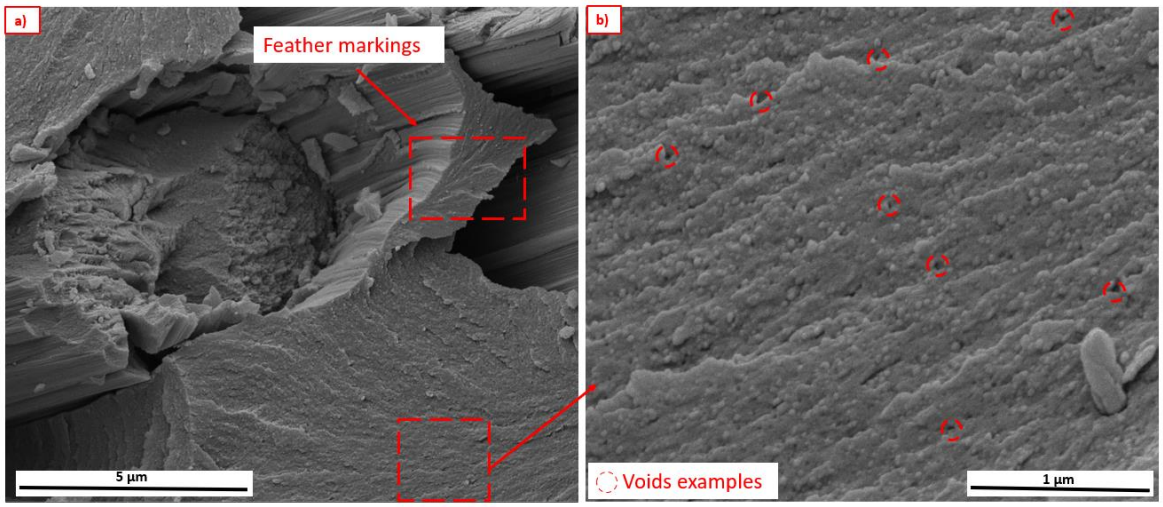

Figure 86 – Enlarged view of the machined surface of Si20 samples showing a) Fibre – matrix debonding and pullout and b) Associated voids highlighted in circles

6.7 Summary

The addition of rubber microparticles and silica nanoparticles to the epoxy matrix of CFRP is found to influence the chip formation process and the subsequent machining induced damage during orthogonal cutting. The lowest average cutting force was recorded for rubber modified samples, followed by silica and then by unmodified epoxy CFRPs. Rubber modified samples showed a stable cutting force, with regular oscillations, compared with the higher, more random oscillations experienced by unmodified and silica reinforced

specimens. The presence of rubber microparticles increased the elastic recovery of the material, which resulted in the largest springback measured for all samples. The low magnitude of cutting forces was correlated with the lower depth of cut measured and reduced subsurface damage for rubber-modified samples. Strain map contours illustrate that material deformation in the chip formation zone is characterised by two zones, one that is extended ahead of the cutting tool for DGEBA and silica samples (> 100 µm) and one that penetrates approximately 45° into the subsurface, compared to more localised contours of rubber-modified samples, in front and below the cutting tool.

The material removal mechanism and subsequent machining induced damage for 45°, 90° and 135° fibre orientation plies of the woven CFRP material are affected by the presence of fillers. Rubber modified samples (R20) show the least subsurface damage (75% decrease for 45°plies, 66% decrease for 90° plies and 21% decrease for 135° plies) and measured areal damage (77% decrease for 45°plies, 60% decrease for 90° plies and 64% decrease for 135° plies) compared to DGEBA samples. A 50.8% decrease in surface craters is found between R20 and DGEBA samples in 135° plies. No notable difference was found for subsurface damage measurements in 0° plies. Surface metrics were found to be in good agreement with subsurface damage results, however, surface metric assessment of the machined surfaces is insufficient to fully characterise damage occurring during cutting. These results were linked to the particle toughening mechanism, which was found to take place during cutting, as particle cavitation for rubber microparticles and debonding for silica nanoparticles.

Rubber toughening mechanism ensured an efficient energy dissipation mechanism limiting crack propagation and the extent of subsurface damage. The brittle state of epoxy matrix and the fact that not all silica nanoparticles debonded in the silica toughening process resulted in fibre pullout and matrix-fibre debonding which proved in effective in reducing the machining induced damage. Further studies will investigate the effect of reinforcement particles in an edge trimming or milling process where higher feed rates result in higher strain rates and higher temperatures, which could lead to different damage and cutting mechanics.

Whilst this chapter proved that machining induced damage and chip formation process are influenced by the presence of reinforcement particles in epoxy modified CFRPs in orthogonal cutting conditions, further work is required to investigate their effect in an industrial CFRP machining process. Based on the post machining methodology developed in this study, similar methods will be used to quantify machining induced damage in an edge trimming study presented in Chapter 7. Gaining understanding of chip formation process of modified polymer composites will enable designers and engineers a greater ability to introduce polymer-fillers during Design for Manufacture (DFM) stages of product design leading towards damage-free machining of high-value parts.

7 MACHINING PERFORMANCE OF EPOXY MODIFIED CFRPs UNDER EDGE TRIMMING CONDITIONS

In this chapter, a DoE was implemented to quantify the effect of particulate reinforcements and cutting parameters on machinability of modified epoxy CFRPs during an industrial level edge trimming operation. The cutting force behaviour is discussed and linked with underlying material removal mechanism. Surface metrics along with surface morphology assessment are presented and cross corelated with ANOVA results which provided a statistically significant difference in terms of cutting force averages, specific cutting power and machining induced damage.

7.1 Introduction of new particle concentrations for the modified epoxy CFRPs

According to the previous orthogonal cutting results where the effect of silica and rubber particles in 10 and 20% concentration were investigated, it is hypothesised that the optimum machining performance for the developed material might be in between the selected concentrations, therefore new materials were introduced as per Table 25. These materials have been tested in an edge trimming process with industrially approved cutting parameters as described in section 3.6.3 based on the DoE matrix discussed in section 3.6.4.

Table 26 – Particle concentration of the samples used in the edge trimming experiment

Nanoparticles by weight (%)	**Name**
Control	D (DGEBA)
5 % silica, 0 % rubber	Si5
10 % silica, 0 % rubber	Si10
15 % silica, 0 % rubber	Si15
20 % silica, 0 % rubber	Si20
5 % rubber, 0 % silica	R5

10 % rubber, 0 % silica	R10
15 % rubber, 0 % silica	R15
20 % rubber, 0 % silica	R20
5 % silica, 5 % rubber	Si5R5
10 % silica, 10 % rubber	Si10R10

7.2 Cutting force evolution

An example of cutting force evolution for DGEBA and R20 CFRP samples is shown in Figure 87. After the full engagement of the cutting tool with material, cutting forces experience a steady state zone with cyclic behaviour. For a better understanding of the cutting mechanics and force evolutions, the cut force is plotted as a function of tool rotational angle in Figure 88. At both low (1140 mm/min) and high cutting feeds (1900 mm/min), DGEBA, rubber and silica samples experienced a different cutting force behaviour which could lead to the conclusion that material removal mechanism is different depending on the effectiveness of particle toughening mechanisms, cutting feed and the dominant fibre failure mode across the thickness of the samples.

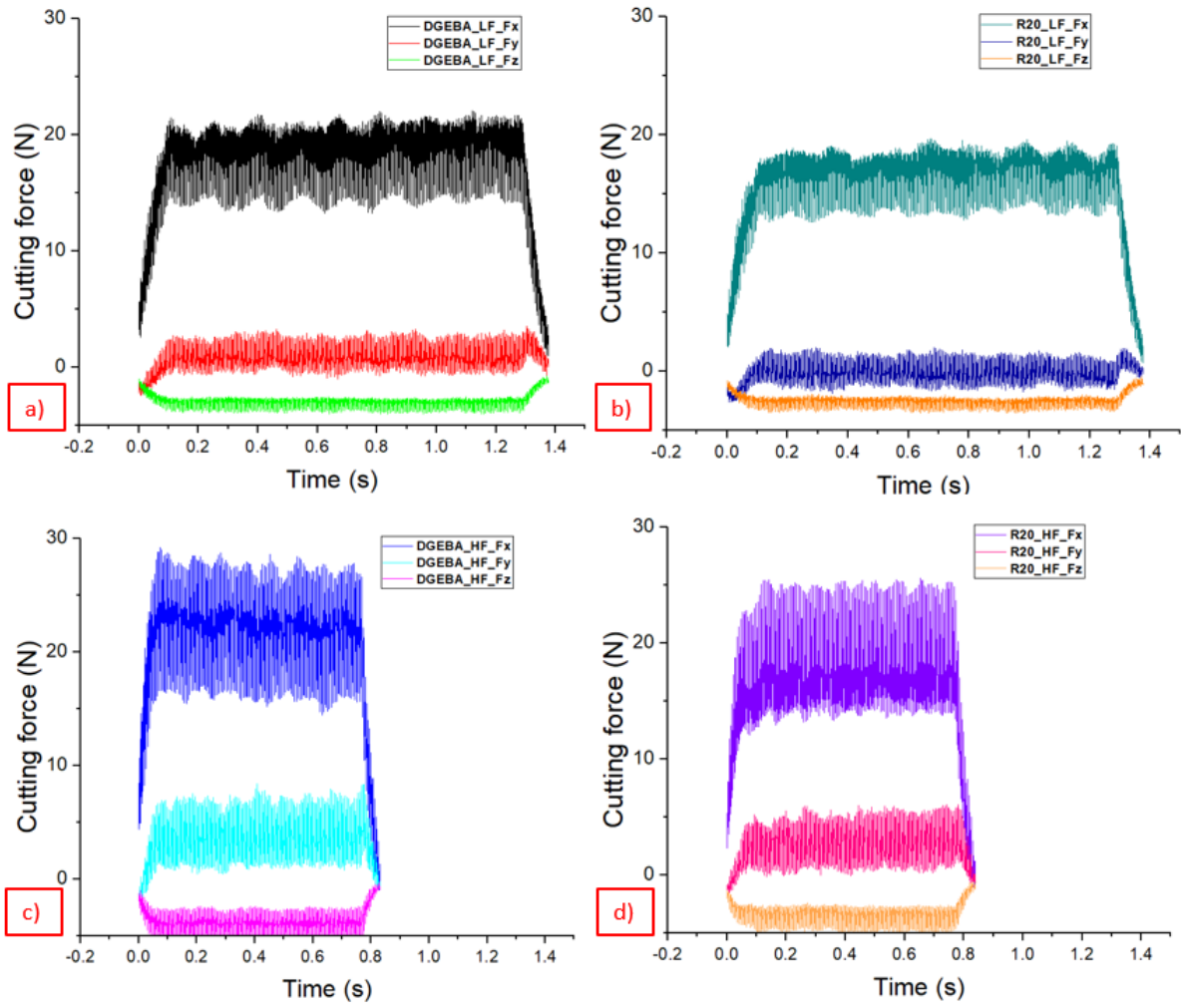

Figure 87 – Cutting force evolution for DGEBA and R20 sample at a) & b) Low Feed 1140 mm/min and c), d) High Feed 1900 mm/min

In the Si20, Si20 and Si10R10 material cut in low feed conditions and within the first half rotation of the tool (i.e. 0° to 90°) as shown in Figure 88 – a), b), a high peak in the cutting force is noticed which is attributed to the brittleness and stiffness of the material. The peak cutting force in DGEBA and rubber samples are smaller for the same tool rotations under both low and high cutting feeds (Figure 88 – a), c)). For the second part of the first half of tool rotation (i.e. 90° to 180°) a drop in the cutting force is noticed for silica, DGEBA and Si10R10 sample which is attributed to the chip load release and at this stage the flank face of the tool is not fully engaged with the material along its axis of rotation (Figure 88 – a), b)). Same behaviour is observed at higher cutting feed for the last part of the tool rotation (i.e. 270° to 360°) for silica, rubber and DGEBA sample (Figure 88 – c), d)). Rubber modified samples experienced the lowest cutting force oscillations (R20, LF: 14 to 18N, HF: 14 to 24

N), while silica (Si20, LF: 14 to 22 N, HF: 17 to 30 N) and DGEBA (DGEBA, LF: 14 to 21 N, HF: 16 to 27N) variations were higher. This trend is similar to low-speed orthogonal cutting results (Figure 74) where it was concluded that cutting force behaviour is governed by the toughening mechanism of particulate fillers.

On the other hand, the 'hybrid' Si10R10 sample showed cutting force peaks as high as silica samples. This contradicts the behaviour of 'hybrid' sample in orthogonal cutting conditions where the rubber toughening mechanism was found to be the dominant failure mechanism.

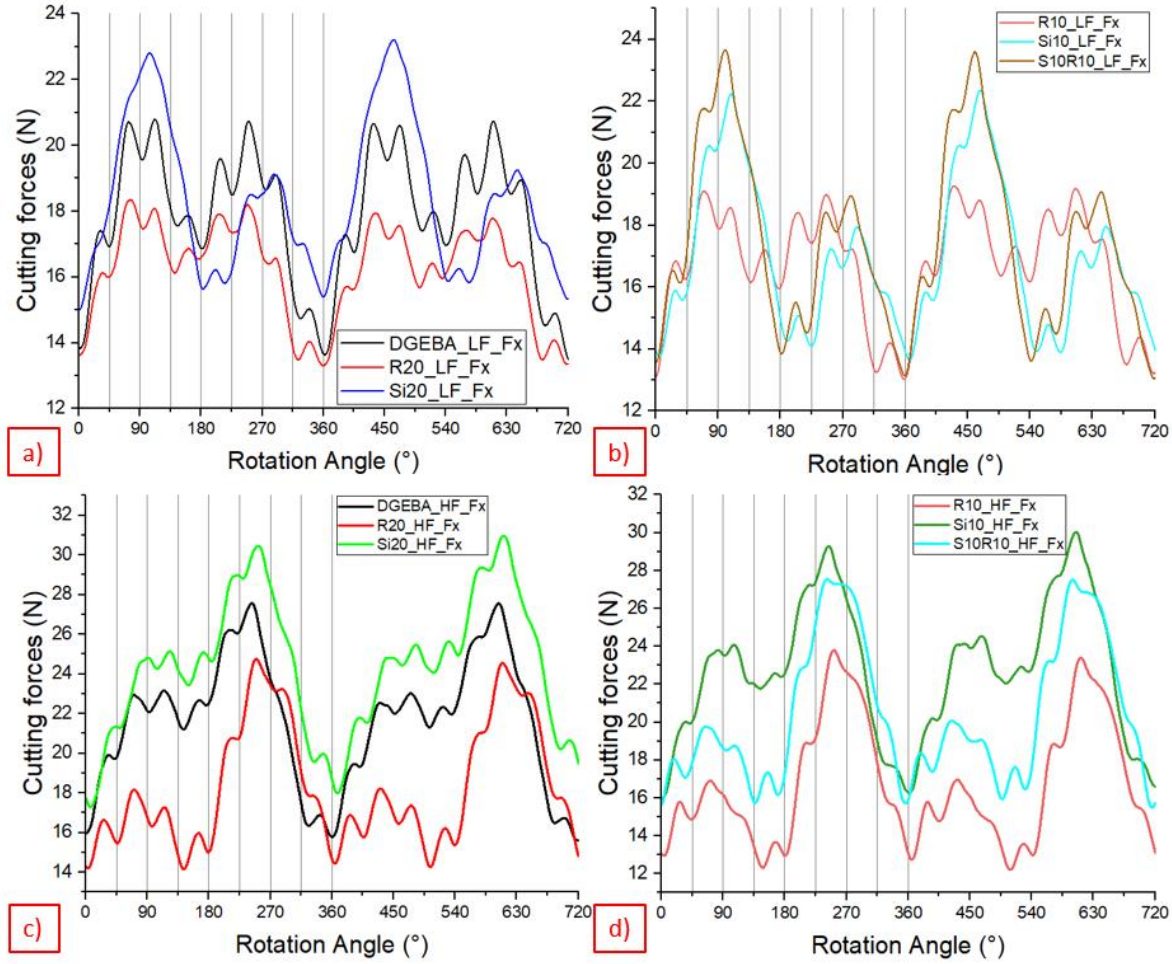

Figure 88 – Cutting force vs tool rotation angle for a) DGEBA, R20 and Si20 at Low Feed b) R10, Si10 and Si10R10 at Low feed c) DGEBA, R20 and Si20 at High Feed d) R10, Si10 and Si10R10 at High Feed (Low Feed: 1140 mm/min, High Feed 1900 mm/min)

Average cutting force is decreasing with rubber content for both cutting feeds (Figure 89 – a), where error bars are standard deviation for individual population depending on

reinforcement type, concentration and feed) which follows the pattern found in orthogonal cutting results (Figure 65). This is related to the toughening mechanism of rubber particles which was previously discussed in section 6.6 and experimental evidence of the cavitation occurring in edge trimming experiment and further discussion is provided in section 7.3. Similar trend is found for the cutting range (Figure 89 – b)) and the average of the peaks (Figure 90 – a, b)). The average cutting force decrease from control sample (DGEBA) is more noticeable for higher cutting feeds (R5: 17.5%, R10: 24%, R15: 28%, R20: 31%) compared to lower cutting feed where R5, R10 and R15 are not significant compared to DGEBA samples and R20 showed a decrease of 13%. Higher cutting peaks (Figure 90 – a)) are noticed for rubber samples machined at higher feeds, which is attributed to higher chip thickness due to increased feed. At the same time, the measured cutting range is decreasing with increased rubber content at high cutting feeds (Figure 89 – b)), while there is no statistically significant difference in cutting force measurements between rubber samples machined at lower/ higher cutting feed. This highlights the fact that rubber toughening mechanism is not strain rate dependent at the loading rates induced by the input combination of feed and speed of the cutting tool. This aspect coupled with experimental evidence of the rubber toughening mechanism is thoroughly discussed in section 7.3.

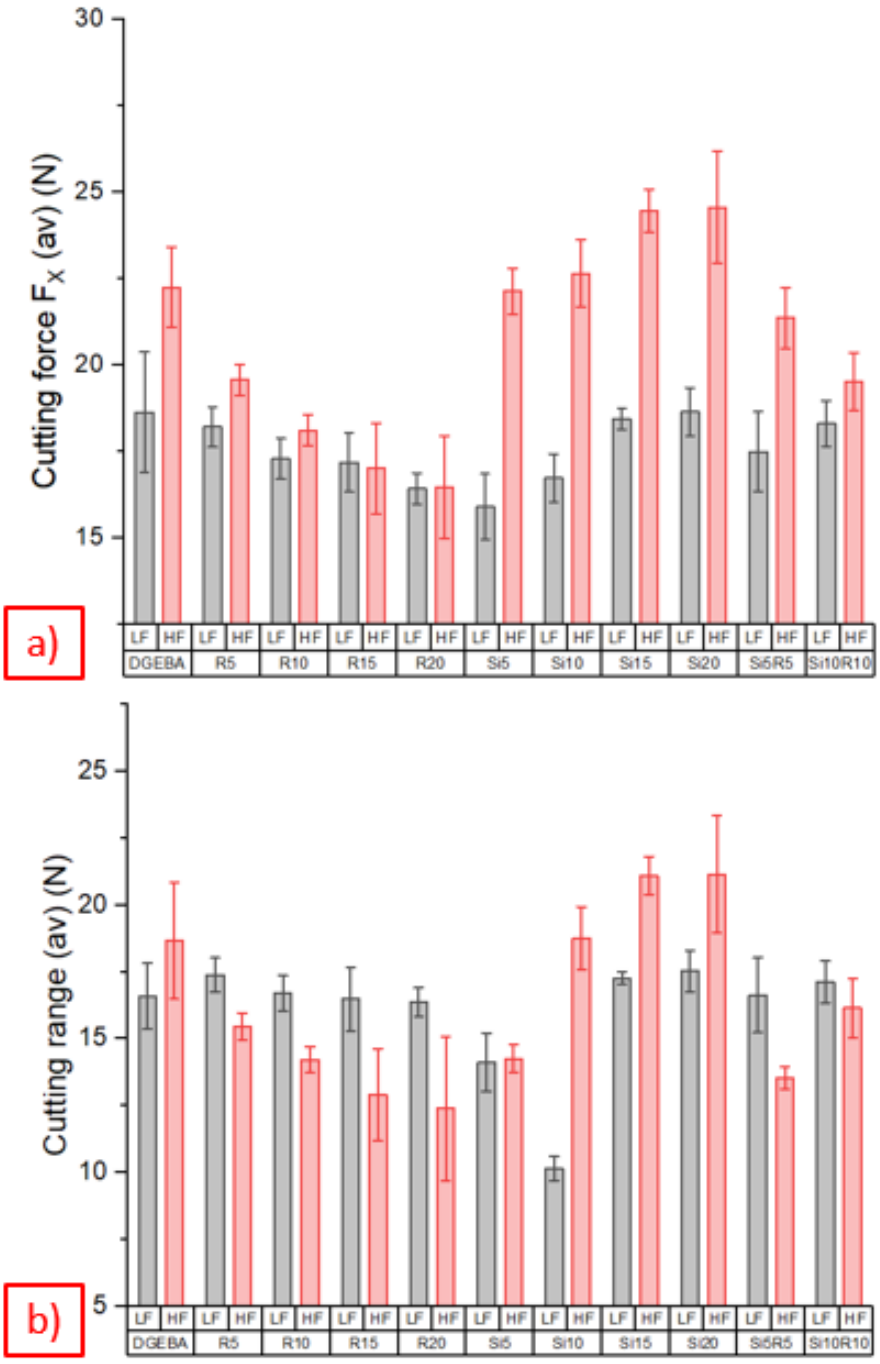

Figure 89 – Cutting force graphs where LF is Low Feed, 1140 mm/min, and HF is High Feed 1900 m/min a) Cutting force average b) Cutting range average

Average cutting force (Figure 89 – a)), lower and higher peak average (Figure 90 – a, b)) is increasing with silica content for both cutting feeds. However, at the lower cutting feed, the cutting force average is within the standard deviation of DGEBA sample. At higher feed rate, the cutting force average is increased compared to control sample (Si5: 0.44% , Si10: 1.33% , Si15: 7.14% , Si20: 7.5%). A higher % increase in cutting force is noticed between

silica samples machined at a low vs high cutting feed (Si5: 29.41% , Si10: 35.23% , Si15: 42.36% , Si20: 46.11%). Similar significant increasing trend is noticed for cutting range (Figure 89 – b)), lower/ higher peak averages (Figure 90 – a, b)). This behaviour at higher cutting feeds could be attributed to the following: (i) increased chip thickness due to the increased feed and (ii) interaction of epoxy matrix/ silica nanoparticles at higher strain rates, which is discussed in-depth in section 7.3. Overall, silica samples experienced higher cutting forces (22.5 to 25N) at the higher cutting feed compared to rubber samples (16 to 18N), while at lower cutting feed no statistically significant conclusion could be established.

It is noticed that for the Si5R5 sample there is a 22.6 % increase in cutting force when feed is increased, while for Si10R10 sample is 11.23 %, which is a similar trend to the cutting force evolution of samples containing only rubber as particle reinforcement. This demonstrates that at higher rubber concentrations of the 'hybrid' sample and increased feed, rubber toughening mechanism governs the failure mechanism, while silica does not have a significant effect. This behaviour was previously identified in orthogonal cutting of 'hybrid' epoxy/ CFPRs and discussed thoroughly in section 5.1 and 6.2. The chip formation process was mainly influenced by the presence of rubber microparticles, rather than silica nanoparticles in the 'hybrid' sample.

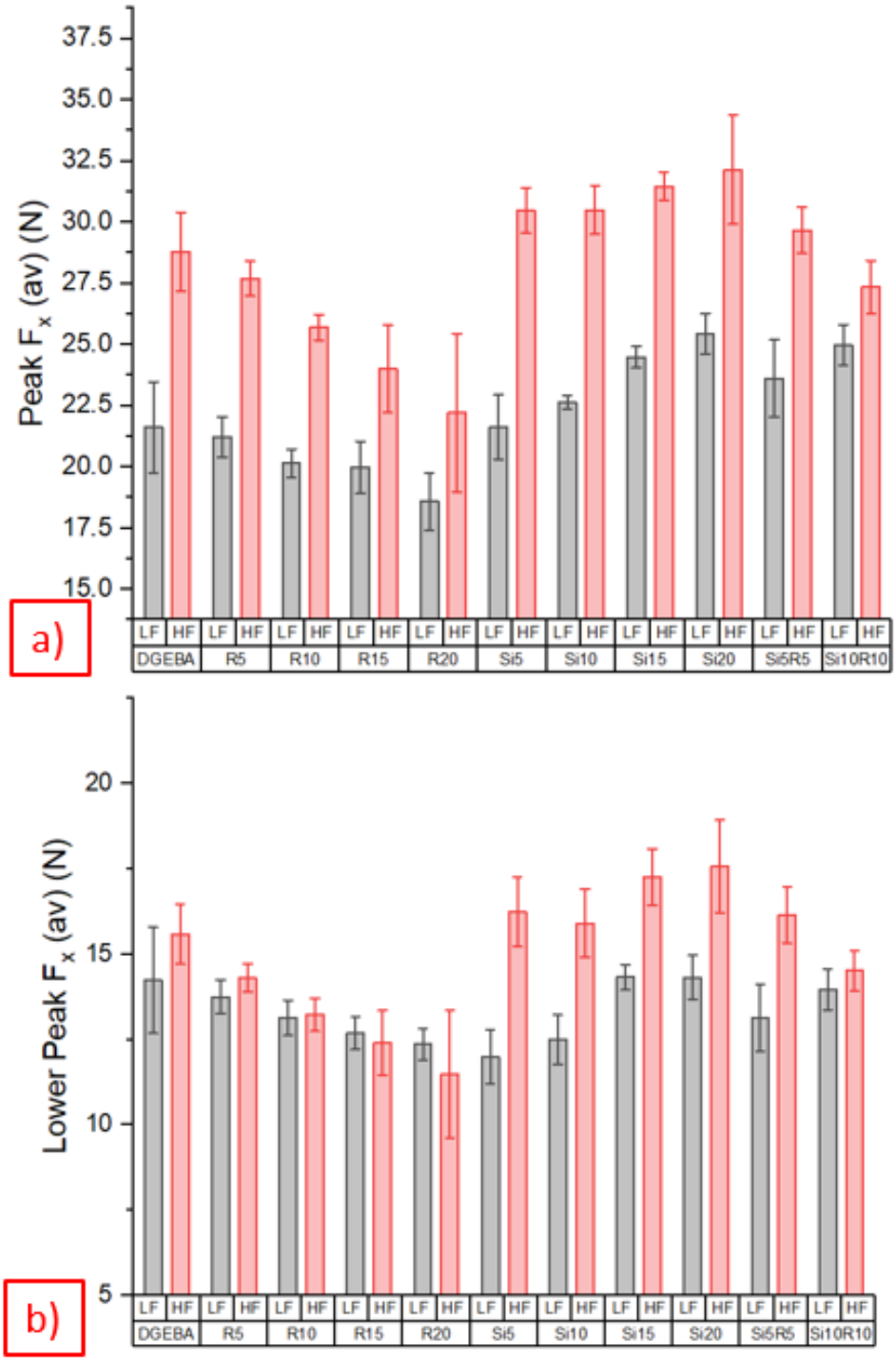

Figure 90 - Cutting force graphs where LF is Low Feed, 1140 mm/min, and HF is High Feed 1900 m/min a) Average of higher peak of cutting force b) Average of lower peak of cutting force

The calculated specific cutting power (Figure 91), U_T (N/mm^2), showed similar behaviour to the cutting force graphs. This is expected as U_T is calculated using on the cutting force behaviour (section 3.6.2). U_T is decreasing with the increase of rubber content, while silica

showed an inverse trend for both cutting feeds. As F_x is the dominant factor in the calculation of U_T, the combination of rubber/silica content and high/ low feed has a significant effect on the calculated specific power.

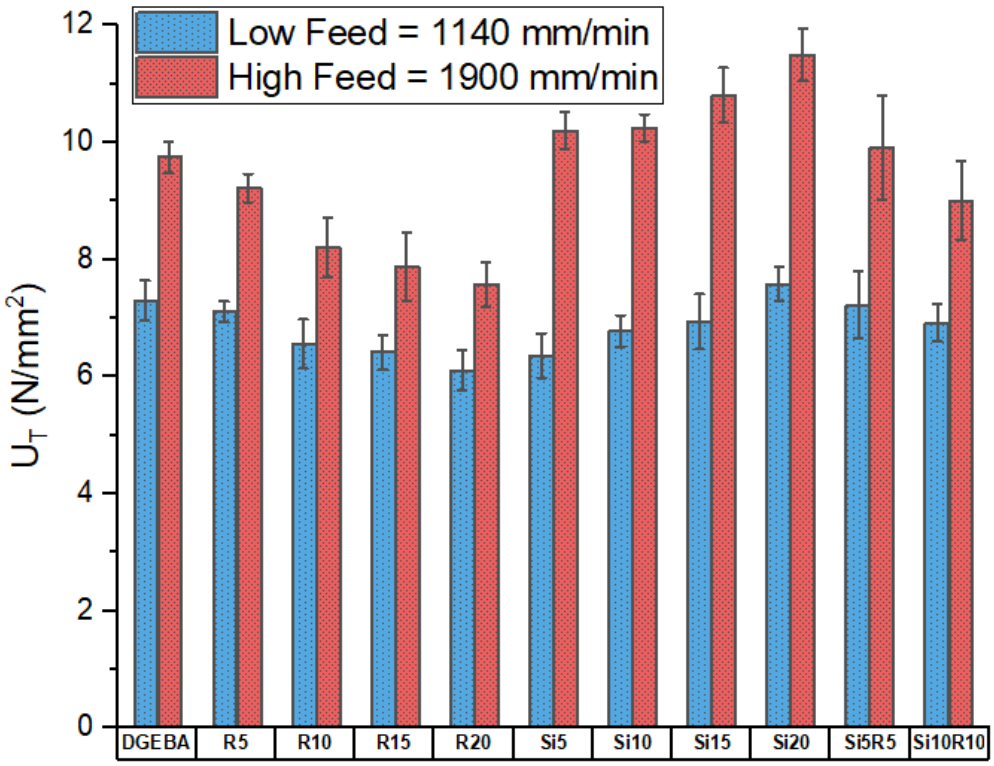

Figure 91 – Specific cutting power for edge trimming of CFRP samples Surface metrics characterisation

Figure 92 shows the variation of S_a parameter which was found to be statistically significant in the ANOVA results (Section 7.3). For the low cutting feed, S_a had a lower value than DGEBA for all particle modified samples. A sharp drop was measured in S_a value compared to DGEBA as follows: Si5: 28.57%, Si10: 22.31%, Si15: 26.72%, Si20: 17.14%, R5: 2.85%, R10: 3.01%, R15: 4.25%, R20: 14.28%, while 'hybrid' samples showed S_a values similar to silica samples (Si5R5: 28.32%, Si10R10: 16.94%). At the higher cutting feed, rubber samples experienced the lowest surface roughness, while silica and DGEBA had the highest values. This behaviour of DGEBA and silica modified samples for low/ high feed was previously found in the cutting force behaviour of edge trimmed samples (Figure 89 – a)) where cutting force is decreasing with rubber content at both low/high feeds, while at higher feed silica experienced high peaks.

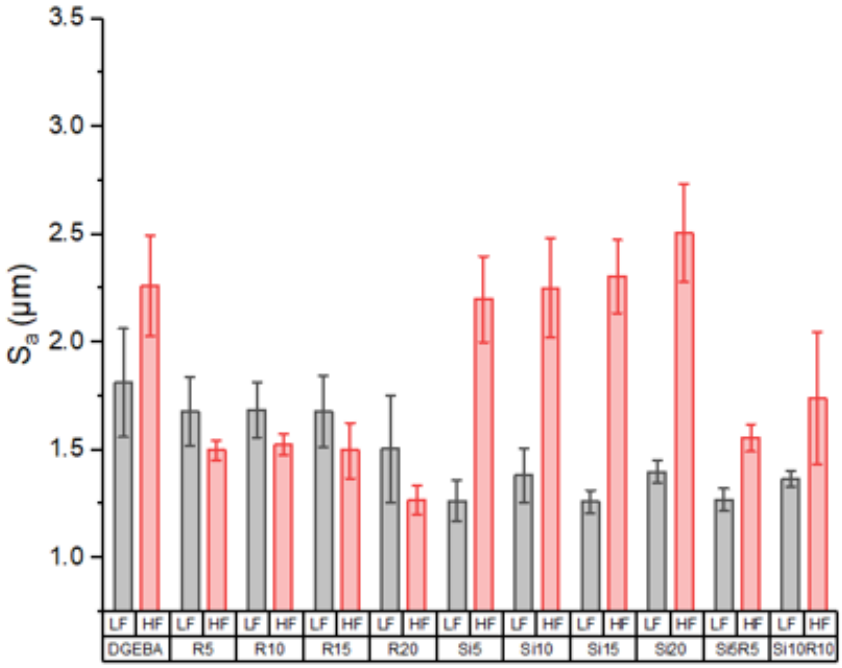

Figure 92 – Areal textural parameter S_a , Average height of selected area (µm)

To further investigate this behaviour, specific cutting power, U_T vs S_a for both cutting feeds is plotted in Figure 93 which shows the optimum necessary concentration which will provide the lowest specific cutting power and surface roughness. It is noticed that data points cluster together depending on reinforcement type and concentration. At the lower cutting feed, DGEBA experienced the highest S_a and U_T, while Si5 and R20 had a low of U_T and S_a. This might be attributed to a combination of the individual effect of particle reinforcement and a change in the chip formation process for each fibre orientation. An attempt to further explain this result is done in section 7.3, where experimental evidence of the machined surface is provided. At higher cutting feed, DGEBA and silica samples had the highest S_a and U_T as shown in Figure 93 – b). This is correlated with the reduced mobility of the polymer chains at higher strain rates [192], which increased the brittleness of the material and reduced the plastic deformation of the matrix, hence it produced a change in the material removal mechanism resulting in an increased surface roughness. As U_T is a function of cutting force, this explanation is valid for the identified cutting force shown in Figure 89. On the other hand, at the higher cutting feed, R20 sample showed the lowest Sa average (1.25 ± 0.12 µm) and U_T (7.56 ± 0.2 N/mm^2) that can be explained by the fact that rubber toughening mechanism facilitated the fracture energy dissipation,

ultimately limiting the machining induced damage. This was previously discussed in orthogonal cutting results, section 6.6 and further experimental evidence and assessment of the edge trimmed surface morphology is provided in section 7.3.

In this context, the R20 sample has the most favourable combination showing a low specific cutting power required which translates in a low energy consumption of the machine saving costs, a high feed which is translated in less time required for machining and a low surface roughness, which correlates with improved surface quality. At the same time, the combination and concentration of reinforcement particles needs to be taken into consideration in terms of mechanical properties based on the required application.

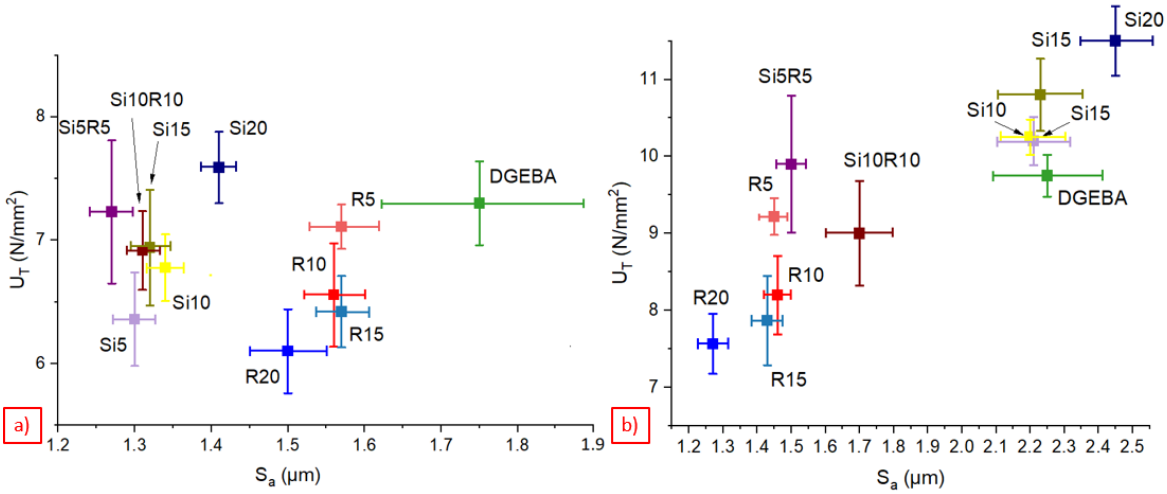

Figure 93 – Specific cutting power vs Sa for a) Low Feed b) High feed conditions

It has been previously concluded (section 6.5) that individual surface metrics are insufficient to characterise machining induced damage of CFRP samples machined under orthogonal cutting conditions. Figure 94 shows a graphical representation volumetric textural parameters which illustrate surface pits, cavities, valleys and high peaks identified in the CFRP machined surface. Figure 95 and Figure 96 show V_{mc}, V_{vc}, and V_{vv} parameters further used to characterise machining induced damage. V_{mc} shows a sharp increase with silica content compared to DGEBA sample for the higher feed (Si5: 0.92 %, Si10: 1.44 %, Si15: 3.84%, Si20: 7.69%) that is similar to the trend observed in the cutting force and S_a measurements. Silica samples experienced the highest % difference at low and high cutting feeds for V_{mc} parameter (Si5: 61.9%, Si10: 56.29%, Si15: 68.75%, Si20: 61.15%). This suggests a surface with areas of uncut fibres which protrude over the machined surface.

On the other hand, V_{mc} reduces with increasing the rubber content for both cutting feeds, which suggests a surface with limited amount of uncut fibres. The 'hybrid' Si10R10 sample showed a low value (LF: 1.36, HF: 1.38 ml/m^2) for both feeds. This suggests that the feed does not have a significant effect on the V_{mc} volumetric parameter. V_{vc} and V_{vv} parameters (Figure 96) which are representative for surfaces with voids and peak valleys show an increasing trend with silica content at high feed machining. It will be presented that these particular surface features are found for the 135° fibre orientation (section 7.3). This trend was previously found for cutting forces and surface roughness, while at the lower feed rate this effect is not visible. This suggest that strain rate induced by the higher feed rate significantly affects the chip formation process for silica samples at 135° fibre orientation. On the other hand, V_{vc} parameter decreased with increasing rubber content for both cutting feeds, while the lowest values were recorded for silica modified samples at the lower cutting feed. These results are correlated with surface morphology micrographs and are further discussed in section 7.3.

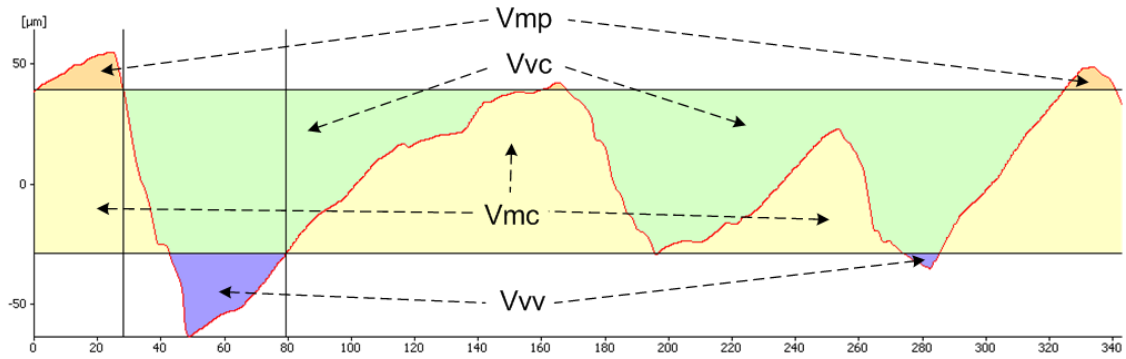

Figure 94 – Profile visualisation of volumetric textural parameters [175]

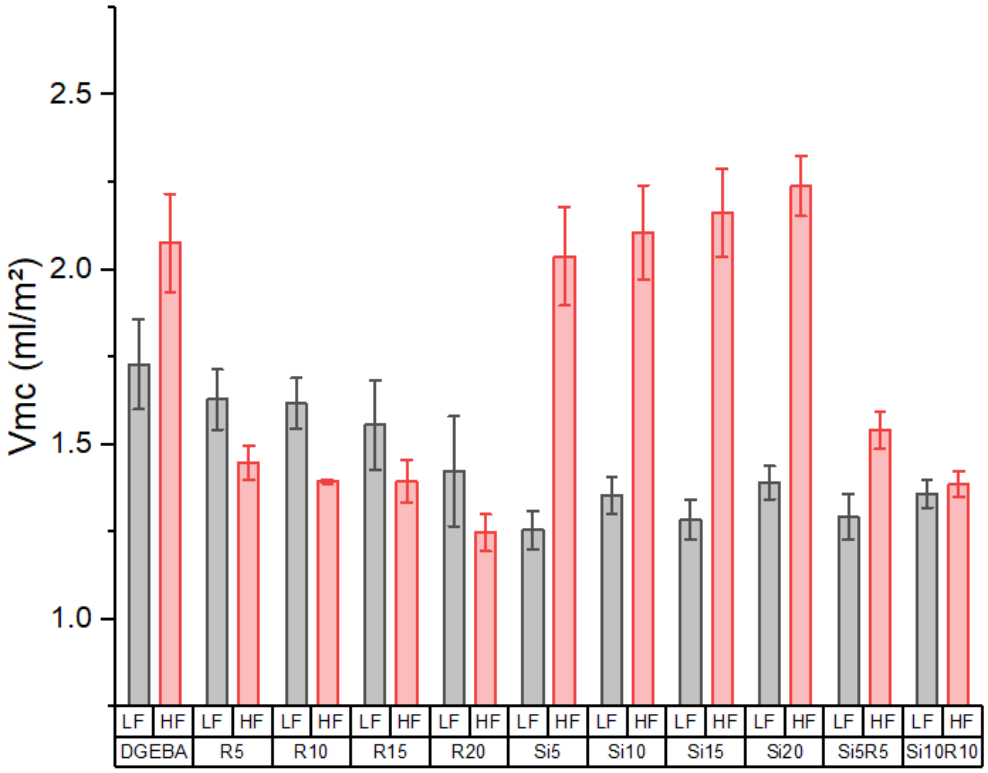

Figure 95 – Volumetric textural parameters for edge trimmed surface: Core material volume of the topographic surface (ml/m²)

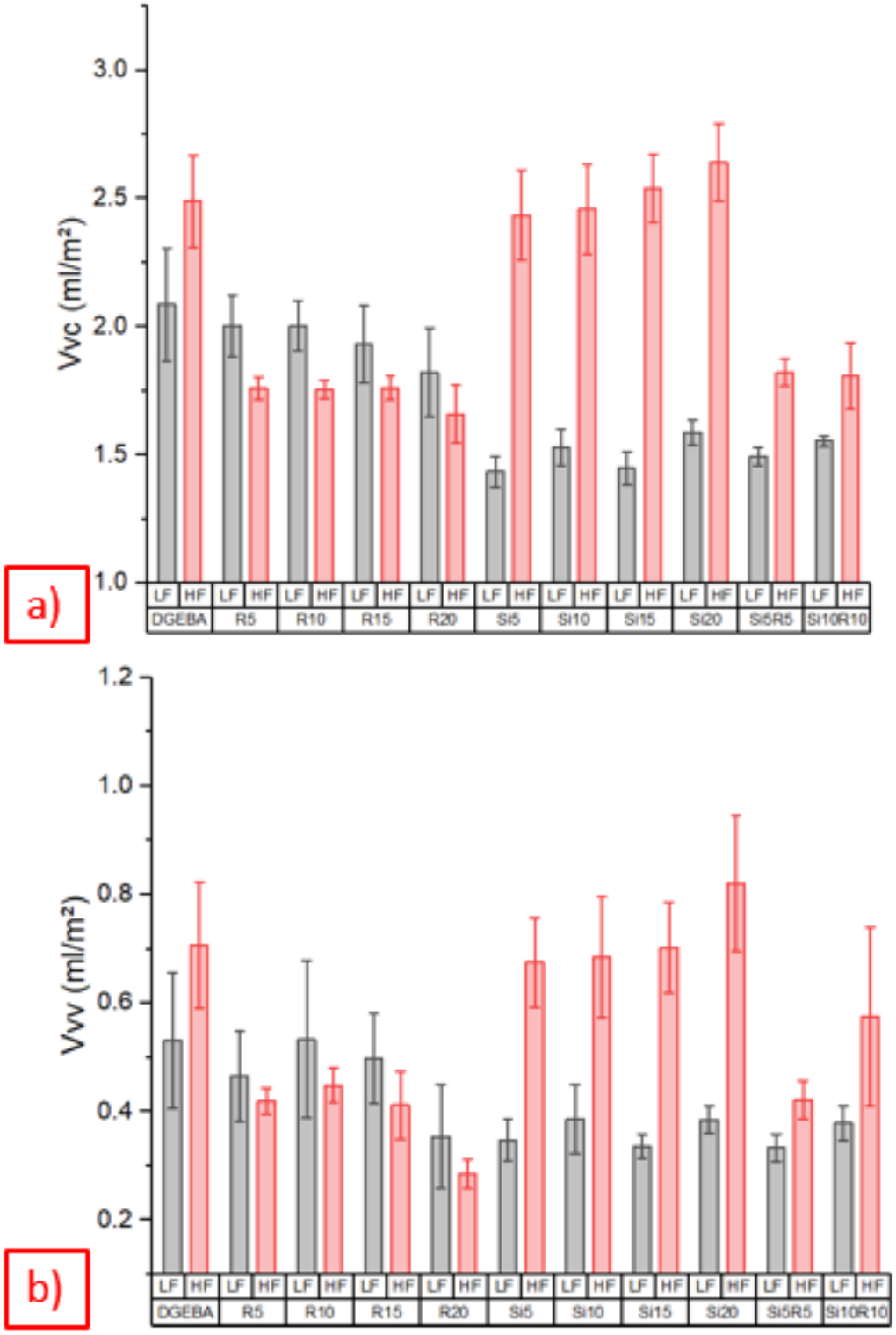

Figure 96 – Volumetric textural parameters for edge trimmed surface a) Core void volume of the surface (ml/m²) b) Valley void volume of the surface (ml/m²)

7.3 Analysis of variance results

ANOVA results of the DoE presented in Table 21 are shown in Figure 97. The r^2 of the response for each interaction is attached to Appendix E. Cutting forces and surface metrics are used as responses, where the inner grey area shows statistically significant factors (p – value < .05). The interactions between %Rubber * %Silica and %Rubber * %Silica * Feed could not be estimated and were removed from the model as not enough cutting tests were done as proposed in Section 3.6.4 due to limited resources in manufacturing of CFRP test samples. Only the 2-way interactions of %Rubber * Feed and %Silica * Feed were used along with linear of %rubber, %silica and Feed. The cutting force, F_x, is found to be statistically significant (p – value < 0.001) for all of the used factors. This is similar to orthogonal cutting results of both polymer and CFRP modified samples, where the difference in cutting force magnitude between modified and bulk epoxy was statistically significant (Figure 65 and Figure 73). The surface parameters S_a and S_q (root-mean-square heigh of selected area) was found statistically significant for all factors (p – value < .05). However, S_p (maximum peak height of selected area) was found non-statistically significant, while S_v had % silica and % rubber/feed factors as non-statistically significant (p – value > .05). The Kurtosis and Skewness parameters S_{ku} and S_{sk}, respectively were found non-statistically significant (p – value > .05), which highlights the fact that these types of parameters which were used to characterise the damage in previous CFRP machining literature [171], [186] and current orthogonal cutting study (Figure 83), are not useful to create a statistical link between particle concentration, cutting feed and machining induced damage in an edge trimming operation. On the other hand, S_k (core roughness depth) and S_{vk} (mean depth of the valleys below the core material) showed a statistically significant response (p – value < .05) which highlights those craters created under the machined surface level have a different morphology depending on the interaction of factors. This aspect is further discussed in surface morphology section, 7.3. Moreover, volumetric parameters such as V_{mc} (core material of the topographic surface, ml/m^2), V_{vc} (Core void volume of the surface ml/m^2) and V_{vv} (valley void volume of the surface ml/m^2) showed a statistically significant response (p – value < 0.001), which could potentially highlight a difference in the volume of the created craters due to the extent of fibre pullout in the 135° fibre orientation.

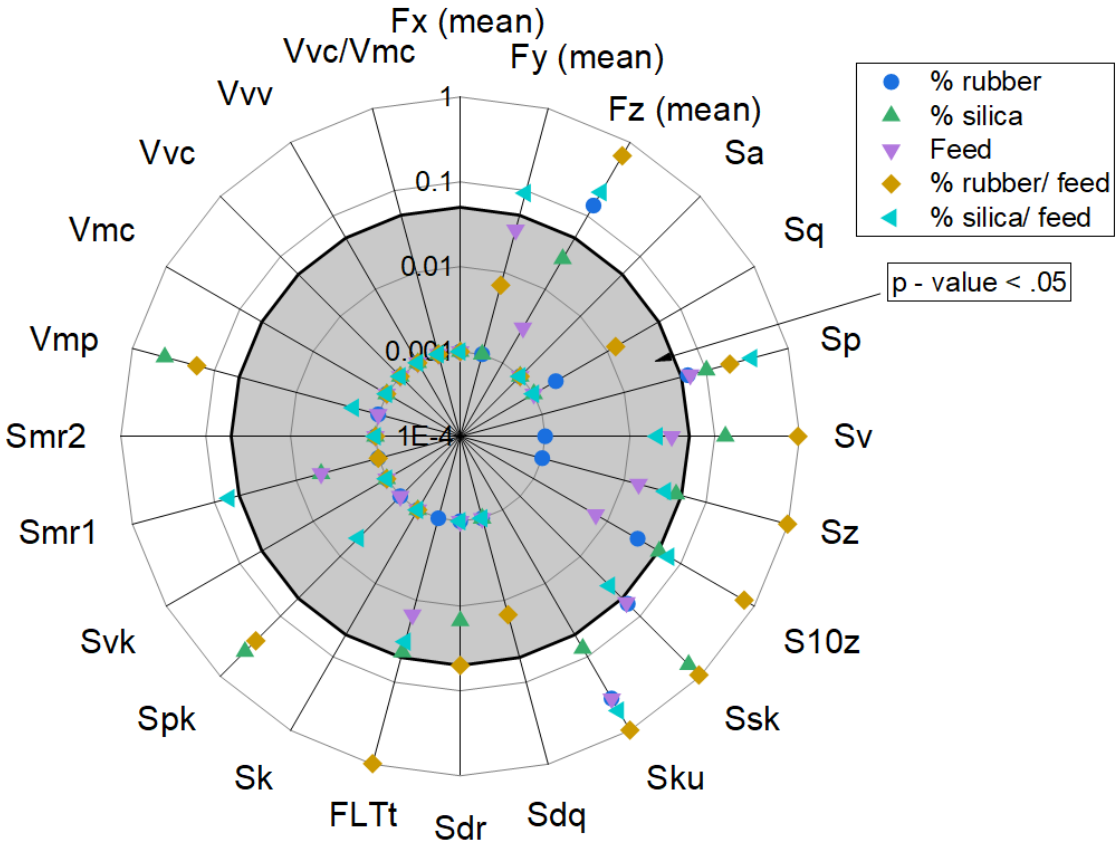

Figure 97 – Spyder plot of ANOVA results (y – scale is logarithmic for better representation of the results)

7.4 Surface morphology assessment of the edge trimmed CFRP samples

An example of SEM micrograph of the machined surface is shown in Figure 98. The global view is in line with previous literature [22], [74], [116], [171], [173] with significant matrix smearing occurring in the 90° fibre orientation. Surface morphology features for each fibre orientations of the edge trimmed samples are linked with the cutting mechanism identified in orthogonal cutting conditions and discussed in section 6.4: 0° fibre orientation – Type I chip formation, 45° fibre orientation – Type III chip formation where fibre spring back is noticed (Figure 98), 90° fibre orientation – Type IV chip formation, 135° fibre orientation – Type V chip formation. The maximum surface damage is due to the formation of craters below the cut surface in the 135° fibre orientation as shown in Figure 99. It is noticed that the size and depth of craters are increasing with feed for DGEBA and silica samples, while micrographs of samples with rubber fillers do not show a significant difference. These

qualitative results are linked with the quantitative volumetric parameters discussed in section 0, which highlights the fact that localised SEM observations are representative to overall machined surface assessment.

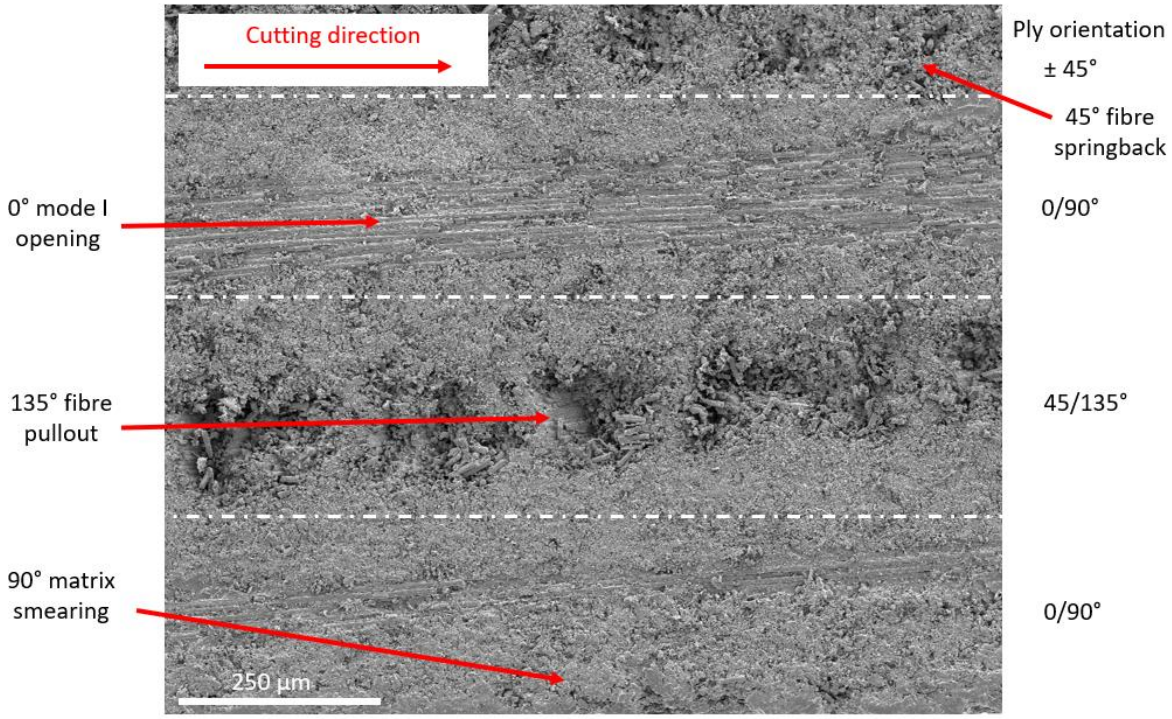

Figure 98 – SEM micrograph of the machined surface for DGEBA sample at Low Feed cutting conditions

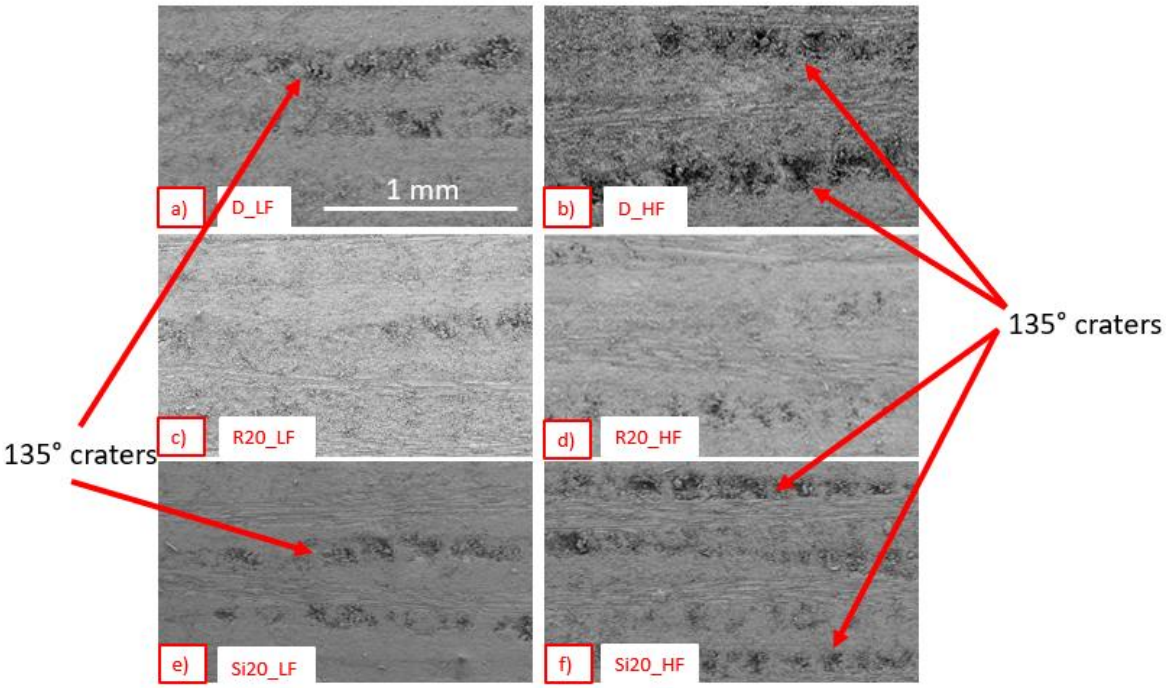

Figure 99 – Example of craters formed in the 135° fibre orientation machined at both Low/High cutting feeds a) D_LF b) D_HF c) R20_LF d) R20_HF e) Si20_LF f) Si20_HF

The cutting force evolution for one tool rotation are shown to be correlated with the identified machined surface patterns for 135° fibre orientation as shown in Figure 100. A full tool rotation at a low cutting feed covers a linear distance of 120 µm (Figure 100 – a)), while at high feed, 200 µm (Figure 100 – b)). Based on the cutting force evolution in section 7.2, Figure 88, the size of the craters is linked with a full tool rotation. This behaviour was observed for all cutting conditions and materials used. The machined surfaces of 0°, 45° and 90° plies for all CFRP samples showed features corresponding to Type I, III and IV chip formation process discussed in section 6.4. On the other hand, the machined surface of 135° showed a significant difference in the size of the measured craters which corresponds to Type V chip formation process. As the cutting edge contacts the fibres, the rotational motion of the cutting edge results in uplifting of the fibres and hence develops a bending moment. Fibres then fractures under the tensile stress due to the bending moment, which leads to material pull out (Figure 99) and the formation of craters below the cut surface. At the same time, this phenomenon is also affected by the combination of cutting feed, fibre/matrix adhesion, particle/epoxy adhesion, reinforcement type and the efficiency of particle toughening mechanism.

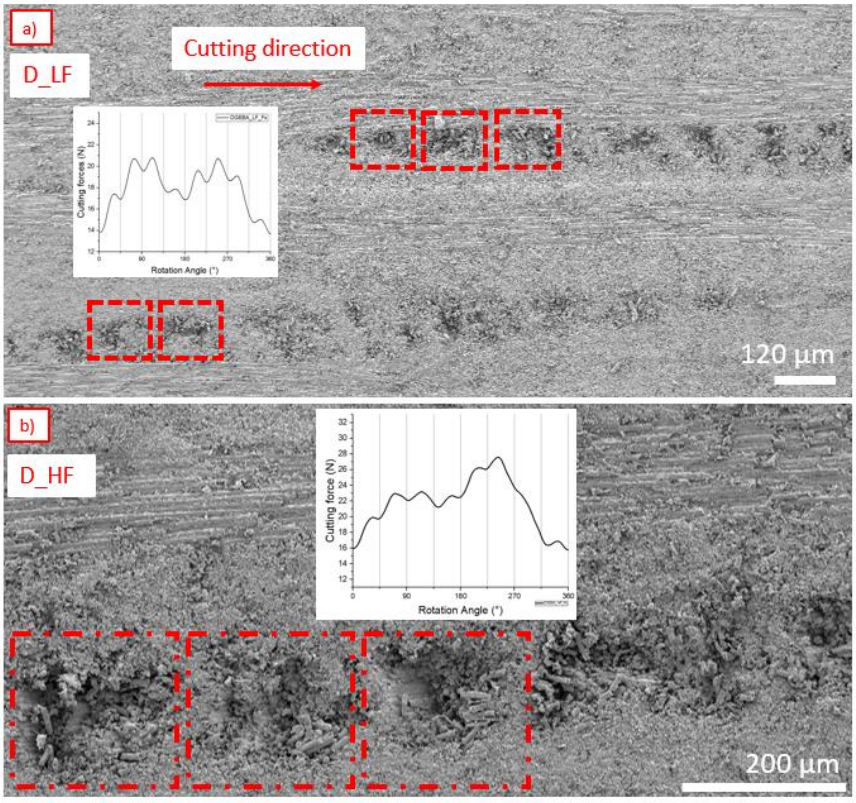

Figure 100 – SEM micrographs coupled with cutting force behaviour for one tool rotation a) DGEBA at Low feed conditions b) DGEBA at High feed conditions

At the higher cutting feed, DGEBA samples experienced higher cutting peaks (Figure 100 – b)). The higher cutting peaks are to the following: (i) the increased stiffness of the sample due to increase in strain rate, where ±45° fibre orientation plies are much more strain sensitive compared to the other [193], (ii) the debonding of fibre from matrix at higher strain rate, which leads to an increased bending of the fibres which subsequently create an increased chip load and increased cutting force. The increased feed results in an increased strain rate experienced by the epoxy matrix. When the bending achieves the critical failure value, the chip formed detaches from the machined surface shown by a significant drop in the cutting force graph (Figure 100 – a), b) - tool rotation 270° to 360°). Similar phenomenon is observed in the silica samples at low and high cutting feeds.

Figure 101 shows fibre – matrix debonding and pullout regions observed in the machined surface craters of 135° plies of Si20 samples. High magnification SEM micrographs show the presence of silica nanoparticles on the fractured matrix (Figure 101 – b)). As noted previously (section 6.6), the silica nanoparticles were not observed on the coated surfaces

of unmodified epoxy composite which were gold coated prior to SEM analysis. This shows that the identified particles are not an artefact of the applied gold coating. It is noticed that the debonding of silica nanoparticles is limited at high feed conditions (Figure 102). At high strain rates, the viscoelastic resin does not have enough time to fully deform due to reduced molecular mobility of the polymer chains [192]. This reduced molecular mobility at high strain rates could decrease the interaction between the resin and the silica nanoparticles [194], [195], which limits the plastic deformation of the epoxy matrix. The increased strength and stiffness due to presence of silica nanoparticles and high cutting feed leads to a statistical increase in measured cutting forces as discussed in section 7.2.

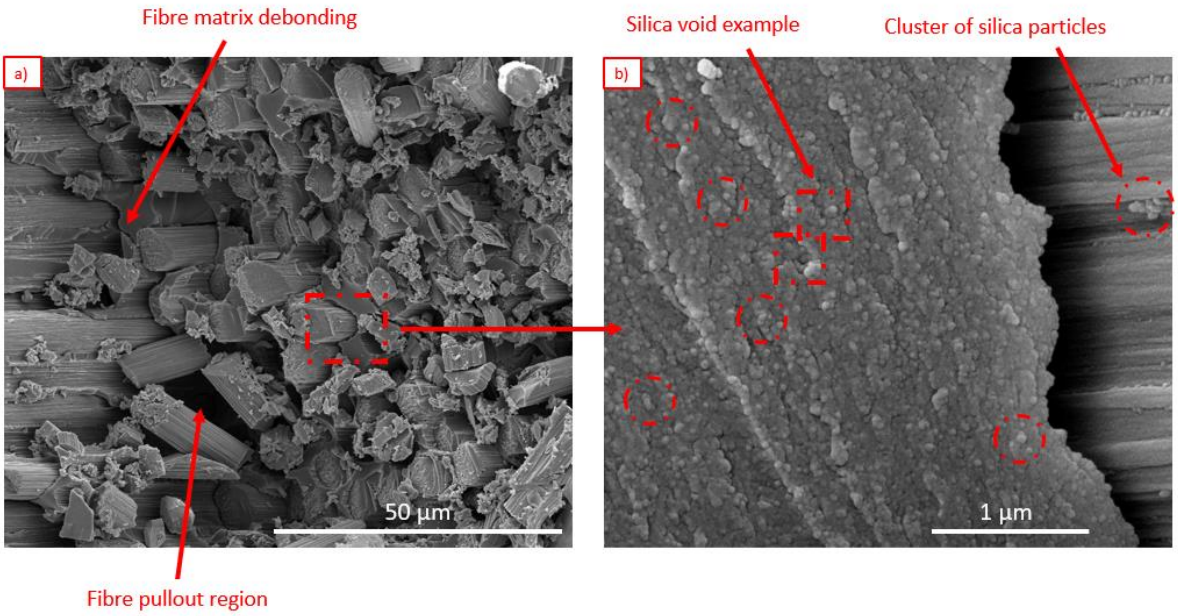

Figure 101 – Surface morphology of Si20 sample at high cutting feed a) Fibre – matrix debonding & fibre pullout region b) High-magnification of fibre – matrix debonding

The increased strength and stiffness due to presence of silica nanoparticles and high cutting feed leads to a statistical increase in measured cutting forces as discussed in section 7.2. However, at lower cutting feed, silica samples showed partial debonding (Figure 102 – a)) and lower cutting forces (Figure 89 – a)) compared to DGEBA sample. This may be attributed to the fact that at low strain rates, the viscoelastic resin has enough time to deform [194]. This allows the transfer of forces from the matrix to the higher strength and higher stiffness of silica nanoparticles and carbon fibres. However, at the same time, no evidence of epoxy plastic deformation was found for silica modified samples and fibre –

matrix debonding is found to be the dominant mechanism(Figure 101), which highlights the fact that the failure mechanism is dominated by interface failure. Therefore, the behaviour of silica samples at low feed conditions needs to be further investigated to be able to draw solid conclusions on the observed experimental evidence.

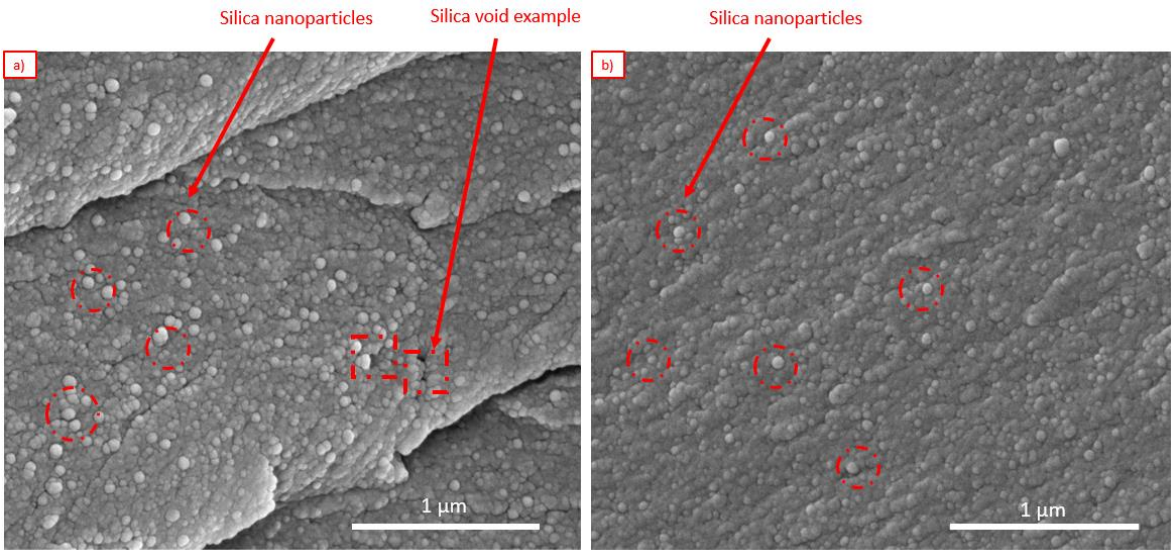

Figure 102 – High-magnification SEM image of machined Si20 sample showing behaviour of silica nanoparticles a) Low feed conditions b) High feed conditions

High-resolution SEM micrographs of the machined surface of rubber samples (Figure 103) show that particles cavitate at both low/ high cutting feeds. The average diameter of the dimples observed in Figure 103 – b) is 0.93 ± 0.134 µm, while the individual diameter of CTBN particles is 0.54 ± 0.15 µm [8]. This shows that cavitation process as part of the rubber toughening mechanism took place. The change in feed does not have a noticeable effect on the machined surface micrographs as the size of the voids created, the plastic deformation of the matrix, the number of particles that cavitate does not significantly change. It has been previously reported that changing the loading rate by a factor of 200 in fracture toughness tests produced a modest change in the behaviour of CBTN modified epoxy samples [196]. Moreover, fibres are well attached to the matrix at both cutting feeds, which highlights that fibre-matrix interface failure did not occur in rubber-modified samples. The rubber toughening mechanism allows the dissipation of energy within the CFRP material which is shown by the cavitation artefacts on the epoxy matrix which confirms the epoxy matrix has been plastically deformed (Figure 103 – b)). This was

previously found in orthogonal cutting tests (section 6.6) and ultimately limits the extent of damage generated by fibre-matrix debonding and fibre pullout in the 135° fibre orientation. This is correlated with the low cutting forces (Figure 89), specific cutting power (Figure 91), surface roughness (Figure 92) and volumetric parameters (Figure 95 and Figure 96) recorded for rubber modified samples at both cutting feeds.

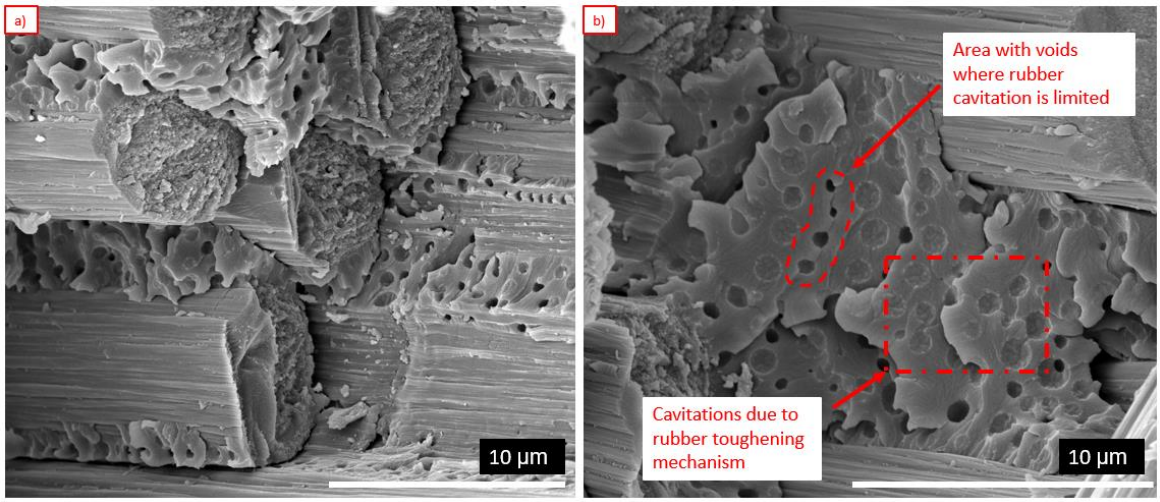

Figure 103 – High-resolution SEM micrographs of R20 machined surface a) Carbon fibres well bonded to the epoxy matrix at low cutting feed b) High-magnification example of plastic deformation due to cavitation process at high cutting feed

7.5 Summary

The addition of rubber microparticles and silica nanoparticles to a modified epoxy CFRP affected the material removal mechanism and the subsequent machining induced damage during edge trimming of CFRP samples. ANOVA results showed that the silica nanoparticles and rubber particles combined with a low/ high cutting feed are statistically significant on cutting force, areal and volumetric textural parameters. Silica modified samples experienced high peaks in the cutting force behaviour, which were corelated to the brittleness and stiffness of the material, while DGEBA and rubber samples produced lower cutting peaks. A decreasing trend in cutting force is found for rubber samples (R5: 17.5%, R10: 24%, R15: 28%, R20: 31%), while silica showed an increasing trend (Si5: 0.44% , Si10: 1.33% , Si15: 7.14% , Si20: 7.5%). Moreover, a higher % increase in cutting force is noticed between silica samples machined at a low vs high cutting feed (Si5: 29.41% , Si10: 35.23% , Si15: 42.36% , Si20: 46.11%). This is associated with the increased stiffness of the sample

due to increase in strain rate and the debonding of fibres from matrix at higher strain, which resulted in an increased bending of the fibres which subsequently created an increased chip load and increased cutting force.

Surface roughness, S_a of particle modified samples showed a lower value than DGEBA for the low cutting feed. The highest decrease was experienced by silica modified samples followed by rubber samples, while 'hybrid' samples showed S_a values similar to silica samples. At the higher cutting feed, rubber samples experienced the lowest surface roughness, while silica and DGEBA had the highest values. Similar trend was found for the volumetric textural parameters, which were found representative for the 135° fibre orientation. V_{mc} showed a linear increase with silica content compared to DGEBA sample for the higher feed. Silica samples experienced the highest % difference at low and high cutting feeds for V_{mc} parameter. This suggests a surface with areas of uncut fibres which protrude over the machined surface. On the other hand, V_{mc} showed a decrease with increasing the rubber content for both cutting feeds, which suggests a surface with limited amount of uncut fibres. V_{vc} and V_{vv} parameters, which are representative for surfaces with voids and peak showed an increasing trend with silica content at high feed machining. On the other hand, V_{vc} parameter decreased with increasing rubber content for both cutting feeds.

Rubber toughening mechanism ensured an efficient energy dissipation mechanism limiting crack propagation, fibre – matrix debonding and the extent of subsurface damage. On the other hand, due to high strain rate effect the debonding of silica nanoparticles did not occur which resulted in fibre pullout and fibre – matrix debonding which ultimately increased measured cutting forces, surface textural metrics and machining induced damage.

8 CONCLUSIONS & FUTURE WORK

8.1 Conclusions

The aim of this thesis was to understand and expand the knowledge on the effect of particulate reinforcements on chip formation process and machining induced damage of modified epoxy CFRPs. The experimental results generated novel data which helped the understanding of material removal mechanism in the machining of modified epoxy CFRPs and created a statistical link between the presence of particulate reinforcements, chip formation process and machining induced damage.

In the orthogonal cutting of epoxy modified samples it was determined that rubber modified epoxies experienced the highest cutting force, while no significant difference was found between DGEBA vs silica vs 'hybrid' Si10R10 epoxy. Experimental evidence showed that the chip formation process is governed by a series of intermittent fractures occurring in front of the cutting tool. Chip formation in DGEBA and silica-modified epoxy produced discontinuous chips with large cracks at the machined surface and subsurface within the chip formation zone. This was linked with the low fracture toughness as measured for the brittle epoxies. On the other hand, rubber modified material produced a continuous curly chip due to large plastic deformation of material as the toughening mechanism of rubber microparticles was present. At the same time, the microcracks were constrained within the chip formation zone. The 'hybrid' Si10R10 epoxy experienced similar chip formation processes as rubber samples, while the mechanical properties (strength and tensile elastic modulus) were close to the bulk epoxy.

In the orthogonal cutting of epoxy modified CFRPs, the lowest average cutting force was recorded for rubber modified samples (R20: 103N, R10: 140N), followed by silica (Si20: 150N, Si10: 165N) and then by unmodified epoxy CFRPs (DGEBA: 183N). Rubber modified samples showed a stable cutting force, with regular oscillations, compared with the higher, more random oscillations experienced by unmodified and silica reinforced specimens. The presence of rubber microparticles increased the elastic recovery of the material, which resulted in the largest springback measured for all samples. The low magnitude of cutting forces was correlated with the lower depth of cut measured and reduced subsurface

damage for rubber-modified samples. Rubber modified samples (R20) show the least subsurface damage as measured by depth of damage (75% decrease for 45°plies, 66% decrease for 90° plies and 21% decrease for 135° plies) and measured areal damage (77% decrease for 45°plies, 60% decrease for 90° plies and 64% decrease for 135° plies) compared to DGEBA samples. A 50.8% decrease in surface craters is found between R20 and DGEBA samples in 135° plies. Surface metrics were found to be in good agreement with subsurface damage results, however, surface metric assessment of the machined surfaces is insufficient to fully characterise damage occurring during cutting. These results were linked to the particle toughening mechanism, which was found to take place during cutting, as particle cavitation for rubber microparticles and debonding for silica nanoparticles.

In edge trimming of epoxy modified CFRP samples, ANOVA results showed that the silica and rubber particles combined with a low or high cutting feeds are statistically different when comparing cutting force; specific areal and volumetric textural parameters. This represented a starting point in analysing the individual behaviour of samples based on reinforcement type and concentration. Silica modified samples experienced large amplitude peaks in the cutting force behaviour, which were correlated to the brittle and stiff nature of the material, while DGEBA and rubber samples produced lower amplitude peaks. A decreasing trend in cutting force is found for rubber samples, while silica showed an increasing trend.

Surface roughness, S_a, of the particle modified samples was lower for DGEBA at low cutting feed (HF: 1900 mm/min, S_a: 2.25 µm, LF: 1140 mm/min, S_a: 1.62 µm). The highest decrease in S_a was experienced by silica modified samples followed by rubber samples, while 'hybrid' samples showed S_a values similar to silica samples. At the higher cutting feed, rubber samples experienced the lowest surface roughness, while silica and DGEBA had the highest values. This behaviour of DGEBA and silica modified samples for low/ high feed was previously found in the cutting force behaviour of edge trimmed samples where cutting force is decreasing with rubber content at both low/high feeds, while at higher feed silica experienced high peaks. Similar trend was found for the volumetric textural parameters, which were found representative for the 135° fibre orientation. V_{mc} showed

a linear increase with silica content compared to DGEBA for the higher feed. Silica samples experienced the highest % difference at low and high cutting feeds for V_{mc}. V_{mc} and V_{vc} showed a decrease with increasing rubber content for both cutting feeds. The presence of rubber particles significantly limits the machining induced damage generated in the 135° plies, which are reported to create the greatest extent of damage in machining of CFRPs.

R20 sample showed the most favourable combination of specific cutting power, U_T and resulting surface roughness, S_a. Calculated U_T had a low value which translated in a low energy consumption during machining saving machining costs, while the higher feed (1900 mm/min) translated into less time required for the machining and the lowest values of measured surface roughness, which is correlated with improved surface quality. These initial statistically significant results coupled with the knowledge generated in understanding the effect of particulate reinforcements on the mechanics of chip formation process in machining of CFRPs will enable engineers and designers to create a trade-off between filler properties vs CFRP material properties vs machining induced damage leading towards damage-free composite machining.

8.2 Future work

Based on the experimental work conducted in this thesis, it was concluded that the chip formation process of particle modified epoxy CFRPs is affected by the particle reinforcement failure mechanism in both orthogonal cutting and industrial level machining conditions. As woven materials were used and smearing was present on the machined surfaces for 0°, 45° and 90° fibre orientation plies, experimental evidence could not conclude which fibre orientation and their individual machining induced damage is affected the most by the presence of reinforcement particles. Therefore, a UD fibre architecture should be used in further studies to quantify the effect of reinforcement particles on cutting force responses and machining induced damage for each fibre orientation. The experimental results can be further incorporated in multiscale modelling studies which will include the effect of particle reinforcements in the material removal mechanism at both micro and macro scale level. This will be able to provide high-quality characterisation of the chip formation process and machining induced damage of particulate modified composites.

The aim of this thesis was the study of the effect of particle reinforcements of modified epoxy CFRPs in machining conditions. Fresh cutting tools were used for all machining trials in order to avoid any kind of tool wear which could possibly lead to higher extent of damage and misleading information on cutting forces, surface and subsurface damage attributed to the presence of particulate fillers. Therefore, future studies should focus on the effect of particulate modified epoxy CFRPs on tool wear for various machining operations. The premature failure of the HSS tools in the orthogonal cutting experiment for trial testing of UD laminates was also discussed. Therefore, new tools should be manufactured from a material with a higher hardness (i.e., solid carbide or diamond coated tools), which will allow the study of chip formation process of UD laminates at a micro-scale level without the issue of tool failure.

The cutting rig could be modified to measure the cutting forces in x-direction that will help to investigate the spring back effect of the fibres in 45° and 90° orientation. To better understand the effect of higher cutting speeds on edge trimming operations, a spindle attachment can be connected to existing CNC router to increase the cutting speed and maintain the cutting stability at the same time. This will result in a higher strain rate effect which could possibly affect the failure mechanism of the particle reinforcements, thus affecting the material removal mechanism and subsequent machining induced damage. Moreover, experimental adjustments should be done to measure the temperature in future CFRP machining studies, which can be used as a validation in thermo-mechanical machining modelling studies.

Additionally, it would be important to know whether the particulate fillers interact differently with different matrix and fibre systems that require a different CFRP manufacturing method which will overcome the limitations imposed by the RTM and VARTM manufacturing techniques. The T300 fibre used in this study is widely available and cost effective, however the intermediate modulus and high modulus fibres are available which would change the generated cutting forces.

9 REFERENCES

[1] C. R. C. EADS Deutschland GmbH, “The research requirements of the transport sectors to facilitate an increased usage of composite materials Part I: The Composite Material Research Requirements of the Aerospace Industry.” 2004.

[2] A. J. Kinloch, A. C. Taylor, M. Techapaitoon, W. S. Teo, and S. Sprenger, “From matrix nano- And micro-phase toughening to composite macro-properties,” *Philos. Trans. R. Soc. A Math. Phys. Eng. Sci.*, vol. 374, no. 2071, 2016, doi: 10.1098/rsta.2015.0275.

[3] R. Bagheri, B. T. Marouf, and R. A. Pearson, “Rubber-toughened epoxies: A critical review,” *Polym. Rev.*, vol. 49, no. 3, pp. 201–225, 2009, doi: 10.1080/15583720903048227.

[4] D. Carolan, A. Ivankovic, A. J. Kinloch, S. Sprenger, and A. C. Taylor, “Toughened carbon fibre-reinforced polymer composites with nanoparticle-modified epoxy matrices,” *J. Mater. Sci.*, vol. 52, no. 3, pp. 1767–1788, 2017, doi: 10.1007/s10853-016-0468-5.

[5] T. H. Hsieh, A. J. Kinloch, K. Masania, A. C. Taylor, and S. Sprenger, “The mechanisms and mechanics of the toughening of epoxy polymers modified with silica nanoparticles,” *Polymer (Guildf).*, vol. 51, no. 26, pp. 6284–6294, 2010, doi: 10.1016/j.polymer.2010.10.048.

[6] B. B. Johnsen, A. J. Kinloch, R. D. Mohammed, A. C. Taylor, and S. Sprenger, “Toughening mechanisms of nanoparticle-modified epoxy polymers,” *Polymer (Guildf).*, vol. 48, no. 2, pp. 530–541, 2007, doi: 10.1016/j.polymer.2006.11.038.

[7] Y. Huang and A. J. Kinloch, “The role of plastic void growth in the fracture of rubber-toughened epoxy polymers,” *J. Mater. Sci. Lett.*, vol. 11, no. 8, pp. 484–487, 1992, doi: 10.1007/BF00731112.

[8] T. H. Hsieh, A. J. Kinloch, K. Masania, J. Sohn Lee, A. C. Taylor, and S. Sprenger, “The toughness of epoxy polymers and fibre composites modified with rubber microparticles and silica nanoparticles,” *J. Mater. Sci.*, vol. 45, no. 5, pp. 1193–1210,

2010, doi: 10.1007/s10853-009-4064-9.

[9] Y. Zeng, H. Y. Liu, Y. W. Mai, and X. S. Du, “Improving interlaminar fracture toughness of carbon fibre/epoxy laminates by incorporation of nano-particles,” *Compos. Part B Eng.*, vol. 43, no. 1, pp. 90–94, 2012, doi: 10.1016/j.compositesb.2011.04.036.

[10] H.-Y. Liu, G.-T. Wang, and Y. Zeng, “On fracture toughness of nano-particle modified epoxy,” *Compos. Part B Eng.*, vol. 42, no. 8, pp. 2170–2175, Dec. 2011, doi: 10.1016/J.COMPOSITESB.2011.05.014.

[11] S. Sprenger, “Improving mechanical properties of fiber-reinforced composites based on epoxy resins containing industrial surface-modified silica nanoparticles: Review and outlook,” *J. Compos. Mater.*, vol. 49, no. 1, pp. 53–63, 2015, doi: 10.1177/0021998313514260.

[12] H. Zhang, L. C. Tang, Z. Zhang, K. Friedrich, and S. Sprenger, “Fracture behaviours of in situ silica nanoparticle-filled epoxy at different temperatures,” *Polymer (Guildf).*, vol. 49, no. 17, pp. 3816–3825, 2008, doi: 10.1016/j.polymer.2008.06.040.

[13] R. K. Thakur and K. K. Singh, “Influence of fillers on polymeric composite during conventional machining processes: a review,” *J. Brazilian Soc. Mech. Sci. Eng.*, vol. 43, no. 2, 2021, doi: 10.1007/s40430-021-02813-z.

[14] B. Ellis, *Chemistry and technology of epoxy resins*. London: London : Blackie Academic & Professional, 1992, 1993.

[15] H. S. Katz, “Particulate Fillers BT - Handbook of Composites,” S. T. Peters, Ed. Boston, MA: Springer US, 1998, pp. 242–253.

[16] J. Baur and E. Silverman, “Challenges and Opportunities in Multifunctional Nanocomposites Structures for Aerospace Applications,” *MRS Bull.*, vol. 32, no. April, pp. 328–334, 2007.

[17] J. M. Garcés, D. J. Moll, J. Bicerano, R. Fibiger, and D. G. McLeod, “Polymeric nanocomposites for automotive applications,” *Adv. Mater.*, vol. 12, no. 23, pp. 1835–1839, 2000, doi: 10.1002/1521-4095(200012)12:23<1835::AID-ADMA1835>3.0.CO;2-T.

[18] D. Feldman, “Polymer nanocomposites in medicine,” *J. Macromol. Sci. Part A Pure Appl. Chem.*, vol. 53, no. 1, pp. 55–62, 2016, doi: 10.1080/10601325.2016.1110459.

[19] H. Tang and H. A. Sodano, “High energy density nanocomposite capacitors using non-ferroelectric nanowires,” *Appl. Phys. Lett.*, vol. 102, no. 6, p. 63901, 2013, doi: 10.1063/1.4792513.

[20] Q. Y. Tang, Y. C. Chan, N. B. Wong, and R. Cheungc, “Surfactant-assisted processing of polyimide/multiwall carbon nanotube nanocomposites for microelectronics applications,” *Polym. Int.*, vol. 59, no. 9, pp. 1240–1245, 2010, doi: 10.1002/pi.2855.

[21] L. Mishnaevsky, K. Branner, H. N. Petersen, J. Beauson, M. McGugan, and B. F. Sørensen, “Materials for wind turbine blades: An overview,” *Materials (Basel).*, vol. 10, no. 11, pp. 1–24, 2017, doi: 10.3390/ma10111285.

[22] J. Sheikh-Ahmad, *Machining of polymer composites*. Springer Verlag, 2008.

[23] M. Monoranu *et al.*, “A comparative study of the effects of milling and abrasive water jet cutting on flexural performance of CFRP,” in *Procedia CIRP*, 2020, vol. 85, pp. 274–280, doi: 10.1016/j.procir.2019.09.036.

[24] P. Cheremisinoff, *Handbook of Engineering Polymeric Materials*. Taylor & Francis, 1997.

[25] M. Rahman, S. Ramakrishna, and H. C. Thoo, “MACHINABILITY STUDY OF CARBON/PEEK COMPOSITES,” *Mach. Sci. Technol.*, vol. 3, no. 1, pp. 49–59, 1999, doi: 10.1080/10940349908945682.

[26] D. Hull, *An Introduction to Composite Materials*, 2nd ed. Cambridge : Cambridge University Press, 1996, 1996.

[27] S. W. Tsai, *Introduction to composite materials*. Westport, Conn.: Westport, Conn. : Technomic, 1980, 1980.

[28] T. W. Clyne, *An introduction to composite materials.*, Third edit. Cambridge, United Kingdom: Cambridge, United Kingdom : Cambridge University Press, 2019, 2019.

[29] U. of Sheffield, “Lecture Notes.” 2017.

[30] C. Soutis, “Fibre reinforced composites in aircraft construction,” *Prog. Aerosp. Sci.*, vol. 41, no. 2, pp. 143–151, 2005, doi: 10.1016/j.paerosci.2005.02.004.

[31] E. J. Barbero, *Introduction to composite materials design*, 2nd ed. Boca Raton: Boca Raton : Taylor & Francis, 2011, 2011.

[32] M. A. Karataş and H. Gökkaya, “A review on machinability of carbon fiber reinforced polymer (CFRP) and glass fiber reinforced polymer (GFRP) composite materials,” *Def. Technol.*, doi: https://doi.org/10.1016/j.dt.2018.02.001.

[33] S. Park, *Interface science and composites*, First edit. Amsterdam: Amsterdam : Academic Press, 2011, 2011.

[34] M. Applications and M. Fibers, *High-performance and specialty fibers: Concepts, technology and modern applications of man-made fibers for the future*. 2016.

[35] Michelman, “Fiber sizing - Reinforced composites.” https://www.michelman.com/markets/reinforced-plastic-composites/fiber-sizing/.

[36] M. INAGAKI, “CHAPTER 4 - Carbon Fibers,” M. B. T.-N. C.-C. of S. and F. INAGAKI, Ed. Oxford: Elsevier Science, 2000, pp. 82–123.

[37] Gurit, “Guite to composites.” https://www.gurit.com/-/media/Gurit/Datasheets/guide-to-composites.pdf (accessed Jan. 20, 2001).

[38] M. H. El-Hofy, “Milling/routing of carbon fibre reinforced plastic (CFRP) composites,” no. May, 2014, [Online]. Available: https://etheses.bham.ac.uk//id/eprint/5529/.

[39] S. T. Peters, “Introduction, Composite Basics and Road Map BT - Handbook of Composites,” S. T. Peters, Ed. Boston, MA: Springer US, 1998, pp. 1–20.

[40] L. S. Penn and H. Wang, “Epoxy Resins,” in *Handbook of Composites*, S. T. Peters, Ed. Boston, MA: Springer US, 1998, pp. 48–74.

[41] “Epoxy-based composite materials in aerospace industry,” 2021. https://epoxy-europe.eu/application/aerospace/.

[42] S. Ashworth, “Edge milled carbon fibre reinforced polymers: surface metrics and mechanical performance,” no. June, 2020, [Online]. Available: http://etheses.whiterose.ac.uk/27393/.

[43] S.T.Peters, *Handbook of composites*. 2002.

[44] S. Sprenger, “Epoxy resins modified with elastomers and surface-modified silica nanoparticles,” *Polymer (Guildf).*, vol. 54, no. 18, pp. 4790–4797, 2013, doi: 10.1016/j.polymer.2013.06.011.

[45] A. C. Garg and Y. W. Mai, “Failure mechanisms in toughened epoxy resins-A review,” *Compos. Sci. Technol.*, vol. 31, no. 3, pp. 179–223, 1988, doi: 10.1016/0266-3538(88)90009-7.

[46] R. A. Pearson and A. F. Yee, “Toughening mechanisms in thermoplastic-modified epoxies: 1. Modification using poly(phenylene oxide),” *Polymer (Guildf).*, vol. 34, no. 17, pp. 3658–3670, 1993, doi: 10.1016/0032-3861(93)90051-B.

[47] F. J. Guild, A. J. Kinloch, and A. C. Taylor, “Particle cavitation in rubber toughened epoxies: The role of particle size,” *J. Mater. Sci.*, vol. 45, no. 14, pp. 3882–3894, 2010, doi: 10.1007/s10853-010-4447-y.

[48] A.F.Yee and R. A. Pearson, “Toughening mechanisms in elastomer-modified epoxies,” vol. 21, pp. 2462–2474, 1986.

[49] A. J. Kinloch, S. J. Shaw, D. A. Tod, and D. L. Hunston, “Deformation and fracture behaviour of a rubber-toughened epoxy: 1. Microstructure and fracture studies,” *Polymer (Guildf).*, vol. 24, no. 10, pp. 1341–1354, 1983, doi: 10.1016/0032-3861(83)90070-8.

[50] D. J. Bray *et al.*, “The modelling of the toughening of epoxy polymers via silica nanoparticles: The effects of volume fraction and particle size,” *Polymer (Guildf).*, vol. 54, no. 26, pp. 7022–7032, 2013, doi: 10.1016/j.polymer.2013.10.034.

[51] J. G. Williams, “Particle toughening of polymers by plastic void growth,” *Compos. Sci. Technol.*, vol. 70, no. 6, pp. 885–891, 2010, doi: 10.1016/j.compscitech.2009.12.024.

[52] S. Sprenger and S. Sprenger, *The Effects of Silica Nanoparticles in Toughened Epoxy Resins and Fiber-Reinforced Composites*. 2015.

[53] V. Altstädt, D. Gerth, M. Stängle, and H. G. Recker, "Interlaminar crack growth in third-generation thermoset prepreg systems," *Polymer (Guildf).*, vol. 34, no. 4, pp. 907–909, 1993, doi: 10.1016/0032-3861(93)90379-O.

[54] J. Kim, C. Baillie, J. Poh, and Y. W. Mai, "Fracture toughness of CFRP with modified epoxy resin matrices," *Compos. Sci. Technol.*, vol. 43, no. 3, pp. 283–297, 1992, doi: 10.1016/0266-3538(92)90099-O.

[55] S. Sprenger, "Fiber-reinforced composites based on epoxy resins modified with elastomers and surface-modified silica nanoparticles," *J. Mater. Sci.*, vol. 49, no. 6, pp. 2391–2402, 2014, doi: 10.1007/s10853-013-7963-8.

[56] Y. Tang, L. Ye, D. Zhang, and S. Deng, "Characterization of transverse tensile, interlaminar shear and interlaminate fracture in CF/EP laminates with 10 wt% and 20 wt% silica nanoparticles in matrix resins," *Compos. Part A Appl. Sci. Manuf.*, vol. 42, no. 12, pp. 1943–1950, 2011, doi: 10.1016/j.compositesa.2011.08.019.

[57] J. L. Tsai, B. H. Huang, and Y. L. Cheng, "Enhancing fracture toughness of glass/epoxy composites by using rubber particles together with silica nanoparticles," *J. Compos. Mater.*, vol. 43, no. 25, pp. 3107–3123, 2009, doi: 10.1177/0021998309345299.

[58] C. M. Manjunatha, N. Jagannathan, K. Padmalatha, A. J. Kinloch, and A. C. Taylor, "Improved variable-amplitude fatigue behavior of a glass-fiber-reinforced hybrid-toughened epoxy composite," *J. Reinf. Plast. Compos.*, vol. 30, no. 21, pp. 1783–1793, 2011, doi: 10.1177/0731684411426202.

[59] D. L. Hunston, R. J. Moulton, N. J. Johnston, and W. Bascom, *Matrix resin effects in composite delamination: mode I fracture aspects*. ASTM International, 1987.

[60] W. L. Bradley, "Understanding the translation of neat resin toughness into delamination toughness in composites," in *Key Engineering Materials*, 1989, vol. 37, pp. 161–198.

[61] K. Potter, "An Introduction to Composite Products: Design, Development and

Manufacture.” Springer, 5th Ed. Chapman & Hall, London, 1996.

[62] S. Mazumdar, *Composites Manufacturing*. 2001.

[63] J. R. Lowe, “Void formation in resin transfer moulding,” 1993.

[64] S. G. Advani and K. T. Hsiao, *Manufacturing techniques for polymer matrix composites (PMCs)*. 2012.

[65] N. K. Naik, M. Sirisha, and A. Inani, “Permeability characterization of polymer matrix composites by RTM/VARTM,” *Prog. Aerosp. Sci.*, vol. 65, pp. 22–40, 2014, doi: https://doi.org/10.1016/j.paerosci.2013.09.002.

[66] B. Jensen *et al.*, “Fiber Metal Laminates Made by the VARTM Process,” 2009.

[67] Mikell P. Groovers, “Fundamentals of Modern Manufacturing - Materials, Processes, and Systems,” *Mech. Eng.*, vol. 118, no. 1, p. 98, 1996.

[68] R. Teti, “Machining of Composite Materials,” *CIRP Ann. - Manuf. Technol.*, vol. 51, no. 2, pp. 611–634, 2002, doi: 10.1016/S0007-8506(07)61703-X.

[69] W. F. Gale and T. C. B. T.-S. M. R. B. (Eighth E. Totemeier, Eds., “30 - Metal cutting and forming,” Oxford: Butterworth-Heinemann, 2004, pp. 16–30.

[70] J. P. Davim, *Machining of Metal Matrix Composites*. Springer-Verlag London, 2012.

[71] M. P. Groover, *Principles of modern manufacturing*, 4th ed., S. Hoboken, N.J.: Hoboken, N.J. : John Wiley, c2011, 2011.

[72] V. P. Astakhov, “Geometry of Single-point Turning Tools and Drills.” doi: 10.1007/978-1-84996-053-3.

[73] A. Koplev, A. Lystrup, and T. Vorm, “The cutting process, chips, and cutting forces in machining CFRP,” *Composites*, vol. 14, pp. 371–376, 1983.

[74] D. Wang, M. Ramulu, and D. Arola, “Orthogonal cutting mechanisms of graphite/ epoxy composite. II. Multi-directional laminate,” *Int. J. Mach. Tools Manuf.*, vol. 35, no. 12, pp. 1639–1648, 1995.

[75] D. H. Wang, M. Ramulu, and D. Arola, “Orthogonal cutting mechanisms of

graphite/epoxy composite. Part I: unidirectional laminate," *Int. J. Mach. Tools Manuf.*, vol. 35, no. 12, pp. 1623–1638, 1995, doi: 10.1016/0890-6955(95)00014-O.

[76] D. Arola, M. Ramulu, and D. H. Wang, "Chip formation in orthogonal trimming of graphite/epoxy composite," *Compos. Part A Appl. Sci. Manuf.*, vol. 27, no. 2, pp. 121–133, 1996, doi: https://doi.org/10.1016/1359-835X(95)00013-R.

[77] X. M. Wang and L. C. Zhang, "An experimental investigation into the orthogonal cutting of unidirectional fibre reinforced plastics," *Int. J. Mach. Tools Manuf.*, vol. 43, no. 10, pp. 1015–1022, 2003, doi: https://doi.org/10.1016/S0890-6955(03)00090-7.

[78] Q. An, W. Ming, X. Cai, and M. Chen, "Study on the cutting mechanics characteristics of high-strength UD-CFRP laminates based on orthogonal cutting method," *Compos. Struct.*, vol. 131, pp. 374–383, Nov. 2015, doi: 10.1016/j.compstruct.2015.05.035.

[79] Y. Su, "Effect of the cutting speed on the cutting mechanism in machining CFRP," *Compos. Struct.*, vol. 220, no. March, pp. 662–676, 2019, doi: 10.1016/j.compstruct.2019.04.052.

[80] T. Kaneeda and M. Takahashi, *CFRP Cutting Mechanism (1st Report): —Surface Generation Mechanism at Very Low Cutting Speeds—*, vol. 55. 1989.

[81] H. Agarwal, A. Amaranath, Y. Jamthe, and S. Gururaja, "An Investigation of Cutting Mechanisms and Strain Fields during Orthogonal Cutting in CFRPs," *Mach. Sci. Technol.*, vol. 19, no. 3, pp. 416–439, 2015, doi: 10.1080/10910344.2015.1051539.

[82] H. Li, X. Qin, G. He, M. A. Price, Y. Jin, and D. Sun, "An energy based force prediction method for UD-CFRP orthogonal machining," *Compos. Struct.*, vol. 159, pp. 34–43, 2017, doi: https://doi.org/10.1016/j.compstruct.2016.09.051.

[83] Y. Su, Z. Jia, B. Niu, and G. Bi, "Size effect of depth of cut on chip formation mechanism in machining of CFRP," *Compos. Struct.*, vol. 164, pp. 316–327, 2017, doi: https://doi.org/10.1016/j.compstruct.2016.11.044.

[84] Y. Su, "Effect of the cutting speed on the cutting mechanism in machining CFRP," *Compos. Struct.*, vol. 220, pp. 662–676, 2019, doi:

https://doi.org/10.1016/j.compstruct.2019.04.052.

[85] Q. An, W. Ming, X. Cai, and M. Chen, “Effects of tool parameters on cutting force in orthogonal machining of T700/LT03A unidirectional carbon fiber reinforced polymer laminates,” *J. Reinf. Plast. Compos.*, vol. 34, no. 7, pp. 591–602, 2015, doi: 10.1177/0731684415577688.

[86] J. P. Davim, *Machining composite materials*. London : Hoboken, NJ: London : ISTE Hoboken, NJ : Wiley, 2010, 2010.

[87] A. Di Ilio and A. Paoletti, “Machinability aspects of polymer matrix composites,” no. January, pp. 63–77, 2012, doi: 10.1007/978-0-85729-938-3_3.

[88] J. Sheikh-Ahmad and G. Sridhar, “Edge trimming of CFRP composites with diamond coated tools: Edge wear and surface characteristics,” *SAE Tech. Pap.*, no. April 2002, 2002, doi: 10.4271/2002-01-1526.

[89] W. Zhang, *Milling simulation : metal milling mechanics, dynamics and clamping principles*. London, England : London, England , 2016.

[90] E. M. (Edward M. Trent, *Metal cutting [electronic resource]*, 4th ed. Boston: Boston : Butterworth-Heinemann, c2000, 2000.

[91] Y. Karpat and N. Polat, “Mechanistic force modeling for milling of carbon fiber reinforced polymers with double helix tools,” *CIRP Ann.*, vol. 62, no. 1, pp. 95–98, 2013, doi: https://doi.org/10.1016/j.cirp.2013.03.105.

[92] S. Ashworth *et al.*, “Effects of machine stiffness and cutting tool design on the surface quality and flexural strength of edge trimmed carbon fibre reinforced polymers,” *Compos. Part A Appl. Sci. Manuf.*, vol. 119, pp. 88–100, 2019, doi: https://doi.org/10.1016/j.compositesa.2019.01.019.

[93] S. Ashworth *et al.*, “Varying CFRP workpiece temperature during slotting: Effects on surface metrics, cutting forces and chip geometry,” *Procedia CIRP*, vol. 85, pp. 36–41, 2020, doi: 10.1016/j.procir.2019.09.021.

[94] K. Kerrigan and G. E. O’Donnell, “On the Relationship between Cutting Temperature

and Workpiece Polymer Degradation during CFRP Edge Trimming," *Procedia CIRP*, vol. 55, pp. 170–175, 2016, doi: 10.1016/j.procir.2016.08.041.

[95] C. Sauder, J. Lamon, and R. Pailler, "The tensile behavior of carbon fibers at high temperatures up to 2400 °C," *Carbon N. Y.*, vol. 42, no. 4, pp. 715–725, 2004, doi: 10.1016/j.carbon.2003.11.020.

[96] H. Wang, L. Chang, Y. W. Mai, L. Ye, and J. G. Williams, "An experimental study of orthogonal cutting mechanisms for epoxies with two different crosslink densities," *Int. J. Mach. Tools Manuf.*, vol. 124, pp. 117–125, 2018, doi: 10.1016/j.ijmachtools.2017.10.003.

[97] J. L. Merino-Pérez, R. Royer, E. Merson, A. Lockwood, S. Ayvar-Soberanis, and M. B. Marshall, "Influence of workpiece constituents and cutting speed on the cutting forces developed in the conventional drilling of CFRP composites," *Compos. Struct.*, vol. 140, pp. 621–629, 2016, doi: https://doi.org/10.1016/j.compstruct.2016.01.008.

[98] D. Sharma, K. K. Singh, and R. K. Thakur, "Parametric Optimization of Surface Roughness and Delamination Damage in End Milling Operation of GFRP Laminate Modified with MWCNT," *Mater. Today Proc.*, vol. 22, pp. 2798–2807, 2019, doi: 10.1016/j.matpr.2020.03.411.

[99] I. Arora, J. Samuel, and N. Koratkar, "Experimental investigation of the machinability of epoxy reinforced with graphene platelets," *J. Manuf. Sci. Eng. Trans. ASME*, vol. 135, no. 4, pp. 1–7, 2013, doi: 10.1115/1.4024814.

[100] G. Fu, D. Huo, I. Shyha, K. Pancholi, and B. Alzahrani, "Experimental investigation on micromachining of epoxy/graphene nano platelet nanocomposites," *Int. J. Adv. Manuf. Technol.*, vol. 107, no. 7–8, pp. 3169–3183, 2020, doi: 10.1007/s00170-020-05190-4.

[101] K. El-Ghaoui, J. F. Chatelain, and C. Ouellet-Plamondon, "Effect of graphene on machinability of glass fiber reinforced polymer (GFRP)," *J. Manuf. Mater. Process.*, vol. 3, no. 3, pp. 1–12, 2019, doi: 10.3390/jmmp3030078.

[102] R. K. Thakur, D. Sharma, and K. K. Singh, “Optimization of surface roughness and delamination factor in end milling of graphene modified GFRP using response surface methodology,” *Mater. Today Proc.*, vol. 19, pp. 133–139, 2019, doi: 10.1016/j.matpr.2019.06.153.

[103] R. K. Thakur, K. K. Singh, and K. Kumar, “Investigation of milling characteristics in graphene-embedded epoxy/carbon fibre reinforced composite,” *Mater. Today Proc.*, vol. 33, pp. 5643–5648, 2020, doi: 10.1016/j.matpr.2020.04.022.

[104] I. Shyha *et al.*, “Micro-machining of nano-polymer composites reinforced with graphene and nano-clay fillers,” *Key Eng. Mater.*, vol. 786 KEM, pp. 197–205, 2018, doi: 10.4028/www.scientific.net/KEM.786.197.

[105] R. K. Thakur, K. K. Singh, and D. Sharma, “Modeling and optimization of surface roughness in end milling of graphene/epoxy nanocomposite,” *Mater. Today Proc.*, vol. 19, pp. 302–306, 2019, doi: 10.1016/j.matpr.2019.07.213.

[106] R. Leach, *Characterisation of areal surface texture*, vol. 9783642364. 2013.

[107] L. Blunt, “1 - Introduction: The History and Current State of 3D Surface Characterisation,” L. Blunt and X. B. T.-A. T. for A. S. T. Jiang, Eds. Oxford: Kogan Page Science, 2003, pp. 1–13.

[108] D. Arola and C. L. Williams, “Estimating the fatigue stress concentration factor of machined surfaces,” *Int. J. Fatigue*, vol. 24, no. 9, pp. 923–930, 2002, doi: https://doi.org/10.1016/S0142-1123(02)00012-9.

[109] R. A. K. J. T. Black, “DeGarmo’s Materials and Processes in Manufacturing, .” 2017.

[110] “BSI. Geometrical Product Specifications (GPS) - Surface texture: Profile method - Rules and procedures for the assessment of surface texture. ISO 4288:1998.” .

[111] H. Hocheng, *Machining technology for composite materials : principles and practice*. Cambridge, UK ; Philadelphia, PA: Cambridge, UK ; Philadelphia, PA : Woodhead Pub., 2012, 2012.

[112] U. Teicher, T. Rosenbaum, A. Nestler, and A. Brosius, “Characterization of the

Surface Roughness of Milled Carbon Fiber Reinforced Plastic Structures," *Procedia CIRP*, vol. 66, pp. 199–203, 2017, doi: https://doi.org/10.1016/j.procir.2017.03.282.

[113] U. C. Nwaogu, N. S. Tiedje, and H. N. Hansen, "A non-contact 3D method to characterize the surface roughness of castings," *J. Mater. Process. Technol.*, vol. 213, no. 1, pp. 59–68, 2013, doi: https://doi.org/10.1016/j.jmatprotec.2012.08.008.

[114] N. Duboust *et al.*, "An optical method for measuring surface roughness of machined Carbon Fibre Reinforced Plastic composites," 2016.

[115] R. K. Leach, *Fundamental principles of engineering nanometrology [electronic resource]*, Second edi. Oxford : Elsevier Science/William Andrew, 2014, 2014.

[116] N. Duboust *et al.*, "Machining of Carbon Fibre: Optical Surface Damage Characterisation and Tool Wear Study," *Procedia CIRP*, vol. 45, pp. 71–74, 2016, doi: 10.1016/j.procir.2016.02.170.

[117] A. Davila, P. D. Ruiz, G. H. Kaufmann, and J. M. Huntley, "Measurement of sub-surface delaminations in carbon fibre composites using high-speed phase-shifted speckle interferometry and temporal phase unwrapping," *Opt. Lasers Eng.*, vol. 40, no. 5, pp. 447–458, 2003, doi: https://doi.org/10.1016/S0143-8166(02)00082-9.

[118] H. Dhieb, J. G. Buijnsters, F. Eddoumy, and J. P. Celis, "Surface damage of unidirectional carbon fiber reinforced epoxy composites under reciprocating sliding in ambient air," *Compos. Sci. Technol.*, vol. 71, no. 15, pp. 1769–1776, 2011, doi: 10.1016/j.compscitech.2011.08.012.

[119] J. P. Dunkers, D. P. Sanders, D. L. Hunston, M. J. Everett, and W. H. Green, "Comparison of optical coherence tomography, x-ray computed tomography, and confocal microscopy results from an impact damaged epoxy/e-glass composite," *J. Adhes.*, vol. 78, no. 2, pp. 129–154, 2002, doi: 10.1080/00218460210386.

[120] D. J. Mortell, D. A. Tanner, and C. T. McCarthy, "In-situ SEM study of transverse cracking and delamination in laminated composite materials," *Compos. Sci. Technol.*, vol. 105, no. Supplement C, pp. 118–126, 2014, doi: https://doi.org/10.1016/j.compscitech.2014.10.012.

[121] M. Monoranu *et al.*, “A comparative study of the effects of milling and abrasive water jet cutting on flexural performance of CFRP,” *Procedia CIRP*, vol. 85, pp. 277–283, 2019, doi: https://doi.org/10.1016/j.procir.2019.09.036.

[122] C. Wang, G. Liu, Q. An, and M. Chen, “Occurrence and formation mechanism of surface cavity defects during orthogonal milling of CFRP laminates,” *Compos. Part B Eng.*, vol. 109, no. Supplement C, pp. 10–22, 2017, doi: https://doi.org/10.1016/j.compositesb.2016.10.015.

[123] X. M. Wang and L. C. Zhang, “An experimental investigation into the orthogonal cutting of unidirectional fibre reinforced plastics,” *Int. J. Mach. Tools Manuf.*, vol. 43, no. 10, pp. 1015–1022, 2003, doi: 10.1016/S0890-6955(03)00090-7.

[124] C. C. Tsao and H. Hocheng, “Computerized tomography and C- Scan for measuring delamination in the drilling of composite materials using various drills,” *Int. J. Mach. Tools Manuf.*, vol. 45, no. 11, pp. 1282–1287, 2005, doi: 10.1016/j.ijmachtools.2005.01.009.

[125] S. C. Garcea, Y. Wang, and P. J. Withers, “X-ray computed tomography of polymer composites,” *Compos. Sci. Technol.*, vol. 156, pp. 305–319, 2018, doi: 10.1016/j.compscitech.2017.10.023.

[126] H. Schreier, J.-J. Orteu, and M. A. Sutton, *Image Correlation for Shape, Motion and Deformation Measurements*. 2009.

[127] W. M. Cummings, *Thermoelastic stress analysis*. Bristol: Bristol : IOP, 1991, 1991.

[128] J. William N. Sharpe, Ed., *Handbook of Experimental Solid Mechanics*. Springer US, 2008.

[129] N. McCormick and J. Lord, “Digital Image Correlation,” *Mater. Today*, vol. 13, no. 12, pp. 52–54, 2010, doi: 10.1016/S1369-7021(10)70235-2.

[130] M. L. Aparna, G. Chaitanya, K. Srinivas, and J. A. Rao, “Fatigue Testing of Continuous GFRP Composites Using Digital Image Correlation (DIC) Technique a Review,” *Mater. Today Proc.*, vol. 2, no. 4, pp. 3125–3131, 2015, doi: https://doi.org/10.1016/j.matpr.2015.07.275.

[131] S. M.A., “Digital Image Correlation for Shape and Deformation Measurements,” vol. Sharpe W. Springer, Boston, MA.

[132] G. Crammond, S. W. Boyd, and J. M. Dulieu-Barton, “Dynamic analysis of composite marine structures using full-field measurement techniques,” *J. Mar. Eng. Technol.*, vol. 13, no. 1, pp. 23–35, 2014, doi: 10.1080/20464177.2014.11020290.

[133] B. Koohbor, S. Mallon, A. Kidane, and M. A. Sutton, “A DIC-based study of in-plane mechanical response and fracture of orthotropic carbon fiber reinforced composite,” *Compos. Part B Eng.*, vol. 66, pp. 388–399, 2014, doi: https://doi.org/10.1016/j.compositesb.2014.05.022.

[134] P. Pollock, L. Yu, M. A. Sutton, S. Guo, P. Majumdar, and M. Gresil, “Full-Field Measurements for Determining Orthotropic Elastic Parameters of Woven Glass-Epoxy Composites Using Off-Axis Tensile Specimens,” *Exp. Tech.*, vol. 38, no. 4, pp. 61–71, May 2012, doi: 10.1111/j.1747-1567.2012.00824.x.

[135] T. Scalici, V. Fiore, G. Orlando, and A. Valenza, “A DIC-based study of flexural behaviour of roving/mat/roving pultruded composites,” *Compos. Struct.*, vol. 131, pp. 82–89, 2015, doi: https://doi.org/10.1016/j.compstruct.2015.04.058.

[136] M. Tekieli, S. De Santis, G. de Felice, A. Kwiecień, and F. Roscini, “Application of Digital Image Correlation to composite reinforcements testing,” *Compos. Struct.*, vol. 160, pp. 670–688, 2017, doi: https://doi.org/10.1016/j.compstruct.2016.10.096.

[137] T. Baizeau, S. Campocasso, G. Fromentin, and R. Besnard, “Kinematic Field Measurements During Orthogonal Cutting Tests via DIC with Double-frame Camera and Pulsed Laser Lighting,” *Exp. Mech.*, vol. 57, no. 4, pp. 581–591, 2017, doi: 10.1007/s11340-016-0248-9.

[138] D. Zhang, X. M. Zhang, W. J. Xu, and H. Ding, “Stress Field Analysis in Orthogonal Cutting Process Using Digital Image Correlation Technique,” *J. Manuf. Sci. Eng. Trans. ASME*, vol. 139, no. 3, pp. 1–13, 2017, doi: 10.1115/1.4033928.

[139] Y. L. Dong and B. Pan, “A Review of Speckle Pattern Fabrication and Assessment for

Digital Image Correlation," *An Int. J.*, vol. 57, no. 8, pp. 1161–1181, 2017, doi: 10.1007/s11340-017-0283-1.

[140] H. Wang, H. Xie, Y. Li, and J. Zhu, "Fabrication of micro-scale speckle pattern and its applications for deformation measurement," *Meas. Sci. Technol.*, vol. 23, no. 3, p. 35402, 2012, doi: 10.1088/0957-0233/23/3/035402.

[141] J. Zhu, G. Yan, G. He, and L. Chen, "Fabrication and optimization of micro-scale speckle patterns for digital image correlation," *Meas. Sci. Technol.*, vol. 27, no. 1, p. 15203, 2016, doi: 10.1088/0957-0233/27/1/015203.

[142] J. Zhang, A. Sweedy, F. Gitzhofer, and G. Baroud, "A novel method for repeatedly generating speckle patterns used in digital image correlation," *Opt. Lasers Eng.*, vol. 100, pp. 259–266, 2018, doi: https://doi.org/10.1016/j.optlaseng.2017.09.012.

[143] G. Crammond, S. W. Boyd, and J. M. Dulieu-Barton, "Speckle pattern quality assessment for digital image correlation," *Opt. Lasers Eng.*, vol. 51, no. 12, pp. 1368–1378, 2013, doi: https://doi.org/10.1016/j.optlaseng.2013.03.014.

[144] B. Pan, H. Xie, Z. Wang, K. Qian, and Z. Wang, "Study on subset size selection in digital image correlation for speckle patterns," *Opt. Express*, vol. 16, no. 10, pp. 7037–7048, 2008, doi: 10.1364/OE.16.007037.

[145] S. Yaofeng and J. H. L. Pang, "Study of optimal subset size in digital image correlation of speckle pattern images," *Opt. Lasers Eng.*, vol. 45, no. 9, pp. 967–974, 2007, doi: 10.1016/j.optlaseng.2007.01.012.

[146] B. Pan, Z. Lu, and H. Xie, "Mean intensity gradient: An effective global parameter for quality assessment of the speckle patterns used in digital image correlation," *Opt. Lasers Eng.*, vol. 48, no. 4, pp. 469–477, 2010, doi: https://doi.org/10.1016/j.optlaseng.2009.08.010.

[147] X.-Y. Liu *et al.*, "Quality assessment of speckle patterns for digital image correlation by Shannon entropy," *Opt. - Int. J. Light Electron Opt.*, vol. 126, no. 23, pp. 4206–4211, 2015, doi: 10.1016/j.ijleo.2015.08.034.

[148] D. Lecompte *et al.*, "Quality assessment of speckle patterns for digital image

correlation," *Opt. Lasers Eng.*, vol. 44, no. 11, pp. 1132–1145, 2006, doi: https://doi.org/10.1016/j.optlaseng.2005.10.004.

[149] P. Zhou and K. Goodson, "Subpixel displacement and deformation gradient measurement using digital image/speckle correlation (DISC)," *Opt. Eng.*, vol. 40, no. 8, pp. 1613–1620, 2001, doi: 10.1117/1.1387992.

[150] P.-C. Hung and A. S. Voloshin, "In-plane strain measurement by digital image correlation," *J. Brazilian Soc. Mech. Sci. Eng.*, vol. 25, pp. 215–221, 2003.

[151] O. Faruk, J. Tjong, and M. Sain, *Lightweight and Sustainable Materials for Automotive Applications*, 1st ed. New York, N.Y.: Taylor & Francis, 2017.

[152] Huntsman, "Trade name of the Resins," 2010.

[153] Toray, "T300 Standard Modulus Carbon Fiber Data Sheet," p. 2, 2018.

[154] Toray, "Toray T700SC-12K Data sheet," 2022, [Online]. Available: https://www.toraycma.com/wp-content/uploads/T700S-Technical-Data-Sheet-1.pdf.pdf.

[155] A. Materials, "Araldite ® LY 1564 SP / Aradur ® 2954," no. October, pp. 4–7, 2010.

[156] R. B. Heslehurst, *Defects and Damage in Composite Materials and Structures*. 2014.

[157] ASTM, "Astm D3039/D3039M," *Annu. B. ASTM Stand.*, pp. 1–13, 2014, doi: 10.1520/D3039.

[158] PerkinElmer, "Differential Scanning Calorimetry (DSC)," 2014. [Online]. Available: https://resources.perkinelmer.com/lab-solutions/resources/docs/GDE_DSCBeginnersGuide.pdf.

[159] PerkinElmer Inc., "Dynamic Mechanical Analysis (DMA) - A Beginner's Guide," *Introd. to DMA*, pp. 1–23, 2008, [Online]. Available: https://www.perkinelmer.com/CMSResources/Images/44-74546GDE_IntroductionToDMA.pdf.

[160] K. Menard and B. Cassel, "Basics of Thermomechanical Analysis," 2013. [Online]. Available: https://www.perkinelmer.com/CMSResources/Images/44-

154962TCH_TMA_4000.pdf.

[161] “BSI. Plastics - Thermomechanical analysis (TMA) - Determination of coefficient of linear thermal expansion and glass transition temperature. ISO 11359-2: 1999.”

[162] “ASTM D638-14, Standard Test Method for Tensile Properties of Plastics,” West Conshohocken, PA, 2004. doi: 10.1520/D0638-14.1.

[163] “ASTM D5045-14, Standard Test Methods for Plane-Strain Fracture Toughness and Strain Energy Release Rate of Plastic Materials,” West Conshohocken, PA, 2014. doi: 10.1520/D5045-14.

[164] “British Standards Institution, BS ISO 13586:2000, Plastics, Determination of fracture toughness (GIc and KIc): Linear elastic fracture mechanics (LEFM) approach,” 2000.

[165] J. S. A, “An experimental investigation of the fracture behaviour of particulate toughened epoxies,” no. July, p. 224, 2013.

[166] A. Jones, “An experimental investigation of the fracture behaviour of particulate toughened epoxies,” University of Sheffield, 2013.

[167] Y. Guo, W. D. Compton, and S. Chandrasekar, “In situ analysis of flow dynamics and deformation fields in cutting and sliding of metals,” *Proc. R. Soc. A Math. Phys. Eng. Sci.*, vol. 471, 2015.

[168] K. Group, “Cutting force measurements in research and development.” [Online]. Available: https://www.kistler.com/files/download/960-002e.pdf.

[169] H. Haddadi and S. Belhabib, “Use of rigid-body motion for the investigation and estimation of the measurement errors related to digital image correlation technique,” *Opt. Lasers Eng.*, vol. 46, no. 2, pp. 185–196, 2008, doi: 10.1016/j.optlaseng.2007.05.008.

[170] Lavision, “DaVis 10.2 Software,” 2021.

[171] S. Ashworth *et al.*, “Effects of machine stiffness and cutting tool design on the surface quality and flexural strength of edge trimmed carbon fibre reinforced

polymers," *Compos. Part A Appl. Sci. Manuf.*, vol. 119, no. January, pp. 88–100, 2019, doi: 10.1016/j.compositesa.2019.01.019.

[172] OSG, "Aerospace Solutions - Composite," [Online]. Available: https://de.osgeurope.com/media/pdf/Brochure-CFRP-VOL3-EU-EN-WEB.pdf.

[173] J. Sheikh-Ahmad, N. Urban, and H. Cheraghi, "Machining damage in edge trimming of CFRP," *Mater. Manuf. Process.*, vol. 27, no. 7, pp. 802–808, 2012, doi: 10.1080/10426914.2011.648253.

[174] R. Prakash, V. Krishnaraj, and J. Sheikh-Ahmad, "High-speed edge trimming of carbon fiber-reinforced polymer composites using coated router tools," *J. Compos. Mater.*, vol. 53, no. 28–30, pp. 4189–4202, 2019, doi: 10.1177/0021998319856071.

[175] Alicona Imaging GmbH, "Alicona MeasureSuite Version 5.3.4 Manual." 2018.

[176] I. S. O. 25178, "No Title." [Online]. Available: https://www.iso.org.

[177] "An overview of 3D X-ray microscopy," 2020. [Online]. Available: https://pages.zeiss.com/rs/896-XMS-794/images/Ebook_3D-X-ray-Microscopy-Second-Edition.pdf.

[178] M. Haddad, R. Zitoune, F. Eyma, and B. Castanie, "Study of the surface defects and dust generated during trimming of CFRP: Influence of tool geometry, machining parameters and cutting speed range," *Compos. Part A Appl. Sci. Manuf.*, vol. 66, no. Supplement C, pp. 142–154, 2014, doi: https://doi.org/10.1016/j.compositesa.2014.07.005.

[179] Y. L. Liang and R. A. Pearson, "The toughening mechanism in hybrid epoxy-silica-rubber nanocomposites (HESRNs)," *Polymer (Guildf).*, vol. 51, no. 21, pp. 4880–4890, 2010, doi: 10.1016/j.polymer.2010.08.052.

[180] A. G. Atkins, "Slice-push, formation of grooves and the scale effect in cutting," *Interface Focus*, vol. 6, no. 3, 2016, doi: 10.1098/rsfs.2016.0019.

[181] H. Wang, L. Chang, J. G. Williams, L. Ye, and Y. W. Mai, "On the machinability and surface finish of cutting nanoparticle and elastomer modified epoxy," *Mater. Des.*,

vol. 109, pp. 580–589, 2016, doi: 10.1016/j.matdes.2016.07.112.

[182] P. A. R. Rosa, O. Kolednik, P. A. F. Martins, and A. G. Atkins, “The transient beginning to machining and the transition to steady-state cutting,” *Int. J. Mach. Tools Manuf.*, vol. 47, no. 12–13, pp. 1904–1915, 2007, doi: 10.1016/j.ijmachtools.2007.03.005.

[183] G. (Geoffrey) Boothroyd, *Fundamentals of metal machining*. London: London : Edward Arnold, 1965, 1965.

[184] T. Atkins, *The Science and Engineering of Cutting, The Mechanics and Processes of Seperating, Scratching and Puncturing Biomaterials, Metals and Non-Metals*. 2009.

[185] S. Ashworth *et al.*, “Epifluorescent microscopy of edge-trimmed carbon fibre-reinforced polymers: An alternative to computed tomography scanning,” *Adv. Compos. Lett.*, vol. 29, pp. 1–8, 2020, doi: 10.1177/2633366X20924676.

[186] N. Duboust, M. Watson, M. Marshall, G. E. O’Donnel, and K. Kerrigan, “Towards intelligent CFRP composite machining: Surface analysis methods and statistical data analysis of machined fibre laminate surfaces,” *Proc. Inst. Mech. Eng. Part B J. Eng. Manuf.*, no. October, 2020, doi: 10.1177/0954405420960920.

[187] N. Nguyen-Dinh, C. Bouvet, and R. Zitoune, “Influence of machining damage generated during trimming of CFRP composite on the compressive strength,” *J. Compos. Mater.*, vol. 54, no. 11, pp. 1413–1430, 2020, doi: 10.1177/0021998319883335.

[188] N. Nguyen-Dinh, R. Zitoune, C. Bouvet, and S. Leroux, “Surface integrity while trimming of composite structures: X-ray tomography analysis,” *Compos. Struct.*, vol. 210, no. December 2018, pp. 735–746, 2019, doi: 10.1016/j.compstruct.2018.12.006.

[189] F. ji Wang, J. wei Yin, J. wei Ma, Z. yuan Jia, F. Yang, and B. Niu, “Effects of cutting edge radius and fiber cutting angle on the cutting-induced surface damage in machining of unidirectional CFRP composite laminates,” *Int. J. Adv. Manuf. Technol.*, vol. 91, no. 9–12, pp. 3107–3120, 2017, doi: 10.1007/s00170-017-0023-9.

[190] N. Duboust *et al.*, “An optical method for measuring surface roughness of machined

carbon fibre- reinforced plastic composites," *J. Compos. Mater.*, vol. 51, no. 3, pp. 289–302, 2017, doi: 10.1177/0021998316644849.

[191] A. Cenna and P. Mathew, "Evaluation of cut quality of fibre- reinforced plastics--a review," *Int. J. Mach. Tools Manuf.*, vol. 37, no. 6, pp. 723–736, 1997.

[192] L. P. Chen, A. F. Yee, and E. J. Moskala, "The Molecular Basis for the Relationship between the Secondary Relaxation and Mechanical Properties of a Series of Polyester Copolymer Glasses," *Macromolecules*, vol. 32, no. 18, pp. 5944–5955, 1999, doi: 10.1021/ma981363a.

[193] L. Ma, F. Liu, D. Liu, and Y. Liu, "Review of strain rate effects of fiber-reinforced polymer composites," *Polymers (Basel).*, vol. 13, no. 17, 2021, doi: 10.3390/polym13172839.

[194] A. Elmahdy, A. Zotti, S. Zuppolini, M. Zarrelli, A. Borriello, and P. Verleysen, "Effect of Strain Rate and Silica Filler Content on the Compressive Behavior of RTM6 Epoxy - Based Nanocomposites," *Polymers (Basel).*, vol. 13, no. 31, p. 3735, 2021, doi: 10.3390/polym13213735.

[195] S. Rose, A. Dizeux, T. Narita, D. Hourdet, and A. Marcellan, "Time dependence of dissipative and recovery processes in nanohybrid hydrogels," *Macromolecules*, vol. 46, no. 10, pp. 4095–4104, 2013, doi: 10.1021/ma400447j.

[196] D. Raghavan, J. He, D. Hunston, and D. Hoffman, "Strain rate dependence of fracture in a rubber-toughened epoxy system," *J. Adhes.*, vol. 78, no. 8, pp. 723–739, 2002, doi: 10.1080/00218460213493.

10 APPENDICES

10.1 Appendix A – Surface roughness parameters [175]

Name	Unit	Description
Sa	µm	Average height of selected area
Sq	µm	Root-Mean-Square height of selected area
Sp	µm	Maximum peak height of selected area
Sv	µm	Maximum valley depth of selected area
Sz	µm	Maximum height of selected area
S10z	µm	Ten point height of selected area
Ssk	-	Skewness of selected area
Sku	-	Kurtosis of selected area
Sdq	-	Root mean square gradient
Sdr	%	Developed interfacial area ratio
Sk	µm	Core roughness depth, Height of the core material
Spk	µm	Reduced peak height, mean height of the peaks above the core material
Svk	µm	Reduced valley height, mean depth of the valleys below the core material
Smr1	%	Peak material component, the fraction of the surface which consists of peaks above the core material
Smr2	%	Peak material component, the fraction of the surface which will carry the load
Vmp	ml/m^2	Peak material volume of the topographic surface (ml/m^2)
Vmc	ml/m^2	Core material volume of the topographic surface (ml/m^2)
Vvc	ml/m^2	Core void volume of the surface (ml/m^2)
Vvv	ml/m^2	Valley void volume of the surface (ml/m^2)
Vvc/Vmc	-	Ratio of Vvc parameter to Vmc parameter
Ra	µm	Average roughness of profile
Rq	µm	Root-Mean-Square roughness of profile
Rt	µm	Maximum peak to valley height of roughness profile
Rz	µm	Mean peak to valley height of roughness profile

Rmax	µm	Maximum peak to valley height of roughness profile within a sampling length
Rp	µm	Maximum peak height of roughness profile
Rv	µm	Maximum valley height of roughness profile
Rc	µm	Mean height of profile irregularities of roughness profile
Rsm	µm	Mean spacing of profile irregularities of roughness profile
Rsk	-	Skewness of roughness profile
Rku	-	Kurtosis of roughness profile
Rdq	-	Root-Mean-Square slope of roughness profile
Rt/Rz	-	Extreme Scratch/Peak value of roughness profile, (>=1), higher values represent larger scratches/peaks
Rk	µm	Core roughness depth, Height of the core material
Rpk	µm	Reduced peak height, mean height of the peaks above the core material
Rvk	µm	Reduced valley height, mean depth of the valleys below the core material

10.2 Appendix B – CT Scan parameters

Sample Name	kV	µA	W	Filter	BIN	Projections	Exposure (s)	pixel size (microns)	FOV (um)	Average intensity	Average Transmission (%)	Scan length (h:m)	Scan angle
D_S	60	108	6.5	AIR	2	1601	3	2.5	2540	12-27K	55-75%	2 HR 08	360
Si20_S	60	108	6.5	AIR	2	1601	3	2.5	2542	32-41K	60-65%	2 HR 08	360
D_m	50	90	4.5	LE2	2	1601	3	2.5	2539	11-22K	60-85%	2 HR 08	360
R20_m	50	90	4.5	AIR	2	1601	3	2.5	2539	14-26K	50-75%	2 HR 08	360
Si20_m	60	108	6.5	LE2	2	1601	3	2.5	2538	22-34K	60-80%	2 HR 08	360
D_S	50	90	4.5	AIR	2	1601	2	2.5	2538	15-24K	55-70%	2 HR 08	360

10.3 Appendix C – Validation of fracture toughness results

	Crack length	Crack length	Specimen width	Specimen thickness	alpha										Stress intensity factor	Stress intensity factor			
		m	m	m	-							N	Energy	Yield Stress	Pa m^1/2	MPa m^1/2		J/m2	
Unit	mm	m	w	H	a/w	f	A	B	tetha	hw^1/2	Force	Nm	Pa	Kq	Kic	Gq with teta	2.5 *r1	Validation
Sample	a	a																
D2	10.786	0.0108	0.032	0.0039	0.337	6.183194	7.446049	8.389147	0.212028	0.000698	100	0.009	45000000	886284.6974	0.886284697	340.1227169	0.00097	Valid
D3	10.969	0.011	0.032	0.0039	0.343	6.274555	7.518026	8.226899	0.212397	0.000698	90	0.008	45000000	809442.2149	0.809442215	301.8050124	0.000809	Valid
R10 1	9.447	0.0094	0.032	0.0039	0.295	5.551622	6.895268	9.63853	0.20742	0.000698	140	0.024	30000000	1114059.368	1.114059368	927.1417413	0.003448	Valid
R10 3	9.299	0.0093	0.032	0.0039	0.291	5.485229	6.831753	9.782807	0.206706	0.000698	139	0.026	30000000	1092873.656	1.092873656	1007.873828	0.003318	Valid
R10 5	10.499	0.0105	0.032	0.0039	0.328	6.042589	7.331586	8.647913	0.211322	0.000698	141	0.029	30000000	1221244.382	1.221244382	1099.611541	0.004143	Valid
R10 6	10.389	0.0104	0.032	0.0039	0.325	5.989522	7.2872	8.748455	0.21101	0.000698	145	0.032	30000000	1244860.148	1.244860148	1215.154628	0.004305	Valid
R20 2	10.162	0.0102	0.032	0.0039	0.318	5.881373	7.194694	8.958262	0.210297	0.000698	160	0.037	20000000	1348835.856	1.348835856	1409.792148	0.011371	Valid
R20 5	10.715	0.0107	0.032	0.0039	0.335	6.148112	7.417913	8.452677	0.211867	0.000698	159	0.039	20000000	1401197.395	1.40119739	1474.980163	0.012271	Valid
Si10 6	11.8	0.0118	0.032	0.0039	0.369	6.708211	7.835156	7.518372	0.213291	0.000698	92	0.011	45000000	884616.3416	0.884616342	413.2426668	0.000966	Valid
Si10 10	10.889	0.0109	0.032	0.0039	0.34	6.234446	7.486657	8.29756	0.212243	0.000698	93	0.011	45000000	831076.9603	0.83107696	415.2828799	0.000853	Valid
Si10 11	10.5	0.0105	0.032	0.0039	0.328	6.043074	7.331988	8.647003	0.211324	0.000698	97	0.011	45000000	840214.2033	0.840214203	417.0886516	0.000872	Valid
D1 10	11.641	0.0116	0.032	0.0039	0.364	6.622673	7.775693	7.650258	0.213219	0.000698	78.9	0.008	45000000	748980.8797	0.74898088	300.6412632	0.000693	Valid
Si10 3 10	11.121	0.0111	0.032	0.0039	0.348	6.351508	7.577217	8.093803	0.212657	0.000698	93	0.011	45000000	846681.7854	0.846681785	414.4753378	0.000885	Valid
Si20 6 10	10.845	0.0108	0.032	0.0039	0.339	6.212499	7.46934	8.3366	0.212154	0.000698	103	0.013	60000000	917199.8496	0.91719985	490.9965072	0.000584	Valid
Si20 7 10	11.723	0.0117	0.032	0.0039	0.366	6.666626	7.80643	7.582019	0.213262	0.000698	95.1	0.013	60000000	908755.3649	0.908755365	488.4438811	0.000573	Valid
SR 3 10	9.359	0.0094	0.032	0.0039	0.292	5.512074	6.857566	9.72418	0.207	0.000698	134	0.02	30000000	1058717.845	1.058717845	774.1848211	0.003114	Valid
SR 4 10	9.468	0.0095	0.032	0.0039	0.296	5.561091	6.904238	9.61815	0.207518	0.000698	136	0.02	30000000	1084074.98	1.08407498	772.2530861	0.003264	Valid
R10 7 10	10.53	0.0105	0.032	0.0039	0.329	6.057625	7.344043	8.619714	0.211405	0.000698	145	0.022	40000000	1259014.644	1.259014644	833.8579794	0.002477	Valid
R10 8 10	10.33	0.0103	0.032	0.0039	0.323	5.961239	7.263274	8.802688	0.210834	0.000698	135	0.021	40000000	1153534.794	1.153534794	798.1120253	0.002079	Valid
R10 10	10.58	0.0106	0.032	0.0039	0.331	6.081952	7.364087	8.574356	0.211537	0.000698	120	0.02	40000000	1046127.546	1.046127546	757.5827596	0.00171	Valid
SR 10 10	10.2	0.0102	0.032	0.0039	0.319	5.899353	7.210265	8.922925	0.210423	0.000698	145	0.022	30000000	1226119.411	1.226119411	837.7520075	0.004176	Valid
Sr 10 11	9.8	0.0098	0.032	0.0039	0.306	5.712468	7.04463	9.299106	0.208959	0.000698	145	0.021	30000000	1187277.313	1.187277313	805.2734814	0.003916	Valid

10.4 Appendix D – 3D micro – CT images

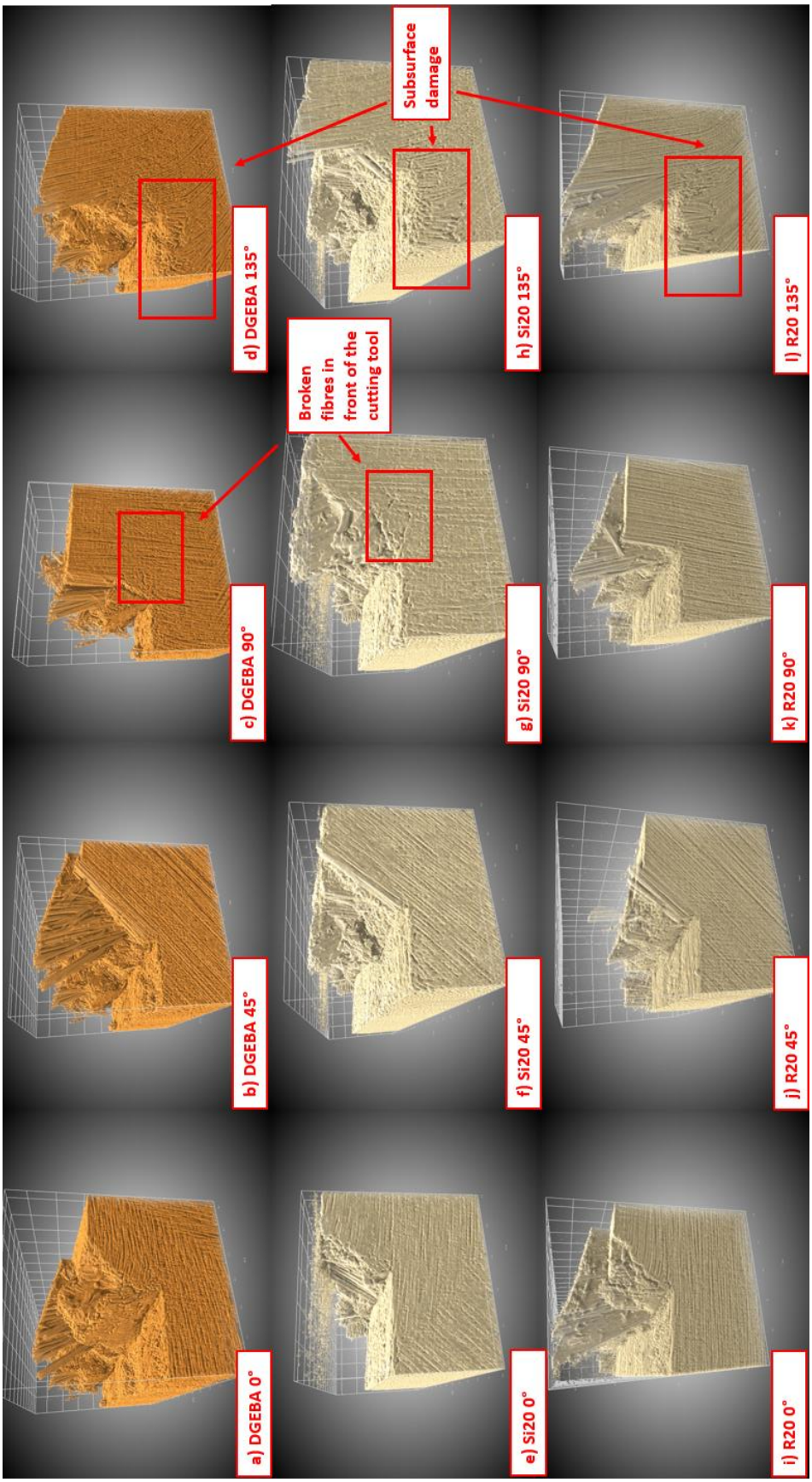

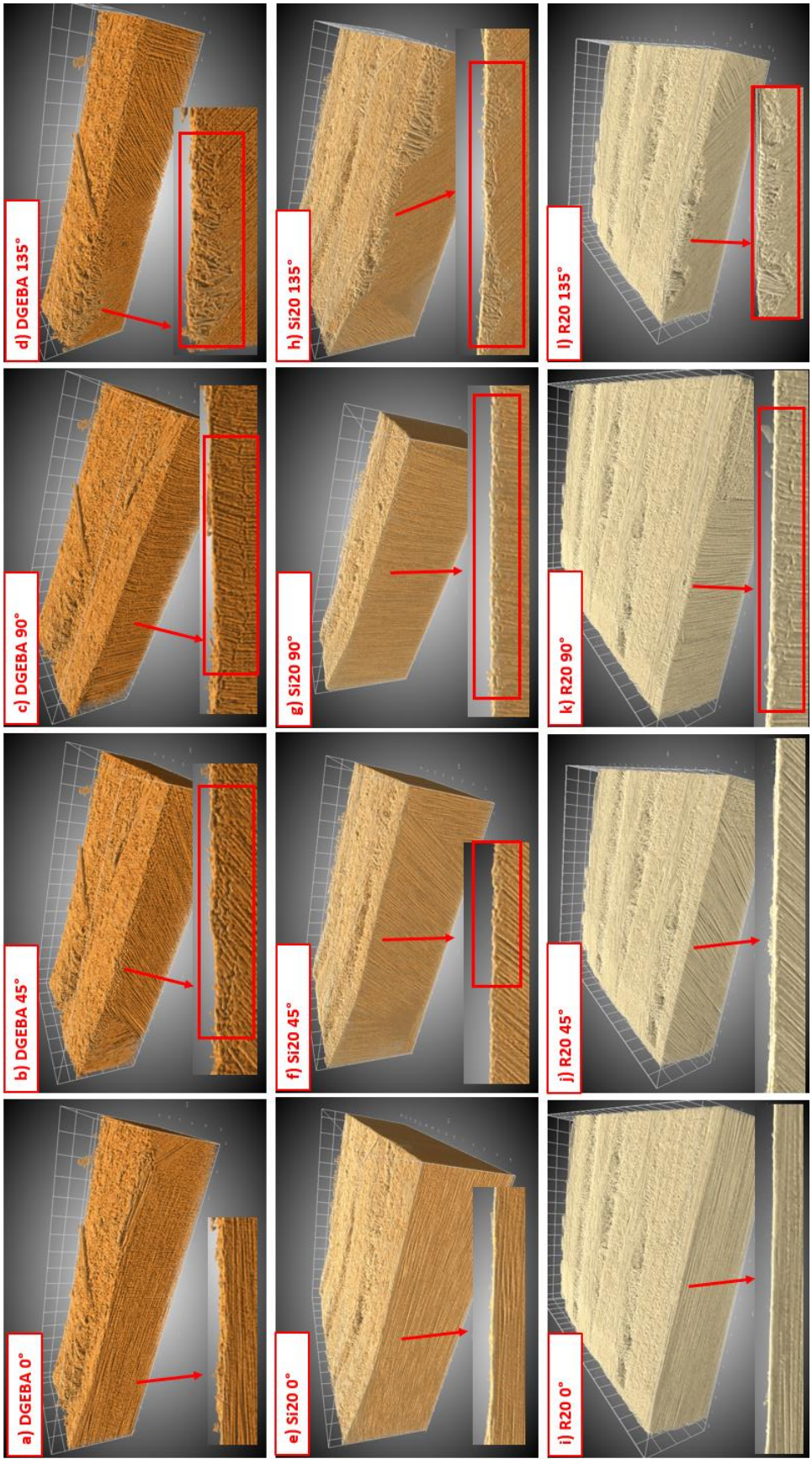
a) DGEBA 0°
b) DGEBA 45°
c) DGEBA 90°
d) DGEBA 135°
e) Si20 0°
f) Si20 45°
g) Si20 90°
h) Si20 135°
i) R20 0°
j) R20 45°
k) R20 90°
l) R20 135°

10.5 Appendix E – ANOVA model errors

General Factorial Regression	R-sq
F_x av vs %Rubber,%Silica, Feed	87.06%
F_y av vs %Rubber,%Silica, Feed	73.98%
F_z av vs %Rubber,%Silica, Feed	90.12%
S_a vs %Rubber,%Silica, Feed	83.15%
S_q vs %Rubber,%Silica, Feed	88.22%
S_v vs %Rubber,%Silica, Feed	84.58%
S_z vs %Rubber,%Silica, Feed	65.20%
S_{sk} vs %Rubber,%Silica, Feed	28.22%
S_{ku} vs %Rubber,%Silica, Feed	32.05%
S_{dq} vs %Rubber,%Silica, Feed	54.06%
S_{dr} vs %Rubber,%Silica, Feed	44.81%
S_k vs %Rubber,%Silica, Feed	93.43%
S_{pk} vs %Rubber,%Silica, Feed	32.86%
S_{vk} vs %Rubber,%Silica, Feed	73.71%
S_{mr1} vs %Rubber,%Silica, Feed	61.77%
S_{mr2} vs %Rubber,%Silica, Feed	79.05%
V_{mp} vs %Rubber,%Silica, Feed	45.74%
V_{mc} vs %Rubber,%Silica, Feed	92.59%
V_{vc} vs %Rubber,%Silica, Feed	88.07%
V_{vv} vs %Rubber,%Silica, Feed	87.20%
V_{vc}/V_{mc} vs %Rubber,%Silica, Feed	82.12%
The following terms cannot be estimated and were removed: %Rubber*%silica, %Rubber*%silica*Feed	